

# Nanomaterial Synthesis, Characterization, and Application

Guest Editors: Mahmood Ghoranneviss, Ajay Soni, Alireza Talebitaher,  
and Necdet Aslan





---

# **Nanomaterial Synthesis, Characterization, and Application**

Journal of Nanomaterials

---

# **Nanomaterial Synthesis, Characterization, and Application**

Guest Editors: Mahmood Ghoranneviss, Ajay Soni,  
Alireza Talebitaher, and Necdet Aslan



---

Copyright © 2015 Hindawi Publishing Corporation. All rights reserved.

This is a special issue published in "Journal of Nanomaterials." All articles are open access articles distributed under the Creative Commons Attribution License, which permits unrestricted use, distribution, and reproduction in any medium, provided the original work is properly cited.

## Editorial Board

- Saeid Abbasbandy, Iran  
Mina B. Abd-El-Malek, Egypt  
Mohamed A. Abdou, Egypt  
Subhas Abel, India  
Mostafa Adimy, France  
Carlos J. S. Alves, Portugal  
Mohamad Alwash, USA  
Igor Andrianov, Germany  
Sabri Arik, Turkey  
Francis T.K. Au, Hong Kong  
Olivier Bahn, Canada  
Roberto Barrio, Spain  
Alfredo Bellen, Italy  
Jafar Biazar, Iran  
Hester Bijl, The Netherlands  
Anjan Biswas, Saudi Arabia  
Stephane P.A. Bordas, USA  
James Robert Buchanan, USA  
Alberto Cabada, Spain  
Xiao Chuan Cai, USA  
Jinde Cao, China  
Alexandre Carvalho, Brazil  
Song Cen, China  
Qianshun S. Chang, China  
Tai-Ping Chang, Taiwan  
Shih-sen Chang, China  
Rushan Chen, China  
Xinfu Chen, USA  
Ke Chen, UK  
Eric Cheng, Hong Kong  
Francisco Chiclana, UK  
Jen-Tzung Chien, Taiwan  
C. S. Chien, Taiwan  
Han H. Choi, Republic of Korea  
Tin-Tai Chow, China  
M. S. H. Chowdhury, Malaysia  
Carlos Conca, Chile  
Vitor Costa, Portugal  
Livija Cveticanin, Serbia  
Eric de Sturler, USA  
Orazio Descalzi, Chile  
Kai Diethelm, Germany  
Vit Dolejsi, Czech Republic  
Bo-Qing Dong, China  
Magdy A. Ezzat, Egypt
- Meng Fan, China  
Ya Ping Fang, China  
Antonio J. M. Ferreira, Portugal  
Michel Fliess, France  
M. A. Fontelos, Spain  
Huijun Gao, China  
Bernard J. Geurts, The Netherlands  
Jamshid Ghaboussi, USA  
Pablo González-Vera, Spain  
Laurent Gosse, Italy  
K. S. Govinder, South Africa  
Jose L. Gracia, Spain  
Yuantong Gu, Australia  
Zhihong GUAN, China  
Nicola Guglielmi, Italy  
Frederico G. Guimarães, Brazil  
Vijay Gupta, India  
Bo Han, China  
Maoan Han, China  
Pierre Hansen, Canada  
Ferenc Hartung, Hungary  
Xiaoqiao He, Hong Kong  
Luis Javier Herrera, Spain  
J. Hoenderkamp, The Netherlands  
Ying Hu, France  
Ning Hu, Japan  
Zhilong L. Huang, China  
Kazufumi Ito, USA  
Takeshi Iwamoto, Japan  
George Jaiani, Georgia  
Zhongxiao Jia, China  
Tarun Kant, India  
Ido Kanter, Israel  
Abdul Hamid Kara, South Africa  
Hamid Reza Karimi, Norway  
Jae-Wook Kim, UK  
Jong Hae Kim, Republic of Korea  
Kazutake Komori, Japan  
Fanrong Kong, USA  
Vadim . Krysko, Russia  
Jin L. Kuang, Singapore  
Miroslaw Lachowicz, Poland  
Hak-Keung Lam, UK  
Tak-Wah Lam, Hong Kong  
PGL Leach, Cyprus
- Yongkun Li, China  
Wan-Tong Li, China  
J. Liang, China  
Ching-Jong Liao, Taiwan  
Chong Lin, China  
Mingzhu Liu, China  
Chein-Shan Liu, Taiwan  
Kang Liu, USA  
Yansheng Liu, China  
Fawang Liu, Australia  
Shutian Liu, China  
Zhijun Liu, China  
Julián López-Gómez, Spain  
Shiping Lu, China  
Gert Lube, Germany  
Nazim Idrisoglu Mahmudov, Turkey  
Oluwole Daniel Makinde, South Africa  
Francisco J. Marcellán, Spain  
Guiomar Martín-Herrán, Spain  
Nicola Mastronardi, Italy  
Michael McAleer, The Netherlands  
Stephane Metens, France  
Michael Meylan, Australia  
Alain Miranville, France  
Ram N. Mohapatra, USA  
Jaime E. Munoz Rivera, Brazil  
Javier Murillo, Spain  
Roberto Natalini, Italy  
Srinivasan Natesan, India  
Jiri Nedoma, Czech Republic  
Jianlei Niu, Hong Kong  
Roger Ohayon, France  
Javier Oliver, Spain  
Donal O'Regan, Ireland  
Martin Ostojja-Starzewski, USA  
Turgut Öziş, Turkey  
Claudio Padra, Argentina  
Reinaldo Martinez Palhares, Brazil  
Francesco Pellicano, Italy  
Juan Manuel Peña, Spain  
Ricardo Perera, Spain  
Malgorzata Peszynska, USA  
James F. Peters, Canada  
Mark A. Petersen, South Africa  
Miodrag Petkovic, Serbia

Vu Ngoc Phat, Vietnam  
Andrew Pickering, Spain  
Hector Pomares, Spain  
Maurizio Porfiri, USA  
Mario Primicerio, Italy  
Morteza Rafei, The Netherlands  
Roberto Renò, Italy  
Jacek Rokicki, Poland  
Dirk Roose, Belgium  
Carla Roque, Portugal  
Debasish Roy, India  
Samir H. Saker, Egypt  
Marcelo A. Savi, Brazil  
Wolfgang Schmidt, Germany  
Eckart Schnack, Germany  
Mehmet Sezer, Turkey  
Naseer Shahzad, Saudi Arabia  
Fatemeh Shakeri, Iran  
Jian Hua Shen, China  
Hui-Shen Shen, China  
Fernando Simões, Portugal  
Theodore E. Simos, Greece

Abdel-Maksoud A. Soliman, Egypt  
Xinyu Song, China  
Qiankun Song, China  
Yuri N. Sotskov, Belarus  
Peter J. C. Spreij, The Netherlands  
Niclas Strömberg, Sweden  
Ray KL Su, Hong Kong  
Jitao Sun, China  
Wenyu Sun, China  
XianHua Tang, China  
Alexander Timokha, Norway  
Mariano Torrisi, Italy  
Jung-Fa Tsai, Taiwan  
Ch Tsitouras, Greece  
Kuppalapalle Vajravelu, USA  
Alvaro Valencia, Chile  
Erik Van Vleck, USA  
Ezio Venturino, Italy  
Jesus Vigo-Aguiar, Spain  
Michael N. Vrahatis, Greece  
Baolin Wang, China  
Mingxin Wang, China

Qing-Wen Wang, China  
Guangchen Wang, China  
Junjie Wei, China  
Li Weili, China  
Martin Weiser, Germany  
Frank Werner, Germany  
Shanhe Wu, China  
Dongmei Xiao, China  
Gongnan Xie, China  
Yuesheng Xu, USA  
Suh-Yuh Yang, Taiwan  
Bo Yu, China  
Jinyun Yuan, Brazil  
Alejandro Zarzo, Spain  
Guisheng Zhai, Japan  
Jianming Zhan, China  
Zhihua Zhang, China  
Jingxin Zhang, Australia  
Shan Zhao, USA  
Chongbin Zhao, Australia  
Renat Zhdanov, USA  
Hongping Zhu, China

## Contents

**Nanomaterial Synthesis, Characterization, and Application**, Mahmood Ghoranneviss, Ajay Soni, Alireza Talebitaher, and Necdet Aslan  
Volume 2015, Article ID 892542, 2 pages

**Arc-Discharge Synthesis of Iron Encapsulated in Carbon Nanoparticles for Biomedical Applications**, S. Chaitoglou, M. Reza Sanaee, N. Aguiló-Aguayo, and E. Bertran  
Volume 2014, Article ID 178524, 8 pages

**Horizontal Assembly of Single Nanowire Diode Fabricated by *p-n* Junction GaN NW Grown by MOCVD**, Ji-Hyeon Park, Suthan Kissinger, Yong Ho Ra, Kang San, Min Ji Park, Kyung-Hwa Yoo, and Cheul-Ro Lee  
Volume 2014, Article ID 951360, 9 pages

**Improving the Microstructure and Electrical Properties of Aluminum Induced Polysilicon Thin Films Using Silicon Nitride Capping Layer**, Min-Hang Weng, Cheng-Tang Pan, Chien-Wei Huang, and Ru-Yuan Yang  
Volume 2014, Article ID 342478, 9 pages

**Upconversion luminescence and Visible-Infrared Properties of  $\beta$ -NaLuF<sub>4</sub>:Er<sup>3+</sup> Microcrystals Synthesized by the Surfactant-Assisted Hydrothermal Method**, Han Lin, Xiaohong Yan, Jin Zheng, Changjie Dai, and Yuan Chen  
Volume 2014, Article ID 903208, 11 pages

**Application of Gold Nanoparticles for Electrochemical DNA Biosensor**, Ahmed Mishaal Mohammed, Ruslinda A. Rahim, Ibraheem Jaleel Ibraheem, Foo Kai Loong, Hasrul Hisham, Uda Hashim, and Yarub Al-Douri  
Volume 2014, Article ID 683460, 7 pages

**Synthesis of Nanocobalt Powders for an Anode Material of Lithium-Ion Batteries by Chemical Reduction and Carbon Coating**, Seong-Hyeon Hong, Yeong-Mi Jin, Kyung Tae Kim, Cheol-Woo Ahn, Dong-Su Park, and Myoung Youp Song  
Volume 2014, Article ID 378103, 8 pages

**Efficient Rapid Microwave-Assisted Route to Synthesize Monodispersive Pt Nanoparticles and Their Electrocatalytic Activity for Methanol Oxidation**, Libin Wang, Wenjun Xu, Xiao Wu, Qian Li, Zhiming Wang, and Xiuwen Zheng  
Volume 2014, Article ID 401617, 5 pages

**Radiolytic Preparation of Electrocatalysts with Pt-Co and Pt-Sn Nanoparticles for a Proton Exchange Membrane Fuel Cell**, Sang Kyum Kim, Ji Yun Park, Soon Choel Hwang, Do Kyun Lee, Sang Heon Lee, Moon Hee Han, and Young Woo Rhee  
Volume 2014, Article ID 960379, 8 pages

**Optimization of the Electrodeposition Parameters to Improve the Stoichiometry of In<sub>2</sub>S<sub>3</sub> Films for Solar Applications Using the Taguchi Method**, Maqsood Ali Mughal, M. Jason Newell, Joshua Vangilder, Shyam Thapa, Kayla Wood, Robert Engelken, B. Ross Carroll, and J. Bruce Johnson  
Volume 2014, Article ID 302159, 10 pages

**A Novel Approach to the Fabrication of CdSe Quantum Dots in Aqueous Solution: Procedures for Controlling Size, Fluorescence Intensity, and Stability over Time**, M. J. Almendral-Parra, A. Alonso-Mateos, J. F. Boyero-Benito, S. Sánchez-Paradinas, and E. Rodríguez-Fernández  
Volume 2014, Article ID 397469, 7 pages

**Sm:HAP Nanopowders Present Antibacterial Activity against *Enterococcus faecalis***, Carmen Steluta Ciobanu, Cristina Liana Popa, and Daniela Predoi  
Volume 2014, Article ID 780686, 9 pages

**Hydrothermal Synthesis, Characterization, and Optical Properties of Ce Doped Bi<sub>2</sub>MoO<sub>6</sub> Nanoplates**, Anukorn Phuruangrat, Nuengruethai Ekthammathat, Budsabong Kuntalue, Phattranit Dumrongrojthanath, Somchai Thongtem, and Titipun Thongtem  
Volume 2014, Article ID 934165, 7 pages

**Probing Photocatalytic Characteristics of Sb-Doped TiO<sub>2</sub> under Visible Light Irradiation**, Lingjing Luo, Tianfeng Li, Xia Ran, Pan Wang, and Lijun Guo  
Volume 2014, Article ID 947289, 6 pages

**Synthesis and Characterization of Hollow Magnetic Alloy GdNi<sub>2</sub>, Co<sub>5</sub>Gd Nanospheres Coated with Gd<sub>2</sub>O<sub>3</sub>**, Wang Li, Fa-gen Li, Jun Wang, and Guo-meng Zhao  
Volume 2014, Article ID 604035, 9 pages

**Indium-Nitrogen Codoped Zinc Oxide Thin Film Deposited by Ultrasonic Spray Pyrolysis on n-(111) Si Substrate: The Effect of Film Thickness**, Cheng-Chang Yu, Wen-How Lan, and Kai-Feng Huang  
Volume 2014, Article ID 861234, 7 pages

**Synthesis of Vertically Aligned Carbon Nanotubes on Silicalite-1 Monolayer-Supported Substrate**, Wei Zhao, Bijay Basnet, Sukyoung Kim, and Ik Jin Kim  
Volume 2014, Article ID 327398, 5 pages

## Editorial

# Nanomaterial Synthesis, Characterization, and Application

**Mahmood Ghoranneviss,<sup>1</sup> Ajay Soni,<sup>2</sup> Alireza Talebitaher,<sup>3</sup> and Necdet Aslan<sup>4</sup>**

<sup>1</sup>Plasma Physics Research Center, Islamic Azad University, Science & Research Branch, Tehran, Iran

<sup>2</sup>School of Basic Sciences, Indian Institute of Technology Mandi, Himachal Pradesh, Mandi 175001, India

<sup>3</sup>Energy Research Institute, Nanyang Technological University, 1 CleanTech Loop, Singapore 637141

<sup>4</sup>Physics Department, Yeditepe University, 34755 Istanbul, Turkey

Correspondence should be addressed to Mahmood Ghoranneviss; ghoranneviss@gmail.com

Received 27 November 2014; Accepted 27 November 2014

Copyright © 2015 Mahmood Ghoranneviss et al. This is an open access article distributed under the Creative Commons Attribution License, which permits unrestricted use, distribution, and reproduction in any medium, provided the original work is properly cited.

Nanotechnology is a promising science with wide applications from cosmetics, food products, clothing, and household appliances to fuel catalyst, disease treatment, and renewable energies. Nanotechnology is also being applied to a variety of industrial and purification processes including construction materials, nanomachining of nanowires, nanorods, graphene, water filtration, and wastewater treatment.

Their applications are becoming wider in “nanomedicine” by interfacing the nanomaterials with biological molecules or structures, “green technology” to enhance the environmental sustainability and “renewable energy” to develop the new ways to capture, store, and transfer energy. For instance, carbon nanotube productions have been used for applications in energy storage, automotive parts, thin-film electronics, coatings, and so forth.

Nanomaterials are found as important and keep growing in the field of Nanoscience and Nanotechnology and in recent years researchers are investing much effort on the synthesis and applications of various nanomaterials, due to their potential applications in science and industry. For example, biocompatible nanomaterials are applied directly or they are used to replace natural materials to function or to be in contact with the living systems.

This special issue provides some new research and developments in nanomaterials. It presents the principles of the synthesis and fabrication of self-assembly nanostructures and their applications and also some important tools and challenges associated with these techniques for engineers and scientists.

First group of papers are explaining some novel approaches to enhance the optical and physical parameters of material with different techniques. For instance, one paper describes a synergistic effect combining dual-mode (down- and upconversion) with enhancement rate of the red emission in hexagonal prisms  $\beta$ -NaLuF<sub>4</sub>:Er<sup>3+</sup> phosphors by employing the dual wavelength source. Another one describes the optimization of the parameters voltage, time, solution composition, and temperature on the properties of electrodeposited semiconductor thin films such as ECD In<sub>2</sub>S<sub>3</sub> with respect to the layer stoichiometry which can be applied to manifold optimizations.

Second group of papers are about the thin films and their physical properties. One tried to describe how monodisperse magnetic Fe<sub>3</sub>O<sub>4</sub> nanoparticles can be used as the catalysts for the synthesis of vertically aligned carbon nanotube arrays and another investigated the capping layer effect of silicon-nitrogen on the microstructure and electrical and optical properties of polycrystalline silicon prepared by aluminum induced crystallization and showed the improvement of the grain growth with reduction of the metal content in the induced polycrystalline silicon film.

The third group of papers addresses the new techniques of nanomaterials fabrication for electronics and magnetic application where one of them explains the synthesis of axially p-n junction gallium nitride nanowires via metal-organic chemical vapor deposition method and shows a substantial increase in conductance under UV light exposure with extremely short response time, and the other one addresses

the preparation of highly monodispersive Pt nanoparticles via two facile and environmental-friendly procedures which show very high catalytic activity for a methanol oxidation reaction and have a great potential for preparing other metal and alloy NPs.

*Mahmood Ghoranneviss*

*Ajay Soni*

*Alireza Talebitaher*

*Necdet Aslan*

## Research Article

# Arc-Discharge Synthesis of Iron Encapsulated in Carbon Nanoparticles for Biomedical Applications

S. Chaitoglou,<sup>1</sup> M. Reza Sanaee,<sup>1</sup> N. Aguiló-Aguayo,<sup>1,2</sup> and E. Bertran<sup>1</sup>

<sup>1</sup>FEMAN Group, IN2UB, Departament de Física Aplicada i Òptica, Universitat de Barcelona, Martí i Franquès 1, E08028 Barcelona, Catalonia, Spain

<sup>2</sup>Institut für Textilchemie und Textilphysik, Universität Innsbruck, HöchsterstraÙ 73, 6850 Dornbirn, Austria

Correspondence should be addressed to S. Chaitoglou; [schaitog@gmail.com](mailto:schaitog@gmail.com)

Received 24 January 2014; Revised 22 June 2014; Accepted 23 June 2014; Published 13 July 2014

Academic Editor: Ajay Soni

Copyright © 2014 S. Chaitoglou et al. This is an open access article distributed under the Creative Commons Attribution License, which permits unrestricted use, distribution, and reproduction in any medium, provided the original work is properly cited.

The objective of the present work is to improve the protection against the oxidation that usually appears in core@shell nanoparticles. Spherical iron nanoparticles coated with a carbon shell were obtained by a modified arc-discharge reactor, which permits controlling the diameter of the iron core and the carbon shell of the particles. Oxidized iron nanoparticles involve a loss of the magnetic characteristics and also changes in the chemical properties. Our nanoparticles show superparamagnetic behavior and high magnetic saturation owing to the high purity  $\alpha$ -Fe of core and to the high core sealing, provided by the carbon shell. A liquid iron precursor was injected in the plasma spot dragged by an inert gas flow. A fixed arc-discharge current of 40 A was used to secure a stable discharge, and several samples were produced at different conditions. Transmission electron microscopy indicated an iron core diameter between 5 and 9 nm. Selected area electron diffraction provided evidences of a highly crystalline and dense iron core. The magnetic properties were studied up to 5 K temperature using a superconducting quantum interference device. The results reveal a superparamagnetic behaviour, a narrow size distribution ( $\sigma_g = 1.22$ ), and an average diameter of 6 nm for nanoparticles having a blocking temperature near 40 K.

## 1. Introduction

In the recent years the superparamagnetic particles appear to be important agents for a variety of applications in the fields of drug delivery, magnetic resonance imaging (MRI), and cancer treatments like hyperthermia. This is due to the special magnetic characteristic of these particles. That is the reason of our interest in studying the size limits under which the nanoparticles present a superparamagnetic behaviour [1].

In order to synthesize nanoparticles in the vapor phase, appropriate conditions should be created. Like in the case described in the capillary theory of nucleation and under supersaturation conditions, a vapor phase mixture in thermal plasma (arc-discharge) can become thermodynamically unstable giving place to a nucleation process [2]. From that and setting particular conditions, it is possible to produce solid phase homogeneous particles in the vapor phase surrounding the hot spot of the arc-discharge.

The method varies depending on the phase of the precursor we are interested to use.

Here, the precursor is injected into thermal plasma which provides the necessary conditions to induce reactions that lead to supersaturation and particle nucleation. Under the condition of thermal plasma, the precursor decomposes in radicals, atoms, and ions forming a high temperature ionized gas. The high concentration of species and high temperatures in the plasma arc induce a diffusion process associated with a fast quenching of gas species. During this process, the gas species react and condense to form particles in a similar way to a vaporized material when cooled down by mixing with a cool gas or expanded through a nozzle [3].

The objective of this work is the control of the synthesis of iron encapsulated in carbon nanoparticles, regarding the size of the Fe core, the diameter of the C shell, and moreover the quantity of the obtained nanoparticles. Fe is one of the most common materials used for the formation of magnetic

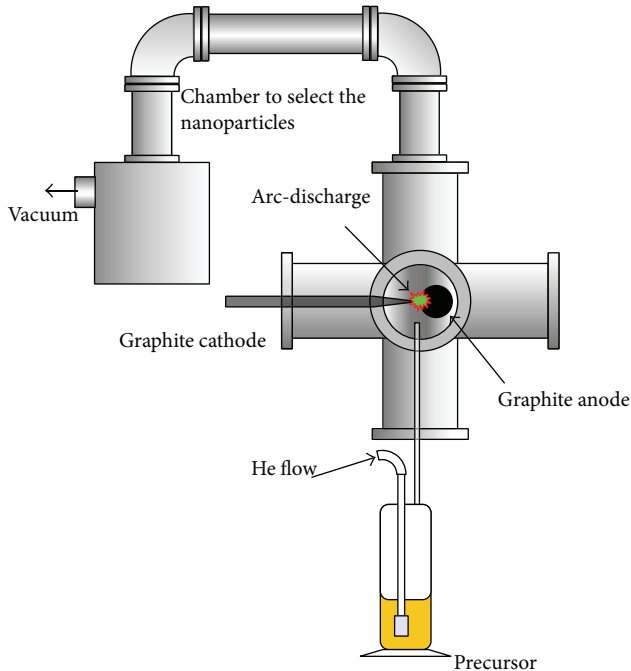


FIGURE 1: General picture of the “home made” reactor we used for the synthesis of the iron encapsulated in carbon nanoparticles.

nanoparticles. It is due to its superparamagnetic behaviour, which is easily controlled by the nanometric size of the magnetic core, and because the Fe is suitable for biomedical applications. The use of a carbon shell is intended to achieve the required biocompatibility and prevents oxidation of the iron core and formation of agglomerations of nanoparticles [4].

The structural and morphological characteristics like shape and size distribution were studied using transmission electron microscopy (TEM) and selected area electron diffraction (SAED). The absence of oxygen was preliminarily evidenced by the energy-dispersive X-ray analysis (STEM-EDX). The magnetic characteristics were determined using a superconducting quantum interference device (SQUID).

## 2. Materials and Methods

In order to facilitate the study of magnetic behavior and other characteristics of core@shell nanoparticles, we modified an arc-discharge reactor in order to operate for longer time and produce bigger amounts of them (Figure 1).

To facilitate the complete collection of the produced nanoparticles we dragged them out of the arc-discharge chamber, by a laminar flow of an inert gas (He) to a flask cooled by liquid nitrogen. The flow of the dragging gas that we used was 3 L/min of volumetric flow of He (at 1 atm), providing a moderated velocity of 65 cm/s in the nozzle outlet. The precursor was in the gas phase. Helium is used to drag microdroplets of ferrocene. The carbon electrodes can be rotated and moved in order to avoid problems that the consumption of carbon could cause. One of the electrodes

TABLE 1: Flow rate and resulting velocity and residence time for a precursor vapor with 1% of ferrocene concentration.

He flow rate, $\Phi$ (mL/min)	Precursor vapor velocity, $U$ (cm/s)	Residence time, $\tau$ (ms)
$30 \pm 2$	$7.07 \pm 0.50$	$71 \pm 1.5$
$60 \pm 2$	$14.13 \pm 0.50$	$35 \pm 1.5$
$120 \pm 2$	$28.28 \pm 0.50$	$18 \pm 1.5$

has a sharp conical tip shape (cathode) and the other has a cylindrical shape with an approximate diameter of 4 mm and can rotate and move backward and forward (anode). The plasma is being generated by a power supply to produce an arc DC current of 40 A.

The pressure was kept stable at near-atmospheric conditions ( $5\text{--}8 \times 10^4$  Pa). The run period of one experiment was 30 min. Although, to obtain more quantity of product, in principle we can extend the time, it requires having stable conditions during the production process. We used pure He to drag the precursor compound because plasma becomes more stable [5].

We investigated the effects of two technological parameters, the concentration of the Fe precursor into the solvent isooctane and the total gas flow (He).

Both the isooctane and the Fe precursor (ferrocene) were of a purity of 99.9%.

Residence time is the period that the nucleus of the precursor is spending inside the plasma zone. The time that gas atoms and precursor radicals stay inside the plasma zone depends on the gas flow rate. This has an effect on the size of the particles as the longer they stay inside the plasma zone, the larger they grow [6].

The velocity  $u$  and the He flow rate,  $\Phi$ , are related through the equation

$$u = \frac{4\Phi}{\pi d^2}, \quad (1)$$

where  $d$  is the internal diameter of the cannula through which the gas is targeted in the plasma zone ( $\sim 3$  mm).

By measuring the size of the plasma zone  $h$  ( $\sim 5$  mm) we can estimate the residence time:

$$\tau = \frac{h}{u}. \quad (2)$$

Table 1 shows the different residence times for several values of He flow rate.

Different concentrations of Fe precursor into the isooctane, from 1% to 4% w/w, were used to determine the effect on the size of the particles and on the total amount of the obtained product.

## 3. Results and Discussion

Images of nanoparticles were observed by TEM (JEOL 2100) in high resolution mode, using 200 kV and a probe size of 0.5 nm [7]. Prior to TEM observations, the formed nanoparticles were diluted in methanol and then magnetically filtrated.

TABLE 2: The iron core diameter average and its standard deviation of all our samples in relation to the two set parameters, He flow rate and ferrocene/isooctane concentration. Samples with  $1.1 < \sigma_g < 1.4$  are quite monodisperse. Samples having  $\sigma_g$  above 1.4 (He flow of 60 sccm and low ferrocene concentration) are bimodal.

He flow rate (sccm)	Iron core size (nm)/geometric standard deviation, $\sigma_g$		
	[Ferrocene/isooctane] 1% w/w	[Ferrocene/isooctane] 2% w/w	[Ferrocene/isooctane] 4% w/w
30	8.18/1.22 (Figure 2(a))	5.43/1.34 (Figure 2(b))	5.34/1.33 (Figure 2(c))
60	6.23/1.47	6.12/1.46	5.22/1.22 (Figure 3)
120	5.22/1.25	—	—

The size distribution of the nanoparticles follows the lognormal function described by Granqvist and Buhrman [8]:

$$f(D) = \frac{1}{\sqrt{2D} \ln \sigma_g} \exp\left(-\frac{\ln^2(D/\bar{D})}{2 \ln^2 \sigma_g}\right). \quad (3)$$

Here,  $D$  is the particle diameter,  $\bar{D}$  is the geometric mean, which in a lognormal distribution is equal to its median, and  $\sigma_g$  is the geometric standard deviation (dimensionless) which describes how spread out are the set of core diameters from the geometric mean. Figure 2 shows several pictures as example of the obtained particles for different flows and concentrations. Figure 2(a) shows a TEM image of nanoparticles obtained with a precursor flow of 30 mL/min, in a concentration of 1% w/w. Actually, this is the only sample that presents an important difference in the size distribution from all the others (average diameter of 8.18 nm). When the precursor concentration was doubled to 2% w/w, the iron core average size decreased to 5.43 nm (Figure 2(b)). Figure 2(a) shows how the carbon forms a shell around the Fe core. The shell of carbon in this sample is measured to be between 4 and 6 nm thick. After doubling the precursor concentration to 4% w/w, the size of these particles remains quite constant to 5.34 nm, but the total amount and density of nanoparticles increase (Figure 2(c)). From Table 2, when the precursor concentration is kept to 1% w/w, an increase of the He flow produces a decrease in the iron core size. Residence time can explain this behavior only for conditions of low precursor concentrations. At higher precursor concentrations, residence time seems to have no influence on the iron core size. This behavior could be associated with the increase of the nucleation inducing an increase in the particle concentration, as evidenced by comparing Figures 2(b) and 2(c). This phenomenon could be related to the reduction of the supersaturation conditions, establishing a competitive mechanism limiting the resulting iron core size.

Another detail in the micrographs of Figure 2 is the absence of coalescence. This indicates a low concentration of nucleus during the growth process for the conditions listed in Table 2.

By treating all the size distribution results with ORIGIN tools,  $\bar{D}$  and  $\sigma_g$  were determined. To measure the diameter of the nanoparticles we used ImageJ, a free software tool for

image processing and analysis. Figure 3 shows the histogram of the size distribution for the nanoparticles which have been synthesized under a precursor flow of 60 mL/min and a ferrocene concentration of 4% w/w. The resulting geometric size average is 5.22 nm and the geometric standard deviation 1.22.

All the studied samples (Table 2) present a size distribution of the iron core between 5.22 nm and 8.18 nm. This could be due to the stabilization of the growth of the carbon shell after reaching the critical radius of a carbon sphere. Under this hypothesis, the formation of a stable carbon shell would limit the Fe core growth. According to the studies reported by Kuznetsov et al. [9], the nucleation of carbon on the surface of the metal catalyst is something common for all kinds of carbon deposits. The difference in morphology of the carbon deposits depends on the reaction conditions and on the nature of the metal catalyst. A thermodynamic analysis of the effect of different reaction parameters on the critical radius of the carbon nucleus was performed and showed that an increase in the temperature can be responsible for the formation of smaller nuclei.

Another interesting fact supporting the formation of a carbon shell on the iron nanoparticles is that the use of metals, which are characterized by a higher metal-carbon energy bond, yields nanotubes of smaller radius [9]. In these studies, the critical radius of the carbon is related to the change in Gibbs free energy during the nucleation [9]. The only sample that seems not to follow this assumption is the one grown under conditions of 1% w/w of Fe concentration and precursor flow of 30 mL/min. This result could be related to the higher residence time associated with a low flow rate, which leads to an increase in the core size and a delay in reaching the conditions of carbon supersaturation located outside the hot plasma region.

To discuss the size distribution of our samples we can rely on the geometric standard deviation,  $\sigma_g$ . The results of size and dispersion of iron cores along with their experimental parameters are listed in Table 2. A geometric standard deviation lower than 1.1 indicates a monodisperse size distribution, whereas for values above 1.4 indicates a wide distribution of size. Between these two values the size distribution is considered quite monodispersed. When the dispersion is larger than 1.4, the size distribution is considered to be

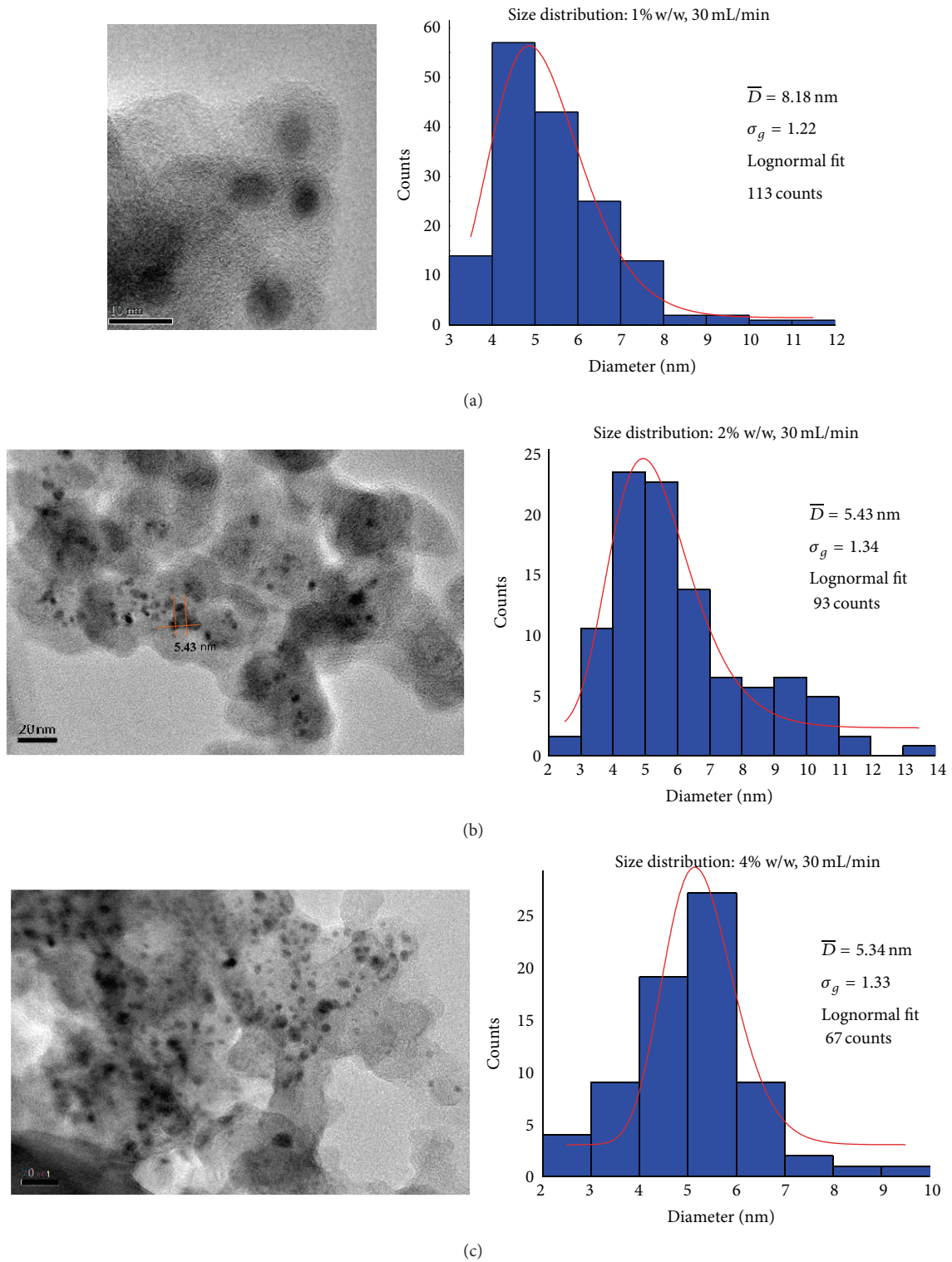


FIGURE 2: TEM images of iron encapsulated in carbon nanoparticles produced by arc-discharge ( $40 \pm 5$  A of current) using different flows and concentrations accompanied by their size distribution histograms. (a) 30 mL/min with a concentration of 1% w/w, (b) 30 mL/min with a precursor concentration of 2% w/w, and (c) 30 mL/min with a concentration of 4% w/w.

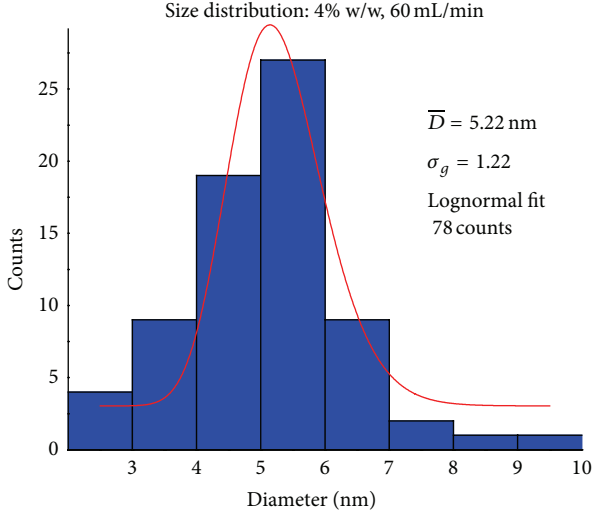


FIGURE 3: Histogram of the size distribution for iron nanoparticles grown under precursor concentration of 4% w/w and He flow of 60 mL/min. The iron core is 5.22 nm and the geometric standard deviation  $\sigma$  1.22.

bimodal [10]. Table 2 lists the level of dispersion of the different samples.

The absence of oxygen in the spectrum was preliminarily evidenced by the energy-dispersive X-ray analysis (STEM-EDX). Oxygen peak is not present in the spectrum in the expected energy (O-K $\alpha$  at 525 eV), which indicates a low level of oxygen. In addition, an HRTEM picture of a iron encapsulated in carbon nanoparticle was taken (Figure 4). To obtain the crystal structure of the iron core and the carbon shell, we calculated its fast Fourier transform (inset of Figure 4). The only phases evidenced from this figure were the  $\alpha$ -Fe ( $d$ -spacing = 0,202 nm) and the iron carbide ( $d$ -spacing = 0,221 nm). No diffraction points of iron oxides were detected [11] in any of our samples. The phases of iron carbide probably are located in the interface between the iron core and the carbon shell. As we comment below from the magnetic measurements, the content of the iron carbide phase is minor if compared with the  $\alpha$ -Fe.

In addition carbon shell appears surrounding completely the iron cores forming crystalline domains with a structure similar to the fullerene one.

This result suggests that iron core is completely sealed into the cover shell, which is of great importance and interest in biomedical applications [12].

SQUID measurements were used to investigate the magnetic characteristics of our samples. Two hysteresis loops (Figure 5) of different samples were studied to compare their characteristics. Samples of Figures 5(a) and 5(b) were produced by means of a precursor gas flow of 30 mL/min and with a precursor concentration of 1% w/w and 2% w/w, respectively.

From the hysteresis loop measured by SQUID at 5 K we have obtained the coercive field  $H_C$ . For the sample of the 2% w/w concentration having a diameter 5.43 nm, this is 0.03 T and, for the sample of 1% w/w with a diameter

of 8.18 nm, it is 0.05 T. These results come in agreement with other results which indicates the influence of the size on the magnetization when it comes to superparamagnetic nanoparticles [13].

Subsequently we compare the values of the coercive field with those reported in the bibliography for magnetic nanoparticles encapsulated in carbon nanotubes [14]. We have calculated the critical radius of the iron consisting of uniaxial nanoparticles. To achieve this, we use the Neel-Arrhenius equation [15] for blocking temperatures  $T_B = 40$  K and  $k_B = 1.380 \cdot 10^{-23}$  J/K assumed. Then, from the equation,

$$T_B = \frac{K \cdot V}{k_B \cdot \log(t_m/t_0)}, \quad (4)$$

where the factor  $\log(t_m/t_0) = 25$ ,  $t_m$  is the measuring time of the SQUID (100 s), and  $t_0$  is the characteristic relaxation time. The value  $K$  is the anisotropy energy density ( $K = 4.8 \times 10^4$  J/m<sup>3</sup> for Fe bulk) and the volume is as follows:

$$V = \frac{4\pi d^3}{3 \cdot 8}, \quad (5)$$

where  $d$  is the diameter of the core. From the above relations the critical radius is calculated to be 4.09 nm. The theoretical graph shows the connection of the radius of the nanoparticles to  $H_C$  and the comparison with the values of the samples shows an agreement. To obtain the curve, the following equation is used [16]:

$$H_C = H_{CO} \left[ 1 - \left( \frac{D_p}{D} \right)^{3/2} \right]. \quad (6)$$

In this equation,  $H_{CO}$  is the field that should be applied in order to demagnetize the bulk material,  $D_p$  is the critical radius below which our particles become superparamagnetic, and  $D$  is the real radius of the sample. For particles of 5.43 nm we expect a coercive field  $H_C = 0.035$  T. The coercive field from our sample of this size is measured to be 0.030 T, which is a value very close to the theoretical one. For nanoparticles of a diameter around 8.1 nm the theoretical value of  $H_C$  is expected to be 0.053 T. The value of our sample of this diameter is 0.050 T which is also in agreement with the theoretical one. In the case of very small nanoparticles, one can observe superparamagnetic behavior related to the fact that a demagnetization effect arises from the additional energy of the magnetic fields outside the graphitic carbon encapsulation [17].

SQUID measurements of a sample in concentration of 1%, in a precursor gas flow of 60 mL/min, and in temperatures of 5 and 300 K were taken. In Figure 6 the normalized magnetization versus the applied field can be seen. The ratio of remnant to saturation magnetization both at 5 K and in room temperature is 0.9, less than 0.25 which is the value for the paramagnetic materials, so the carbon-coated iron nanoparticles are superparamagnetic materials [18].

From the zero field cooled and the field cooled curve it can be seen that the nanoparticles are superparamagnetic in room temperature. The blocking temperature appears near 40 K, where the maximum of the ZFC magnetization is localised.

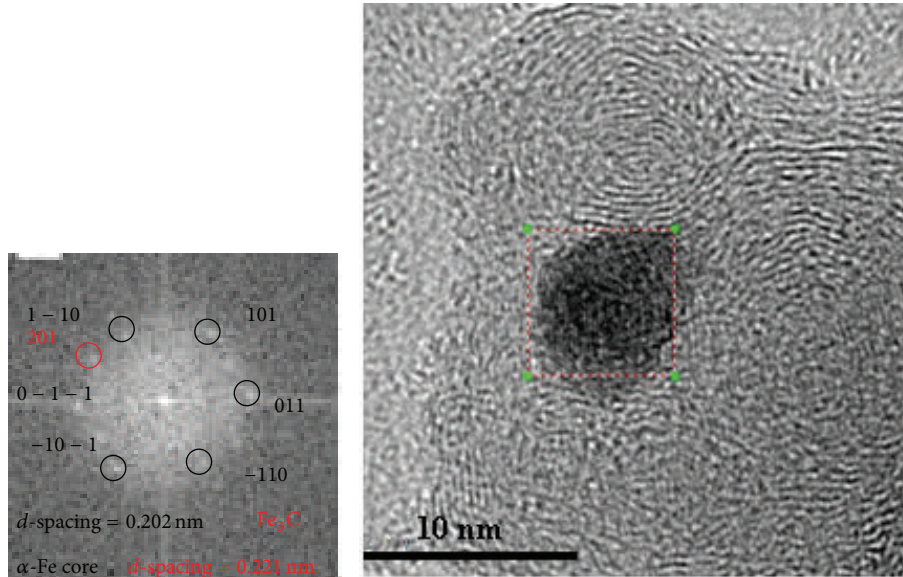


FIGURE 4: TEM image of a nanoparticle. In the small picture we can see the diffraction pattern from which we obtain the crystalline structure of the iron core. Here it corresponds to the  $\alpha$ -phase.

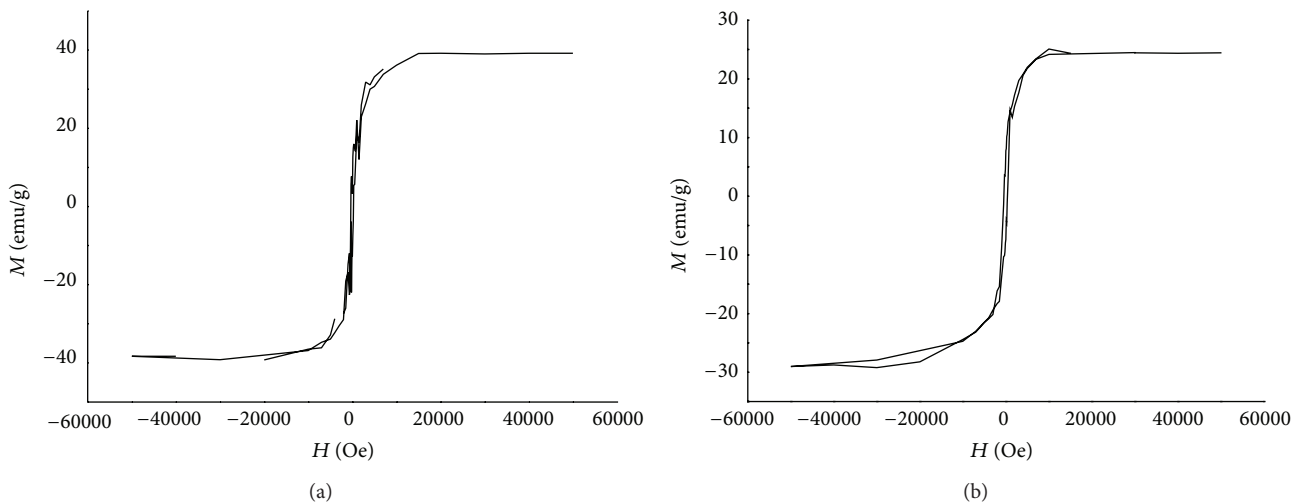


FIGURE 5: The hysteresis loops measured at 5 K for samples with different precursor concentrations: (a) 1% w/w and (b) 2% w/w. Both were obtained at a precursor gas flow of 30 mL/min.

Gittleman's model describes blocking temperature and the critical volume that separates nanoparticles from the blocked state ( $V > V_P$ ) and superparamagnetic state ( $V_P > V$ ) [19]. Also, as the peak of the zero field cooled curve is quite narrow, we can assume that the size distribution is narrow as well (Figure 7) [20].

#### 4. Conclusions

Our proposed synthesis method provides us with the capability of a very good control in the size of the synthesized nanoparticles. Morphological and structural characterization revealed a quite good monodispersity as well as the  $\alpha$ -phase crystallinity of the iron core, the iron carbide phase, and the

absence of oxygen. These are very important factors when it comes to large scale productions, necessary for biomedical applications. The iron core is completely shielded by carbon. The magnetic characterization revealed the superparamagnetic behavior of the particles in temperatures above 300 K. Further research will be done concerning the improvement of the collection process of the nanoparticles in order to have the highest amounts possible per experimental round.

#### Conflict of Interests

The authors declare that there is no conflict of interests regarding the publication of this paper.

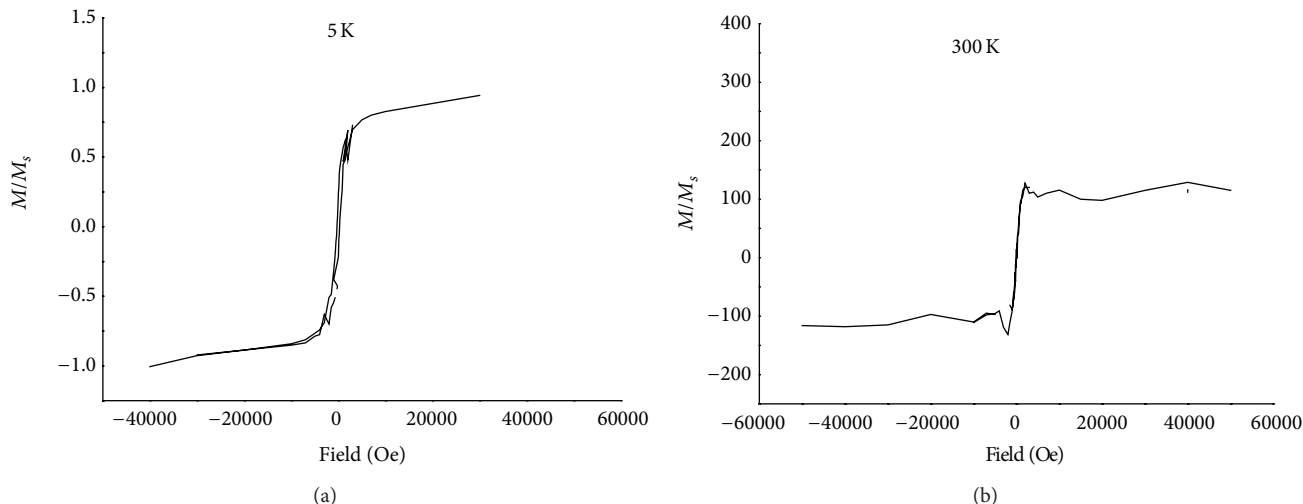


FIGURE 6: Graphs of the normalized magnetization  $M/M_s$  ratio with the field in 5 K and room temperature.

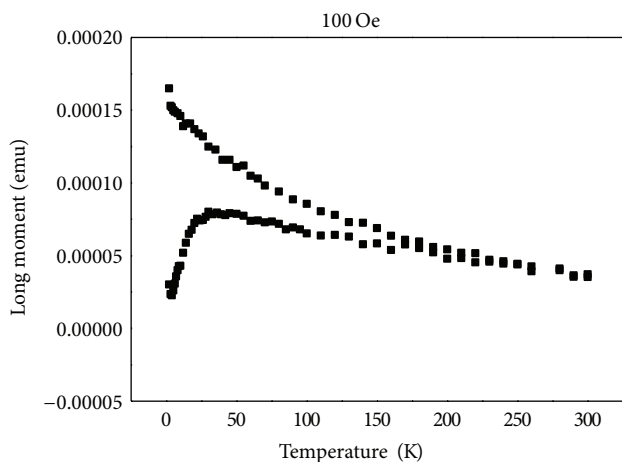


FIGURE 7: Zero fields cooled and the field cooled magnetization curves for 100 Oe field.

## Acknowledgments

This work was supported by AGAUR of Generalitat de Catalunya, Project 2009SGR00185, and by MICINN of Spanish Government, Projects CTQ2009-14674-CO2-01 and CSD2006-12. The authors would like to thank the State Scholarships Foundation of Greece (IKY) for the financial support. Also, they would like to thank the people of the Centres Científics i Tecnològics de la UB, CCiTUB, and Nuria Clos for the help with the SQUID measurements.

## References

- [1] C. Martínez-Boubeta, K. Simeonidis, M. Angelakeris et al., "Critical radius for exchange bias in naturally oxidized Fe nanoparticles," *Physical Review B*, vol. 74, no. 5, Article ID 054430, 2006.
- [2] B. I. Kharisov, H. V. Rasika Dias, O. V. Kharissova, V. Manuel Jiménez-Pérez, B. Olvera Pérez, and B. Muñoz Flores, "Iron-containing nanomaterials: synthesis, properties, and environmental applications," *RSC Advances*, vol. 2, no. 25, pp. 9325–9358, 2012.
- [3] M. T. Swihart, "Vapor-phase synthesis of nanoparticles," *Current Opinion in Colloid and Interface Science*, vol. 8, no. 1-2, pp. 127–133, 2003.
- [4] N. Sounderya and Y. Zhang, "Use of core/shell structured nanoparticles for biomedical applications," *Recent Patents on Biomedical Engineering*, vol. 1, pp. 34–42, 2008.
- [5] Y. Ando and X. Zhao, "Synthesis of carbon nanotubes by arc-discharge method," *New Diamond and Frontier Carbon Technology*, vol. 16, no. 3, pp. 123–137, 2006.
- [6] M. Vardelle, A. Vardelle, P. Fauchais, K. Li, B. Dussoubs, and N. J. Themelis, "Controlling particle injection in plasma spraying," *Journal of Thermal Spray Technology*, vol. 10, no. 2, pp. 267–284, 2001.
- [7] <http://www.jeol.com/products/electronoptics/transmissionelectronmicroscopem/200kv/jem2100f/tabid/124/default.aspx>.
- [8] C. G. Granqvist and R. A. Buhrman, "Log-normal size distributions of ultrafine metal particles," *Solid State Communications*, vol. 18, no. 1, pp. 123–126, 1976.
- [9] V. L. Kuznetsov, A. N. Usoltseva, A. L. Chuvilin et al., "Thermodynamic analysis of nucleation of carbon deposits on metal particles and its implications for the growth of carbon nanotubes," *Physical Review B. Condensed Matter and Materials Physics*, vol. 64, no. 23, Article ID 235401, 2001.
- [10] H. G. Merkus, *Particle Size Measurements: Fundamentals, Practice, Quality*, vol. 17 of *Overview of Size Characterization Techniques*, Springer Particle Technology Series, Springer, New York, NY, USA, 2009.
- [11] N. Aguiló-Aguayo, M. J. Inestrosa-Izurieta, J. García-Céspedes, and E. Bertran, "Morphological and magnetic properties of superparamagnetic carbon-coated Fe nanoparticles produced by arc discharge," *ASP Journal of Nanoscience and Nanotechnology*, vol. 10, no. 4, pp. 2646–2649, 2010.

- [12] K. D. Bakoglidis, K. Simeonidis, D. Sakellari, G. Stefanou, and M. Angelakeris, "Size-dependent mechanisms in AC magnetic hyperthermia response of iron-oxide nanoparticles," *IEEE Transactions on Magnetics*, vol. 48, no. 4, pp. 1320–1323, 2012.
- [13] B. S. Han, C. K. Rhee, M. K. Lee, and Y. R. Uhm, "Synthesis of nano crystalline Ni and Fe by levitational gas condensation method," *IEEE Transactions on Magnetics*, vol. 42, no. 11, pp. 3779–3781, 2006.
- [14] D. Gozzi, A. Latini, G. Capannelli et al., "Synthesis and magnetic characterization of Ni nanoparticles and Ni nanoparticles in multiwalled carbon nanotubes," *Journal of Alloys and Compounds*, vol. 419, no. 1-2, pp. 32–39, 2006.
- [15] L. Néel, "Théorie du trainage magnétique des ferromagnétiques en grains fins avec applications aux terres cuites," *Annals of Geophysics*, vol. 5, pp. 99–136, 1949.
- [16] B. D. Cullity and C. D. Graham, *Introduction to Magnetic Materials*, Wiley, 2009.
- [17] Y. R. Uhm, C. K. Rhee, H. M. Lee, and C. S. Kim, "Magnetic properties and dispersion stability of carbon encapsulated Fe nano particles," *Journal of the Korean Physical Society*, vol. 57, no. 6, pp. 1609–1613, 2010.
- [18] C. Jin, Z. Haiyan, L. Liping et al., "Super-paramagnetic carbon coated iron nanoparticles and biological magnetic induction heating properties," *Digest Journal of Nanomaterials and Biostructures*, vol. 8, no. 1, pp. 43–51, 2013.
- [19] J. I. Gittleman, B. Abeles, and S. Bozowski, "Superparamagnetism and relaxation effects in granular Ni-SiO<sub>2</sub> and Ni-Al<sub>2</sub>O<sub>3</sub> films," *Physical Review B*, vol. 9, no. 9, pp. 3891–3897, 1974.
- [20] M. F. Hansen and S. Mørup, "Estimation of blocking temperatures from ZFC/FC curves," *Journal of Magnetism and Magnetic Materials*, vol. 203, no. 1–3, pp. 214–216, 1999.

## Research Article

# Horizontal Assembly of Single Nanowire Diode Fabricated by *p-n* Junction GaN NW Grown by MOCVD

Ji-Hyeon Park,<sup>1</sup> Suthan Kissinger,<sup>2</sup> Yong Ho Ra,<sup>1</sup> Kang San,<sup>1</sup>  
Min Ji Park,<sup>3</sup> Kyung-Hwa Yoo,<sup>3</sup> and Cheul-Ro Lee<sup>1</sup>

<sup>1</sup> Semiconductor Materials and Process Laboratory, School of Advanced Materials Engineering, Research Center for Advanced Materials Development (RCAMD), Chonbuk National University, Jeonju 561-756, Republic of Korea

<sup>2</sup> Department of General Studies, Physics Group, Jubail University College, Royal Commission for Jubail, Jubail 10074, Saudi Arabia

<sup>3</sup> Department of Physics, Yonsei University, Seoul 120-749, Republic of Korea

Correspondence should be addressed to Cheul-Ro Lee; [crlee7@jbnu.ac.kr](mailto:crlee7@jbnu.ac.kr)

Received 24 January 2014; Accepted 16 June 2014; Published 10 July 2014

Academic Editor: Alireza Talebitaher

Copyright © 2014 Ji-Hyeon Park et al. This is an open access article distributed under the Creative Commons Attribution License, which permits unrestricted use, distribution, and reproduction in any medium, provided the original work is properly cited.

Uniaxially *p-n* junction gallium nitride nanowires have been synthesized via metal-organic chemical vapor deposition method. Nanowires prepared on Si(111) substrates were found to grow perpendicular to the substrate, and the transmission electron microscopy studies demonstrated that the nanowires had singlecrystalline structures with a  $\langle 0001 \rangle$  growth axis. The parallel assembly of the *p-n* junction nanowire was prepared on a Si substrate with a thermally grown SiO<sub>2</sub> layer. The transport studies of horizontal gallium nitride nanowire structures assembled from *p*- and *n*-type materials show that these junctions correspond to well-defined *p-n* junction diodes. The *p-n* junction devices based on GaN nanowires suspended over the electrodes were fabricated and their electrical properties were investigated. The horizontally assembled gallium nitride nanowire diodes suspended over the electrodes exhibited a substantial increase in conductance under UV light exposure. Apart from the selectivity to different light wavelengths, high responsivity and extremely short response time have also been obtained.

## 1. Introduction

Over the past several years, wide band gap gallium nitride (GaN) nanowires (NWs) have been extensively studied due to their extremely dense logic and unique physical properties with tunable and well-defined atomic composition [1–7]. Recently, single-crystalline semiconductor nanostructures have received great attention due to their superior properties and potential applications in comparison with their bulk form. Among the nanostructured materials, nanowires are very interesting with the charge carrier confined in a one-dimensional (1D) space owing to their special configuration.

Successful growth of GaN nanowires on silicon and other mismatched substrates has been demonstrated by several workers [8–11]. The nanowires exhibit significantly reduced defect density due to their large surface-to-volume ratio. A reduced strain distribution in the nanostructures also leads to a weaker piezoelectric polarization field. In addition, the

enhanced light collection efficiency [12, 13] as well as the highly reduced material consumption [14] with respect to the conventional thin film devices makes nanowires quite attractive for the development of optoelectronic devices. Also, nanoscale control during device fabrication allows systematic exploitation of quantum confinement effects in LEDs [15–17]. It is noted that the luminescence wavelength can be tuned precisely by controlling the dimensions of the nanostructures [18]. Fabricating vertically aligned nanostructures enables the formation of three-dimensional LED architectures, which have a great potential for improved device efficiency due to an enhanced light extraction efficiency [19], increased light emitting active area, and reduced quantum Stark effect [20].

The range of potential applications of semiconductor nanowires keeps increasing in the fields of device miniaturization [21], field-effect transistors [2, 22, 23], photovoltaic cells and light emitting devices [24–27], and so forth. To fabricate nanometer-scale devices, with bottom-up techniques,

a conventional approach is to start with random dispersion from a nanowire or nanostructure suspension, followed by electrode fabrication at a known nanostructure location on the substrate [28, 29]. Several experimental techniques have been reported for manipulation of GaN nanowires into well-defined arrays for integrated devices. A high-brightness *n*-GaN nanowire on *p*-GaN has been synthesized using dielectrophoresis method by Lee et al. [30]. One-dimensional GaN, nanostructure arrays with low defect density are fabricated employing porous anodic alumina films as the template and lead to high-performance devices [31]. The aligned and dislocation free GaN one-dimensional nanostructures have been fabricated using molecular beam epitaxy (MBE) [32, 33], metal-organic chemical vapor deposition (MOCVD) [34–37], and hydride vapor-phase epitaxy (HVPE) [38, 39]. Tang et al. [40] have conducted controlled synthesis of a vertically aligned *p*-GaN nanorod array on an *n*-Si substrate by thermal evaporation of GaCl<sub>3</sub>.

In the study reported here, we have conducted a detailed investigation of the horizontal assembly of *p*-*n* junction GaN nanowires directly on Si(111) substrates by MOCVD. The structural, optical, and electrical characteristics of the nanowires have been measured and are discussed. *p*- and *n*-type doping of the nanowires is accomplished by introducing trace amounts of Mg and Si, respectively. This doping capability enables the formation of an epitaxial *p*-*n* homojunction, which leads to highly efficient radiative recombination between electrons and holes [41, 42]. Finally, *p*-*n* junction GaN array diode has been fabricated horizontally with an ensemble of nanowires and the properties of these diodes are also presented. The grown *p*-*n* junction GaN nanowires were characterized by field emission scanning electron microscopy (FE-SEM), X-ray diffraction (XRD), photoluminescence (PL), and cathodoluminescence (CL) spectroscopy. The morphology of as-grown nanowires was further analyzed by high resolution transmission electron microscopy (HR-TEM). The response time of the *p*-*n* junction GaN nanowire was measured by using Nd-YAG laser at the fourth frequency (266 nm) with 6 ns Gaussian pulses.

**1.1. Materials and Methods.** Horizontally aligned *p*-*n* junction GaN nanowires were grown on Si(111) substrates in a handmade MOCVD system with a horizontal quartz reactor. Before the substrate was loaded into the reactor, it was cleaned by ultrasonic cleaning in acetone and methyl alcohol for 5 min. After that the substrates were overflowed with DI water for 5 min and etched by HF (2%) acid for 5 min to remove the native oxide layer.

To investigate the more complex nanowire structures required for active *p*-*n* junction devices, we exploited MOCVD, which is a technique used extensively for the growth of planar GaN-based heterostructures, as a means of Ga and NH<sub>3</sub> reactants as well as silicon and magnesium dopants in a highly controlled and reproducible manner. Trimethylgallium (TMG), ammonia (NH<sub>3</sub>), silane (SiH<sub>4</sub>, 10 ppm diluted in H<sub>2</sub>), and Cp<sub>2</sub>Mg are the precursors for Ga, N, and Mg, respectively. Hydrogen (H<sub>2</sub>) was used as the carrier gas in the present experiment. Figure 1 illustrates the fabrication flow chart of *p*-*n* junction nanowires on

Si(111) substrates after providing several procedures. We have fabricated *n*-GaN:Si nanowire on Si substrate by newly developed two-step growth process. The first stage of the two-step growth process typically begins with a coated Au film on Si(111) substrate by ion sputtering system. The Au + Ga nanodroplets were formed by MOCVD under hydrogen ambient for 10 min. These nanodroplets act as a nucleation seed for the growth of GaN nanowire. After that, the pulsed *n*-GaN seeds were grown on Au + Ga nanodroplets using pulsed flow method. Pulsed *n*-GaN seeds were grown up to 10 pairs at a working pressure and temperature of about 600 torr and 710°C, respectively. During the pulsed growth mode, group III and group V precursors were introduced alternately in the following sequence: TMG, 3 min; NH<sub>3</sub>, 3 min. In the last step, *n*-GaN/*p*-GaN nanowires were grown on pulsed *n*-GaN seeds at 920°C (1 hour) and 890°C (20 min), respectively, by continuous flow mode. During the continuous flow mode, group III and group V precursors were introduced simultaneously. The *n*-GaN nanowires were grown with the doping of silane gas, which is a critical factor to initiate the vertical nanowire growth. The experiment was carried out for the Cp<sub>2</sub>Mg flow rate of 5 sccm (standard cubic centimeters per minute). The single-crystalline GaN nanowires were horizontally assembled on a degenerately doped silicon wafer covered with 300 nm SiO<sub>2</sub>. The GaN nanowires were dispersed on the grid using a micropipette. After the evaporation of the ethanol, polymethyl methacrylate (PMMA) was spin coated for 40 sec on the grid at 5000 rpm. Using e-beam lithography process the PMMA was removed partially. 5/100 nm thick Ti/Pt electrodes were deposited on both ends of the aligned nanowires by DC sputtering method. The remaining PMMA was removed using lift-off technique using acetone.

In our present study, we have intentionally reduced the growth temperature/pressure, so that the drift velocities of the adatoms were increased dramatically. At this stage, the adatoms could move all along the surface of the nanowires to form the sheath structure. Hence in order to induce the smooth growth surface we have changed our growth temperature from 920°C to 890°C. The dopant was changed during the growth procedure in order to obtain the middle point of the nanowire. This process enhances the linear shape of the nanowire and controls the tape-like growth. During the first stage of the growth, we can obtain an *n*-type nanowire in nominally Si doped GaN according to the presence of nitrogen vacancies and/or oxygen impurities. Magnesium doping follows, carried out by supplying Cp<sub>2</sub>Mg during the latter half of the growth, thus leading to *p*-type growth. Finally, the as-prepared *p*-*n* junction nanowires were assembled horizontally on a Cr/Au metal grid by using e-beam lithography, DC sputter, and lift-off techniques.

The morphology of the *p*-*n* junction nanowire arrays was investigated by field emission scanning electron microscopy (FE-SEM/JEOL JSM-6500F, KBSI in Jeonju). Field emission measurements were conducted in a vacuum chamber with a pressure of  $1.2 \times 10^{-6}$  Pa at room temperature. A rod-like stainless steel probe with 1 mm diameter and 0.78 mm<sup>2</sup> in area was used as anode. The sample was used as cathode. The spacing between the two electrodes is 100 μm. A ballast resistor of 10 MV was used to protect the apparatus

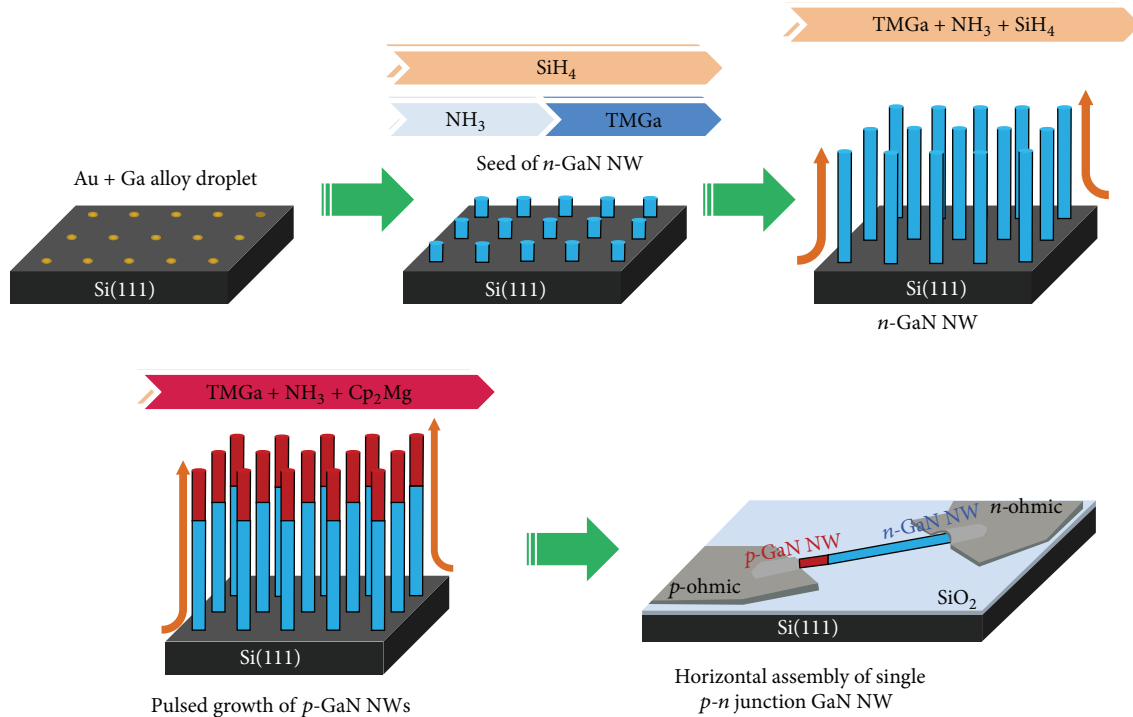


FIGURE 1: Schematic illustration of horizontally assembled single *p-n* junction nanowire diode fabricated on SiO<sub>2</sub>/Si substrates. (i) Au + Ga droplets formation on Si(111) substrate, (ii) *n*-GaN seed formation at 710°C, (iii) *n*-GaN/Si nanowire formation at 920°C (1 hour), (iv) formation of *p*-GaN/Mg nanowire at 850°C (20 min), and (v) horizontal assembly of *p-n* junction nanowire using e-beam lithography and lift-off techniques.

against short circuiting. The optical properties of the as-grown nanowire arrays were characterized by photoluminescence (PL) spectrum using a 325 nm He-Cd laser and a cathodoluminescence (CL) attached to the FE-SEM system. Microstructure and single crystallinity of the nanowires were confirmed by the high resolution transmission electron microscopy (HR-TEM) and selected area electron diffraction (SAED) analysis. The current-voltage (*I/V*) measurements for the horizontally assembled nanowires were carried out under different illumination environments.

## 2. Results of the Experimentation

Figure 2(a) shows the tilt-view FE-SEM images of *n*-GaN:Si nanowires on *n*-GaN seeds. In the early stage of the *n*-GaN seed growth, Au catalyst is known to play an important role to nucleate the seed growth. But at high temperature it is difficult to nucleate *n*-GaN:Si nanowires with Au catalyst alone. The number of seed pairs is a crucial factor in determining the dimension and density of nanowires. The density of *n*-GaN nanowires was increased monotonically with increase in number of seed pairs. Moreover, it is observed from the figure that large-scale, vertically, or slantingly aligned GaN nanowires were uniformly grown in high density on the Si(111) substrate and have clean surface. Notably, Au clusters after supporting the formation of GaN nuclei may leave the location owing to the high diffusion rate of Au atoms at high growth temperatures [43, 44]. Most probably, small Au clusters react with the GaN layer chemically during the wire

growth. Therefore, in this case the Au particle catalyzing the GaN nanowire growth remains neither at the root nor at the tip after extended nanowire growth period. From the FE-SEM data, the average diameters of the nanowires were about 300–400 nm and their lengths are mainly approximately 4 μm. The diameters of the *n*-GaN nanowires were observed to be uniform from the top to the bottom.

Figure 2(b) shows panchromatic CL spectra of *n*-GaN nanowires grown on *n*-GaN seed. The emitted CL was collimated by mirrors located near the sample, transmitted through a fused-silica window in the SEM, and refocused onto the entrance slit of a 0.34 mm spectrograph, with a 600 line/mm grating and entrance slit width of 0.05 mm. The spectra were recorded by a computer-controlled, nitrogen-cooled CCD camera. The wavelength resolution was 0.29 nm, which is equivalent to an energy resolution of  $2.3 \times 10^{-4} E^2$  eV, where *E* is photon energy. The CL experiments were carried out at a temperature of 300 K. The GaN signature in the 290–360 nm wavelength range was used to optimize the CL signal. The applied accelerating voltage (*V<sub>a</sub>*) and beam current (*I<sub>b</sub>*) are 5 kV and 1000 pA, respectively. The slit widths were set at 1 mm, which is the optimum width for achieving high count rates. From the CL spectra we could observe that the *n*-GaN:Si nanowires show a near-band-edge emission (NBE) centered at 370 nm in the ultraviolet range of the spectrum due to the increased excitation rates associated with CL. We could not observe any deep-level (yellow) CL for the *n*-GaN nanowires arising either directly from the atomic structure of the dislocations or associated with the clustering of native

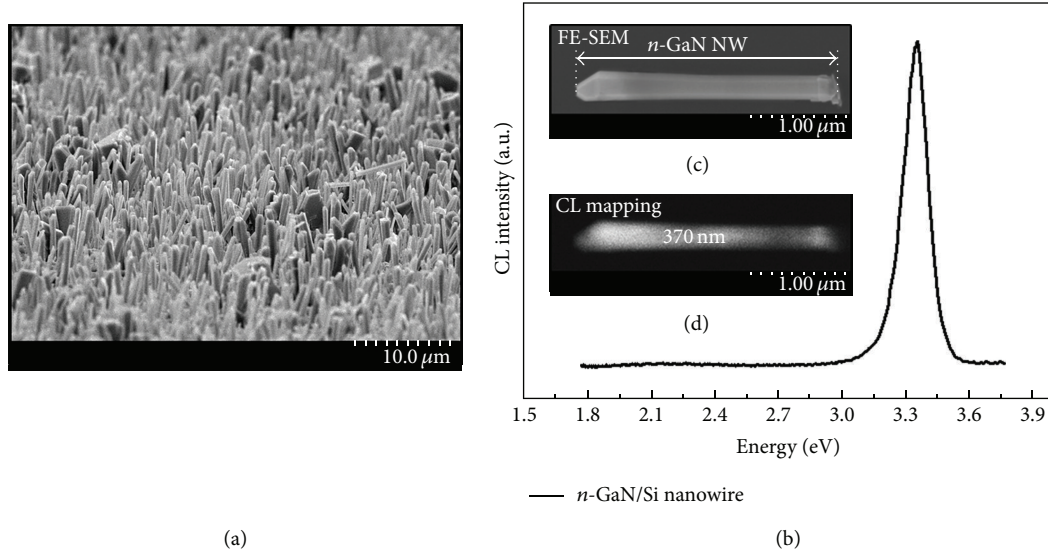


FIGURE 2: Tilt-view FE-SEM image of (a) *n*-GaN/Si nanowires fabricated on Si(111) substrate, (b) CL spectra of *n*-GaN/Si nanowires, (c) FE-SEM image of single *n*-GaN/Si nanowire, and (d) CL mapping image at 370 nm.

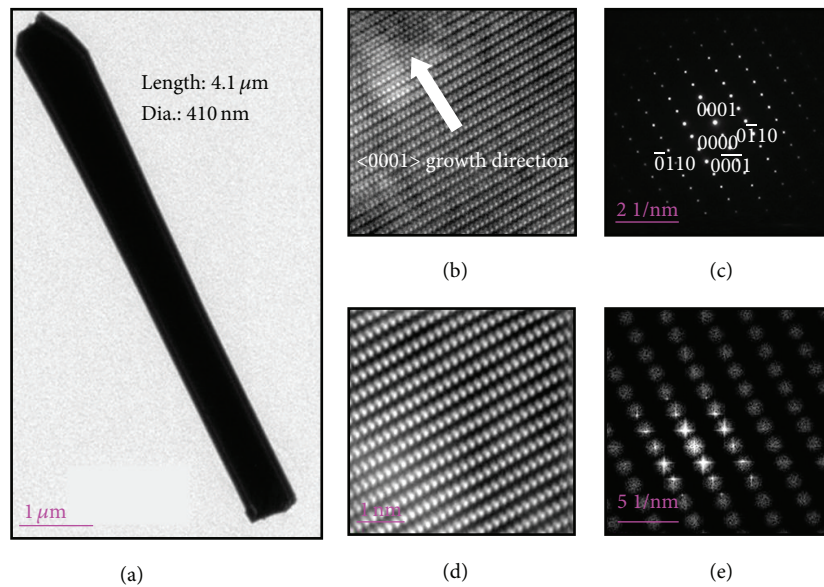


FIGURE 3: HR-TEM image of the *n*-GaN:Si NWs grown on pulsed *u*-GaN seed: (a) single *n*-GaN:Si NW, (b) lattice structure of *n*-GaN:Si NWs, (c) SAED pattern of the *n*-GaN NW/Si, (d) the lattice image obtained by inverse fast Fourier transform (IFFT), and (e) fast Fourier transform image (FFT).

point defects (vacancies, interstitials) [45]. From this data, one can understand that the grown *n*-GaN:Si nanowires were high quality with lower defect. Figure 2(c) shows a FE-SEM image of a single *n*-GaN:Si nanowire and its corresponding CL mapping received at wavelength 370 nm is presented in Figure 2(d). The wavelength 370 nm is corresponding to the maximum peak energy of the band emission. From the CL image, it is observed that the 370 nm emission is quite uniform throughout the GaN structure which appeared as white color. From Figure 2(d), one can also see that the emission intensities are quite uniform, which might be related to the homogenous distribution of strain within the self-organized *n*-GaN nanowires.

Figure 3 shows bright field and high resolution TEM images as well as selected area diffraction (SAED) pattern. Figure 3(a) shows the HR-TEM image of a single *n*-GaN:Si nanowire. The stacking of hexagonal basal planes along the growth orientation of the wire and the  $\langle 0001 \rangle$  direction can be seen in the high resolution mode. The GaN nanowire exhibits a 2H hexagonal structure. Figure 3(b) shows a high-magnification TEM image of *n*-GaN nanowire. The clear lattice fringes confirmed in the HRTEM image indicate that the nanowire is hexagonal single-crystalline structure without defect or secondary phases. This is consistent with wurtzite GaN structure and corresponds to the lattice spacing between the (0 0 0 1) planes in the GaN phase. Figure 3(c) reveals

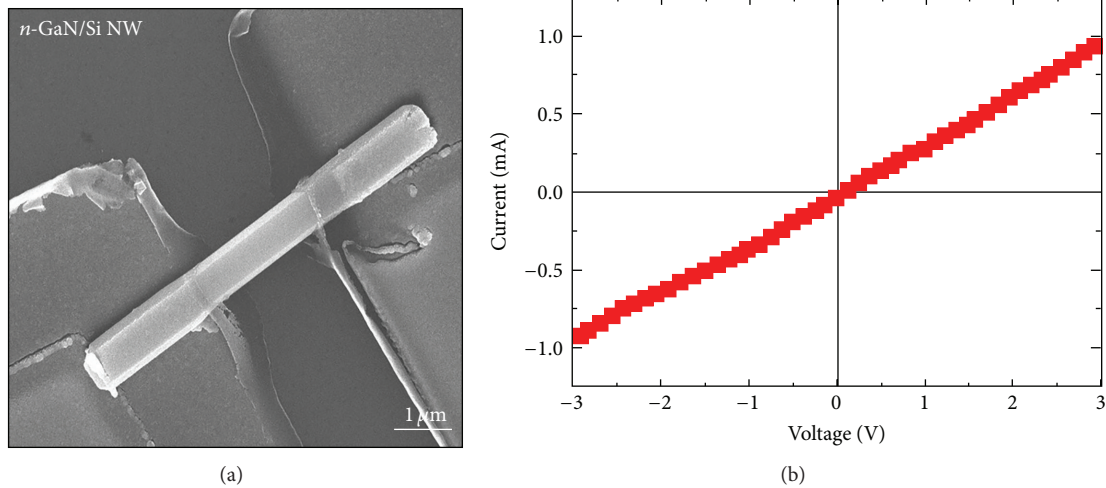


FIGURE 4: (a) FE-SEM image of horizontally assembled  $n$ -GaN/Si nanowire, (b) the current-voltage measurements of  $n$ -GaN/Si nanowire.

the representative SAED pattern, with the (1100), (0001), (0001), and (1100) diffraction spots. These regular diffraction spots demonstrated that  $n$ -GaN nanowires grew along a  $\langle 0001 \rangle$  direction. The lattice structure shown in Figure 3(d) represents the IFFT image of high resolution. Such images clearly show the (0001) atomic planes perpendicular to the nanowire axis. Figure 3(e) represents the corresponding FFT pattern of the HRTEM image that indicates the  $n$ -GaN nanowires are preferentially oriented along the  $c$ -axis direction, as well, and are indexed to the reflections of the wurtzite structure.

Figure 4(a) shows the horizontal assembly of single  $n$ -GaN:Si nanowire. The single-crystalline  $n$ -GaN nanowires fabricated by two-step growth process were horizontally assembled on a degenerately doped silicon wafer covered with 300 nm  $\text{SiO}_2$ . In the next process, 5/50 nm thick Cr/Au metal grid was formed by e-beam lithography, e-beam evaporator, and lift-off techniques. In order to disperse the  $n$ -GaN nanowires, Si substrate was immersed in ethanol. The substrate immersed in ethanol was sonicated for 5 min. The  $n$ -GaN nanowires were dispersed on the grid using a micropipette. After the evaporation of the ethanol, PMMA was spin coated for 40 sec on the grid at 5000 rpm. Using e-beam lithography process the PMMA was removed partially. 5/100 nm thick Ti/Pt electrodes were deposited on both ends of the aligned nanowires by DC sputtering method. The  $I/V$  characteristics of the single  $n$ -GaN nanowire suspended over the electrodes are shown in Figure 4(b). The  $I/V$  curve of the  $n$ -GaN nanowire shows obvious ohmic behaviour of the fabricated nanowire. The linear  $I/V$  curve for the fabricated GaN nanowire reveals that good ohmic contacts have been obtained.

Figure 5 shows the FE-SEM image of a single  $p$ - $n$  junction nanowire. It is observed from the figure that the  $n$ -GaN and  $p$ -GaN growth regions are not distinguishable from each other due to the smooth morphology. This diverse growth rate is due to the reduction in temperature from  $920^\circ\text{C}$  to  $890^\circ\text{C}$ . Distinctly different from the morphology of  $n$ -doped GaN nanowires,  $p$ -doped GaN nanowires exhibit smooth

morphology throughout the wire with uniform diameter along the length of the nanowire, as observed in SEM image (Figure 5(a)). The  $p$ -doping leads to a clear morphology evolution from the smooth to the rough one, and thus the aspect ratio of GaN nanowires increased greatly. Obviously we could observe that the  $p$ -doping has resulted in the formation of some sharp tips protruding from the GaN nanowire surface (Figure 5(a)). In fact it has been demonstrated that the morphology and geometrical shape of nanostructures are quite sensitive to the adding of foreign impurities even though their content is less than the limit of X-ray energy dispersive spectrometer (EDS) measurement. The introduction of doping elements may affect the growth behaviour or thermodynamics of GaN nanostructures and leads to the changes of morphology and geometry shape. Figures 5(b) and 5(c) represent the CL spectra measured from the  $n$ -GaN:Si/ $p$ -GaN:Mg regions. The emissions of both regions were centered at 370 nm and 436 nm, respectively. The CL peak of  $p$ -GaN:Mg region is smooth corresponding to the  $n$ -GaN:Si region without any defect luminescence. The major luminescence at 436 nm was demonstrated to be contributed uniformly from the whole  $p$ -GaN:Mg nanowire region. These emissions originated from the transition between the conduction band and Mg-related acceptors. This wavelength is consistent with band-edge emission from a  $p$ -GaN:Mg structure.

Figure 6(a) represents the FE-SEM image of the horizontally assembled GaN nanowire  $p$ - $n$  junction device structure. The current-voltage ( $I/V$ ) measurements with the GaN nanowire  $p$ - $n$  junction diode were carried out under different illumination environment. Our experiment involved a double-wavelength handheld UV lamp of 254 and 365 nm in fixed wavelength at a distance of approximately 3 cm away from the nanodiode. The nanostructured device was kept under practical conditions, that is, in air, at room temperature, and under indoor incandescent light during the measurements. The power density was  $0.3 \text{ mW}/\text{cm}^2$  for both UV wavelengths. Figure 6(b) shows three  $I/V$  curves plotted at gate voltage ( $V_g$ ) = 0 V under incandescent light and

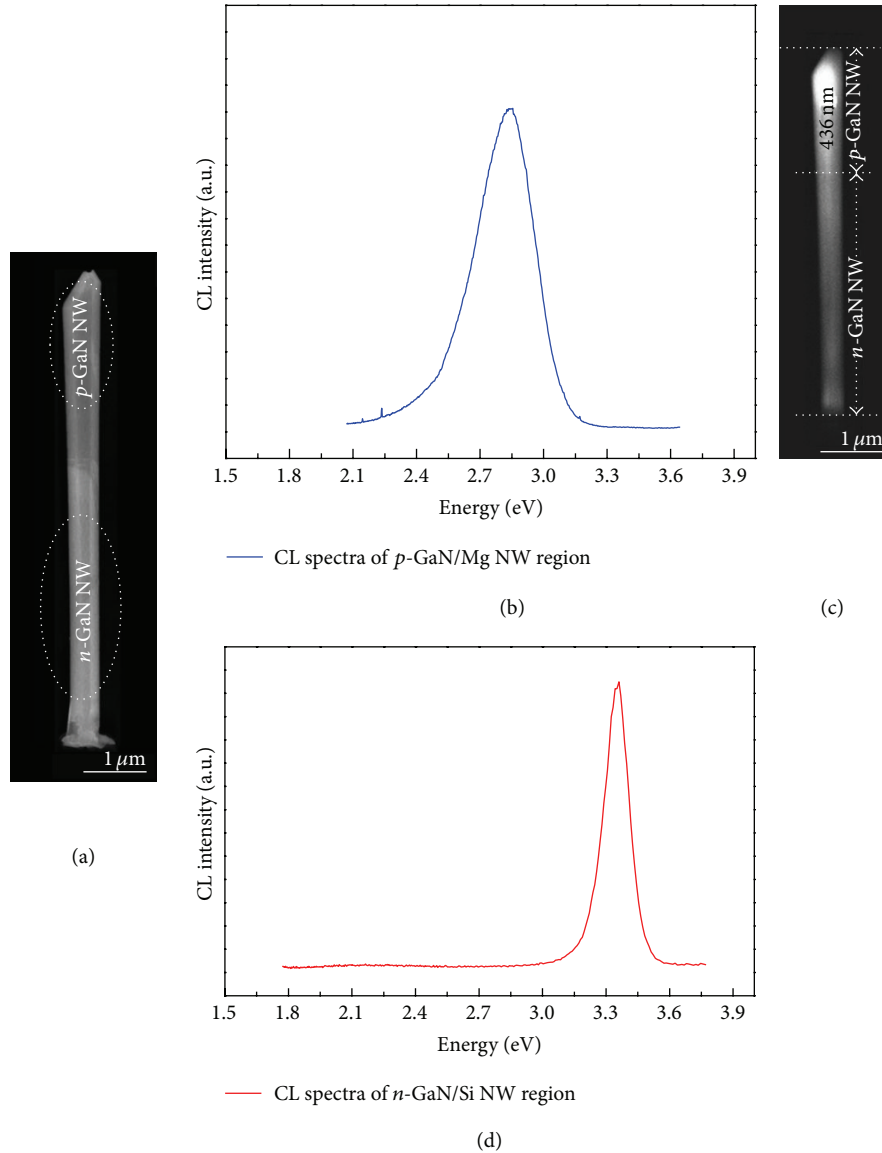


FIGURE 5: FE-SEM image of (a)  $p$ - $n$  junction GaN nanowire, (b) and (c) the CL spectrum and mapping (436 nm) taken at  $p$ -GaN/Mg region, and (d) the CL spectrum taken at  $n$ -GaN/Si region.

upon exposure to UV light at wavelengths of 254 and 365 nm, respectively. Enhanced conduction behaviour was observed for UV illumination of both the wavelengths; nevertheless, the magnitude of both wavelengths differed significantly. The observed data clearly exhibits that under UV exposure the nanowire conductivity increases greatly. The enhanced conductivity under UV light illumination is attributed to the excess photogenerated carriers in the semiconducting nanowire. We have also observed that a higher power density of UV light produces more carriers for conduction. The UV light with a wavelength of 254 nm has photon energy of 4.88 eV, which is sufficient enough to excite electrons across the 3.4 eV bandgap of GaN. Furthermore, the energy of UV light with a wavelength of 365 nm corresponds to 3.39 eV, which is slightly lower than the GaN bandgap. On the other hand, there are still some photons that exist with higher

energies due to the nonzero spectrum width, which can generate electron-hole pairs and thus increase the carrier combination of the nanowire. Figure 7(a) shows the spectral response curve of the  $p$ - $n$  junction device structure at zero bias. Spectral photoresponse measurement was done in the 250–500 nm range with a 150 W Xenon arc lamp light source and a Jobin-Yvon H10-UV monochromator. The monochromated output light was coupled into a multimode UV fiber by which the sample was illuminated. Calibration of the light source output was carried out by using a calibrated Si photodetector and a Newport 1835-C optical power meter. The responsivity was quite flat over the band gap with an abrupt cutoff wavelength at 365 nm. The maximum responsivity value was 0.17 A/W around 250 nm. An UV/visible contrast of more than three orders of magnitude was obtained. This indicates that the GaN  $p$ - $n$  junction diode has good spectral

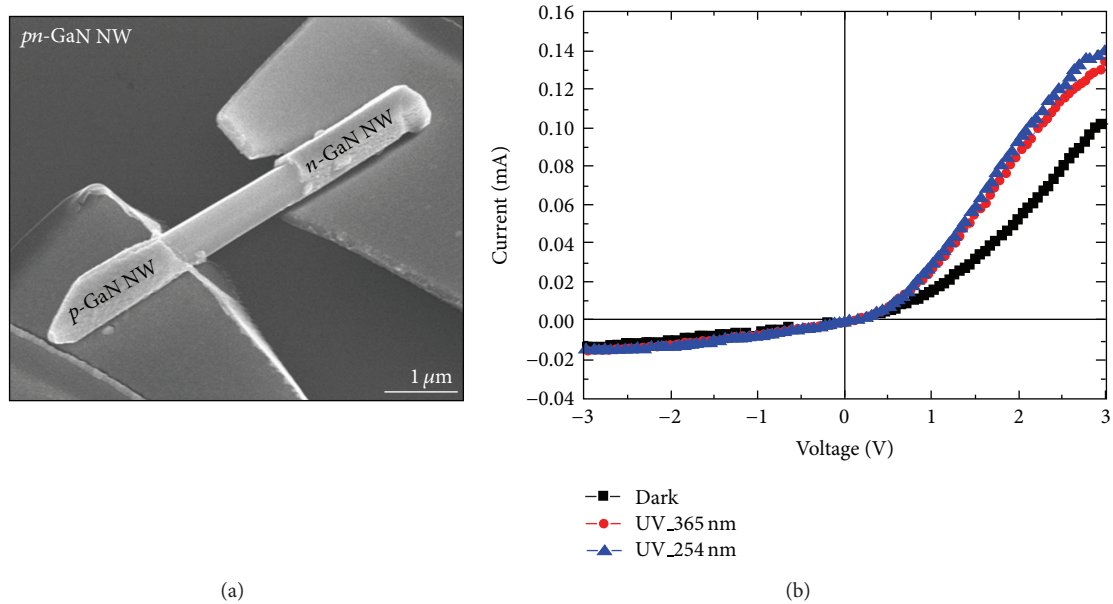


FIGURE 6: FE-SEM image of (a) horizontally assembled  $p$ - $n$  junction diode by single GaN nanowire, (b) the  $I/V$  measurements of GaN nanowire device in the dark and under UV illumination (wavelength  $\lambda = 365$  and  $254$  nm).

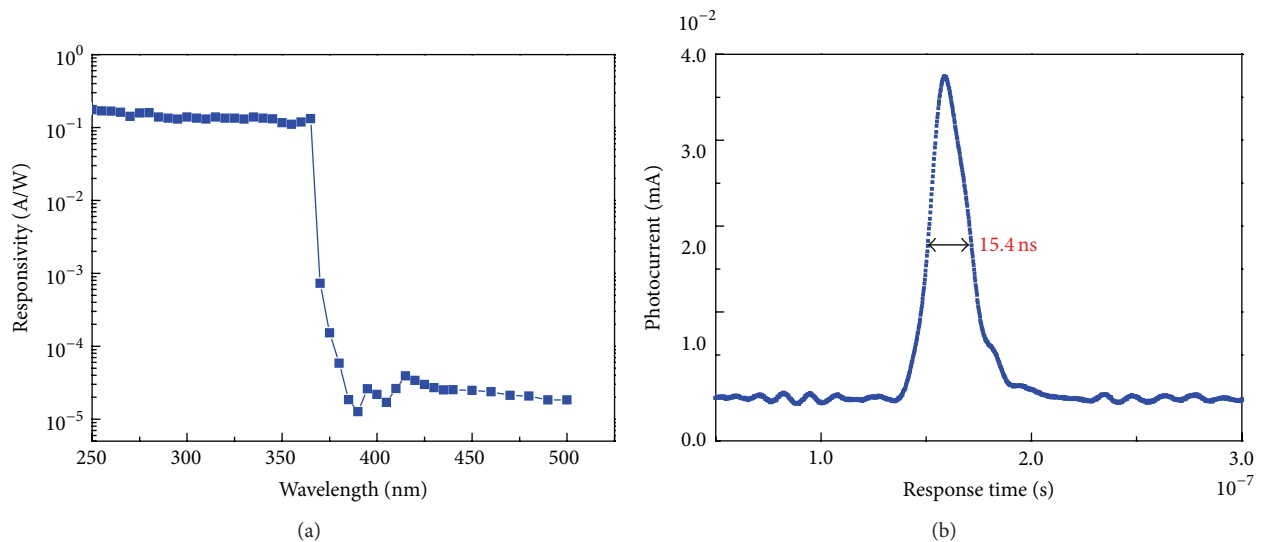


FIGURE 7: (a) The responsivity and (b) response time spectra for the single  $p$ - $n$  junction GaN nanowire grown on Si(111) substrate.

selectivity. Figure 7(b) shows the response time for the  $p$ - $n$  junction single GaN nanowire. The response time of the  $p$ - $n$  junction GaN nanowire was measured by using the fourth frequency of Nd-YAG laser (266 nm) with 6 ns Gaussian pulses. The  $p$ - $n$  junction GaN nanowire shows a response time with a full width at half maximum (FWHM) of 15.4 ns under nonbiased condition. The device was Measured at zero bias, but resulted a very fast response time. The response time is significantly faster than the 118 ns for  $n$ -GaN Schottky device [46]. It clearly shows that the perturbation induces an electric field along the nanowire that enhances the collection of photogenerated carriers with higher photo response.

### 3. Conclusions

In summary, horizontal assembly of  $p$ - $n$  junction single-crystalline GaN nanowires has been fabricated via metal-organic chemical vapor deposition method using Mg as the  $p$ -type dopant. Nanowires prepared on Si(111) substrates grow epitaxially with a (002) direction. The prepared GaN nanowires show excellent rectification properties.  $n$ -doped GaN nanowires fabricated under similar conditions invariably produce linear current-voltage curves, suggesting that the observed rectification comes from the  $p$ - $n$  junction. In addition to that, the transport studies of GaN nanowire structures assembled horizontally from  $p$ -type and  $n$ -type

materials show that the nanoscale junctions behave as the well-defined  $p$ - $n$  junction diodes. The photoresponse properties reveal that the nanodiode fabricated in our present study exhibits advantages in high responsivity and response time. And also, it can be concluded that this nanowire photodetector having low dislocation density will show higher sensitivity than the device fabricated by GaN epitaxial layer having high defect density in missile detection and flame sensing applications.

## Conflict of Interests

The authors declare that there is no conflict of interests regarding the publication of this paper.

## Acknowledgments

This research was supported by Basic Science Research Program through the National Research Foundation of Korea (NRF) funded by the Ministry of Education (BRL no. 2010-0019626). This research was financially supported by the Ministry of Education, Science and Technology (MEST) and National Research Foundation of Korea (NRF) through the Human Resource Training Project for Regional Innovation. This research was financially supported by the Ministry of Knowledge Economy (MKE), Korea Institute for Advancement of Technology (KIAT), and Honam Leading Industry Office through the Leading Industry Development for Economic Region.

## References

- [1] F. A. Ponce and D. P. Bour, "Nitride-based semiconductors for blue and green light-emitting devices," *Nature*, vol. 386, no. 6623, pp. 351–359, 1997.
- [2] J. Xiang, W. Lu, Y. Hu, Y. Wu, H. Yan, and C. M. Lieber, "Ge/Si nanowire heterostructures as high-performance field-effect transistors," *Nature*, vol. 441, no. 7092, pp. 489–493, 2006.
- [3] S. J. Pearton, J. C. Zolper, R. J. Shul, and F. Ren, "GaN: processing, defects, and devices," *Journal of Applied Physics*, vol. 86, no. 1, pp. 1–15, 1999.
- [4] D. Wang, B. A. Sheriff, and J. R. Heath, "Complementary symmetry silicon nanowire logic: power-efficient inverters with gain," *Small*, vol. 2, no. 10, pp. 1153–1158, 2006.
- [5] P. Waltereit, O. Brandt, A. Trampert et al., "Nitride semiconductors free of electrostatic fields for efficient white light-emitting diodes," *Nature*, vol. 406, no. 6798, pp. 865–868, 2000.
- [6] L. Polenta, M. Rossi, A. Cavallini et al., "Investigation on localized states in GaN nanowires," *ACS Nano*, vol. 2, no. 2, pp. 287–292, 2008.
- [7] E. Lai, W. Kim, and P. Yang, "Vertical nanowire array-based light emitting diodes," *Nano Research*, vol. 1, no. 2, pp. 123–128, 2008.
- [8] J. Miao, W. Guo, N. Lu et al., "Single InAs nanowire room-temperature near-infrared photodetectors," *ACS Nano*, vol. 8, no. 4, pp. 3628–3635, 2014.
- [9] A. Afal, S. Coskun, and H. E. Unalan, "All solution processed, nanowire enhanced ultraviolet photodetectors," *Applied Physics Letters*, vol. 102, no. 4, Article ID 043503, 2013.
- [10] T. Kuykendall, P. Ulrich, S. Aloni, and P. Yang, "Complete composition tunability of InGaN nanowires using a combinatorial approach," *Nature Materials*, vol. 6, no. 12, pp. 951–956, 2007.
- [11] R. Armitage and K. Tsubaki, "Multicolour luminescence from InGaN quantum wells grown over GaN nanowire arrays by molecular-beam epitaxy," *Nanotechnology*, vol. 21, no. 19, Article ID 195202, 2010.
- [12] E. Garnett and P. Yang, "Light trapping in silicon nanowire solar cells," *Nano Letters*, vol. 10, no. 3, pp. 1082–1087, 2010.
- [13] S. L. Diedenhofen, G. Vecchi, R. E. Algra et al., "Broad-band and omnidirectional antireflection coatings based on semiconductor nanorods," *Advanced Materials*, vol. 21, no. 9, pp. 973–978, 2009.
- [14] J. Kupec, R. L. Stoop, and B. Witzigmann, "Light absorption and emission in nanowire array solar cells," *Optics Express*, vol. 18, no. 26, pp. 27589–27605, 2010.
- [15] R. Ghosh and D. Basak, "Quantum confinement of excitons in dendrite-like GaN nanowires," *Journal of Applied Physics*, vol. 98, no. 8, Article ID 086104, 2005.
- [16] J. Ristić, C. Rivera, E. Calleja, S. Fernández-Garrido, M. Povoloskyi, and A. Di Carlo, "Carrier-confinement effects in nanocolumnar GaN AlxGal-xN quantum disks grown by molecular-beam epitaxy," *Physical Review B—Condensed Matter and Materials Physics*, vol. 72, no. 8, Article ID 085330, 2005.
- [17] H. S. Chen, D. Yeh, Y. Lu et al., "Strain relaxation and quantum confinement in InGaN/GaN nanoposts," *Nanotechnology*, vol. 17, no. 5, pp. 1454–1457, 2006.
- [18] H. Im, Y. S. Park, S.-K. Lee, Y.-H. Cho, and R. A. Taylor, "Micro- and time-resolved photoluminescence in GaN nanorods with different diameters," *Journal of the Korean Physical Society*, vol. 57, no. 4, pp. 756–759, 2010.
- [19] S. J. An, J. H. Chae, G. Yi, and G. H. Park, "Enhanced light output of GaN-based light-emitting diodes with ZnO nanorod arrays," *Applied Physics Letters*, vol. 92, no. 12, Article ID 121108, 2008.
- [20] C. Wang, L. Chen, G. Chen et al., "GaN nanorod light emitting diode arrays with a nearly constant electroluminescent peak wavelength," *Optics Express*, vol. 16, no. 14, pp. 10549–10556, 2008.
- [21] Y. Huang, X. F. Duan, Y. Cui, L. J. Lauhon, K. H. Kim, and C. M. Lieber, "Logic gates and computation from assembled nanowire building blocks," *Science*, vol. 294, no. 5545, pp. 1313–1317, 2001.
- [22] Y. Cui, Z. Zhong, D. Wang, W. U. Wang, and C. M. Lieber, "High performance silicon nanowire field effect transistors," *Nano Letters*, vol. 3, no. 2, pp. 149–152, 2003.
- [23] A. L. Vallett, S. Minassian, P. Kaszuba, S. Datta, J. M. Redwing, and T. S. Mayer, "Fabrication and characterization of axially doped silicon nanowire tunnel field-effect transistors," *Nano Letters*, vol. 10, no. 12, pp. 4813–4818, 2010.
- [24] A. Hagfeld and M. Grätzel, "Light-induced redox reactions in nanocrystalline systems," *Chemical Reviews*, vol. 95, no. 1, pp. 49–68, 1995.
- [25] B. Tian, X. Zheng, T. J. Kempa et al., "Coaxial silicon nanowires as solar cells and nanoelectronic power sources," *Nature*, vol. 449, no. 7164, pp. 885–889, 2007.
- [26] M. R. Lee, R. D. Eckert, K. Forberich, G. Dennler, C. J. Brabec, and R. A. Gaudiana, "Solar power wires based on organic photovoltaic materials," *Science*, vol. 324, no. 5924, pp. 232–235, 2009.
- [27] H. Zhang, Y. Li, Q. Tang, L. Liu, and Z. Zhou, "First-principles studies on structural and electronic properties of GaN-AlN heterostructure nanowires," *Nanoscale*, vol. 4, no. 4, pp. 1078–1084, 2012.

- [28] Y. Xia, P. Yang, Y. Sun et al., "One-dimensional nanostructures: synthesis, characterization, and applications," *Advanced Materials*, vol. 15, no. 5, pp. 353–389, 2003.
- [29] T. Kuykendall, P. Pauzauskie, S. Lee, Y. Zhang, J. Goldberger, and P. Yang, "Metalorganic chemical vapor deposition route to GaN nanowires with triangular cross sections," *Nano Letters*, vol. 3, no. 8, pp. 1063–1066, 2003.
- [30] S.-K. Lee, T.-H. Kim, K.-C. Choi, and P. Yang, "High-brightness gallium nitride nanowire UV-blue light emitting diodes," *Philosophical Magazine*, vol. 87, no. 14-15, pp. 2105–2115, 2007.
- [31] P. Deb, H. Kim, Y. Qin et al., "GaN nanorod schottky and p-n junction diodes," *Nano Letters*, vol. 6, no. 12, pp. 2893–2898, 2006.
- [32] R. Calarco, R. J. Meijers, R. K. Debnath, T. Stoical, E. Sutter, and H. Lüth, "Nucleation and growth of GaN nanowires on Si(111) performed by molecular beam epitaxy," *Nano Letters*, vol. 7, no. 8, pp. 2248–2251, 2007.
- [33] Y. S. Park, C. M. Park, D. J. Fu, T. W. Kang, and J. E. Oh, "Photoluminescence studies of GaN nanorods on Si (111) substrates grown by molecular-beam epitaxy," *Applied Physics Letters*, vol. 85, no. 23, pp. 5718–5720, 2004.
- [34] J. Goldberger, R. He, Y. Zhang et al., "Single-crystal gallium nitride nanotubes," *Nature*, vol. 422, no. 6932, pp. 599–602, 2003.
- [35] Y. Wang, K. Zang, S. Chua, M. S. Sander, S. Tripathy, and C. G. Fonstad, "High-density arrays of InGaN nanorings, nanodots, and nanoarrows fabricated by a template-assisted approach," *Journal of Physical Chemistry B*, vol. 110, no. 23, pp. 11081–11087, 2006.
- [36] Y. M. Lee, R. Navamathavan, K. Song et al., "Bicrystalline GaN nanowires grown by the formation of PtGa solid solution nanodroplets on Si(111) using MOCVD," *Journal of Crystal Growth*, vol. 312, no. 16-17, pp. 2339–2344, 2010.
- [37] P. Deb, H. Kim, V. Rawat et al., "Faceted and vertically aligned GaN nanorod arrays fabricated without catalysts or lithography," *Nano Letters*, vol. 5, no. 9, pp. 1847–1851, 2005.
- [38] H.-M. Kim, D. S. Kim, Y. S. Park, D. Y. Kim, T. W. Kang, and K. S. Chung, "Growth of GaN nanorods by a hybrid vapour phase epitaxy method," *Advanced Materials*, vol. 14, no. 13-14, pp. 991–993, 2002.
- [39] H.-M. Kim, T. W. Kang, and K. S. Chung, "Growth of GaN nanorods by a hydride vapor phase epitaxy method," *Advanced Materials*, vol. 15, pp. 567–569, 2003.
- [40] Y. B. Tang, Z. H. Chen, H. S. Song et al., "Vertically aligned p-type single-crystalline GaN nanorod arrays on n-type Si for heterojunction photovoltaic cells," *Nano Letters*, vol. 8, no. 12, pp. 4191–4195, 2008.
- [41] H. Amano, M. Kito, K. Hiramatsu, and I. Akasaki, "P-type conduction in Mg-doped GaN treated with low-energy electron beam irradiation (LEEBI)," *Japanese Journal of Applied Physics*, vol. 28, pp. L2112–L2114, 1989.
- [42] M. E. Lin, B. N. Sverdlov, and H. Morkoç, "Thermal stability of GaN investigated by low-temperature photoluminescence spectroscopy," *Applied Physics Letters*, vol. 63, no. 26, pp. 3625–3627, 1993.
- [43] T. Stoica, E. Sutter, R. J. Meijers et al., "Interface and wetting layer effect on the catalyst-free nucleation and growth of GaN nanowires," *Small*, vol. 4, no. 6, pp. 751–754, 2008.
- [44] L. Qin, C. Xue, Y. Duan, and L. Shi, "Synthesis and characterization of glomerate GaN nanowires," *Nanoscale Research Letters*, vol. 4, no. 6, pp. 584–587, 2009.
- [45] X. Chen, J. Li, Y. Cao et al., "Straight and smooth GaN nanowires," *Advanced Materials*, vol. 12, no. 19, pp. 1432–1434, 2000.
- [46] J. M. van Hove, R. Hickman, J. J. Klaassen, P. P. Chow, and P. P. Ruden, "Ultraviolet-sensitive, visible-blind GaN photodiodes fabricated by molecular beam epitaxy," *Applied Physics Letters*, vol. 70, no. 17, pp. 2282–2284, 1997.

## Research Article

# Improving the Microstructure and Electrical Properties of Aluminum Induced Polysilicon Thin Films Using Silicon Nitride Capping Layer

Min-Hang Weng,<sup>1</sup> Cheng-Tang Pan,<sup>2</sup> Chien-Wei Huang,<sup>2</sup> and Ru-Yuan Yang<sup>3</sup>

<sup>1</sup> Medical Devices and Opto-Electronics Equipment Department, Metal Industry Research and Development Center, Kaohsiung City 821, Taiwan

<sup>2</sup> Department of Mechanical & Electromechanical Engineering, National Sun Yat-sen University, Kaohsiung 804, Taiwan

<sup>3</sup> Graduate Institute of Materials Engineering, National Pingtung University of Science and Technology, Pingtung 912, Taiwan

Correspondence should be addressed to Ru-Yuan Yang; ryyang@mail.npust.edu.tw

Received 23 January 2014; Accepted 30 May 2014; Published 26 June 2014

Academic Editor: Alireza Talebitaher

Copyright © 2014 Min-Hang Weng et al. This is an open access article distributed under the Creative Commons Attribution License, which permits unrestricted use, distribution, and reproduction in any medium, provided the original work is properly cited.

We investigated the capping layer effect of  $\text{SiN}_x$  (silicon nitride) on the microstructure, electrical, and optical properties of poly-Si (polycrystalline silicon) prepared by aluminum induced crystallization (AIC). The primary multilayer structure comprised Al (30 nm)/ $\text{SiN}_x$  (20 nm)/a-Si (amorphous silicon) layer (100 nm)/ITO coated glass and was then annealed in a low annealing temperature of 350°C with different annealing times, 15, 30, 45, and 60 min. The crystallization properties were analyzed and verified by X-ray diffraction (XRD) and Raman spectra. The grain growth was analyzed via optical microscope (OM) and scanning electron microscopy (SEM). The improved electrical properties such as Hall mobility, resistivity, and dark conductivity were investigated by using Hall and current-voltage ( $I$ - $V$ ) measurements. The results show that the amorphous silicon film has been effectively induced even at a low temperature of 350°C and a short annealing time of 15 min and indicate that the  $\text{SiN}_x$  capping layer can improve the grain growth and reduce the metal content in the induced poly-Si film. It is found that the large grain size is over 20  $\mu\text{m}$  and the carrier mobility values are over 80  $\text{cm}^2/\text{V}\cdot\text{s}$ .

## 1. Introduction

Recently, polycrystalline silicon (poly-Si) films fabricated on glass or plastic substrates have attracted much attention because of their applications in optic-electrical devices such as thin-film transistors (TFTs) [1], sensors, thin film solar cells, and active matrix organic light-emitting diode (AMOLED). The reason is that the mobility of the polycrystalline silicon (poly-Si) thin film is 10 to 100 times greater than that of the amorphous silicon (a-Si) thin film which has the mobility value less than 1  $\text{cm}^2/\text{V}\cdot\text{s}$  [2]. Conventional solid phase crystallization (SPC) of a-Si thin film needs a relatively high process temperature larger than 800°C and a long processing time. However, the average grain size of poly-Si was small in the range of 1-2  $\mu\text{m}$  and a poor crystal quality was obtained through SPC method [3]. A low-temperature polysilicon (LTPS) is the polycrystalline silicon film formed

by subsequent low-temperature crystallization of amorphous silicon (a-Si). Usually, there are two common methods for fabrication of LTPS film such as excimer laser annealing (ELA) [4] and metal induced crystallization (MIC) [5–21]. The ELA method is currently used as a low-temperature manufacturing approach; however it needs expensive equipment to be implemented.

Generally, MIC method is studied for the fabrication of the LTPS film. Many different metals can be used, such as Pd [5], Au [6], and Al [7–19]. The aluminum induced crystallization (AIC) fabrication is one of the MIC methods with the advantages of a low annealing temperature less than 577°C [7–10] and large grain sizes [11–13]. However, since the reaction of the Al and a-Si is fast, residual Al metal in the induced poly-Si film as the traps results in a decrease in carrier mobility. Moreover, it is difficult to control the

distribution of the residual Al metal so that the grain size during the grain growth is abnormal [7, 8]. However, the performance of devices fabricated on poly-crystalline silicon strongly depends on grain size because grain boundaries also usually act as traps and recombination centers for carriers [7].

It was reported that the use of capping layer could control the lateral growth of poly-Si through lateral thermal gradients. Formerly, there were different patterned capping layers such as SiO<sub>2</sub>, SiN<sub>x</sub>, and metal capping layers [14] used on the a-Si to reduce metal contamination and obtain a clean and smooth surface [15]. For example, Choi et al. demonstrated a Ni-induced crystallization of a-Si through a SiN<sub>x</sub> capping layer [14] annealed in a rapid thermal annealing system. However, the properties of the LTPS using AIC with the capping layer have not been reported. Additionally, SiN<sub>x</sub> usually acts as an antireflection layer in solar cell device and then a metal layer such as Ag or Al is deposited on the antireflection layer (SiN<sub>x</sub>). After firing, the metal such as Ag or Al will diffuse through SiN<sub>x</sub> layer to react with Si to form an ohmic contact. Therefore, we expected that the Al film is deposited on the capping layer and diffuses through the capping layer to form the seeds in a-Si thin film for crystallization. In this paper, we investigated the capping layer (silicon nitride, SiN<sub>x</sub>) effect on the microstructure, electrical, and optical properties of poly-Si prepared by the AIC method.

## 2. Experiment

Hydrogenated amorphous silicon (a-Si:H) and SiN<sub>x</sub> layers were sequentially deposited on indium tin oxide (ITO) coated glass by plasma-enhanced chemical vapor deposition (PECVD) equipment. Figure 1(a) shows the experimental procedure of this study for poly-Si thin films using AIC with the capping layer. The thickness of a-Si:H was 100 nm and the deposition parameters for the RF power, chamber pressure, substrate temperature, N<sub>2</sub>, and SiH<sub>4</sub> flow rates were controlled at 100 W, 300 mTorr, 350°C, 1140 sccm, and 30 sccm, respectively. The thickness of SiN<sub>x</sub> layer was 20 nm and the deposition parameters for the RF power, chamber pressure, substrate temperature, NH<sub>3</sub>, N<sub>2</sub>, and SiH<sub>4</sub> flow rate were controlled at 20 W, 300 mTorr, 350°C, 30 sccm, 450 sccm, and 25 sccm, respectively. Then, 30 nm thick aluminum film was deposited on the SiN<sub>x</sub> layer using sputter system and the parameters for the DC power, chamber pressure, substrate temperature, and Ar flow rate were controlled at 1000 W, 2 × 10<sup>-6</sup> Torr, 25°C, and 5 sccm, respectively. When the aluminum deposition process was finished, the specimen was cut into small pieces and annealed at 350°C for 15, 30, 45, and 60 minutes in an N<sub>2</sub> atmosphere. After annealing, the Al layer was first removed using wet selective etching solution and the etchants consist of phosphoric acid, nitric acid, and acetic acid. The SiN<sub>x</sub> layer was then removed in the reactive ion etch (RIE) system. The expected transformation procedure for AIC of a-Si:H films on the ITO coated glass substrate is shown in Figure 1(b).

The prepared samples were analyzed for evaluating the influence of AIC process with capping layer. The crystallinity and morphology characteristics were analyzed by using X-ray diffraction (XRD, machine type: Bruker D8 Advance)

TABLE 1: The crystalline size and crystallinity of the poly-Si thin films using AIC with the capping layer for different annealing time.

	Time (min)			
	15	30	45	60
Crystallinity size ( $D$ , nm)	13.1	17.8	19.8	20.8
Crystallinity ( $X_c$ , %)	72	74	74	73

and Raman (machine type: Horiba HR80) analysis. Optical microscopy (OM, machine type: Olympus BX-51) and scanning electron microscope (SEM, machine type: Jeol-6700) were used to observe the morphology of the film surface. Hall measurement (machine type: Ecopia HMS-3000), four-point measurement (machine type: Jandel HM21), and current-voltage measurement ( $I$ - $V$ , machine type: HP4145B) were used to observe the electrical properties of the prepared samples. UV-Vis spectrometer (machine type: Thermo Evolution-300) was used to measure the reflection and absorption coefficient of the prepared samples in the wavelength range of 200–400 nm.

## 3. Results and Discussion

**3.1. Crystallite Structure.** XRD analysis was performed on these induced samples in order to confirm if the samples are crystallized silicon after annealing and etching of Al and SiN<sub>x</sub>. Figure 2 illustrates the XRD of the poly-Si thin films using AIC with capping layer on the ITO coated glass substrate with the annealing time of (a) 15, (b) 30, (c) 45, and (d) 60 min. The highest peaks were around  $2\theta = 28.5^\circ$  and correspond to Si (111) which indicates that the crystallization of a-Si:H is obtained in the AIC specimens even for the low annealing temperature of 350°C with annealing time of 15, 30, 45, and 60 min, respectively. In addition, the peak of Si (220) is enhanced for the long annealing time, indicating that the well crystallization can be obtained in the longer annealing time. The crystalline size is calculated by the Scherrer equation [16]:

$$D = \frac{K\lambda}{\Delta(2\theta) \cos \theta}. \quad (1)$$

$D$  is crystalline size,  $K$  is constant,  $\lambda$  is X-ray wavelength,  $\Delta(2\theta)$  is full width at half maximum (FWHM), and  $\theta$  is diffraction angle. The crystalline sizes were 13.1, 17.8, 19.8, and 20.8 nm, as shown in Table 1, for the poly-Si thin films with the annealing time of 15, 30, 45, and 60 min, respectively.

Figure 3 illustrates the Raman spectra of the poly-Si thin films using AIC with the capping layer annealed at a low temperature of 350°C with the annealing time of (a) 15, (b) 30, (c) 45, and (d) 60 min. It is known that the Raman spectra of the amorphous silicon, polycrystalline silicon, and single crystal silicon are located around 480 cm<sup>-1</sup>, 500~515 cm<sup>-1</sup>, and 520 cm<sup>-1</sup>, respectively [8]. The Raman spectra of the prepared poly-Si thin films with different annealing time all appeared around 510 cm<sup>-1</sup> to the 520 cm<sup>-1</sup>, indicating that the amorphous thin films on the ITO coated glass substrate have been induced successfully at a low temperature of 350°C even at a short annealing time of 15 min.

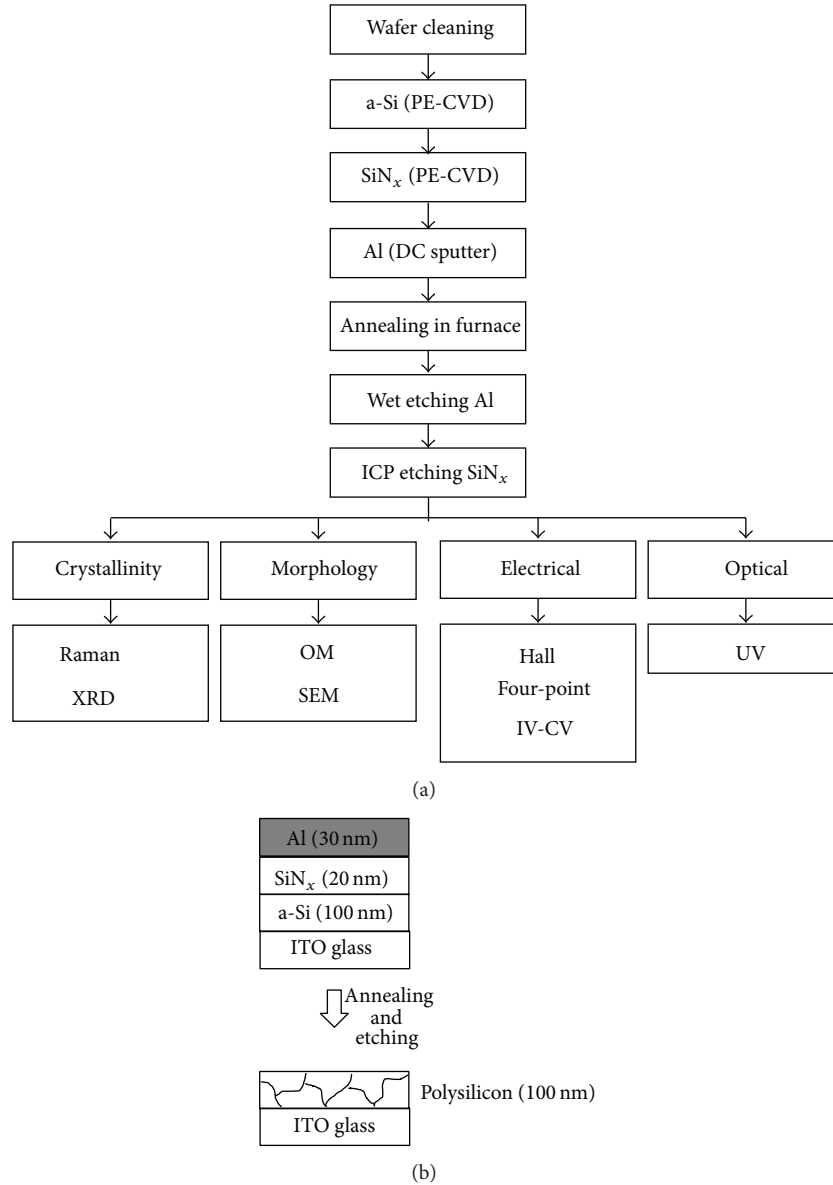


FIGURE 1: (a) The experimental procedure of this study for poly-Si thin films using AIC with the capping layer and (b) transformation procedure for aluminum induced crystallization of a-Si:H films on the ITO coated glass substrate.

To further calculate the crystallinity fraction of the induced samples for different annealing time, the curve fitting of the Raman spectra shall be used as shown in Figure 4. The Raman spectra can be divided into three spectra regions for amorphous silicon, polycrystalline silicon, and single crystal silicon. The crystallinity fraction  $X_c$  of the induced samples for the different annealing time is calculated by (2), and the meaning of  $I_a$ ,  $I_m$ , and  $I_c$  is the intensity of Raman shift on  $480\text{ cm}^{-1}$ ,  $500\sim 515\text{ cm}^{-1}$ , and  $521\text{ cm}^{-1}$ , respectively [5–7]. Consider

$$X_c = \frac{I_m + I_c}{I_a + I_m + I_c}. \quad (2)$$

Table 1 shows the crystallinity ratios of the induced poly-Si thin films using AIC with the capping layer for different

annealing time. It is found that the crystallinity ratios for all films are around 73% and independent of the annealing times. The process parameters of the annealing temperature of  $350^\circ\text{C}$  and the annealing time of 15 min are suitable to induce the amorphous silicon film to be poly-Si film in this study. For the solar cell application, the crystallinity ratio of 73% is desired. If one desires more crystallization of silicon thin film, it is suggested that the Al thickness shall be thick or the silicon nitride layer should not be introduced. However, it will cause more residual Al concentration to decrease the grain size and Hall mobility as discussed later [7].

**3.2. Surface Morphology.** Figure 5 illustrates optical microscope (OM) images of the poly-Si thin films using AIC with

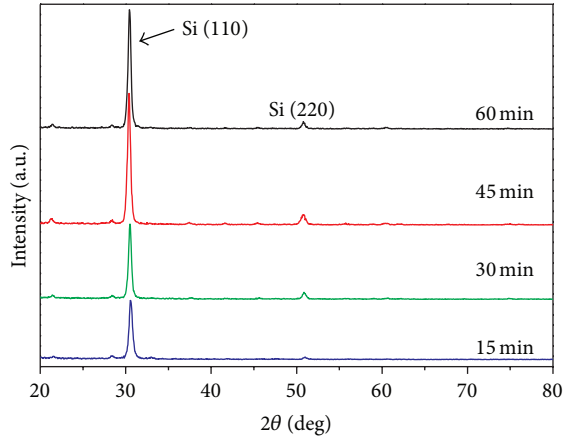


FIGURE 2: The XRD of the poly-Si thin films using AIC with the capping layer for the annealing time of (a) 15, (b) 30, (c) 45, and (d) 60 min.

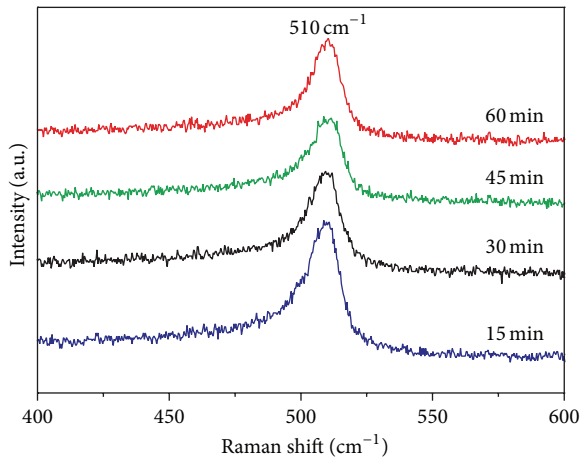


FIGURE 3: The Raman spectra of the poly-Si thin films using AIC with the capping layer for the annealing time of (a) 15, (b) 30, (c) 45, and (d) 60 min.

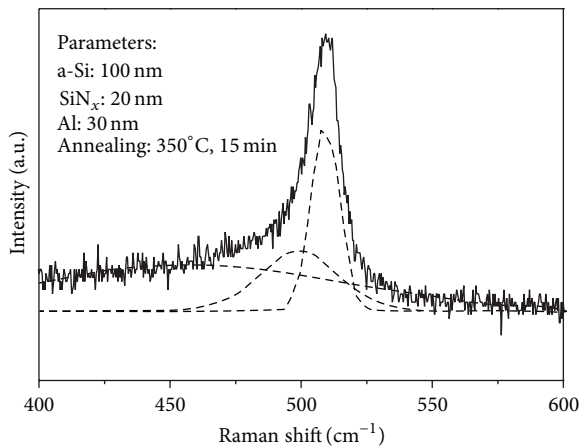


FIGURE 4: Curve fitting of the Raman spectra for the poly-Si thin films using AIC with the capping layer, wherein the Raman spectra can be divided into three spectra for a-silicon ( $480\text{ cm}^{-1}$ ), polysilicon ( $500\text{ cm}^{-1}$ ) and single-silicon ( $521\text{ cm}^{-1}$ ).

the capping layer for different annealing time. It is clearly observed that the grain sizes are growing when the annealing time increases. In order to show the difference of grain size between the AIC with and without the capping layer, the poly-Si thin films on the ITO coated glass substrate using AIC but without the capping layer for the annealing time of 120 min was also prepared and its OM image was shown in Figure 5(b). The bright spots in each grain of Figure 5(a) are believed to be the nucleation sites [17]. It was reported that the difference in intensity/color between the nucleation center and other portions of a grain is attributable to the difference of refractive index in the two regions of the grain [13]. The average grain sizes  $\bar{G}$  of the sample were estimated directly from the OM using the linear intercept method described by the formula [17]:

$$\text{Average grain size, } \bar{G} = 1.56\bar{L}, \quad (3)$$

where  $\bar{L}$  is the average grain boundary intercept length of a series of random lines on the OM image. Figure 5(c) shows the variation of average grain size of the poly-Si thin film using AIC specimens. The average grain sizes are around 18.5, 21, 18, and  $17.5\text{ }\mu\text{m}$  for the annealing time of 15, 30, 45, and 60 min, respectively. It is also observed that the poly-Si thin film using AIC, but without, the capping layer has the grain size of  $6\text{ }\mu\text{m}$  even with the annealing time of 120 min. Namely, the grain size of the poly-Si thin films with the capping layer is three times larger than that without the capping layer. The reason is explained as follows. The Al induced crystallization starts with formation of Si nuclei within the Al layer at the Al/a-Si interface [12]. Then, the Si grains keep growing laterally only until they touch adjacent grains and from a continuous poly-Si film [9]. The capping layer is used in this study to decrease the diffusion rate of Al atoms from Al layer to react with a-Si 9 at the Al/a-Si interface. Therefore, the nucleation sites at the Al/a-Si interface with the capping layer are lower than those without the capping layer, thus enhancing the Si grain to grow laterally.

The result shows that the grain size of the poly-Si thin film induced by AIC is significantly affected by the distance between adjacent nucleation sites. Namely, reducing the density of nucleation sites is a key factor for growing large grains. Thus, using the capping layer of  $\text{SiN}_x$  between the Al and a-Si thin film actually reduces the density of nucleation sites so as to grow the large grains.

Figure 6 shows SEM images of the poly-Si thin films using AIC with the capping layer for the annealing time of (a) 15, (b) 30, (c) 45, and (d) 60 min. No cracks were observed by SEM to ensure that grain boundaries observed by optical microscopy are not cracks in the silicon films. Moreover, the subgrains are clearly observed in the SEM images and the subgrains sizes are around 100 nm to 150 nm for the annealing time from 15 to 60 min. The subgrains sizes estimated from the SEM images are larger than the crystal sizes calculated from the XRD results. It is known that the difference between the average crystalline size and subgrain size determined from XRD and SEM data resulted from the fact that the SEM measurement is more sensitive to the surface structure and the XRD data is sensitive to the structure of the film itself [14].

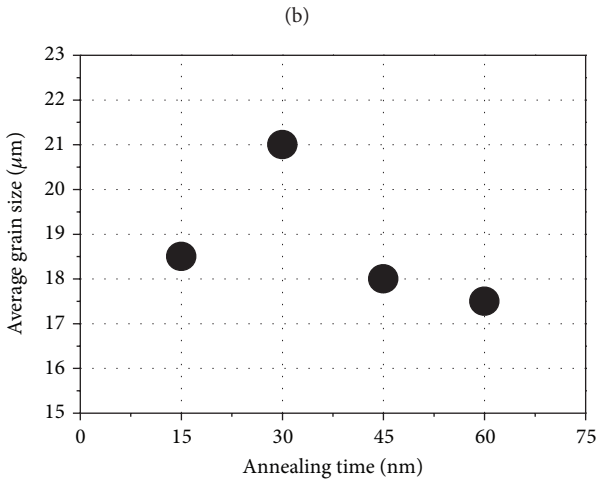
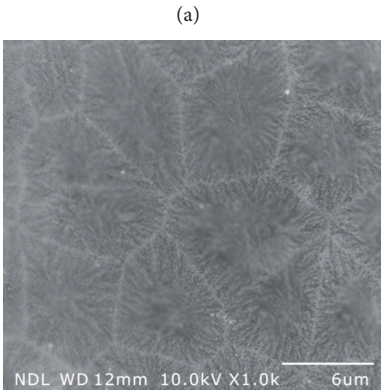
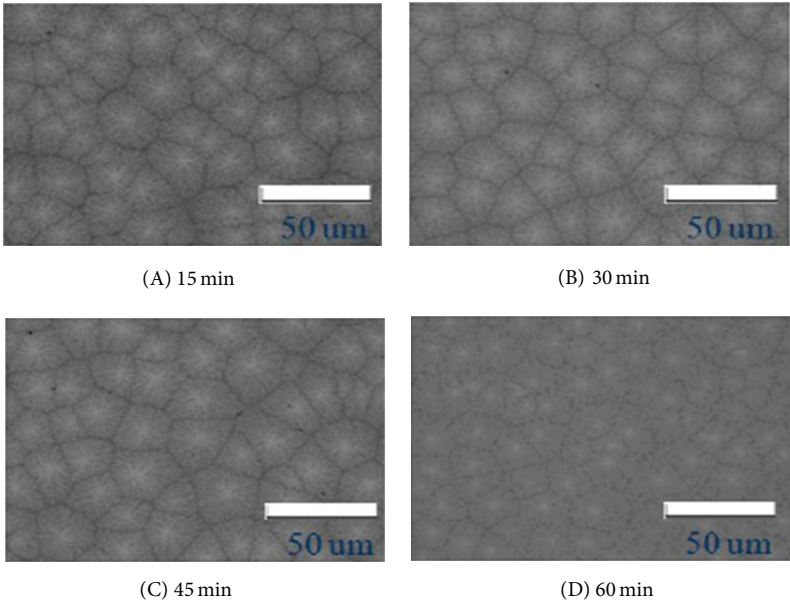


FIGURE 5: OM images of the poly-Si thin films (a) using AIC with the capping layer for the annealing time of 15, 30, 45, and 60 min and (b) using AIC without the capping layer for the annealing time of 120 min; and (c) the variation of average grain sizes of the poly-Si thin films using AIC with the capping layer.

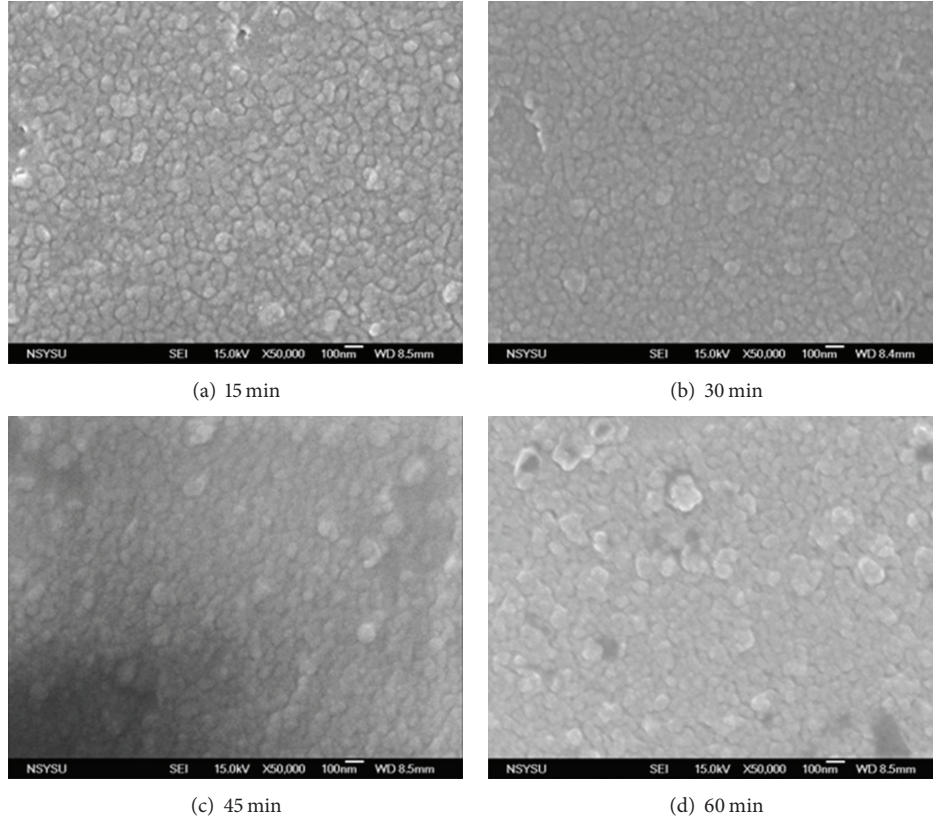


FIGURE 6: SEM images of the poly-Si thin films using AIC with the capping layer for annealing time of (a) 15, (b) 30, (c) 45, and (d) 60 min.

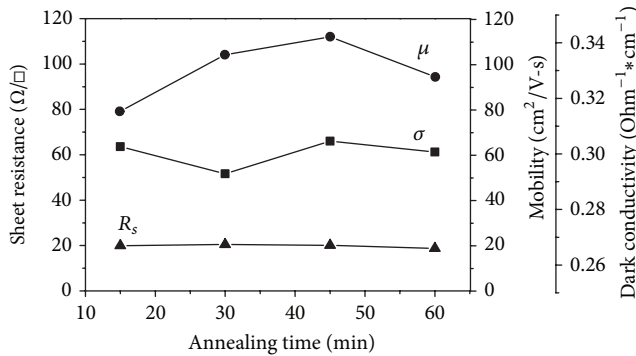


FIGURE 7: Mobility, dark conductivity, and sheet resistance of the poly-Si thin films using AIC with the capping layer for different annealing time.

**3.3. Electrical Properties.** Figure 7 shows mobility ( $\mu$ ), dark conductivity ( $\sigma_d$ ), and sheet resistance ( $R_s$ ) of the poly-Si thin films using AIC with the capping layer for the different annealing time. First, the mobility ( $\mu$ ) and sheet resistance ( $R_s$ ) of the ITO are  $35 \text{ cm}^2/\text{V}\cdot\text{s}$  and  $15 \Omega/\text{squ}$ , respectively. Although the poly-Si thin films using AIC with the capping layer are coated on ITO glass, under this structure, the measured mobility is around 82, 105, 112, and  $92 \text{ cm}^2/\text{V}\cdot\text{s}$ , the dark conductivity is within  $0.29\sim 0.31 \Omega\cdot\text{cm}^{-1}$ , and the sheet resistance is all around  $20 \Omega/\text{squ}$  for the annealing time is

15, 30, 45, and 60 min, respectively. Table 2 summarizes the electrical properties of the prepared poly-Si thin films using AIC with the capping layer and compared them with those in the previous works using conventional AIC without the capping layer. It is clearly found the electrical properties of poly-Si thin films are much improved by using the proposed method, that is, the AIC with the capping layer. The mobility is much improved due to the increased grain size as compared with the previous work, since a large grain size has a few grain boundaries and thus reduces the scattering effect from the defect of the grain boundary. Since the resistivity ( $\rho$ ) is reversal to the conductivity ( $\sigma$ ) and the resistivity of the prepared poly-Si thin films is calculated within  $3.2\sim 3.4 \Omega\cdot\text{cm}$ , the values of resistivity indicate that it is also suitable to be used as the semiconductor material.

Moreover, the carrier concentration ( $n$ ) can be calculated in an order of  $10^{16}/\text{cm}^3$  according to the following equation [7]:

$$\sigma = q\mu n, \quad (4)$$

where  $q$  is  $1.6 \times 10^{-19}$  Coul. Thus, the carrier concentration of the induced poly-Si using the proposed AIC with the capping layer is much lower than those of the previous works since the residual Al metal is not easy to be removed in the traditional AIC without the capping layer. According to the Nast et al. study [9], they emphasized that the number of metal concentrations affects the value of mobility in the MIC

TABLE 2: The electrical properties of the poly-Si thin films using AIC with the capping layer.

	Al (nm)	a-Si (nm)	Substrate	Annealing temperature (°C)	Annealing time (min)	Mobility ( $\mu$ , $\text{cm}^2/\text{V}\cdot\text{s}$ )	Sheet resistance ( $R_s$ , $\Omega/\square$ )	Grain size ( $\mu\text{m}$ )
Kim et al. [6]	200	96	Glass	550	10~40	N/A	4500~5000	N/A
Nast et al. [7]	500	500	Glass	350~500	30	60~70	N/A	N/A
Nast et al. [9]	450~500	500	Glass	500	5~60	56.3	820	N/A
Widenborg et al. [19]	250~450		Glass	400	30	N/A	800~4000	N/A
Our results	30	100	ITO Glass	350	15~60	80~112	19~21	17~21

process. In the Sohn et al. study [15], they indicated the low metal concentration of polysilicon in the MIC process with capping layer than without capping layer. However, the film still has the metal content.

When considering the sheet resistance ( $R_s$ ) of the poly-Si thin films, the typical formula (5) is as follow [6, 7, 19]:

$$R_s = \frac{\rho}{d}, \quad (5)$$

where  $d$  is the film thickness. If we use this formula to calculate the sheet resistance ( $R_s$ ) of the prepared poly-Si thin films, the sheet resistance ( $R_s$ ) is around 4000~5000  $\Omega/\text{sq}$ , which is much higher than our measured results, but is very similar to those of the previous works, as shown in Table 2. The reason is explained as follows. The previous works were done on the glass and obtain their sheet resistance ( $R_s$ ) with the value within 4000~5000  $\Omega/\text{sq}$ , which is similar to our calculated sheet resistance ( $R_s$ ). However, the prepared poly-Si thin films are formed on the ITO coated glass, and it is believed that the low resistance of the ITO can reduce the sheet resistance ( $R_s$ ) of the prepared poly-Si thin films as the results we measured.

**3.4. Optical Properties.** Figure 8 shows the optical energy gaps of the poly-Si thin films using AIC with the capping layer annealed at a low temperature of 350°C with the annealing time of (a) 15, (b) 30, (c) 45, and (d) 60 min using Taucs plot. The optical energy gap ( $E_g$ ) of the films can be further calculated from the transmission spectra using (6), which assumes a direct transition between the edges of the valence and the conduction band. The relationship between the absorption coefficient  $\alpha$  and the photon energy  $h\nu$  can be given as in [22]:

$$(\alpha h\nu)^2 = A(h\nu - E_g), \quad (6)$$

where  $\alpha$  was estimated from the transmittance data,  $A$  is a constant depending on the materials properties, and  $(\alpha h\nu)^2$  is a function of  $h\nu$ . By extrapolating  $\alpha = 0$  from the linear region of "Tauc" plots, the calculated values of the optical energy gaps for the prepared poly-Si thin films in this study were closed to 1.1 eV.

Figure 9 illustrates the reflection spectra of the poly-Si thin films using AIC with the capping layer for different annealing time. It was reported that for intrinsic monocrystalline silicon, two prominent maxima peaks at the wavelength of 274 nm and 365 nm in the reflectance spectrum

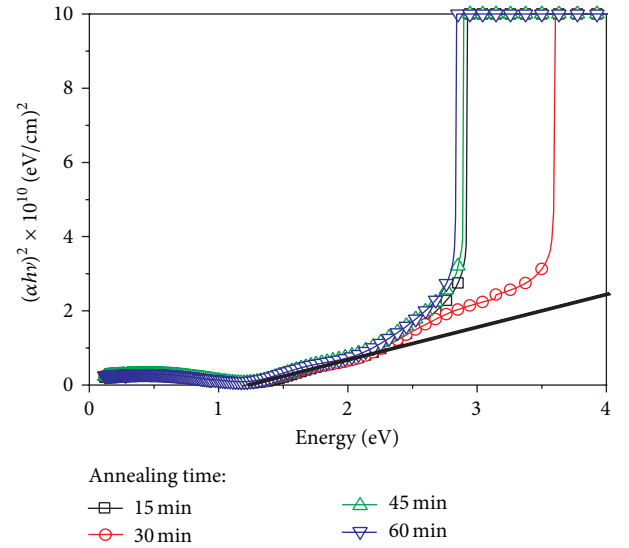


FIGURE 8: Taucs plots for the poly-Si thin films using AIC with the capping layer for annealing time of (a) 15, (b) 30, (c) 45, and (d) 60 min.

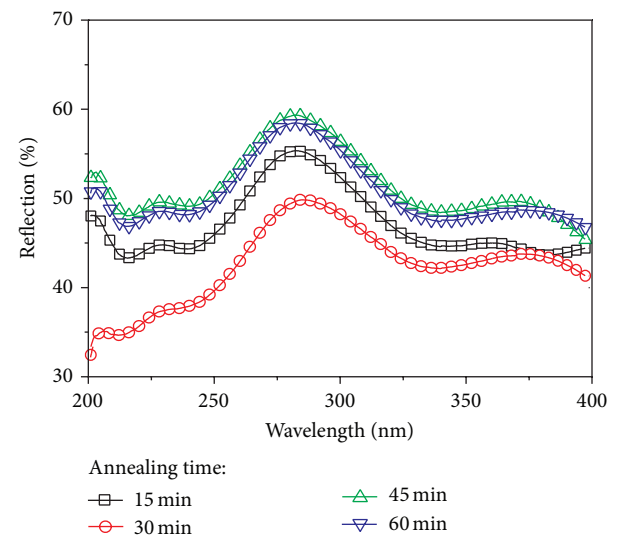


FIGURE 9: Reflection spectra of the poly-Si thin films using AIC with the capping layer for annealing time of (a) 15, (b) 30, (c) 45, and (d) 60 min.

could be clearly obtained. Moreover, a reduction of ultraviolet reflection usually indicates the appearance of a surface oxide, surface roughness, and/or structurally damaged material [19]. It is found in Figure 5 that the large grain sizes between 17 to 21  $\mu\text{m}$  are obtained so as to reduce the structurally damaged boundaries. However, if structural disorder exists in the surface layer, it will cause a broadening and large reduction predominantly at these maximum peaks. As shown in Figure 2, the well crystallization can be obtained in the long annealing time. Therefore, as shown in Figure 9, it is observed that the measured reflection ratio is within 35~60% and two prominent peaks at the wavelength of 280 nm and 370 nm exist which is similar with that of an intrinsic polished monocrystalline silicon. Namely, the crystal quality of the prepared poly-Si using AIC with the capping layer is acceptable, comparable to a polished Si wafer.

#### 4. Conclusions

In this paper, the microstructure, electrical, and optical properties of poly-Si prepared by aluminum induced crystallization with the capping layer of  $\text{SiN}_x$  were investigated. The structure comprising Al (30 nm)/ $\text{SiN}_x$  (20 nm)/a-Si layer (100 nm)/ITO coated glass was annealed at 350°C for the different annealing time of 15, 30, 45, and 60 min. We have verified that the capping layer of the  $\text{SiN}_x$  can effectively reduce the diffusion rate of Al atoms from Al layer through the Al/a-Si interface and thus improve the grain size and electrical properties such as resistivity, residual carrier concentration of the induced poly-Si film. The results of the crystal plane of the Si (110) from the XRD results and the Raman shift around the 510  $\text{cm}^{-1}$  from the Raman spectra confirm that the a-Si thin film has been induced and transferred to be the polysilicon. The high-quality and large grain size poly-Si thin film can be obtained at such low temperature of 350°C. The OM image shows the large grain sizes of the prepared films are around 17 to 21  $\mu\text{m}$ . The values of mobility are 82, 105, 112, and 92  $\text{cm}^2/\text{V}\cdot\text{s}$ , the values of the dark conductivity are within 0.29~0.31  $\Omega\cdot\text{cm}^{-1}$ , and the values of the sheet resistance are all around 20  $\Omega/\text{sq}$  for the different annealing time of 15, 30, 45, and 60 min. The carrier concentration ( $n$ ) can be calculated in an order of  $10^{16}/\text{cm}^3$ . The measured reflection ratio is within 35~60% and two prominent peaks at 280 nm and 370 nm wavelength exist which is similar with that of an intrinsic polished monocrystalline silicon.

#### Conflict of Interests

The authors declare that there is no conflict of interests regarding the publication of this paper.

#### Acknowledgments

The authors would like to thank the financial support from the Ministry of Science and Technology, Southern Taiwan Science Park Administration (STSPA), and Industrial Development Bureau, Ministry of Economic Affairs, Taiwan under Contracts NSC101-2628-E-020-002-MY3, 102CE04,

and 102E2057. The authors would also like to thank the National Nano Device Laboratories and the Precision Instrument Center of the National Pingtung University of Science and Technology for supporting the experimental equipment.

#### References

- [1] S. D. Brotherton, "Polycrystalline silicon thin film transistors," *Semiconductor Science and Technology*, vol. 10, no. 6, pp. 721–738, 1995.
- [2] R. Martins, L. Raniero, L. Pereira et al., "Nanostructured silicon and its application to solar cells, position sensors and thin film transistors," *Philosophical Magazine*, vol. 89, no. 28–30, pp. 2699–2721, 2009.
- [3] M. S. Haque, H. A. Naseem, and W. D. Brown, "Aluminum-induced degradation and failure mechanisms of a-Si:H solar cells," *Solar Energy Materials and Solar Cells*, vol. 41–42, pp. 543–555, 1996.
- [4] L. Mariucci, R. Carluccio, A. Pecora et al., "Lateral growth control in excimer laser crystallized polysilicon," *Thin Solid Films*, vol. 337, no. 1–2, pp. 137–142, 1999.
- [5] S.-W. Lee, Y.-C. Jeon, and S.-K. Joo, "Pd induced lateral crystallization of amorphous Si thin films," *Applied Physics Letters*, vol. 66, pp. 1671–1673, 1995.
- [6] D. Y. Kim, M. Gowtham, M. S. Shim, and J. Yi, "Polycrystalline silicon thin film made by metal-induced crystallization," *Materials Science in Semiconductor Processing*, vol. 7, no. 4–6, pp. 433–437, 2004.
- [7] O. Nast, S. Brehme, D. H. Neuhaus, and S. R. Wenham, "Polycrystalline silicon thin films on glass by aluminum-induced crystallization," *IEEE Transactions on Electron Devices*, vol. 46, no. 10, pp. 2062–2068, 1999.
- [8] O. Nast and S. R. Wenham, "Elucidation of the layer exchange mechanism in the formation of polycrystalline silicon by aluminum-induced crystallization," *Journal of Applied Physics*, vol. 88, no. 1, pp. 124–132, 2000.
- [9] O. Nast, S. Brehme, S. Pritchard, A. G. Aberle, and S. R. Wenham, "Aluminium-induced crystallisation of silicon on glass for thin-film solar cells," *Solar Energy Materials and Solar Cells*, vol. 65, no. 1, pp. 385–392, 2001.
- [10] M. S. Haque, H. A. Naseem, and W. D. Brown, "Interaction of aluminum with hydrogenated amorphous silicon at low temperatures," *Journal of Applied Physics*, vol. 75, no. 8, pp. 3928–3935, 1994.
- [11] L. Cai, H. Wang, W. Brown, and M. Zou, "Large grain polycrystalline silicon film produced by nano-aluminum-enhanced crystallization of amorphous silicon," *Electrochemical and Solid-State Letters*, vol. 8, no. 7, pp. G179–G181, 2005.
- [12] M. Zou, L. Cai, and W. Brown, "Nano-aluminum-induced low-temperature crystallization of PECVD amorphous silicon," *Electrochemical and Solid-State Letters*, vol. 8, no. 5, pp. G103–G105, 2005.
- [13] M. Zou, L. Cai, H. Wang, and W. Brown, "Nano-aluminum-induced crystallization of amorphous silicon," *Materials Letters*, vol. 60, no. 11, pp. 1379–1382, 2006.
- [14] J. H. Choi, D. Y. Kim, B. K. Choo, W. S. Sohn, and J. Jang, "Metal induced lateral crystallization of amorphous silicon through a silicon nitride cap layer," *Electrochemical and Solid-State Letters*, vol. 6, no. 1, pp. G16–G18, 2003.
- [15] W. S. Sohn, J. H. Choi, K. H. Kim, J. H. Oh, S. S. Kim, and J. Jang, "Crystalline orientation of polycrystalline silicon with

- disklike grains produced by silicide-mediated crystallization of amorphous silicon,” *Journal of Applied Physics*, vol. 94, no. 7, pp. 4326–4331, 2003.
- [16] H.-Y. Chu, M.-H. Weng, R.-Y. Yang, C.-W. Huang, and C.-H. Li, “Effect of Al thickness on the Al induced low temperature poly-Si film crystallization process,” in *Proceedings of the 4th IEEE International Conference on Nano/Micro Engineered and Molecular Systems (NEMS '09)*, pp. 641–644, Shenzhen, China, January 2009.
- [17] M. I. Mendelson, “Average grain size in polycrystalline ceramics,” *Journal of the American Ceramic Society*, vol. 52, no. 8, pp. 443–446, 1969.
- [18] C. Ornaghi, G. Beaucarne, J. Poortmans, J. Nijs, and R. Mertens, “Aluminum-induced crystallization of amorphous silicon: influence of materials characteristics on the reaction,” *Thin Solid Films*, vol. 451–452, pp. 476–480, 2004.
- [19] P. I. Widenborg, A. B. Sproul, and A. G. Aberle, “Impurity and defect passivation in poly-Si films fabricated by aluminium-induced crystallisation,” in *Proceedings of the 3rd World Conference on Photovoltaic Energy Conversion*, pp. 1233–1236, Osaka, Japan, May 2003.
- [20] L. Pereira, H. Águas, R. M. S. Martins, P. Vilarinho, E. Fortunato, and R. Martins, “Polycrystalline silicon obtained by metal induced crystallization using different metals,” *Thin Solid Films*, vol. 451–452, pp. 334–339, 2004.
- [21] O. Shamiryan, I. Maidanchuk, N. Ahn, I. Choi, and H. K. Chung, “Electrical characterization of thin silicon films produced by metal-induced crystallization on insulating substrates by conductive AFM,” *Journal of Surface Analysis*, vol. 17, pp. 260–263, 2011.
- [22] Y. G. Wang, S. P. Lau, H. W. Lee et al., “Comprehensive study of ZnO films prepared by filtered cathodic vacuum arc at room temperature,” *Journal of Applied Physics*, vol. 94, no. 3, pp. 1597–1604, 2003.

## Research Article

# Upconversion luminescence and Visible-Infrared Properties of $\beta$ -NaLuF<sub>4</sub>:Er<sup>3+</sup> Microcrystals Synthesized by the Surfactant-Assisted Hydrothermal Method

Han Lin,<sup>1</sup> Xiaohong Yan,<sup>1,2</sup> Jin Zheng,<sup>2</sup> Changjie Dai,<sup>1</sup> and Yuan Chen<sup>1</sup>

<sup>1</sup> College of Science, Nanjing University of Aeronautics and Astronautics, Nanjing 211106, China

<sup>2</sup> School of Electronic Science and Engineering, Nanjing University of Posts and Telecommunications, Nanjing 210046, China

Correspondence should be addressed to Xiaohong Yan; xhyan@nuaa.edu.cn

Received 21 February 2014; Revised 20 May 2014; Accepted 22 May 2014; Published 18 June 2014

Academic Editor: Alireza Talebitahter

Copyright © 2014 Han Lin et al. This is an open access article distributed under the Creative Commons Attribution License, which permits unrestricted use, distribution, and reproduction in any medium, provided the original work is properly cited.

We report the obtention of  $\beta$ -NaLuF<sub>4</sub> microcrystals doped with Er<sup>3+</sup> ions by the surfactant-assisted hydrothermal method. It was found that shape modulation could be realized by changing the surfactants (ethylenediaminetetraacetic acid, polyvinylpyrrolidone, and trisodium citrate) introduced into the reaction system. The surfactants can strongly control the size and shape of as-prepared samples through absorbing on the surface of primary particles and/or coordinating with rare earth ions. Hexagonal prism-like  $\beta$ -NaLuF<sub>4</sub>:Er<sup>3+</sup> microcrystals demonstrate intense upconverted luminescence (UCL) pumped by 1.54  $\mu$ m infrared laser in comparison with hexagonal tube-like, disk-like, and sphere-like microcrystals, which exhibit great distinction. More interestingly, a synergistic effect combined dual mode (i.e., downconversion and upconversion) with 8% absolute enhancement rate of the red emission centered at 659 nm (<sup>4</sup>F<sub>9/2</sub> → <sup>4</sup>I<sub>15/2</sub>) is witnessed in hexagonal prisms  $\beta$ -NaLuF<sub>4</sub>:Er<sup>3+</sup> phosphors by employing the dual wavelength 416 nm and 1.54  $\mu$ m excitation source for the first time.

## 1. Introduction

Rare earth fluorides including REF<sub>3</sub> and AREF<sub>4</sub> (A = alkali; RE = rare earth) have been regarded as excellent downconversion (DC) and upconversion (UC) luminescent hosts for various optically active Ln<sup>3+</sup> ions [1–6]. They normally possess low phonon energy, low probability of nonradiative decay, and high chemical stabilities, and the luminescent quantum yields higher than that in oxide hosts and most inorganic matrices. Thus, rare earth fluorides have attracted much attention of scientific community due to their potential applications in the fields of solid-state lasers, multicolor three dimensional displays, optical storage, and biological fields including fluorescent labels, therapy, and drug delivery [7–10]. One example for this class of fluoride compounds is NaLuF<sub>4</sub>, which is an ideal UC host material [11–16]. Shi et al. [11] synthesized hexagonal nanoplates  $\beta$ -NaLuF<sub>4</sub>:Yb<sup>3+</sup>/Tm<sup>3+</sup> crystals by hydrothermal method using oleic acid as the surfactant and demonstrated that  $\beta$ -NaLuF<sub>4</sub> nanocrystals

might be a better kind of upconversion material than their  $\beta$ -NaYF<sub>4</sub> counterpart. Li et al. [15] prepared multiform morphologies  $\beta$ -NaLuF<sub>4</sub> by changing the solution pH values, F<sup>-</sup> sources, and organic additives and studied the morphological evolution and the growth mechanism for the synthesized lutetium fluorides under different conditions in detail.

In this work, we present our recent efforts on the fabrication of NaLuF<sub>4</sub> crystals with controllable sizes and enhanced PL properties. Emission intensity and energy efficiency are used as measures of the phosphors performance. They are important performance characteristics that determine which applications are appropriate. In most cases, the thermalization losses and subbandgap light transmission are the major bottleneck effect on energy efficiency [17–20]. Erbium (Er) possesses several long-lived intermediate levels and metastable high-energy levels, and the energy gap between the ground level <sup>4</sup>I<sub>15/2</sub> and the first excited level <sup>4</sup>I<sub>13/2</sub> is matched well with the absorption of 1.54  $\mu$ m photon, so it can be considered as a promising candidate among REs

TABLE 1: Summary of morphologies and their corresponding detailed experimental conditions of samples<sup>a</sup>.

Sample	Agents	Agents/ReCl <sub>3</sub> molar ratio	Phase	Morphology	Mean size ( $\mu\text{m}$ )	Graph
S1	EDTA	1:1	Hexagonal	Hexagonal prisms	$L$ : 9	Figure 2(a)
S2	EDTA	2:1	Hexagonal	Hexagonal prisms	$L$ : 3.5	Figure 2(b)
S3	EDTA	3:1	Hexagonal	Hexagonal prisms	$L$ : 1	Figure 2(c)
S4	PVP	1:1	Hexagonal	Tubes with cracks	$H$ : 10	Figure 2(d)
S5	PVP	2:1	Hexagonal	Tubes with cracks	$H$ : 5	Figure 2(e)
S6	PVP	3:1	Hexagonal	Irregular hexagonal tubes	$H$ : 1.5	Figure 2(f)
S7	Cit <sup>3-</sup>	1:1	Orthorhombic (LuF <sub>3</sub> )	Spheres	$D$ : 3.5	Figure 2(g)
S8	Cit <sup>3-</sup>	2:1	Hexagonal	Spheres with coarse surface	$D$ : 2	Figure 2(h)
S9	Cit <sup>3-</sup>	3:1	Hexagonal	Perfect disks	$D$ : 1.5	Figure 2(i)

$D$ : diameter;  $H$ : height;  $L$ : side length.

<sup>a</sup>All samples were hydrothermally treated at 190°C for 24 h.

for UC of photons [21–25]. The current researches mainly focus on the single mode UC or DC. No matter which mode both can enhance and improve the spectral response characteristics of materials. If we combine the two kinds of conversion mechanisms, UC and DC can be achieved in specific materials at the same time. This will make the high-energy and low-energy photons convert to middle-energy photons ultimately, and the middle-energy photon is needed for photovoltaic materials. Therefore, our group proposed a new mechanism named photon-excited synergistic effect [20].

In this paper, we report on the effect of different surfactants, such as ethylenediaminetetraacetic acid (EDTA), polyvinylpyrrolidone (PVP-K30), and trisodium citrate (hereinafter shortened form Cit<sup>3-</sup>), on the growth process and PL properties at room temperature of  $\beta$ -NaLuF<sub>4</sub> microcrystals synthesized by the hydrothermal method. The as-prepared hexagonal prisms  $\beta$ -NaLuF<sub>4</sub> crystals have highly efficient UC luminescence and synergistic effect by employing the 416 nm and 1.54  $\mu\text{m}$  coexcitation source.

## 2. Experimental Details

**2.1. Synthesis of  $\beta$ -NaLuF<sub>4</sub> Microcrystals Doped with Er<sup>3+</sup> Ions.** Rare earth oxides Lu<sub>2</sub>O<sub>3</sub> (99.99%) and Er<sub>2</sub>O<sub>3</sub> (99.99%) were purchased from Beijing Lansu Co., China. Rare earth chlorides (LnCl<sub>3</sub>, Ln:Lu/Er) were prepared by dissolving the corresponding metal oxide in 10% HCl solution at elevated temperature and then evaporating the water completely. NaF (98% purity), NaOH (96% purity), EDTA (99% purity), PVP (95% purity), and Cit<sup>3-</sup> (99% purity) were purchased from Sinopharm Chemical Reagent Co., China. All chemicals were of analytical grade and were used without further purification. Deionized water (H<sub>2</sub>O) was used throughout.

In the typical experiment of NaLuF<sub>4</sub>:Er<sup>3+</sup> micromaterials, a predetermined amount of EDTA was first dissolved in 18 mL distilled water under magnetic stirring to form a solution of desired molar concentration and then stoichiometric amounts of LuCl<sub>3</sub> and ErCl<sub>3</sub> were added to the solution.

Under vigorous stirring for 30 min, 10 mL aqueous solution containing NaF was added dropwise into the above mixture. Then, the pH value of the suspension was adjusted to 7 through the addition of 2 M NaOH solution. The precursor solution was stirred magnetically for 10 min and then transferred to a Teflon lined stainless steel autoclave for hydrothermal treatment maintained at 190°C for 24 h. After the hydrothermal treatment, the autoclave was cooled naturally to room temperature. A light pink colored precipitate settled at the bottom, which was collected and washed repeatedly with distilled water and ethanol to remove the impurities and excessive surfactant. The sample was finally dried at 50°C for 12 h for further characterization. When PVP and Cit<sup>3-</sup> were selected as chelators, the synthesis procedure was basically identical to the above description. Table 1 shows the parameters of hydrothermal synthesis and characteristics of the powders. And the samples prepared under the specific reaction conditions were denoted as S1–S9, respectively.

**2.2. Characterizations.** X-ray powder diffraction (XRD) measurements were performed on an Ultima-III (Rigaku) diffractometer at a scanning rate of 10° min<sup>-1</sup> in the 2 $\theta$  range from 10° to 70°, with graphite monochromatic Cu K $\alpha$  radiation ( $\lambda = 0.15405$  nm). The morphologies were obtained using scanning electron microscopy (SEM, S-3400N II, Hitachi, Japan). Transmission electron microscopy (TEM) and high-resolution transmission electron microscopy (HRTEM) were recorded on a JEOL JEM-200CX with a field emission gun operating at 200 kV. For the UC emission measurement, all the samples were pressed into pellets with 1 cm diameter and 5 mm thickness. The excitation spectra and emission spectra of samples are measured by an Omni- $\lambda$ 3007 spectrophotometer with a CW Xe lamp and infrared lasers with the wavelength at 1.54  $\mu\text{m}$  employed as the excitation source. The dependence of upconverted emission intensity on pumping powers for different samples was obtained by changing the excitation powers. All the measurements above were performed at room temperature.

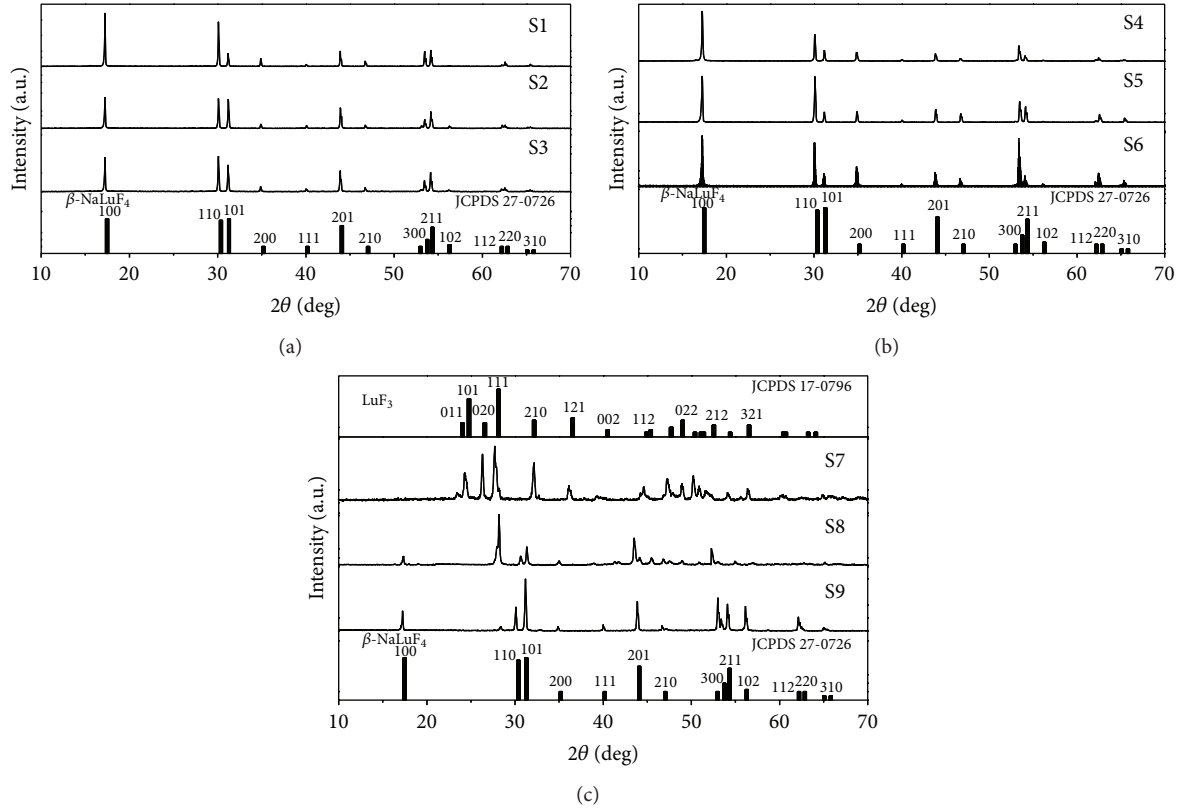


FIGURE 1: XRD patterns of the as-synthesized products obtained in the presence of different surfactants (EDTA: S1 to S3, PVP: S4 to S6, and Cit<sup>3-</sup>: S7 to S9). The standard pattern of hexagonal NaLuF<sub>4</sub> (JCPDS card 27-0726) and orthorhombic LuF<sub>3</sub> (JCPDS card 17-0796) is also presented for comparison.

### 3. Results and Discussions

**3.1. XRD Patterns Analyses.** Figure 1 exhibits XRD patterns of all the prepared products corresponding to Table 1. The regularity indicated from the results is described as follows. For the samples prepared in the presence of EDTA (Figure 1(a)) and PVP (Figure 1(b)) with different agents/Ln<sup>3+</sup> molar ratio, the strong and sharp diffraction peaks suggest that the pure hexagonal structure of NaLuF<sub>4</sub> (JCPDS 27-0726) is successfully achieved through the proposed direct hydrothermal process and the crystal planes for each peak are marked. Besides, the enhanced intensity of peak at ( $\bar{1}00$ ) and ( $\bar{1}10$ ) can be observed in comparison with the standard value, in which the diffraction peaks ( $\bar{1}00$ ) and ( $\bar{1}01$ ) are particularly strong. This result implies that the samples tend to be preferentially oriented. As shown in Figure 1(c), unexpectedly, the as-synthesized samples prepared in the presence of Cit<sup>3-</sup> consist of two different phases, that is, the orthorhombic structure (space group *Pnma*) of LuF<sub>3</sub> (S7) and the hexagonal structure of NaLuF<sub>4</sub> (S8 and S9), which are in good agreement with the standard literature data. This result demonstrates that Cit<sup>3-</sup> plays an important role in the phase for the formation of  $\beta$ -NaLuF<sub>4</sub>, and it may provide a Na<sup>+</sup> source. When the concentration of Cit<sup>3-</sup> is relatively low, there is no sufficient Na<sup>+</sup> source to form NaLuF<sub>4</sub>, but LuF<sub>3</sub>. The calculated cell lattice constants of the samples are summarized in Table 2,

TABLE 2: Unit cell lattice constants and crystallite sizes for hexagonal phase of NaLuF<sub>4</sub> and orthorhombic phase of LuF<sub>3</sub> prepared using different surfactants, respectively.

Samples	<i>a</i> (Å)	<i>c</i> (Å)	Cell volume (Å <sup>3</sup> )
JCPDS 27-0726	5.9010	3.4530	104.13
S1	5.9291	3.4597	105.33
S2	5.9278	3.4583	105.24
S3	5.9354	3.4595	105.54
S4	5.9341	3.4509	105.23
S5	5.9341	3.4545	105.06
S6	5.9341	3.4509	105.23
S8	5.9661	3.4191	105.39
S9	5.9284	3.4597	105.30
JCPDS 17-0796	6.1810	4.4460	184.97
S7	6.1019	4.5715	188.75

and the standard data for hexagonal structure of  $\beta$ -NaLuF<sub>4</sub> and orthorhombic structure of LuF<sub>3</sub> are also given for comparison. Obviously, the calculated cell lattice constants of the samples are consistent with the standard data.

The SEM images of microcrystals prepared using different surfactants are given in Figure 2. It can be seen that all samples exhibit relatively uniform, well-dispersed morphology

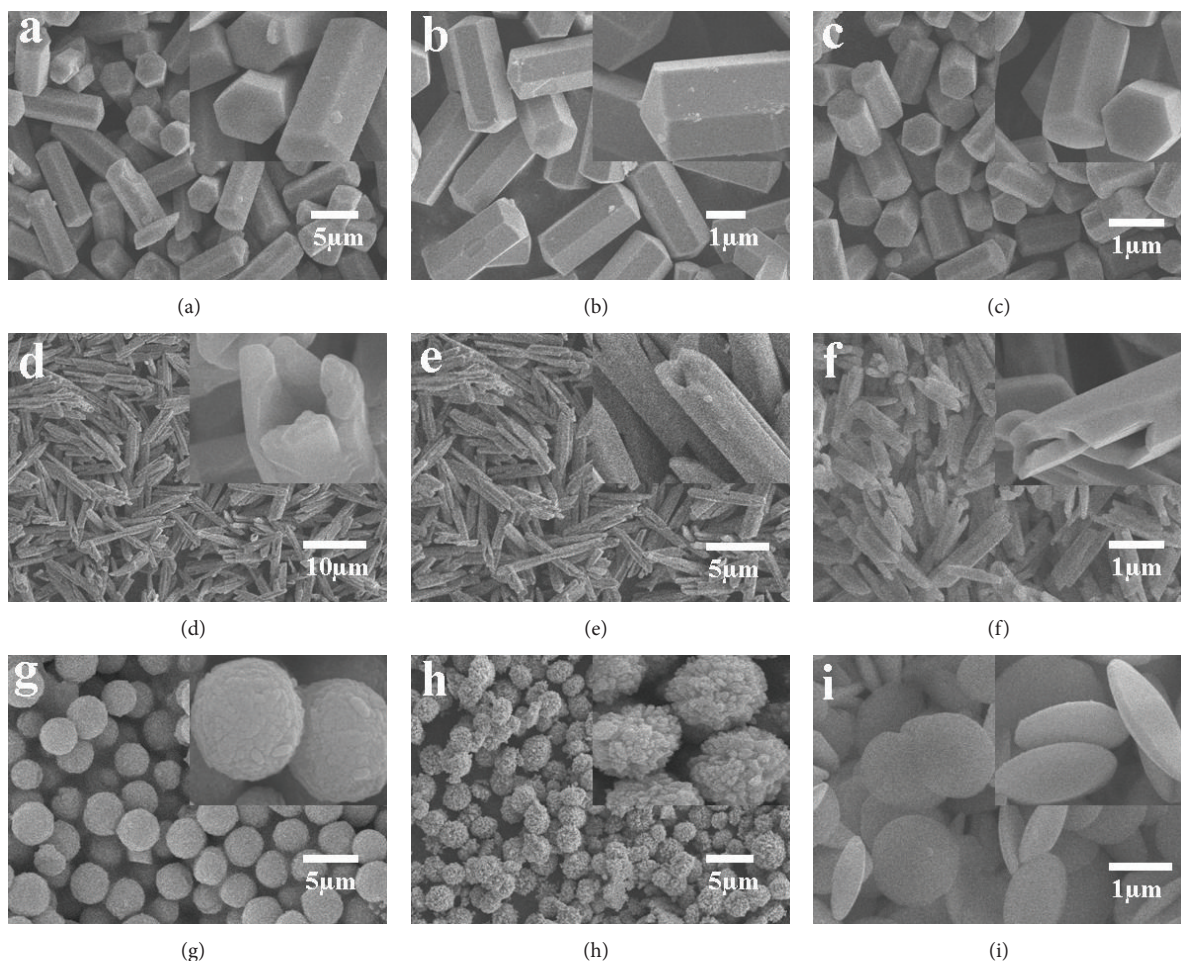


FIGURE 2: SEM images of as-prepared microcrystals using different surfactants with different agents/ $\text{Ln}^{3+}$  molar ratio: (a) S1, (b) S2, (c) S3, (d) S4, (e) S5, (f) S6, (g) S7, (h) S8, and (i) S9. Insets are corresponding high magnification SEM images of the microstructures.

within micrometer size range, yet the specific shapes and sizes of the samples are much different. This distinction is derived from the surfactant, since it is the only difference during the synthesis process. For the samples prepared with EDTA (sample S1–S3), uniform hexagonal prisms are obtained with  $9\ \mu\text{m}$ ,  $3.5\ \mu\text{m}$ , and  $1\ \mu\text{m}$  in length, respectively, except that both ends of S2 are sharp. Samples prepared with PVP (S4–S6) consist of similar tube-shaped aggregates. The diameters of the three tubes are much closer ( $\sim 0.5\ \mu\text{m}$ ), while the lengths differ greatly. As for the samples prepared with  $\text{Ct}^{3-}$  (S7–S9), they are different. Sphere-like  $\beta\text{-NaLuF}_4\text{:Er}^{3+}$  microcrystals are obtained in S7–S8, while S9 consists of fairly uniform and smooth microdisks. The peripheral surface of S8 is rough due to the composition of many small nanoparticles. This finding indicated that any change may result in different morphology and uniformity even when keeping other parameters the same. The morphological difference is caused by the physical and chemical properties of different ligands, and the effects of different surfactants will be discussed thoroughly in the following section.

TEM images, HRTEM images, and SAED patterns of the  $\text{NaLuF}_4\text{:Er}^{3+}$  microcrystals (S3, S6, S8, and S9) are demonstrated in Figure 3, which provide an insight of different structures. TEM image of sample S3 (Figure 3(a)) confirm it as a prism-like structure, which is in good agreement with SEM image. The ED patterns insets in Figure 3(a) show clear and regular diffraction spots, reveal the single crystalline nature of the microprism, and can be indexed as the pure hexagonal structure. The HRTEM image of a single particle confirms the distance of  $0.50\ \text{nm}$  between the adjacent lattice planes, ascribed to that of (110) crystal planes. Unlike sample S3, the tube-like structure of sample S6 is irregular (Figure 3(b)), and ED pattern exhibits the single crystalline nature of the microtube. HRTEM image recorded from the tip of an individual tube verified the lattice fringe separation of  $0.52\ \text{nm}$ . This plane coincides well with the distances between (100) crystal planes. Figures 3(c) and 3(d) exhibit the TEM images of samples prepared with  $\text{Ct}^{3-}$  (samples S8 and S9). We can see that both TEM images show the obvious spherical shape with a uniform size distribution.

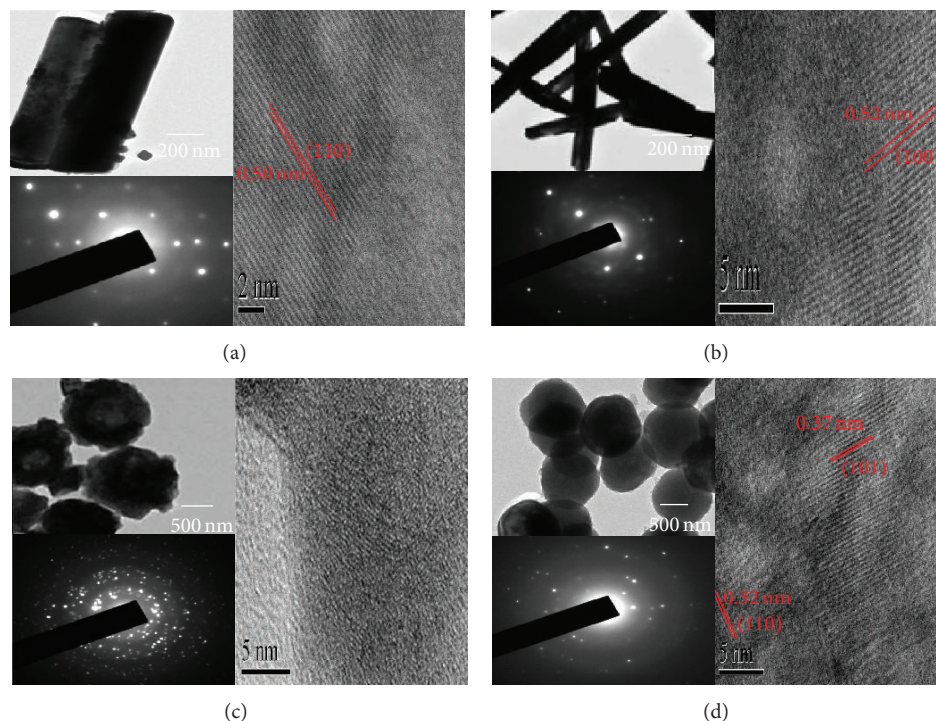


FIGURE 3: The TEM images, HRTEM images, and ED patterns of as-prepared  $\beta$ -NaLuF<sub>4</sub> microcrystals using different surfactants: (a) S3, (b) S6, (c) S8, and (d) S9.

It should be noted that the ED patterns are the polycrystalline. The lattice fringes of the sphere-like sample cannot be seen clearly due to the desultory accumulation of particles. The interplanar distance of the disk-like sample is 0.37 nm and 0.32 nm, which corresponds to the d-spacing value of the (101) and (201) planes, respectively.

**3.2. Growth Mechanism of  $\beta$ -NaLuF<sub>4</sub> Microcrystals.** Based on the above analysis, a possible growth mechanism for the microcrystals was proposed to explain the effect of different surfactants on the shape and size in detail (Figure 4). Firstly Figure 4(a) shows the coordination structures of EDTA, PVP, and Ct<sup>3-</sup>. EDTA molecule possesses four carboxyl groups (-COOH) and two lone pairs of electrons on two nitrogen atoms which can act as binding sites and help to form hydrogen bonds [26]. PVP-K30 is a type of nonionic surfactant with long carbon chains and strong selective adsorption, and lanthanide ions were coordinated with the pyrrolidone groups of PVP [27]. A Ct<sup>3-</sup> molecule has four binding sites, including one hydroxyl group and three COO<sup>-</sup>, among which three sites can be bound with lanthanide ions. After formation of the nuclei (Figure 4(b)), the hydrothermal conditions performed at 190°C for 24 h inside the stainless autoclave intensify the effective collision frequency involving the anisotropic nanoparticles in suspension, producing a mutual aggregation between them. The self-assembly process can occur in a spontaneous way under hydrothermal

conditions, where several nanocrystals are aggregated in a same or different crystallographic plane which can drive the growth of oriented aggregate [28]. The Ln<sup>3+</sup>-EDTA complex can significantly decrease the concentration of free RE<sup>3+</sup> ions and reduce the crystal growth rate, leading to the effective separation of nucleation and growth steps and thus facilitating the synthesis process of crystals. PVP-K30 can be adsorbed onto the surface of nuclei particles to further control its morphology. Furthermore, PVP-K30 can facilitate the nucleation and growth of rare earth compounds on each surface to form tube-like crystals. The Ct<sup>3-</sup> molecule can also control both the crystal nucleation and the growth in the reaction system and it can cap on the side of precursor particles and lead to the selective growth rate of various crystallographic facets.

**3.3. UC Luminescence Properties.** The upconversion (UC) luminescence spectra for the samples (S3, S6, S8, and S9) were recorded upon 1.54  $\mu$ m pumping with power density of 16 mW/mm<sup>2</sup>. Obviously, the four samples exhibit quite different emission intensities and peak positions. Figure 5 shows the upconversion emission spectra of  $\beta$ -NaLuF<sub>4</sub>:x mol%Er<sup>3+</sup> (x = 6, 12, 24, 36) microcrystals. As can be observed, in hexagonal prisms (S3; Figure 5(a)) and hexagonal tubes (S6; Figure 5(b)), there were three well-known intense emission bands centered at 541 nm, 659 nm, and 805 nm, which are

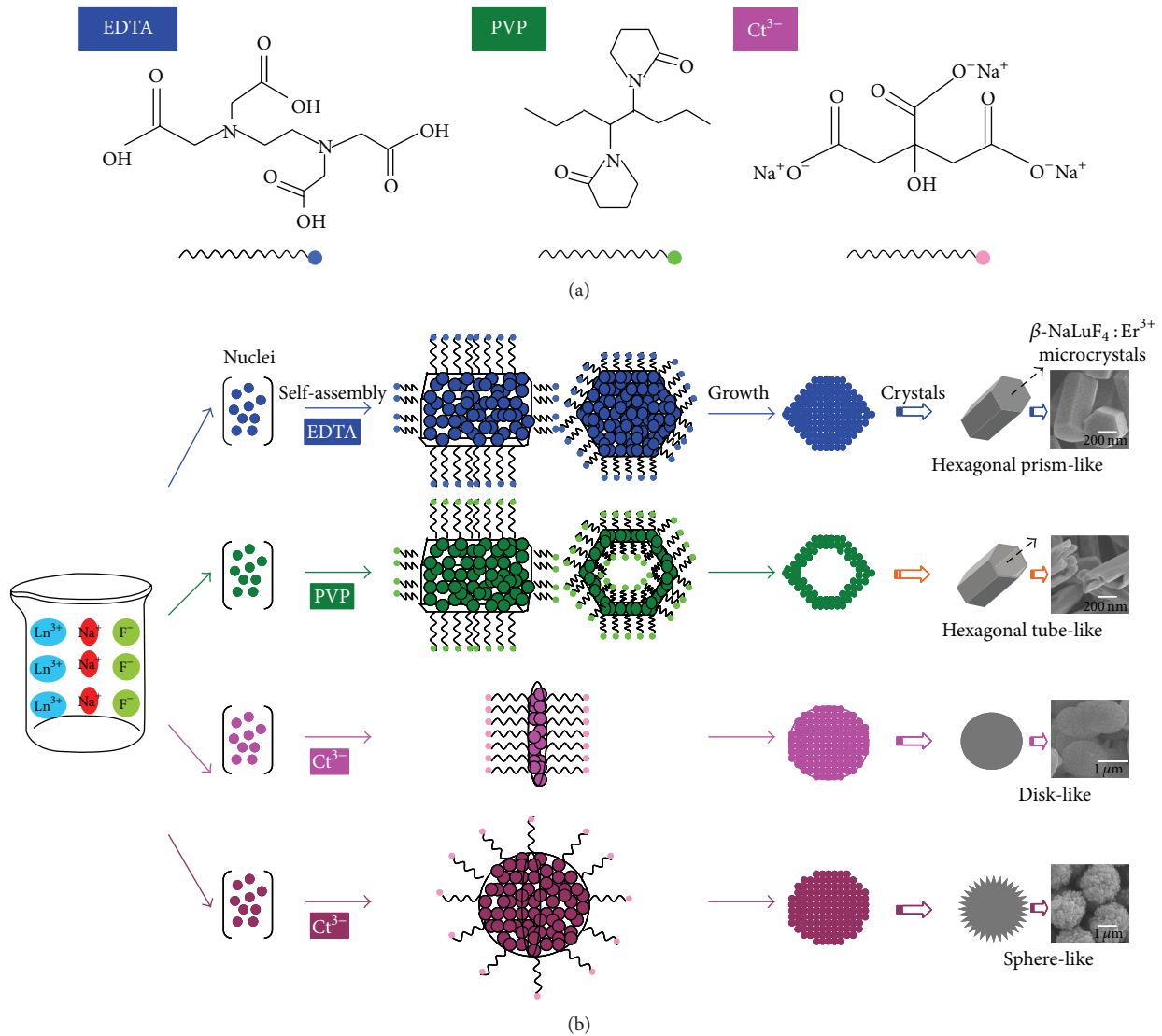


FIGURE 4: (a) Newman representations for coordination compound structure of EDTA, PVP, and  $\text{Ct}^{3-}$ . (b) Schematic illustration of the main stages involved in the growth mechanism of  $\beta\text{-NaLuF}_4$  microcrystals.

associated with the transition from  $^4\text{S}_{3/2}$ ,  $^4\text{F}_{9/2}$ , and  $^4\text{I}_{9/2}$  levels to ground state of  $\text{Er}^{3+}$ , respectively. The intensities of emission bands were so strong that they can be clearly seen by the naked eyes even though they were under a low excitation power. The emission intensities are highly dependent on the  $\text{Er}^{3+}$  concentration. Initially, increasing  $\text{Er}^{3+}$  ion doping concentration, the intensity from all regions of the spectra increases rapidly and reaches a maximum. Then, a decrease appears at higher  $\text{Er}^{3+}$  concentrations due to the concentration quenching effect. As for the red emission, it is determined by the population of the  $^4\text{F}_{9/2}$  level. The  $^4\text{F}_{9/2}$  level is mainly populated by energy transfer between  $\text{Er}^{3+}$  ions when the doping concentration is increased,  $^4\text{I}_{11/2}(\text{Er}^{3+}) + ^4\text{I}_{9/2}(\text{Er}^{3+}) \rightarrow ^4\text{I}_{13/2}(\text{Er}^{3+}) + ^4\text{F}_{9/2}(\text{Er}^{3+})$

[26]. According to our experimental data, the optimum  $\text{Er}^{3+}$  concentration is 12 mol%  $\text{Er}^{3+}$  ions in S3 and 24 mol%  $\text{Er}^{3+}$  ions in S6. It is interesting to point out that the typical 541 nm green and 659 nm red emissions of  $\text{Er}^{3+}$  disappear in the spheres (S8; Figure 5(c)) and disks (S9; Figure 5(d)) and the intensities of emission bands of the two samples are poor. Comparing various morphologies, the emission intensity of hexagonal prism-like  $\beta\text{-NaLuF}_4:\text{Er}^{3+}$  microcrystals was found to be  $\sim 10^5$  more efficient and brighter than others. The ranking of the emission intensities is UC-S3 > UC-S6  $\gg$  UC-S9 > UC-S8.

As for the different UC intensities of the four samples, there may be several factors playing a role. Since the shape and sizes of the microcrystals are different, it will bring a few uncertain factors that influence the UC behaviors through

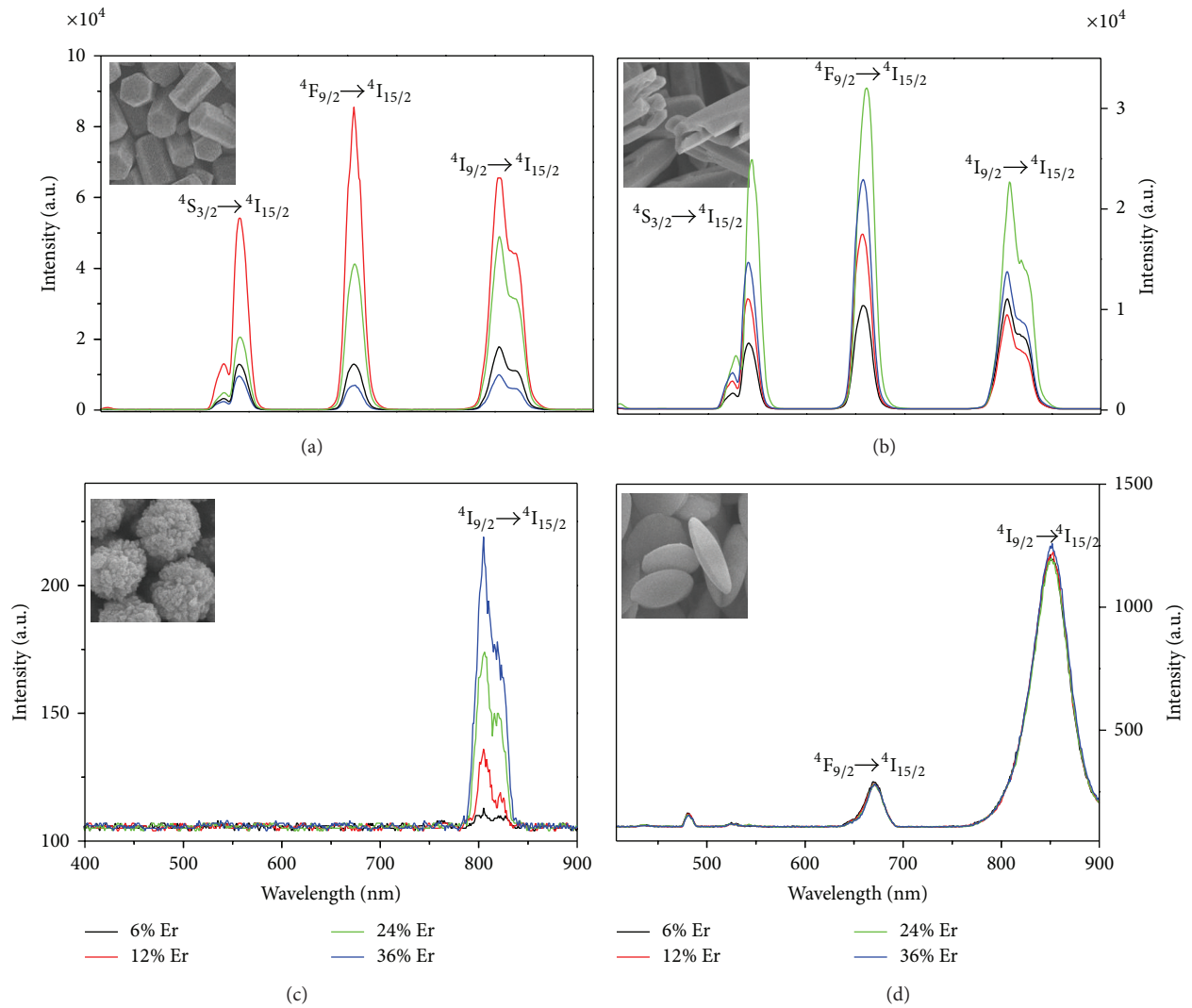


FIGURE 5: UCL spectra pumped by  $1.54 \mu\text{m}$  laser diode with power density of  $16 \text{ mW}/\text{mm}^2$  for  $\beta\text{-NaLuF}_4:x \text{ mol}\% \text{Er}^{3+}$  ( $x = 6, 12, 24, 36$ ) synthesized using EDTA as the chelator for EDTA/ $\text{Ln}^{3+}$  ratio of 3:1 (a), using PVP as the chelator for PVP/ $\text{Ln}^{3+}$  ratio of 3:1 (b), and using  $\text{Ct}^{3-}$  as the chelator for  $\text{Ct}^{3-}/\text{Ln}^{3+}$  ratio of 2:1 (c) and 3:1 (d). Insets are corresponding high magnification SEM images of the samples. All of the samples were hydrothermally treated with the same condition except for the molar ratio of chelators/ $\text{Ln}_3$ .

affecting the scattering and absorption of incident light, which decrease the defect concentrations [26, 29]. Moreover, the distinct difference of the emission intensities could be owing to the chelating and capping ability of surfactants. When an EDTA molecule chelates with one  $\text{Ln}^{3+}$  ion, all of its six binding sites participate in the reaction to develop a hexagonal structure. Furthermore, the chelate constant for EDTA ( $\lg b = 18 \sim 19$ ) is much larger than  $\text{Ct}^{3-}$  ( $\lg b = 8 \sim 9$ ) [7]. The structure stability coefficient of EDTA with  $\text{Ln}^{3+}$  ions is larger than  $\text{Ct}^{3-}$ , owing to its six binding sites (four binding sites in  $\text{Ct}^{3-}$ ). The larger the stability coefficient is, the more closely the chelates combine with rare earth. Based on the above analysis, we can conclude that the difference in chelate structure results in the difference in morphology due to its

influence on growth orientation, which can also be related to the difference in the emission intensity. Depending on the UC emission intensity, it is possible to vary particles size and shape and then to choose S3 for further characterization.

Figure 6 shows the UC emission spectra of hexagonal prisms (S3)  $\text{NaLuF}_4:12 \text{ mol}\% \text{Er}^{3+}$  under  $1.54 \mu\text{m}$  laser diode at various pump powers. The 659 nm red emission is predominant, which is attributed to the  ${}^4\text{F}_{9/2} \rightarrow {}^4\text{I}_{15/2}$  transitions of  $\text{Er}^{3+}$ . Besides, from the spectra, it is obvious that the emission intensities become stronger with increasing pump powers. It is well known that the relationship between the UC emission intensity  $I$  and the pump power  $P$  for unsaturated UC processes could be expressed as follows [30]:

$$I_{\text{em}} \propto P^n, \quad (1)$$

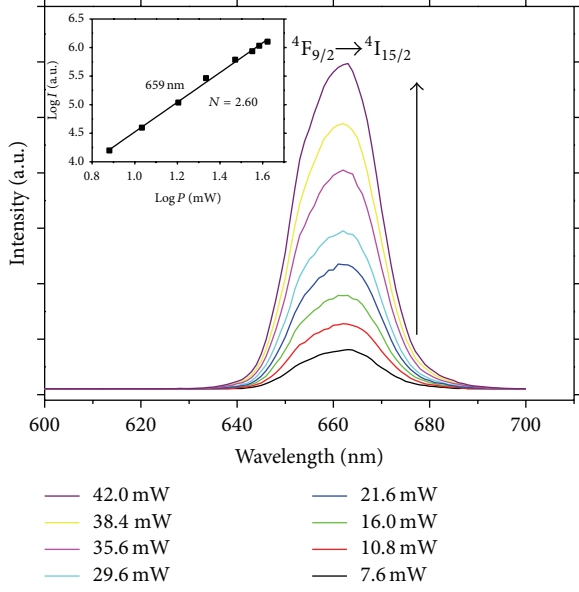


FIGURE 6: Power dependence of UC emission intensity of  ${}^4F_{9/2} \rightarrow {}^4I_{15/2}$  emission of  $\beta$ -NaLuF<sub>4</sub>:12 mol%Er<sup>3+</sup> submicron crystals using EDTA as surfactant under 1.54  $\mu$ m laser diode pump. Inset shows dependence of UC emission intensity on excitation powder.

where  $I_{em}$  is the fluorescent intensity,  $P$  is the pump power, and  $n$  is the absorbed photon numbers per visible photon emitted. For the strongest emission peak at 659 nm, a plot of  $\log(I_{em})$  versus  $\log(P)$  yields a straight line with a slope  $n$  for the various power pumps as shown in the inset of Figure 6, and the  $n$  value obtained is equal to about 2.60. Hence, it is a three-photon process, which agrees with the three-step sequential transitions from the  ${}^4I_{15/2}$  ground state to the  ${}^4I_{13/2}$  intermediate state and then to the  ${}^4F_{9/2}$  state of Er<sup>3+</sup> in the excitation process.

**3.4. Synergistic Effect of  $\beta$ -NaLuF<sub>4</sub>:Er<sup>3+</sup> Microcrystals.** The excitation spectrum (Figure 7(a)) of  $\beta$ -NaLuF<sub>4</sub>:12 mol%Er<sup>3+</sup> (S3) with hexagonal prisms shape shows that if the 659 nm red emission is monitored, an excitation peak centered at 416 nm is observed corresponding to the  ${}^4I_{15/2} \rightarrow {}^2H_{9/2}$  transition of Er<sup>3+</sup> ion. Figure 7(b) presents the room temperature photoluminescence spectra under 416 nm single excitation, 1.54  $\mu$ m single excitation, and 416 nm and 1.54  $\mu$ m dual excitation. The emission band of Er<sup>3+</sup> ions centered at 659 nm is observed under 416 nm and 1.54  $\mu$ m single excitation, respectively. It is inconceivable that an observable enhancement of the red emission band appears under the dual excitation, which is stronger than the sum of red emission intensity under single excitation. To quantitatively describe the synergistic efficiency, the absolute enhancement rate ( $\eta$ ) of red emission intensity can be defined as follows [20]:

$$\eta = \frac{I_3 - (I_1 + I_2)}{I_1 + I_2}, \quad (2)$$

where  $I_1$ ,  $I_2$ , and  $I_3$  are the integrated intensity of red emission bands under 416 nm excitation, under 1.54  $\mu$ m excitation, and under 416 nm and 1.54  $\mu$ m dual excitation, respectively, the excitation power of the 416 nm irradiation was fixed at 0.8 mW, and the excitation power ( $P$ ) of 1.54  $\mu$ m laser was adjusted from 2.2 mW to 42.0 mW. The results of absolute enhancement rate ( $\eta$ ) of red emission (659 nm) for the as-prepared  $\beta$ -NaLuF<sub>4</sub>:12 mol%Er<sup>3+</sup> microcrystals with different shapes morphologies are shown in Figure 7(c). There is no synergistic effect on spheres and disks, because the intensities of emission bands are poor there is not exist the 659 nm emission. The maximum absolute enhancement rate can be up to 8% in hexagonal prisms with the excitation powers  $P_{416\text{ nm}} = 0.8\text{ mW}$  and  $P_{1.54\text{ }\mu\text{m}} = 21.6\text{ mW}$ . It is clear that when  $I_3 > (I_1 + I_2)$  it means that certain thermal energy dissipation should be eliminated and transferred to the excitation energy in the dual excitation process. As can be seen, the ranking of absolute enhancement rate values is  $\eta\text{-S3} > \eta\text{-S6}$ . The red emission of  ${}^4F_{9/2} \rightarrow {}^4I_{15/2}$  shows an unusual enhancement rate using different surfactants. We believe that the surfactants can influence the nonradiative process of these samples and cause these changes. Moreover, the different reflectance losses at the particle-air interface may influence the UC emissions of surface-modified NaYF<sub>4</sub>:Yb, Er, which has been demonstrated in a recent report by Tan and coworkers [31].

**3.5. Synergistic Mechanism Analyses.** Considering the slope  $n$  and energy diagrams of Er<sup>3+</sup>, the proposed pathways for the synergistic mechanism combined downconversion and upconversion under dual excitation are demonstrated in Figure 8. Under 416 nm excitation, which corresponds to the  ${}^4I_{15/2} \rightarrow {}^2H_{9/2}$  transition of Er<sup>3+</sup> ion, the 659 nm red emission band also represents the  ${}^4F_{9/2} \rightarrow {}^4I_{15/2}$  transition of some Er<sup>3+</sup> ions after successive multiphonon nonradiative relaxation from the  ${}^2H_{9/2}$  to  ${}^4F_{9/2}$  state. Under 1.54  $\mu$ m excitation, Er<sup>3+</sup> ions can absorb energy by ground state absorption (GSA) and excited state absorption (ESA) consecutively to populate their  ${}^4I_{13/2}$  and  ${}^4I_{9/2}$  states in succession. Then, some of Er<sup>3+</sup> ions at  ${}^4I_{9/2}$  level will nonradiatively relax (NR) to the  ${}^4I_{11/2}$  level. NaLuF<sub>4</sub> host lattice owns lower phonon energy of less than 400  $\text{cm}^{-1}$ , and the NR process ( $E_{\text{gap}} \sim 2500\text{ cm}^{-1}$ ) can be realized according to energy gap law [32]. Then the crossrelaxation process from  ${}^4I_{13/2}$  to  ${}^4I_{11/2}$  and ESA process occur simultaneously: Er<sup>3+</sup> ( ${}^4I_{13/2} \rightarrow {}^4I_{15/2}$ ) and Er<sup>3+</sup> ( ${}^4I_{11/2} \rightarrow {}^4F_{9/2}$ ), which results in the 659 nm red upconversion emission ( ${}^4F_{9/2} \rightarrow {}^4I_{15/2}$ ). Besides, the  ${}^4I_{11/2}$  and  ${}^4I_{13/2}$  levels are also populated through NR process in downconversion process. The energy in the  ${}^4I_{11/2}$  and  ${}^4I_{13/2}$  levels of Er<sup>3+</sup> ions is usually dissipated via thermal energy; however, under the 416 nm and 1.54  $\mu$ m coexcited, the Er<sup>3+</sup> ions in the  ${}^4I_{11/2}$  and  ${}^4I_{13/2}$  levels from NR process can be

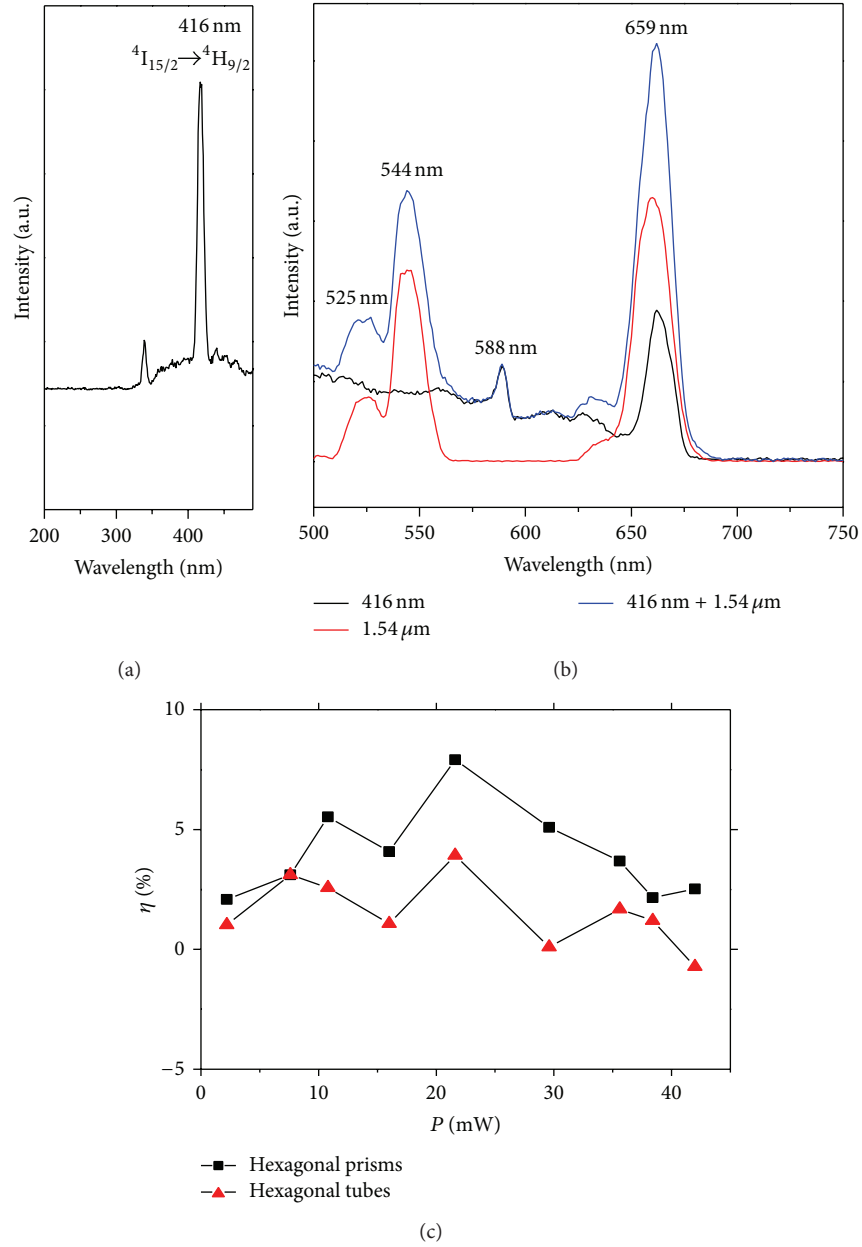
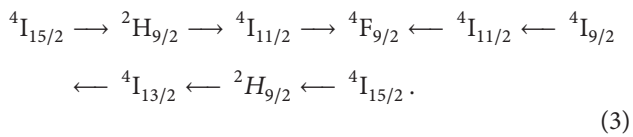


FIGURE 7: (a) Photoluminescence excitation spectra ( $\lambda_{em} = 659$  nm) of  $\beta$ -NaLuF<sub>4</sub>:12 mol%Er<sup>3+</sup> with hexagonal prisms morphology; (b) visible photoluminescence spectra of  $\beta$ -NaLuF<sub>4</sub>:12 mol%Er<sup>3+</sup> under 416 nm excitation (black line), under 1.54  $\mu$ m excitation (red line), and under 416 nm and 1.54  $\mu$ m dual excitation (blue line) ( $P_{416\text{ nm}} = 0.8$  mW,  $P_{1.54\text{ }\mu\text{ m}} = 16$  mW); (c) absolute enhancement ( $\eta$ ) for the as-prepared  $\beta$ -NaLuF<sub>4</sub>:12 mol%Er<sup>3+</sup> crystals using different surfactants with increasing 1.54  $\mu$ m laser power under 416 nm and 1.54  $\mu$ m dual excitation.

excited again to the  $^4F_{9/2}$  level by absorbing 1.54  $\mu$ m photons. An energy loop chain can be described as follows:



Therefore, the energy of nonradiative relaxation is excited again, enhancing the intensity of red emission ( $^4F_{9/2} \rightarrow ^4I_{11/2}$ ) under the dual excitation. As can be concluded,

the Er<sup>3+</sup> ions from the nonradiative relaxation process create a loop chain in the excitation circuit and offer a reexcited source.

#### 4. Conclusions

In summary, we successfully synthesized  $\beta$ -NaLuF<sub>4</sub>:Er<sup>3+</sup> microcrystals with different surfactants by the hydrothermally method. The organic additives employed in the synthesis process played a significant role. It proved that the

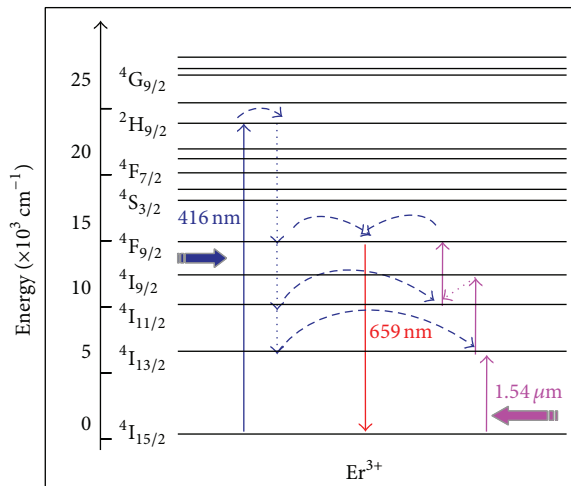


FIGURE 8: Synergistic effect of visible downconversion and IR upconversion in  $\beta$ -NaLuF<sub>4</sub>:Er<sup>3+</sup> phosphors photoexcited with both 416 nm and 1.54  $\mu$ m photons.

chemical nature of the surfactants (EDTA, PVP-K30, and Ct<sup>3-</sup>) differently acts with Ln<sup>3+</sup> ions in solution, influencing the formation and growth process of the microcrystals. The EDTA-modified particles were found to be much more efficient and brighter than others, in which the intense 659 nm red emission band was observed. Under 416 nm and 1.54  $\mu$ m dual excitation, the 8% absolute enhancement rate of the red emission band originating from the <sup>4</sup>I<sub>11/2</sub> and <sup>4</sup>I<sub>13/2</sub> states of Er<sup>3+</sup> ion from the nonradiative relaxation process in the DC route can be excited again by absorbing the 1.54  $\mu$ m IR photons in the UC route.

## Conflict of Interests

The authors declare that there is no conflict of interests regarding the publication of this paper.

## Acknowledgments

This work was supported by the key Project of National High Technology Research and Development Program of China (863 programs) (no. 2011AA050526), National Natural Science Foundation of China (no. 51032002), the Science and Technology Support Plan of Jiangsu Province (BE2011191), and the Funding of Jiangsu Innovation Program for Graduate Education (no. CXZZ12.0137) as well as the Fundamental Research Funds for the Central Universities.

## References

- [1] H.-X. Mai, Y.-W. Zhang, R. Si et al., "High-quality sodium rare-earth fluoride nanocrystals: controlled synthesis and optical properties," *Journal of the American Chemical Society*, vol. 128, no. 19, pp. 6426–6436, 2006.
- [2] J.-C. Boyer, F. Vetrone, L. A. Cuccia, and J. A. Capobianco, "Synthesis of colloidal upconverting NaYF<sub>4</sub> nanocrystals doped with Er<sup>3+</sup>, Yb<sup>3+</sup> and Tm<sup>3+</sup>, Yb<sup>3+</sup> via thermal decomposition of lanthanide trifluoroacetate precursors," *Journal of the American Chemical Society*, vol. 128, no. 23, pp. 7444–7445, 2006.
- [3] C. Li, Z. Quan, J. Yang, P. Yang, and J. Lin, "Highly uniform and monodisperse  $\beta$ -NaYF<sub>4</sub>:Ln<sup>3+</sup> (Ln = Eu, Tb, Yb/Er, and Yb/Tm) hexagonal microprism crystals: hydrothermal synthesis and luminescent properties," *Inorganic Chemistry*, vol. 46, no. 16, pp. 6329–6337, 2007.
- [4] Y. Liu, D. Tu, H. Zhu, R. Li, W. Luo, and X. Chen, "A strategy to achieve efficient dual-mode luminescence of Eu<sup>3+</sup> in lanthanides doped multifunctional NaGdF<sub>4</sub> nanocrystals," *Advanced Materials*, vol. 22, no. 30, pp. 3266–3271, 2010.
- [5] M. Karbowski, A. Mech, A. Bednarkiewicz, W. Stręk, and L. Kępiński, "Comparison of different NaGdF<sub>4</sub>:Eu<sup>3+</sup> synthesis routes and their influence on its structural and luminescent properties," *Journal of Physics and Chemistry of Solids*, vol. 66, no. 6, pp. 1008–1019, 2005.
- [6] L. Wang, M. Lan, Z. Liu et al., "Enhanced deep-ultraviolet upconversion emission of Gd<sup>3+</sup> sensitized by Yb<sup>3+</sup> and Ho<sup>3+</sup> in  $\beta$ -NaLuF<sub>4</sub> microcrystals under 980 nm excitation," *Journal of Materials Chemistry C*, vol. 1, no. 13, pp. 2485–2490, 2013.
- [7] F. Wang and X. Liu, "Recent advances in the chemistry of lanthanide-doped upconversion nanocrystals," *Chemical Society Reviews*, vol. 38, no. 4, pp. 976–989, 2009.
- [8] G. S. He, L.-S. Tan, Q. Zheng, and P. N. Prasad, "Multiphoton absorbing materials: molecular designs, characterizations, and applications," *Chemical Reviews*, vol. 108, no. 4, pp. 1245–1330, 2008.
- [9] J. Zhou, Z. Liu, and F. Li, "Upconversion nanophosphors for small-animal imaging," *Chemical Society Reviews*, vol. 41, no. 3, pp. 1323–1349, 2012.
- [10] D. K. Chatterjee, A. J. Rufaihah, and Y. Zhang, "Upconversion fluorescence imaging of cells and small animals using lanthanide doped nanocrystals," *Biomaterials*, vol. 29, no. 7, pp. 937–943, 2008.
- [11] F. Shi, J. Wang, X. Zhai, D. Zhao, and W. Qin, "Facile synthesis of  $\beta$ -NaLuF<sub>4</sub>:Yb/Tm hexagonal nanoplates with intense ultraviolet upconversion luminescence," *CrystEngComm*, vol. 13, no. 11, pp. 3782–3787, 2011.
- [12] S. Zeng, J. Xiao, Q. Yang, and J. Hao, "Bi-functional NaLuF<sub>4</sub>:Gd<sup>3+</sup>/Yb<sup>3+</sup>/Tm<sup>3+</sup> nanocrystals: structure controlled synthesis, near-infrared upconversion emission and tunable magnetic properties," *Journal of Materials Chemistry*, vol. 22, no. 19, pp. 9870–9874, 2012.
- [13] F. He, N. Niu, Z. Zhang et al., "Morphology-controllable synthesis and enhanced luminescence properties of  $\beta$ -NaLuF<sub>4</sub>:Ln (Ln = Eu, Tb and Ce/Tb) microcrystals by solvothermal process," *RSC Advances*, vol. 2, no. 19, pp. 7569–7577, 2012.
- [14] N. Niu, F. He, S. Huang, S. Gai, X. Zhang, and P. Yang, "Hierarchical bundles structure of  $\beta$ -NaLuF<sub>4</sub>: facile synthesis, shape evolution, and luminescent properties," *RSC Advances*, vol. 2, no. 27, pp. 10337–10344, 2012.
- [15] C. Li, Z. Quan, P. Yang, S. Huang, H. Lian, and J. Lin, "Shape-controllable synthesis and upconversion properties of lutetium fluoride (doped with Yb<sup>3+</sup>/Er<sup>3+</sup>) microcrystals by hydrothermal process," *Journal of Physical Chemistry C*, vol. 112, no. 35, pp. 13395–13404, 2008.
- [16] Q. Liu, Y. Sun, T. Yang, W. Feng, C. Li, and F. Li, "Sub-10 nm hexagonal lanthanide-doped NaLuF<sub>4</sub> upconversion nanocrystals for sensitive bioimaging in vivo," *Journal of the American Chemical Society*, vol. 133, no. 43, pp. 17122–17125, 2011.
- [17] S. Ivanova and F. Pellé, "Strong 1.53  $\mu$ m to NIR-VIS-UV upconversion in Er-doped fluoride glass for high-efficiency

- solar cells,” *Journal of the Optical Society of America B: Optical Physics*, vol. 26, no. 10, pp. 1930–1938, 2009.
- [18] T. Trupke, A. Shalav, B. S. Richards, P. Würfel, and M. A. Green, “Efficiency enhancement of solar cells by luminescent up-conversion of sunlight,” *Solar Energy Materials and Solar Cells*, vol. 90, no. 18–19, pp. 3327–3338, 2006.
- [19] S. Fischer, J. C. Goldschmidt, P. Löper et al., “Enhancement of silicon solar cell efficiency by upconversion: optical and electrical characterization,” *Journal of Applied Physics*, vol. 108, no. 4, Article ID 044912, 2010.
- [20] X. Wang and X. Yan, “Ultraviolet and infrared photon-excited synergistic effect in  $\text{Er}^{3+}$ -doped  $\text{YbF}_3$  phosphors,” *Optics Letters*, vol. 36, no. 22, pp. 4353–4355, 2011.
- [21] K. Zheng, D. Zhao, D. Zhang, N. Liu, and W. Qin, “Ultraviolet upconversion fluorescence of  $\text{Er}^{3+}$  induced by 1560 nm laser excitation,” *Optics Letters*, vol. 35, no. 14, pp. 2442–2444, 2010.
- [22] S. Zheng, Y. Zhou, D. Yin, X. Xu, Y. Qi, and S. Peng, “Improvement of 1.53  $\mu\text{m}$  band fluorescence and energy transfer in  $\text{Er}^{3+}/\text{Ce}^{3+}$  codoped tellurite glasses,” *Journal of Alloys and Compounds*, vol. 566, pp. 90–97, 2013.
- [23] K. Maheshvaran, S. Arunkumar, V. Sudarsan, V. Natarajan, and K. Marimuthu, “Structural and luminescence studies on  $\text{Er}^{3+}/\text{Yb}^{3+}$  co-doped boro-tellurite glasses,” *Journal of Alloys and Compounds*, vol. 561, pp. 142–150, 2013.
- [24] R. Dahal, C. Ugolini, J. Y. Lin, H. X. Jiang, and J. M. Zavada, “Current-injected 1.54  $\mu\text{m}$  light emitting diodes based on erbium-doped GaN,” *Applied Physics Letters*, vol. 93, no. 3, Article ID 033502, 2008.
- [25] G. D. Webler, M. J. M. Zapata, G. S. Maciel et al., “Influence of impurities on the luminescence of  $\text{Er}^{3+}$  doped  $\text{BaTiO}_3$  nanophosphors,” *Journal of Nanomaterials*, vol. 2014, Article ID 708719, 9 pages, 2014.
- [26] S. Shionoya, W. M. Yen, and T. Hase, *Phosphor Handbook*, CRC Press, New York, NY, USA, 2007.
- [27] Z. Q. Li and Y. Zhang, “Monodisperse silica-coated Polyvinylpyrrolidone/ $\text{NaYF}_4$  nanocrystals with multicolor upconversion fluorescence emission,” *Angewandte Chemie*, vol. 118, no. 46, pp. 7896–7899, 2006.
- [28] L. S. Cavalcante, J. C. Sczancoski, M. Siu Li, E. Longo, and J. A. Varela, “ $\beta\text{-ZnMoO}_4$  microcrystals synthesized by the surfactant-assisted hydrothermal method: growth process and photoluminescence properties,” *Colloids and Surfaces A: Physicochemical and Engineering Aspects*, vol. 396, pp. 346–351, 2012.
- [29] C. Huang, *Coordination Chemistry of Rare Earth Elements*, Science Publishing Press, Beijing, China, 1997.
- [30] M. Pollnau, D. R. Gamelin, S. R. Lüthi, H. U. Güdel, and M. P. Hehlen, “Power dependence of upconversion luminescence in lanthanide and transition-metal-ion systems,” *Physical Review B—Condensed Matter and Materials Physics*, vol. 61, no. 5, pp. 3337–3346, 2000.
- [31] M. C. Tan, L. Al-Baroudi, and R. E. Riman, “Surfactant effects on efficiency enhancement of infrared-to-visible upconversion emissions of  $\text{NaYF}_4:\text{Yb-Er}$ ,” *ACS Applied Materials and Interfaces*, vol. 3, no. 10, pp. 3910–3915, 2011.
- [32] J. M. F. Van Dijk and M. F. H. Schuurmans, “On the nonradiative and radiative decay rates and a modified exponential energy gap law for 4f-4f transitions in rare-earth ions,” *The Journal of Chemical Physics*, vol. 78, no. 9, pp. 5317–5323, 1983.

## Research Article

# Application of Gold Nanoparticles for Electrochemical DNA Biosensor

**Ahmed Mishaal Mohammed,<sup>1,2</sup> Ruslinda A. Rahim,<sup>2</sup> Ibraheem Jaleel Ibraheem,<sup>1</sup> Foo Kai Loong,<sup>2</sup> Hasrul Hisham,<sup>2</sup> Uda Hashim,<sup>2</sup> and Yarub Al-Douri<sup>2</sup>**

<sup>1</sup> Chemistry Department, College of Science, Al-Anbar University, Ramadi, Iraq

<sup>2</sup> Institute of Nano Electronic Engineering, Universiti Malaysia Perlis, 01000 Kangar, Perlis, Malaysia

Correspondence should be addressed to Ahmed Mishaal Mohammed; [mishal78\\_2010@yahoo.com](mailto:mishal78_2010@yahoo.com)

Received 20 October 2013; Accepted 3 April 2014; Published 25 May 2014

Academic Editor: M. Ghoranneviss

Copyright © 2014 Ahmed Mishaal Mohammed et al. This is an open access article distributed under the Creative Commons Attribution License, which permits unrestricted use, distribution, and reproduction in any medium, provided the original work is properly cited.

An electrochemical DNA biosensor was successfully fabricated by using (3-aminopropyl)triethoxysilane (APTES) as a linker molecule combined with the gold nanoparticles (GNPs) on thermally oxidized SiO<sub>2</sub> thin films. The SiO<sub>2</sub> thin films surface was chemically modified with a mixture of APTES and GNPs for DNA detection in different time periods of 30 min, 1 hour, 2 hours, and 4 hours, respectively. The DNA immobilization and hybridization were conducted by measuring the differences of the capacitance value within the frequency range of 1 Hz to 1 MHz. The capacitance values for DNA immobilization were 160  $\mu$ F, 77.8  $\mu$ F, 70  $\mu$ F, and 64.6  $\mu$ F, respectively, with the period of time from 30 min to 4 hours. Meanwhile the capacitance values for DNA hybridization were 44  $\mu$ F, 54  $\mu$ F, 55  $\mu$ F, and 61.5  $\mu$ F, respectively. The capacitance value of bare SiO<sub>2</sub> thin film was 0.42  $\mu$ F, which was set as a base line for a reference in DNA detection. The differences of the capacitance value between the DNA immobilization and hybridization revealed that the modified SiO<sub>2</sub> thin films using APTES and GNPs were successfully developed for DNA detection.

## 1. Introduction

Gold nanoparticles (GNPs) with the sizes in the range of units to hundreds of nanometres lately attract a comprehensive attention in different fields of medicine, biology, physics, and chemistry as a result of their unique electronic, magnetic, optical, mechanical, physical, and chemical properties [1–3]. Gold nanoparticles have gained considerable attention in recent years for potential applications in industry and nanomedicine. Also, gold nanoparticles show promising behavior in enhancing the effectiveness of various aimed cancer treatments such as photothermal therapy and radiotherapy [4].

Applications of gold nanoparticles show strong optical dying out at near infrared and visible wavelengths which can be tuned by modifying the size. Recently advances in their high-yield synthesis, functionalization, stabilization and bioconjugation, gold nanoparticles are an increasingly applied nanomaterial. Bulk gold is perfect for being inert; however, the nanoparticulate sizes of gold show astronomically high chemical reactivity [5, 6].

The development of DNA sensors has recently attracted substantial attention in connection with research efforts directed at gene analysis, the detection of genetic disorders, tissue matching, and forensic applications [7].

DNA hybridization detection is a main issue in molecular biodiagnostics [8], determination of genetic diversity [9], food analysis [10, 11], criminal investigation in forensics and immigration [12], and environmental monitoring [8]. Different techniques have been proposed for the detection of target DNA, such as electrochemical sensing [13], fluorescence [14], chromatography in tandem with mass spectrometry [15], surface plasma resonance [16], and oligonucleotide microarray and DNA [17]. The detection of DNA is an area of excellent interest as it plays a main role in clinical, pharmaceutical, and forensic applications. Electrochemical transducer offers several advantages, such as high sensitivity, simplicity, inexpensiveness, and accurate specificity for converting DNA hybridization results into useful analytical signals [18–21].

The electrochemical DNA biosensor devices based on the principle of nanotechnology have become one of the

most exciting fields in analytical chemistry. This has been facilitated by the accessibility of various nanomaterials, for example, nanotubes [22], magnetic particles/nanoparticles [23, 24], and nanowires [25].

Gold nanoparticles are widely used in immobilization of DNA probe because of their unique characteristics, such as strong adsorption ability, high biocompatibility, and great surface area [26]. In this study, we have developed an easy to fabricate which were acted as the electrode for DNA detection by using GNPs synthesis on thermally oxidized SiO<sub>2</sub>. Prior to the probe DNA immobilization and target DNA hybridization detection, the SiO<sub>2</sub> thin films surface was modified with GNPs due to its well-known chemistry, superior capacitance, and huge attachment surfaces. A novel, label-free biosensor and sensitive DNA sensor.

## 2. Materials and Methods

**2.1. Preparation of GNPs Solution.** Gold nanoparticles (GNPs) were used in this project for the immobilization and hybridization of the DNA on the SiO<sub>2</sub> thin films. Firstly, a HAuCl<sub>4</sub> solution with the concentration of 0.49 mol/L was prepared by dissolving 500 mg of HAuCl<sub>4</sub> into 3 mL of 10% HCl. Then, a diluted 0.2 mM of HAuCl<sub>4</sub> solution was made by adding 40  $\mu$ L (19.6  $\mu$ mol) of HAuCl<sub>4</sub> solution into 100 mL of deionized water as to produce solution A. Secondly, 558.79 mg of trisodium citrate was added into 50 mL of deionized water to make a solution B. The concentration of the solution was controlled at 38.8 mmol/L. Solution A was brought to a rolling boil at 150°C with stirring vigorously as to get a homogenous size of the GNPs solution. 10 mL of 38.8 mM of sodium citrate was added rapidly into the vortex of the solution. The solution resulted in a color change from pale yellow to red. Boiling and stirring were continued for another 10 min. The heating was then removed, and stirring was continued for an additional 15 min. When the solution cooled down to room temperature, it was filtered through a 0.8  $\mu$ m membrane filter paper. The prepared solution was kept in the refrigerator with the temperature 4°C and measured by using UV-Vis with the wavelength 400 nm to 800 nm.

**2.2. Modification of SiO<sub>2</sub> with GNPs.** A p-type silicon (100) wafer (1 cm  $\times$  1 cm) was cleaned by using acetone and isopropanol in ultrasonic for about 15 minutes and was immersed into the buffered oxide etch (BOE) solution and washed with deionized water followed by oxidation process for 30 minutes. After oxidation, the silicon oxide (SiO<sub>2</sub>) layer of thickness  $\sim$ 50 nm, the aluminium (99.99% of purity) was deposited on the backside of the Si using thermal evaporator. The selectivity of the DNA biosensor was studied using the GNPs/APTES/SiO<sub>2</sub>/Si/Al electrode. The SiO<sub>2</sub> surface was functionalized with APTES solution which was prepared by mixing of 2% APTES with 93% of ethanol and 5% of deionized water. The silanyl group ( $-\text{SH}_3$ ) presented in APTES was used for the process of silanization, which was chemically attached with the hydroxyl-rich SiO<sub>2</sub> [27]. Besides that, amino group ( $\text{NH}_2$ ) presented in APTES was served as a glue layer to attach the GNPs which linked to probe DNA.

Attachment between APTES and GNPs is shown in Figure 1. For the surface modification of SiO<sub>2</sub> with APTES, 10  $\mu$ L of prepared APTES solution on the SiO<sub>2</sub> surface and incubated for 2 hours. Then, the surface washed for 3 times in blow dried the surface and drop 10  $\mu$ L of GNPs on the surface at 150°C for 20 min on hotplate. This step was repeated 3 times to obtain enough GNPs on the SiO<sub>2</sub> surface and electrode is ready for electrical characterization.

**2.3. Probe DNA Immobilization on Modified GNPs.** Probe DNA was purchased from 1st BASE Pte Ltd. (Malaysia). The probe DNA sequences were 5'-CTG ATA GTA GAT TTG TGA CCG TAGAAA-C6. Probe DNA was dropped onto the GNPs modified SiO<sub>2</sub> electrode for immobilization and incubated at room temperature for 0.5, 1, 2, and 4 hours. After a period of time, the electrode was carefully washed by using deionized water to remove any unbonded DNA probe and dried at room temperature. The probe-modified devices were denoted as DNA/GNPs/APTES/SiO<sub>2</sub>/Si/Al and then were ready for electrochemical measurements.

**2.4. Hybridization of DNA.** Hybridization of DNA used in this project was purchased from 1st BASE Pte Ltd. (Malaysia). Hybridization with complementary DNA sequences was 5'-CTA CGG TCA TCA CAA ATC TAC TAT CAG-3'. To hybridize the DNA, 10  $\mu$ L of 10  $\mu$ M complementary DNA was dropped onto GNPs electrode and incubated for 2 hours. After that, the GNPs electrode was washed by using deionized water to remove any nonhybridized DNA and dried at room temperature. 10  $\mu$ L of 0.5  $\mu$ M methylene blue was then dropped onto the GNPs electrode and incubated again for 3 minutes. Finally, the GNPs electrode will once again be washed with deionized water to remove any excess of methylene blue and the GNPs electrode is ready to be electrically measured once it has dried.

**2.5. Electrochemical Measurements.** Electrochemical measurement was performed by using dielectric analyser. The tests were conducted by using Ag/AgCl as the reference electrode and GNPs-modified electrode as a working electrode. The Al acts as a back gate. The responses of the DNA immobilization were investigated in 10  $\mu$ M potassium hexacyanoferrate III, K<sub>3</sub>Fe(CN)<sub>6</sub> aqueous solution containing 0.1 M KCl as electrolyte. A schematic view of testing measurement for DNA detection is shown in Figure 2.

## 3. Results and Discussion

**3.1. Measurement of UV-Vis Spectroscopy.** The characterization of prepared GNPs solution was examined using an UV-Vis spectroscopy. The measurements were carried out within the wavelength range of 400–800 nm under ambient conditions and the result is shown in Figure 3. The absorbance maximum was found at 530 nm, which was indicative of GNPs of diameter  $35 \pm 5$  nm [28]. The particle size was further confirmed using the method described by Haiss et al. [29].

**3.2. Capacitance Measurement.** The dielectric behaviour of GNPs modified surface for DNA detection was investigated using dielectric analyzer. Figure 4 demonstrates the

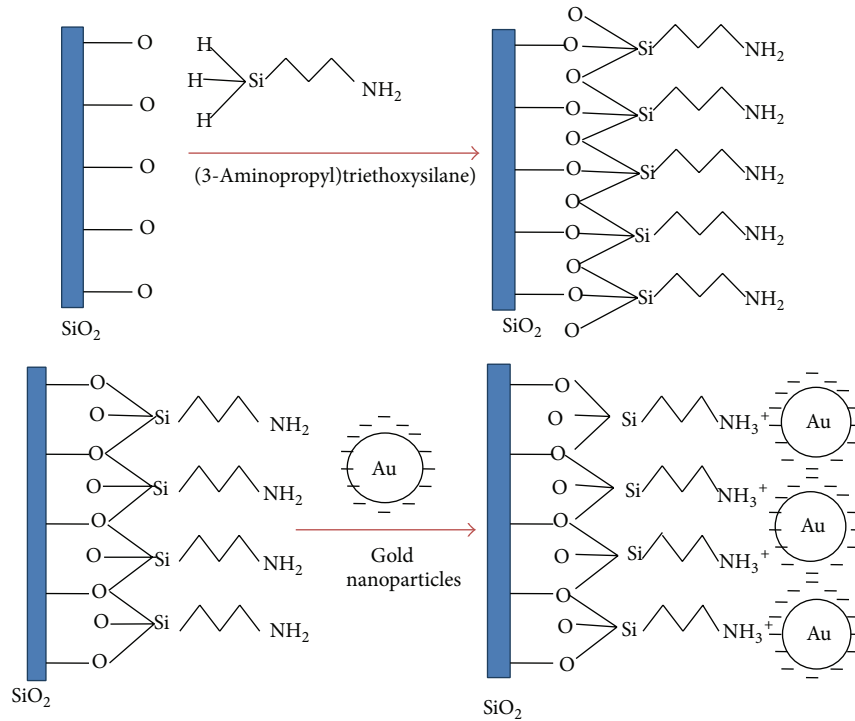


FIGURE 1: Surface modification of SiO<sub>2</sub> with GNPs using APTES.

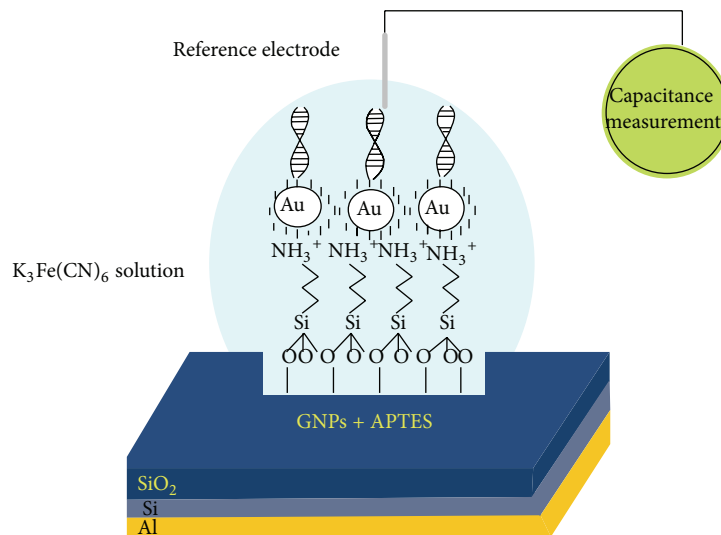


FIGURE 2: A schematic illustration of testing measurement of a modified GNPs electrode and the hybridization of DNA using APTES.

capacitance-frequency (C-F) characterization by connecting two-point probe. The change in capacitance before and after immobilization of the DNA onto the GNPs-modified electrode was carried out in the frequency range of 1 Hz to 1 MHz on the same sample. The result shows that the capacitance values were 160  $\mu\text{F}$ , 77.8  $\mu\text{F}$ , 70  $\mu\text{F}$ , and 64.6  $\mu\text{F}$ , respectively, at 1 Hz for DNA immobilization on the devices during periods of time in 30 min to 4 hours. The capacitance value for bare device was 0.42  $\mu\text{F}$  that was set as a base line. The result indicated that the electrode device exhibited the lowest capacitance value of 64.6  $\mu\text{F}$  at period of 4 hours and

the highest capacitance value of 160  $\mu\text{F}$  in 30 minutes after DNA immobilized onto modified GNPs. The difference value of capacitance in DNA immobilization and hybridization in 30 min has shown the largest capacitance value whereby confirming that 30 min is the best period for DNA immobilization and hybridization. Furthermore, the capacitance values for GNPs modified surface are higher than the bare device. This is probably because the APTES is a conducting polymer material that performs a better capacitance signal compared with the bare device. The immobilization of DNA was successfully detected by showing the highest capacitance

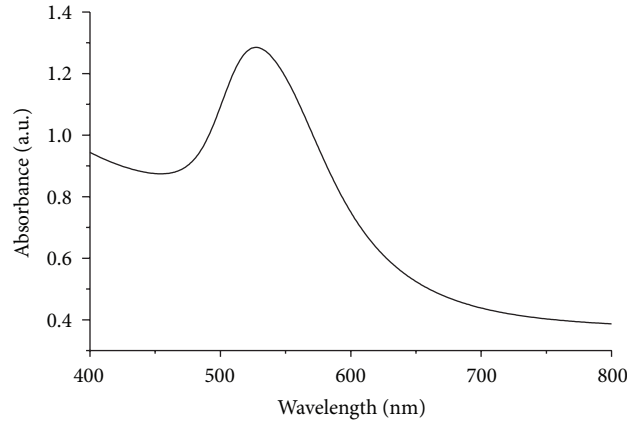


FIGURE 3: UV-visible spectra of Au-nanoparticles solution.

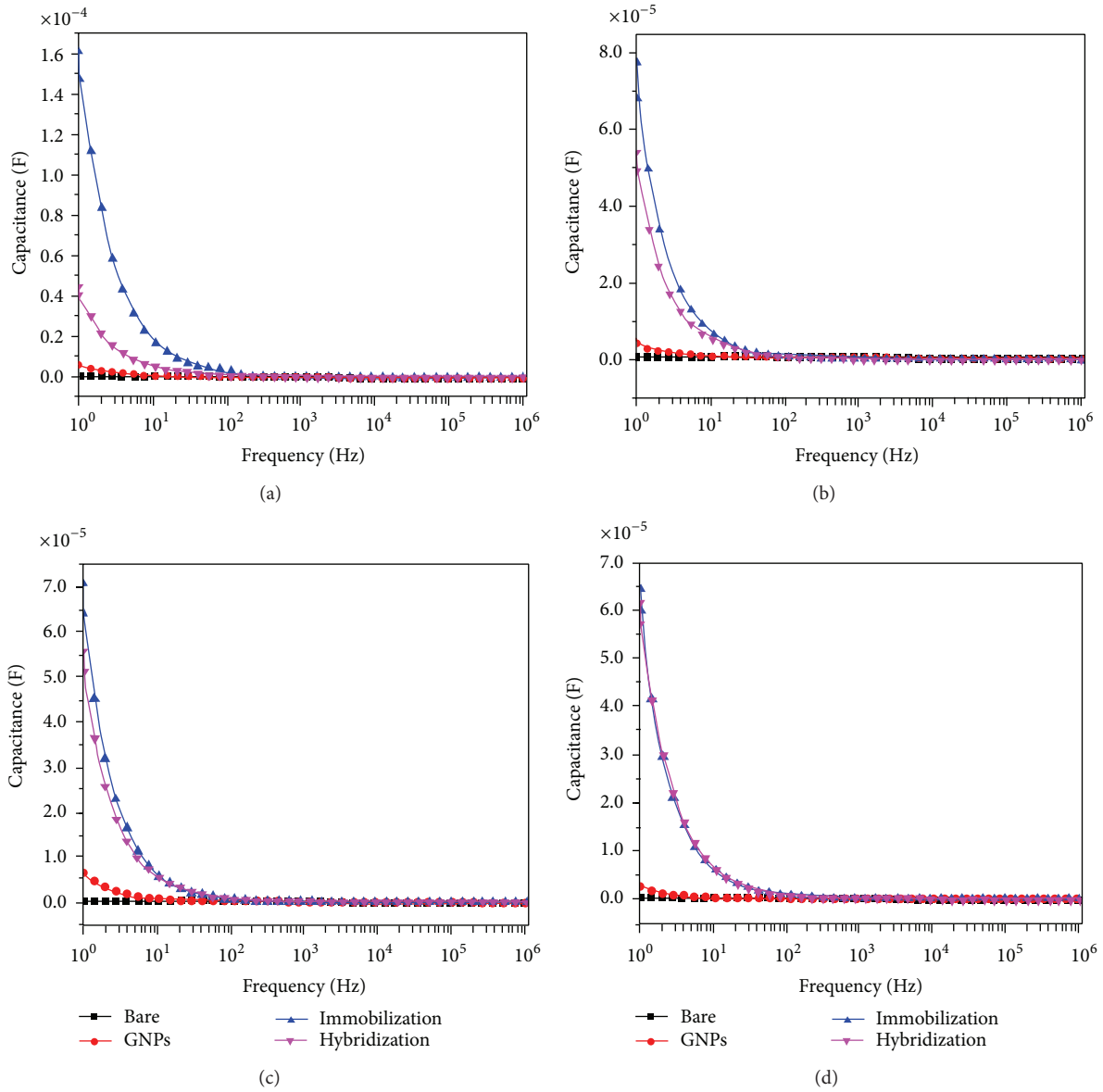


FIGURE 4: A capacitance as a function of frequency for GNPs-modified SiO<sub>2</sub> thin films for DNA immobilization and hybridization detection after (a) 30 minutes, (b) 1 hour, (c) 2 hours, and (d) 4 hours.

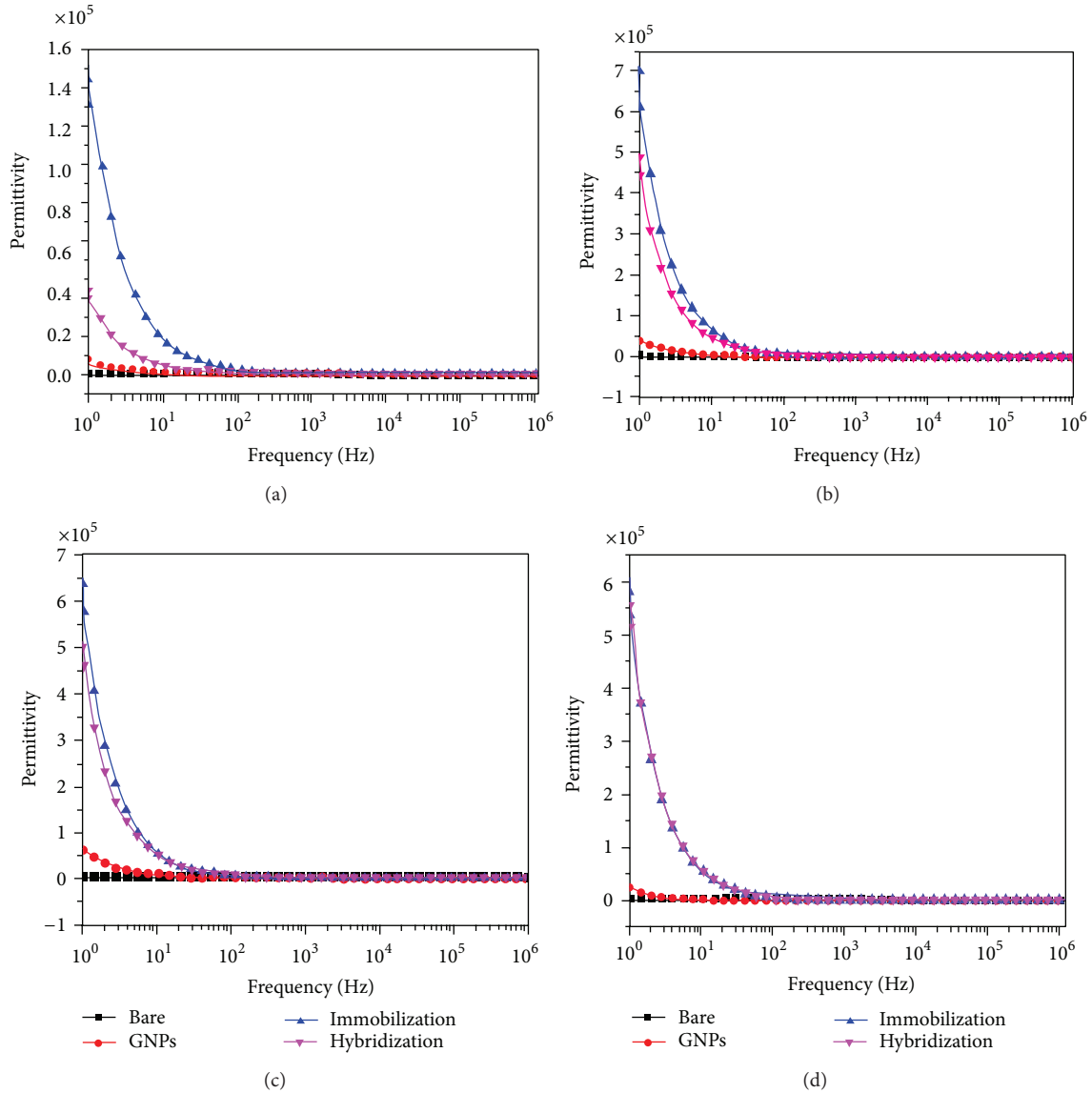


FIGURE 5: A permittivity as a function of frequency for GNPs-modified SiO<sub>2</sub> thin films for DNA immobilization and hybridization detection after (a) 30 minutes, (b) 1 hour, (c) 2 hours, and (d) 4 hours.

values onto the modified GNPs electrode in 30 min. On the other hand, during hybridization of the DNA, the methylene blue was found in base pairs of double strand DNA selectively that reflected the capacitance values of the sample measured were 44  $\mu\text{F}$ , 54  $\mu\text{F}$ , 55  $\mu\text{F}$ , and 61.5  $\mu\text{F}$ , respectively, in 30 min to 4 hours. Therefore, this result confirming the behavior of DNA immobilization and hybridization reaction was successfully detected using a GNPs-modified electrode.

**3.3. Permittivity Measurement.** The permittivity measurements were also performed on the same device as shown in Figure 5. These measurements have the same direction with the capacitance measurement whereby it gives the largest changes in permittivity with probe DNA immobilization. It is clearly observed that permittivity increased dramatically which resulted in the permittivity values being  $1450 \times 10^3$ ,  $700 \times 10^3$ ,  $630.6 \times 10^3$ , and  $580 \times 10^3$  for DNA immobilization

during period of time of 30 min to 4 hours. The capacitance measurements started to significantly increase from a frequency of  $\sim 1$  Hz and degraded as the frequency increases. The result revealed that permittivity measurement gives more sensitivity at lower frequency during hybridization. The permittivity values during hybridization were  $399 \times 10^3$ ,  $480 \times 10^3$ ,  $500 \times 10^3$ , and  $554 \times 10^3$ , respectively. This work demonstrated that changes in capacitance and permittivity value of the GNPs-modified electrode during probe DNA immobilization and hybridization ensure the presence of the DNA during the measurement using GNPs electrode.

## 4. Conclusions

In conclusion, we have demonstrated the DNA immobilization and hybridization on GNPs-modified SiO<sub>2</sub> thin film as electrode device. The difference of the capacitance and

permittivity value during immobilization and hybridization had successfully conducted in electrolyte solution. The capacitance and permittivity value differences in 30 min have shown the best result for DNA immobilization and hybridization. This established GNPs based biosensing platform is potentially applied as the diagnostic or enzyme sensor application.

## Conflict of Interests

The authors declare that there is no conflict of interests regarding the publication of this paper.

## Acknowledgments

The work was supported by INEE at UniMAP, through the Nano Technology project; therefore, the authors thanked and wished to acknowledge the Institute of Nano Electronic Engineering (INEE) at University Malaysia Perlis (UniMAP) for supporting this work.

## References

- [1] D. Imre, "Titanium dioxide and gold nanoparticle for environmental and biological application," *Annals of Faculty Engineering Hunedoara*, vol. 1, pp. 161–166, 2011.
- [2] S. R. Boddu, V. R. Gutti, T. K. Ghosh, R. V. Tompson, and S. K. Loyalka, "Gold, silver, and palladium nanoparticle/nano-agglomerate generation, collection, and characterization," *Journal of Nanoparticle Research*, vol. 13, no. 12, pp. 6591–6601, 2011.
- [3] S. A. C. Carabineiro, "Gold highlights at the 11th "Trends in Nanotechnology" International Conference (TNT 2010) in Braga, Portugal, September 6–10, 2010," *Gold Bulletin*, vol. 44, no. 1, pp. 57–62, 2011.
- [4] V. Kattumuri, *Gold nanoparticles for biomedical applications: synthesis, characterization, in vitro and in vivo studies [Ph.D. thesis]*, University of Missouri-Columbia, Columbia, Mo, USA, 2006.
- [5] D. B. Sanchez, *The Surface plasmon resonance of supported noble metal nanoparticles: characterization, Laser Tailoring, and SERS Application [Ph.D. thesis]*, Madrid University, Madrid, Spain, 2007.
- [6] L. C. Courrol, F. R. de Oliveira Silva, and L. Gomes, "A simple method to synthesize silver nanoparticles by photo-reduction," *Colloids and Surfaces A: Physicochemical and Engineering Aspects*, vol. 305, no. 1–3, pp. 54–57, 2007.
- [7] S.-F. Liu, Y.-F. Li, J.-R. Li, and L. Jiang, "Enhancement of DNA immobilization and hybridization on gold electrode modified by nanogold aggregates," *Biosensors and Bioelectronics*, vol. 21, no. 5, pp. 789–795, 2005.
- [8] M. E. Ali, M. Kashif, K. Uddin, U. Hashim, S. Mustafa, and Y. Che Man, "Species authentication methods in foods and feeds: the present, past, and future of halal forensics," *Food Analytical Methods*, vol. 5, no. 5, pp. 935–955, 2012.
- [9] L. Hood and D. Galas, "The digital code of DNA," *Nature*, vol. 421, no. 6921, pp. 444–448, 2003.
- [10] M. E. Ali, S. Mustafa, U. Hashim, Y. B. Che Man, and K. L. Foo, "Nanobioprobe for the determination of pork adulteration in burger formulations," *Journal of Nanomaterials*, vol. 2012, Article ID 832387, 7 pages, 2012.
- [11] M. E. Ali, S. Mustafa, Y. B. Che Man, K. N. Adam, and K. N. Humayun, "Nanobiosensor for the detection and quantification of pork adulteration in meatball formulation," *Journal of Experimental Nanoscience*, vol. 9, no. 2, pp. 152–160, 2014.
- [12] M. J. Heller, "DNA microarray technology: devices, systems, and applications," *Annual Review of Biomedical Engineering*, vol. 4, pp. 129–153, 2002.
- [13] W. Zhang, T. Yang, D. M. Huang, and K. Jiao, "Electrochemical sensing of DNA immobilization and hybridization based on carbon nanotubes/nano zinc oxide/chitosan composite film," *Chinese Chemical Letters*, vol. 19, no. 5, pp. 589–591, 2008.
- [14] D. W. Selinger, K. J. Cheung, R. Mei et al., "RNA expression analysis using a 30 base pair resolution *Escherichia coli* genome array," *Nature Biotechnology*, vol. 18, no. 12, pp. 1262–1268, 2000.
- [15] P. B. Farmer, K. Brown, E. Tompkins et al., "DNA adducts: mass spectrometry methods and future prospects," *Toxicology and Applied Pharmacology*, vol. 207, no. 2, pp. s293–s301, 2005.
- [16] K. M. Byun, N.-H. Kim, Y. H. Ko, and J. S. Yu, "Enhanced surface plasmon resonance detection of DNA hybridization based on ZnO nanorod arrays," *Sensors and Actuators B: Chemical*, vol. 155, no. 1, pp. 375–379, 2011.
- [17] H. Guan, M. Cai, L. Chen, Y. Wang, and Z. He, "Label-free DNA sensor based on fluorescent cationic polythiophene for the sensitive detection of hepatitis B virus oligonucleotides," *Luminescence*, vol. 25, no. 4, pp. 311–316, 2010.
- [18] D.-J. Chung, K.-C. Kim, and S.-H. Choi, "Electrochemical DNA biosensor based on avidin-biotin conjugation for influenza virus (type A) detection," *Applied Surface Science*, vol. 257, no. 22, pp. 9390–9396, 2011.
- [19] R. Lao, S. Song, H. Wu et al., "Electrochemical interrogation of DNA monolayers on gold surfaces," *Analytical Chemistry*, vol. 77, no. 19, pp. 6475–6480, 2005.
- [20] S. Siddiquee, N. A. Yusof, A. B. Salleh, S. G. Tan, and F. A. Bakar, "Electrochemical DNA biosensor for the detection of *Trichoderma harzianum* based on a gold electrode modified with a composite membrane made from an ionic liquid, ZnO nanoparticles and chitosan, and by using acridine orange as a redox indicator," *Microchimica Acta*, vol. 172, no. 3–4, pp. 357–363, 2011.
- [21] D. Jiang, G. Xiang, C. Liu, J. Yu, L. Liu, and X. Pu, "Development of a cyclic voltammetry method for DNA electrochemical detection on microfluidic gene chip," *International Journal of Electrochemical Science*, vol. 7, pp. 10607–10619, 2012.
- [22] A. Erdem, M. I. Pividori, A. Lermo, A. Bonanni, M. D. Valle, and S. Alegret, "Genomagnetic assay based on label-free electrochemical detection using magneto-composite electrodes," *Sensors and Actuators B: Chemical*, vol. 114, no. 2, pp. 591–598, 2006.
- [23] A. Erdem, F. Sayar, H. Karadeniz, G. Guven, M. Ozsoz, and E. Piskin, "Development of streptavidin carrying magnetic nanoparticles and their applications in electrochemical nucleic acid sensor systems," *Electroanalysis*, vol. 19, no. 7–8, pp. 798–804, 2007.
- [24] H. Karadeniz, A. Erdem, A. Caliskan, C. M. Pereira, E. M. Pereira, and J. A. Ribeiro, "Electrochemical sensing of silver tags labelled DNA immobilized onto disposable graphite electrodes," *Electrochemistry Communications*, vol. 9, no. 9, pp. 2167–2173, 2007.
- [25] M. A. Lapiere-Devlin, C. L. Asher, B. J. Taft, R. Gasparac, M. A. Roberts, and S. O. Kelley, "Amplified electrocatalysis at DNA-modified nanowires," *Nano Letters*, vol. 5, no. 6, pp. 1051–1055, 2005.

- [26] J. Wang, "Nanoparticle-based electrochemical DNA detection," *Analytica Chimica Acta*, vol. 500, no. 1-2, pp. 247–257, 2003.
- [27] X. Hou, L. Wang, G. He, and J. Hao, "Synthesis optical and electrochemical properties of ZnO nanorod hybrids loaded with high-density gold nanoparticles," *CrystEngComm*, vol. 14, no. 16, pp. 5158–5162, 2012.
- [28] M. E. Ali, U. Hashim, S. Mustafa et al., "Nanoparticle sensor for label free detection of swine DNA in mixed biological samples," *Nanotechnology*, vol. 22, no. 19, Article ID 195503, 2011.
- [29] W. Haiss, N. T. K. Thanh, J. Aveyard, and D. G. Fernig, "Determination of size and concentration of gold nanoparticles from UV-Vis spectra," *Analytical Chemistry*, vol. 79, no. 11, pp. 4215–4221, 2007.

## Research Article

# Synthesis of Nanocobalt Powders for an Anode Material of Lithium-Ion Batteries by Chemical Reduction and Carbon Coating

Seong-Hyeon Hong,<sup>1</sup> Yeong-Mi Jin,<sup>2</sup> Kyung Tae Kim,<sup>1</sup> Cheol-Woo Ahn,<sup>3</sup>  
Dong-Su Park,<sup>3</sup> and Myoung Youp Song<sup>4</sup>

<sup>1</sup> Powder Technology Group, Korea Institute of Materials and Science (KIMS), Affiliated with Korea Institute of Machinery and Materials, 797 Changwon-daero, Seongsan-gu, Changwon, Gyeongsangnam-do 642-831, Republic of Korea

<sup>2</sup> Hwa Sung Thermo Co., Ltd., 40 Sandan-ro, 197 Beon-gil, Pyeongtaek-si, Gyeonggi-do 459-050, Republic of Korea

<sup>3</sup> Functional Ceramics Group, Korea Institute of Materials and Science (KIMS), Affiliated with Korea Institute of Machinery and Materials, 797 Changwon-daero, Seongsan-gu, Changwon, Gyeongsangnam-do 642-831, Republic of Korea

<sup>4</sup> Division of Advanced Materials Engineering, Research Center of Advanced Materials Development, Engineering Research Institute, Chonbuk National University, 567 Baekje-daero, Deokjin-gu, Jeonju 561-756, Republic of Korea

Correspondence should be addressed to Myoung Youp Song; [songmy@jbnu.ac.kr](mailto:songmy@jbnu.ac.kr)

Received 25 October 2013; Revised 30 March 2014; Accepted 1 April 2014; Published 19 May 2014

Academic Editor: Necdet Aslan

Copyright © 2014 Seong-Hyeon Hong et al. This is an open access article distributed under the Creative Commons Attribution License, which permits unrestricted use, distribution, and reproduction in any medium, provided the original work is properly cited.

Nanosized Co powders were prepared by a chemical reduction method with and without CTAB (cetyltrimethylammonium bromide,  $C_{19}H_{42}BrN$ ) and carbon-coating heat treatment at 700°C for 1 h, and the electrochemical properties of the prepared nanosized Co powders were examined to evaluate their suitability as an anode material of Li-ion batteries. Nanosized amorphous Co-based powders could be synthesized by a chemical reduction method in which a reducing agent is added to a Co ion-dissolved aqueous solution. When the prepared nanosized Co-based powders were subjected to carbon-coating heat treatment at 700°C for 1 h, the amorphous phase was crystallized, and a Co single phase could be obtained. The Co-based powder prepared by chemical reduction with CTAB and carbon-coating heat treatment had a smaller first discharge capacity (about 557 mAh/g) than the Co-based powder prepared by chemical reduction without CTAB and carbon-coating heat treatment (about 628 mAh/g). However, the former had a better cycling performance than the latter from the third cycle. The carbon-coated layers are believed to have led to quite good cycling performances of the prepared Co-based powders from the third cycle.

## 1. Introduction

There is much interest in several different types of lithium-based rechargeable batteries [1–9], due to the expectation of high specific energies and energy densities. The conventional lithium-ion batteries use carbon-based materials as anodes [10–12], but their theoretical capacity of 372 mAh/g is not sufficient. Therefore, the development of new anode materials with high capacity is needed.

Much work has been conducted on the subject of electrodes using nanosized materials since nanosized powders exhibit good electrochemical performance. Nanosized powder can be synthesized by various methods, such as sol-gel

[13], solvothermal [14], spray conversion [15], and pulsed wire evaporation (PWE) methods [16].

Kim et al. [17] synthesized nanosized Co powder by a pulsed wire evaporation method as an anode material for lithium batteries. The Li/Co cell fabricated with the powder showed a plateau potential of 0.7 V and a capacity of 440 mAh/g at the first discharge, and a reversible capacity of about 280 mAh/g after 30 cycles.

An ordered mesoporous Sn-C composite with Sn nanoparticles confined in carbon nanorods was prepared by Chen et al. [18]. This composite delivered a reversible lithium storage capacity of 554 mAh/g at the 200th cycle as an anode material of Li-ion batteries.

Cobalt composites are potential candidates for use as an anode material. Examples are Co-O [19], Co-C [20, 21], Co-Sb [22], Co-Sn [23, 24], and Co-B [25] composites.

Yue et al. [21] synthesized a novel C/Co composite with Co nanoparticles embedded in carbon matrix by the pyrolysis of polymeric cobalt phthalocyanine (PcCo) at 700°C in argon atmosphere. They reported that the C/Co electrode had a reversible capacity of over 600 mAh/g at a current of 50 mAh/g after 40 cycles and showed better rate capability and less hysteresis in comparison with carbon not containing Co.

He et al. [24] performed hydrothermal synthesis and examined the electrochemical properties of nanosized Co-Sn alloy anodes for lithium-ion batteries. They reported that prolonging the dwelling time at the same hydrothermal temperature could increase the content of Sn oxides, which would lead to a high initial irreversible capacity loss, but better cycling stability, owing to the buffer effect of the irreversible product  $\text{Li}_2\text{O}$ .

Yiping et al. [25] produced Co-B fine particles by the chemical reduction of aqueous solutions of cobalt chloride with sodium borohydride. The particle size was in the range of 20–100 nm. Ultrafine  $\text{Co}_{74.4}\text{B}_{25.6}$  amorphous powder was prepared by Yuan et al. [26] with chemical reduction. The as-prepared sample was formed by many interconnected fine particles with sizes smaller than 100 nm.

Co-based powders were prepared via the chemical reduction method by several researchers. Lu et al. [27] reduced cobalt (II) by chemical reduction. They added sodium borohydride at a controlled rate, with the concentration of NaOH varied in the reducing solution. The synthesized particle size was about 20–100 nm.

Ahn [28] reported that nanosized anode materials had high discharge capacities but showed poor cycling performances. Carbon coating is thought to improve cycling performances of anode materials by preventing the formation of SEI (solid electrolyte interphase) layers between anode materials and electrolyte.

In this study, nanosized Co powders were prepared by a chemical reduction method with and without CTAB (cetyltrimethylammonium bromide,  $\text{C}_{19}\text{H}_{42}\text{BrN}$ ) and carbon-coating heat treatment at 700°C. Then, the electrochemical properties of the prepared nanosized Co powders were examined to evaluate their suitability as an anode material for Li-ion batteries.

## 2. Experimental Details

In order to synthesize nanosized Co-based powders, the materials listed in Table 1 were used.

Figure 1 shows a schematic of the apparatus used for chemical reduction. CTAB is a cationic surfactant (surface active agent) and was added since its addition was expected to facilitate pore formation. CTAB-added Co powders were synthesized as follows. 5.94 g of cobalt (II) chloride hexahydrate ( $\text{CoCl}_2 \cdot 6\text{H}_2\text{O}$ ) and 2.28 g of CTAB were dissolved by stirring in 250 cc of distilled water, which was purged sufficiently with high-purity nitrogen. 9.46 g of a reducing agent granular sodium borohydride was also dissolved by stirring in 250 cc

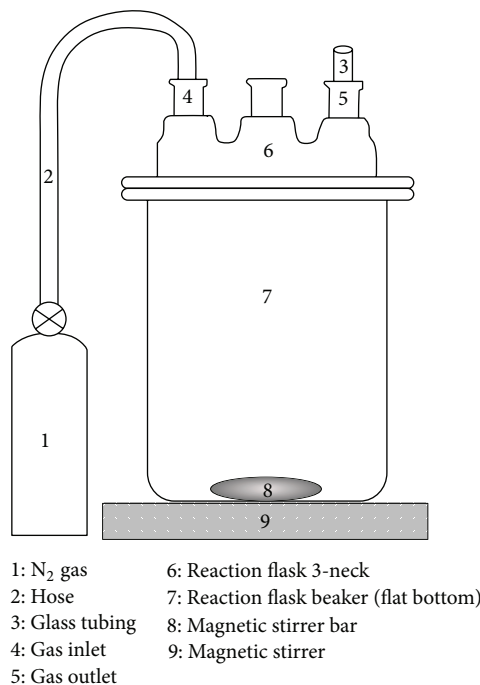


FIGURE 1: Schematic of an apparatus for chemical reduction.

of distilled water, which was also purged sufficiently with high-purity nitrogen. Then, the reducing agent solution was added slowly to the solution containing the solutes in order to prevent abrupt reaction due to CTAB, which can cause boiling over. During this process, nitrogen was purged continuously. After the reaction was completed, the solution was filtered and washed by distilled water and ethanol to prevent oxidation. The prepared powder was then dried.

Co powders without CTAB addition were synthesized as follows. 11.88 g of cobalt (II) chloride hexahydrate ( $\text{CoCl}_2 \cdot 6\text{H}_2\text{O}$ ) and 18.92 g of granular sodium borohydride reducing agent were dissolved separately by stirring in 500 cc of distilled water, which was purged sufficiently with high-purity nitrogen. Then, the reducing agent solution was added to the solute-containing solution at a rate of about 500 cc/min. During this process, nitrogen was purged continuously. After the reaction was completed, the solution was filtered and washed by distilled water and ethanol to prevent oxidation, and the prepared powder was dried.

TGA (thermogravimetric analysis) with an SDT2960 (TA Instruments, USA) and DTA (differential thermal analysis) with an STA409pc (Netzsch, Germany) were performed for the synthesized samples by increasing the temperature to 1000°C at a heating rate of 10°C/min in an Ar atmosphere. The sensitivity of the balance was 0.1  $\mu\text{g}$ .

Then the powder synthesized by the chemical reduction method was carbon-coated in a tube furnace as follows. The powder used as the carbon-coating agent was glucose ( $\text{C}_6\text{H}_{12}\text{O}_6$ , Oriental Chemical Industries, extra pure). The reaction for carbon coating on the particles prepared by chemical reduction is given by



TABLE 1: Raw materials used in this work.

Material	Molecular formula	Purity	Manufacturing company
Cobalt (II) chloride hexahydrate	$\text{CoCl}_2 \cdot 6\text{H}_2\text{O}$	97.0%	Samchun Pure Chemical Co., Ltd.
Sodium borohydride	$\text{NaBH}_4$	98.0%	Samchun Pure Chemical Co., Ltd.
CTAB (cetyltrimethylammonium bromide)	$\text{C}_{19}\text{H}_{42}\text{BrN}$	99.0%	Samchun Pure Chemical Co., Ltd.

When  $\text{C}_6\text{H}_{12}\text{O}_6$  is decomposed, the decrease in weight is 60%, and 40% remains as carbon. The weight of the glucose was determined by planning the Co-based powder containing 20 wt% coated carbon after  $\text{C}_6\text{H}_{12}\text{O}_6$  decomposed to carbon on the Co-based powder. The mixed weight ratio of the Co-based powder to the  $\text{C}_6\text{H}_{12}\text{O}_6$  powder was 61.54 : 38.46. A determined weight of the  $\text{C}_6\text{H}_{12}\text{O}_6$  powder was dissolved in distilled water with a spoon until precipitates were not observed and then mixed with the dried Co powder. The particles were then dispersed by an ultrasonic cleaner and dried. This dried powder was heat-treated at  $700^\circ\text{C}$  for 1 h in Ar atmosphere.

The BET surface areas of the synthesized powders were measured by a BET surface characterizing analyzer (ASAP2010 and TriStar 3000 (Micromeritics, USA)).

The microstructures of the prepared samples were observed by FE-SEM (field emission scanning electron microscope, JXA-8600).

Co-based powder anodes were fabricated by dispersing the powders, carbon (10 wt% or 20 wt%), and polyvinylidene fluoride (PVDF) binder (10 wt%) in N-methyl-2-pyrrolidone (NMP) to form a slurry, which was spread onto copper foil. After drying the coated slurry at  $80^\circ\text{C}$  for 12 h in vacuum, the copper foil coated with the slurry was rolled under a pressure of  $100 \text{ kgf/cm}^2$ . The coated electrode was punched with a  $\Phi 14.6 \text{ mm}$  punch. Li/Co-based powder coin cells (type 2016) were then assembled. Li foil metal was used as the counter and reference electrodes. The electrolyte was 1 M  $\text{LiPF}_6$  in a 1:1 (volume ratio) mixture of ethylene carbonate (EC) and diethyl carbonate (DEC). The charge-discharge tests and CV (cyclic voltammetry) tests were performed with a charge-discharge tester (WBCS3000, WonATech Ltd.). The cells were charged and discharged at a current density of  $0.2 \text{ mA/cm}^2$  in a voltage range of 0.001 V–2.5 V versus  $\text{Li/Li}^+$ .

### 3. Results and Discussion

The XRD patterns of the Co-based powders prepared by chemical reduction method with and without CTAB are shown in Figure 2. The prepared powders are amorphous without crystalline peaks in their X-ray diffraction patterns.

Figure 3 presents the FE-SEM (field emission scanning electron microscope) micrographs of Co-based powders prepared by chemical reduction method, (a)–(c) with CTAB and (d)–(f) without CTAB. The particles were dispersed by an ultrasonic cleaner and dried to observe the microstructure by FE-SEM. The effect of the decrease in grain size can be obtained by the chemical reduction method, since the solute in the solution instantly reacts with the reducing agent. This can be seen clearly in Figure 3. The grain size in the sample prepared with CTAB has a wide particle size distribution

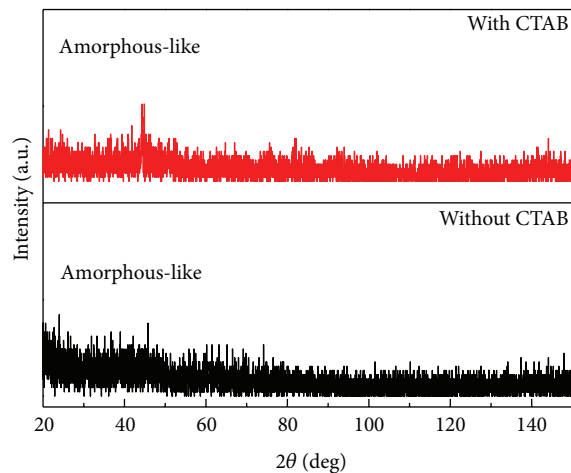


FIGURE 2: XRD patterns of the Co-based powders prepared by chemical reduction with CTAB and without CTAB.

between about 100 nm and 10–20 nm. The grain size in the sample prepared without CTAB is quite homogeneous with a grain size of about 20 nm. In the sample prepared without CTAB, the fine grains are agglomerated, which can be seen distinctly in the micrographs at high magnifications.

The TGA-DTA results of Co-based powders prepared by chemical reduction method (a) with CTAB and (b) without CTAB are shown in Figure 4. Just after the chemical reduction and drying, the Co-based powders were used for these measurements, in which the temperature was increased to  $1,000^\circ\text{C}$  at a heating rate of  $10^\circ\text{C/min}$  in an Ar atmosphere. The absorption peak at  $139.86^\circ\text{C}$  in Figure 4(a) does not appear in Figure 4(b). This absorption peak is believed to result from the decomposition of CTAB. The weight decreases rapidly at the beginning ( $<200^\circ\text{C}$ ) in Figures 4(a) and 4(b). This is believed to be due to the evaporation of the distilled water, ethanol, and water vapor adsorbed during storage. The distilled water and ethanol are those which had not been removed during the chemical reduction. The crystallization of Co is expected to occur at about  $656.78\text{--}730.50^\circ\text{C}$ . This can be verified in the XRD results obtained after heat treatment at  $700^\circ\text{C}$ .

Figure 5 shows the XRD patterns of Co-based powders prepared by chemical reduction with and without CTAB and carbon-coating heat treatment at  $700^\circ\text{C}$  for 1 h. Clear peaks corresponding to Co grains appear. Using the Scherrer formula for the main Co peaks, the grain size of the particles prepared with CTAB and carbon-coated was calculated as 33 nm, which was larger than that of 25 nm obtained for the particles prepared without CTAB and carbon-coated. The XRD patterns of Co-based powders prepared by chemical

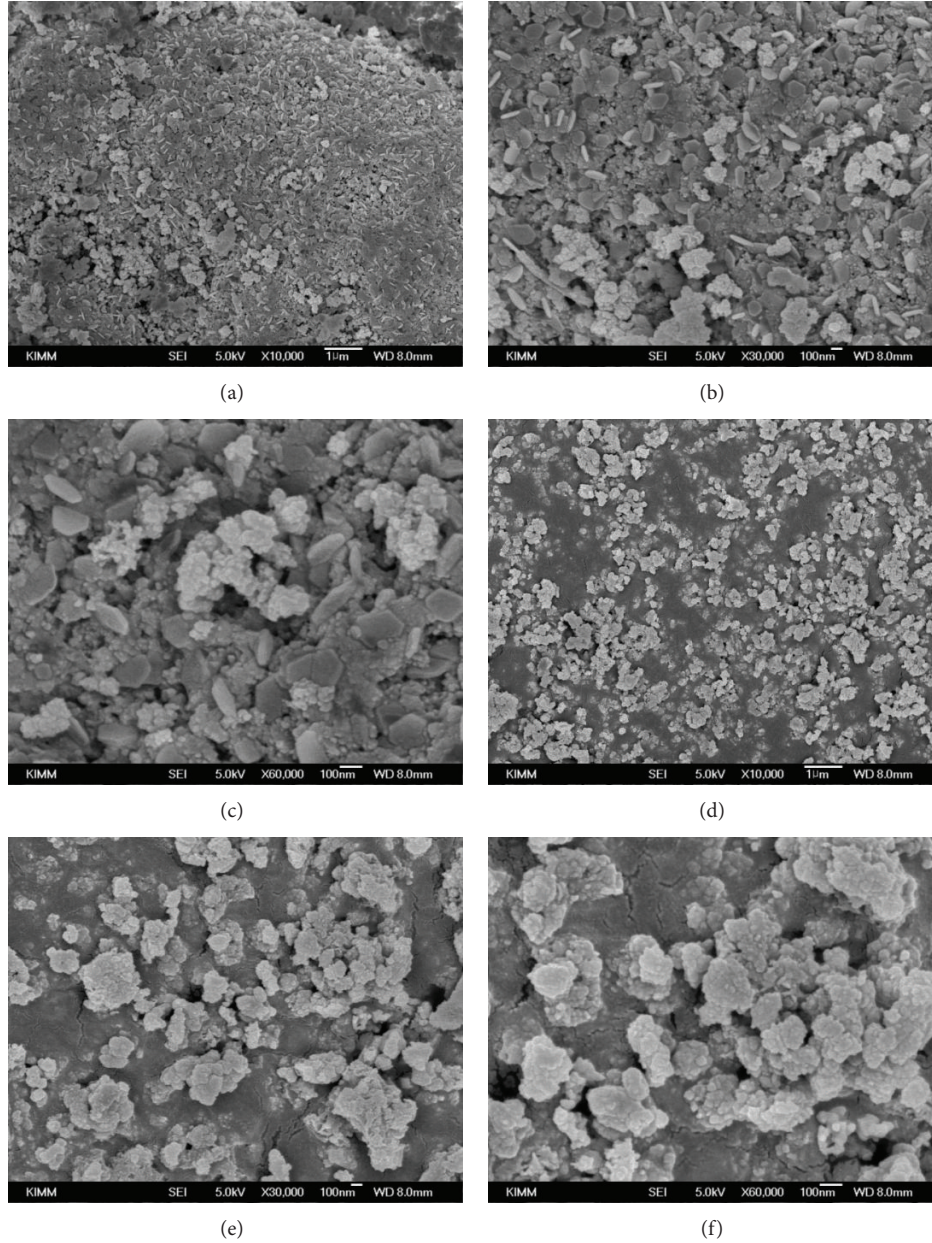
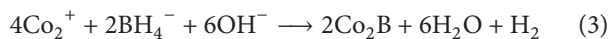
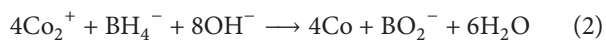


FIGURE 3: FE-SEM micrographs of the Co-based powders prepared by chemical reduction (a)–(c) with CTAB and (d)–(f) without CTAB.

reduction with and without CTAB and carbon-coating heat treatment at 500°C showed that these Co-based powders were not crystallized, as they were just after chemical reduction.

According to Saida et al. [29], the reaction mechanism of Co powder by chemical reduction is as follows:



These reactions equations show that the reaction between  $\text{BH}_4^-$  and Co produces Co or  $\text{Co}_2\text{B}$ . The formation of Co in this work suggests that reaction (2) occurs, forming  $\text{BO}_2^-$  and  $\text{H}_2\text{O}$ .

The FE-SEM micrographs of Co-based powders prepared by chemical reduction (a, b) with CTAB and (c, d) without CTAB and carbon-coating heat treatment at 700°C for 1 h are shown in Figure 6. The particles prepared with CTAB and carbon-coated are larger than those prepared without CTAB and carbon-coated. The particles are believed to have increased in size due to the formation of carbon-coated layers. The particles prepared without CTAB and carbon-coated are spherical, while those prepared with CTAB and carbon-coated have square shapes with edges.

CTAB was added because we expected its addition to facilitate pore formation. The Co-based powder prepared by chemical reduction without CTAB and carbon-coating heat treatment at 500°C for 1 h had a BET surface area of

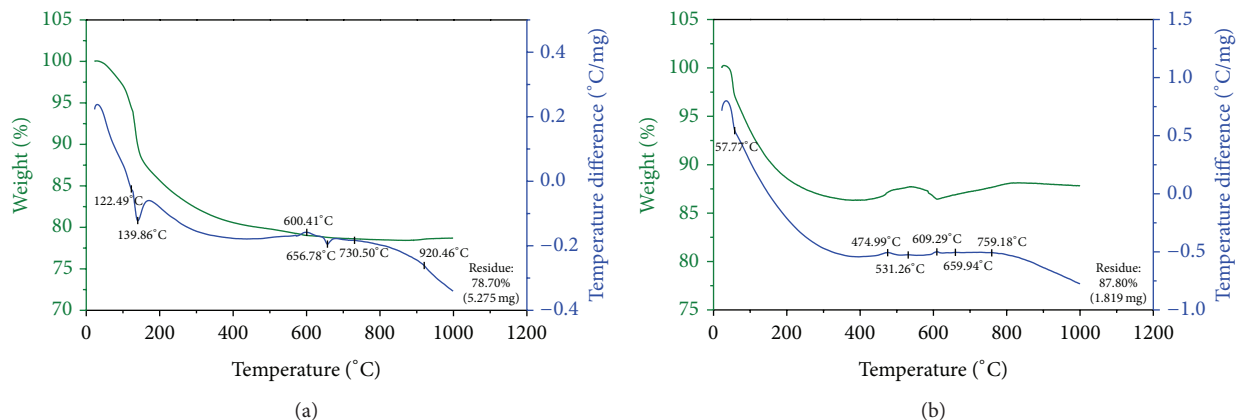


FIGURE 4: TGA-DTA of the Co-based powders prepared by chemical reduction (a) with CTAB and (b) without CTAB.

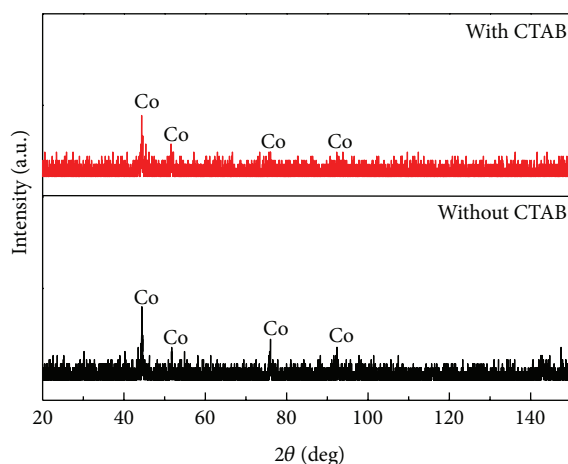


FIGURE 5: XRD patterns of the carbon-coated Co-based powders prepared by chemical reduction with and without CTAB and carbon-coating heat treatment at 700°C for 1 h.

3.80 m<sup>2</sup>/g, indicating a high specific area of the powder. The size of these Co-based particles was calculated as 180 nm from the equation,  $particle\ size = 6 / (specific\ surface\ area \times density)$ , by assuming the particles are spherical. The BET surface area of the Co-based powder prepared by chemical reduction with CTAB and carbon-coating heat treatment at 500°C for 1 h could not be measured due to the difficulty in the maintenance of vacuum. So, it was hard to verify that the addition of CTAB facilitates pore formation.

Figure 7 shows the discharge capacity versus cycle number of Co-based electrodes prepared by chemical reduction with and without CTAB and carbon-coating heat treatment at 700°C for 1 h. The Co-based powder prepared with CTAB and carbon-coated has a smaller first discharge capacity (about 557 mAh/g) than the Co-based powder prepared without CTAB and carbon-coated (about 628 mAh/g). A decrease in particle size of the host material is believed to be able to buffer the volume expansion involved during charge and discharge. Even though the volume expansion was minimized by preparing nanosized particles, at the beginning of cycling, the discharge capacity decreases quite abruptly. This is believed to be due to the formation of an SEI (solid electrolyte interphase), which obstructs the movements of Li

ions and electrons. However, from the third cycle, the two samples exhibit quite good cycling performances, and the Co-based powder prepared with CTAB and carbon-coated has a better cycling performance than the Co-based powder prepared without CTAB and carbon-coated. The reason why these two samples exhibit quite good cycling performance from the third cycle is believed to be due to the carbon-coated layer which prevents the formation of SEI (solid electrolyte interphase) layers between anode materials and electrolyte.

Poizot et al. [30] reported that electrodes made of nanoparticles of transition-metal oxides (MO, where M is Co, Ni, Cu, or Fe) demonstrated electrochemical capacities of 700 mAh/g, with 100% capacity retention for up to 100 cycles and high recharging rates. Carbon-coated silicon anodes were reported by Dimov et al. [31] to have a charge capacity of 1,080 mAh/g at the first cycle and a charge capacity of 1,270 mAh/g at the second cycle, at the current density of 1 mA/cm<sup>2</sup>. Yue et al. [21] reported that the C/Co electrode, in which Co nanoparticles are embedded in carbon matrix, had a reversible capacity of over 600 mAh/g at a current of 50 mAh/g after 40 cycles. Kim et al. [17] reported that the Li/Co cell, fabricated with the nanosized Co powder synthesized by a pulsed wire evaporation method, had a capacity

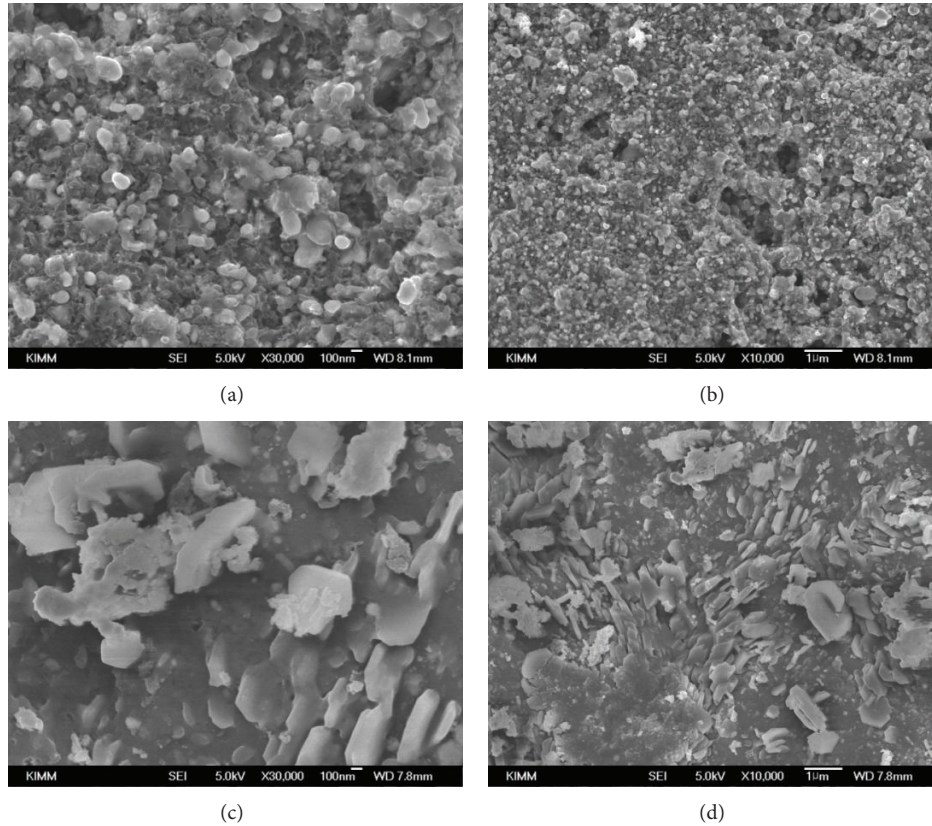


FIGURE 6: FE-SEM micrographs of the carbon-coated Co-based powders prepared by chemical reduction (a, b) with CTAB and (c, d) without CTAB and carbon-coating heat treatment at 700°C for 1 h.

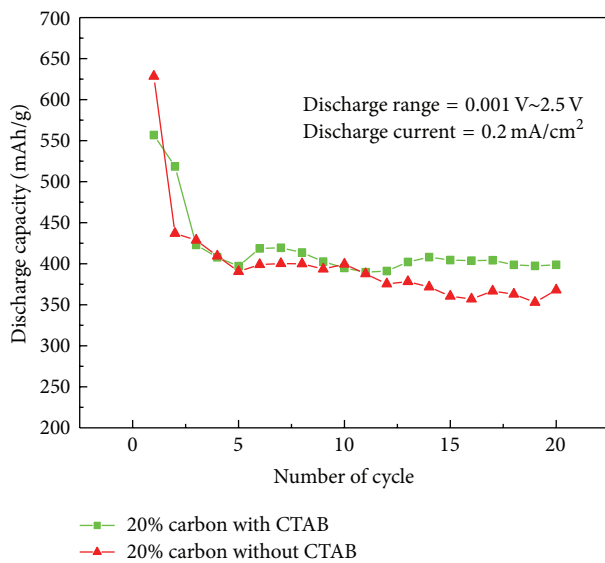


FIGURE 7: Discharge capacity versus cycle number curves of the carbon-coated Co-based electrodes prepared by chemical reduction with and without CTAB and carbon-coating heat treatment at 700°C for 1 h.

of 440 mAh/g at the first discharge and a reversible capacity of about 280 mAh/g after 30 cycles. The Li/carbon-coated graphite electrodes were reported by Lee et al. [32] to have a

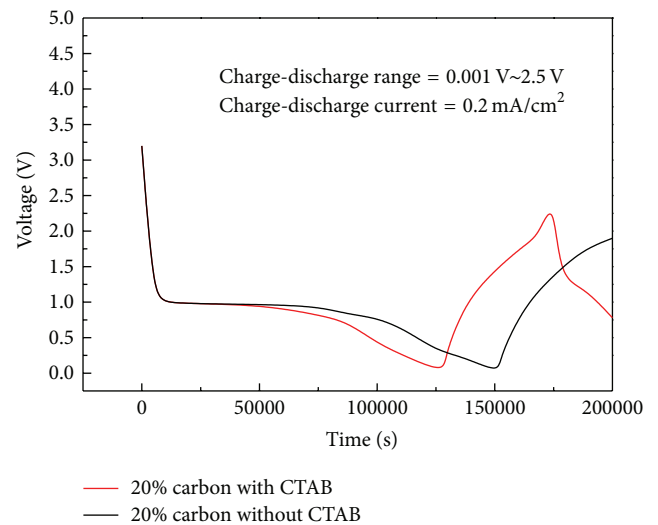


FIGURE 8: Voltage versus time curves at the first cycle of the carbon-coated Co-based electrodes prepared by chemical reduction with and without CTAB and carbon-coating heat treatment at 700°C for 1 h.

reversible capacity of approximately 350 mAh/g. The Li/Co-based cells of this work have smaller discharge capacities than those of nanoparticles of transition-metal oxides [30] and carbon-coated silicon anodes [31] and have the discharge capacities similar to those of the C/Co electrode,

in which Co nanoparticles are embedded in carbon matrix [21]. However, the Li/Co-based cells of this work have larger discharge capacities than those of the Li/Co cell fabricated with the nanosized Co powder synthesized by a pulsed wire evaporation method [17] and the Li/carbon-coated graphite electrodes [32].

The curves of voltage versus time at the first cycle of the Co-based electrodes prepared by chemical reduction with and without CTAB and carbon-coating heat treatment at 700°C for 1 h are shown in Figure 8. The two Co-based electrodes have very similar plateau voltages of about 1 V, and the plateau voltage of the Co-based electrode prepared with CTAB and carbon-coated decreases earlier. These plateau voltages are very similar to that (0.7 V) of the Li/Co cell fabricated with the nanosized Co powder prepared via a pulsed wire evaporation method by Kim et al. [17].

#### 4. Conclusions

Nanosized amorphous Co-based powders could be synthesized by a chemical reduction method in which a reducing agent is added to Co ions dissolved in an aqueous solution. When the prepared nanosized Co powders were subjected to carbon-coating heating treatment at 700°C for 1 h, the amorphous phase was crystallized, and a Co single phase could be obtained. The grain size of the particles prepared by chemical reduction with CTAB and carbon-coating heat treatment was calculated as 33 nm, which was larger than that of 25 nm obtained for the particles prepared by chemical reduction without CTAB and carbon-coating heat treatment. The Co-based powder prepared with CTAB and carbon-coated had a smaller first discharge capacity (about 557 mAh/g) than the Co-based powder prepared without CTAB and carbon-coated (about 628 mAh/g). However, from the third cycle, the former had a better cycling performance than the latter. Even though the volume expansion was minimized by preparing nanosized particles, quite an abrupt decrease in the discharge capacity observed at the beginning of cycling is believed due to the formation of an SEI, which obstructs the movements of Li ions and electrons. The carbon-coated layers are believed to have led to quite good cycling performances of the prepared Co-based powders from the third cycle.

#### Conflict of Interests

The authors declare that there is no conflict of interests regarding the publication of this paper.

#### Acknowledgment

This research was performed for the Research Program funded by Korea Institute of Materials Science (KIMS) in South Korea.

#### References

- [1] L.-L. Xie, X.-Y. Cao, L.-X. Zhang, Z.-X. Dai, and L.-B. Qu, "Synthesis and electrochemical properties of LiV<sub>3</sub>O<sub>8</sub>/PAN composite as a cathode material for lithium secondary batteries," *Electronic Materials Letters*, vol. 9, no. 2, pp. 183–186, 2013.
- [2] M. S. Yoon, M. Islam, Y. M. Park, and S.-C. Ur, "Effect of synthesizing method on the properties of LiFePO<sub>4</sub>/C composite for rechargeable lithium-ion batteries," *Electronic Materials Letters*, vol. 9, no. 2, pp. 187–193, 2013.
- [3] H. R. Bak, J. H. Lee, B. K. Kim, and W. Y. Yoon, "Electrochemical behavior of Li/LiV<sub>3</sub>O<sub>8</sub> secondary cells," *Electronic Materials Letters*, vol. 9, no. 2, pp. 195–199, 2013.
- [4] T. G. Woo, I. S. Park, and K. W. Seol, "The effect of additives and current density on mechanical properties of cathode metal for secondary battery," *Electronic Materials Letters*, vol. 9, no. 4, pp. 535–539, 2013.
- [5] L.-L. Xie, Y.-D. Xu, J.-J. Zhang, C.-P. Zhang, X.-Y. Cao, and L.-B. Qu, "Rheological phase synthesis of Er-doped LiV<sub>3</sub>O<sub>8</sub> as electroactive material for a cathode of secondary lithium storage," *Electronic Materials Letters*, vol. 9, no. 4, pp. 549–553, 2013.
- [6] Y. K. Kwon, W. C. Choi, H.-S. Choi, and J. K. Lee, "Effect of lithium difluoro (oxalato) borate on LiMn<sub>2</sub>O<sub>4</sub>-activated carbon hybrid capacitors," *Electronic Materials Letters*, vol. 9, no. 6, pp. 751–754, 2013.
- [7] Y. Xu, L. Xie, Y. Zhang, and X. Cao, "Hydrothermal synthesis of hexagonal MoO<sub>3</sub> and its reversible electrochemical behavior as a cathode for Li-ion batteries," *Electronic Materials Letters*, vol. 9, no. 5, pp. 693–696, 2013.
- [8] H. J. Kim, B. S. Jin, C. H. Doh, D. S. Bae, and H. S. Kim, "Improved electrochemical performance of doped-LiNi<sub>0.5</sub>Mn<sub>1.5</sub>O<sub>4</sub> cathode material for lithium-ion batteries," *Electronic Materials Letters*, vol. 9, no. 6, pp. 851–854, 2013.
- [9] H. J. Kwon, K. Y. Sohn, and W. W. Park, "Electrochemical properties of rapidly solidified Si-Ti-Ni(-Cu) base anode for Li-ion rechargeable batteries," *Electronic Materials Letters*, vol. 9, no. 6, pp. 859–863, 2013.
- [10] M. M. Atabaki and R. Kovacevic, "Graphene composites as anode materials in lithium-ion batteries," *Electronic Materials Letters*, vol. 9, no. 2, pp. 133–153, 2013.
- [11] Y. Zhao, Y. Huang, Q. Wang et al., "Graphene supported Li<sub>2</sub>SnO<sub>3</sub> as anode material for lithium-ion batteries," *Electronic Materials Letters*, vol. 9, no. 5, pp. 683–686, 2013.
- [12] K. C. Roh, H. J. Lee, and J. W. Lee, "Nanocomposite of LiFePO<sub>4</sub> and mesoporous carbon prepared by microwave heating for rechargeable lithium batteries," *Electronic Materials Letters*, vol. 9, no. 6, pp. 855–858, 2013.
- [13] Y. S. Lee, Y. K. Sun, and K. S. Nahm, "Synthesis and characterization of LiNiO<sub>2</sub> cathode material prepared by an adipic acid-assisted sol-gel method for lithium secondary batteries," *Solid State Ionics*, vol. 118, no. 1-2, pp. 159–168, 1999.
- [14] J. Xie, X. B. Zhao, G. S. Cao, Y. D. Zhong, M. J. Zhao, and J. P. Tu, "Solvothermal synthesis of nanosized CoSb<sub>2</sub> alloy anode for Li-ion batteries," *Electrochimica Acta*, vol. 50, no. 9, pp. 1903–1907, 2005.
- [15] S.-H. Hong, J.-S. Bae, and H.-J. Ann, "Synthesis of nano-sized Co<sub>3</sub>O<sub>4</sub> powder by spray conversion method for anode material of lithium battery," *Metals and Materials International*, vol. 14, no. 2, pp. 229–232, 2008.
- [16] Y. R. Uhm, J. H. Park, W. W. Kim, C.-H. Cho, and C. K. Rhee, "Magnetic properties of nano-size Ni synthesized by the pulsed wire evaporation (PWE) method," *Materials Science and Engineering B*, vol. 106, no. 3, pp. 224–227, 2004.
- [17] D. Y. Kim, H. J. Ahn, J. S. Kim et al., "The electrochemical properties of nano-sized cobalt powder as an anode material for

- lithium batteries," *Electronic Materials Letters*, vol. 5, no. 4, pp. 183–186, 2009.
- [18] J. Chen, L. Yang, S. Fang, and S.-I. Hirano, "Ordered mesoporous Sn-C composite as an anode material for lithium ion batteries," *Electrochemistry Communications*, vol. 13, no. 8, pp. 848–851, 2011.
- [19] Y. Liu, C. Mi, L. Su, and X. Zhang, "Hydrothermal synthesis of  $\text{Co}_3\text{O}_4$  microspheres as anode material for lithium-ion batteries," *Electrochimica Acta*, vol. 53, no. 5, pp. 2507–2513, 2008.
- [20] G. F. Ortiz, R. Alcántara, I. Rodríguez, and J. L. Tirado, "New tin-based materials containing cobalt and carbon for lithium-ion batteries," *Journal of Electroanalytical Chemistry*, vol. 605, no. 2, pp. 98–108, 2007.
- [21] J. Yue, X. Zhao, and D. Xia, "Electrochemical lithium storage of C/Co composite as an anode material for lithium ion batteries," *Electrochemistry Communications*, vol. 18, no. 1, pp. 44–47, 2012.
- [22] J. Xie, X. Zhao, G. Cao, Y. Zhong, and M. Zhao, "Ex-situ XRD studies of  $\text{CoSb}_3$  compound as the anode material for lithium ion batteries," *Journal of Electroanalytical Chemistry*, vol. 542, pp. 1–6, 2003.
- [23] Y. Zheng, J. Yang, Y. NuLi, and J. Wang, "Nano-tin alloys dispersed in oxides for lithium storage materials," *Journal of Power Sources*, vol. 174, no. 2, pp. 624–627, 2007.
- [24] J. He, H. Zhao, J. Wang, J. Wang, and J. Chen, "Hydrothermal synthesis and electrochemical properties of nano-sized Co-Sn alloy anodes for lithium ion batteries," *Journal of Alloys and Compounds*, vol. 508, no. 2, pp. 629–635, 2010.
- [25] L. Yiping, G. C. Hadjipanayis, C. M. Sorensen, and K. J. Klabunde, "Magnetic and structural properties of ultrafine Co-B particles," *Journal of Magnetism and Magnetic Materials*, vol. 79, no. 3, pp. 321–326, 1989.
- [26] Z.-Z. Yuan, X.-D. Chen, H. Xu, X.-L. Qu, and B.-X. Wang, "Crystallization kinetics of ultrafine  $\text{Co}_{7.4}\text{B}_{25.6}$  amorphous powder prepared by chemical reduction," *Journal of Alloys and Compounds*, vol. 422, no. 1-2, pp. 109–115, 2006.
- [27] J. Lu, D. B. Dreisinger, and W. C. Cooper, "Cobalt precipitation by reduction with sodium borohydride," *Hydrometallurgy*, vol. 45, no. 3, pp. 305–322, 1997.
- [28] J. H. Ahn, "New cell electrode materials using nano-sized powder for lithium secondary battery," *Journal of Korean Powder Metallurgy Institute*, vol. 9, no. 5, pp. 370–374, 2002.
- [29] J. Saida, A. Inoue, and T. Masumoto, "The effect of reaction condition on composition and properties of ultrafine amorphous powders in (Fe, Co, Ni)-B systems prepared by chemical reduction," *Metallurgical Transactions A*, vol. 22, no. 9, pp. 2125–2132, 1991.
- [30] P. Poizot, S. Laruelle, S. Grugeon, L. Dupont, and J.-M. Tarascon, "Nano-sized transition-metal oxides as negative-electrode materials for lithium-ion batteries," *Nature*, vol. 407, no. 6803, pp. 496–499, 2000.
- [31] N. Dimov, S. Kugino, and M. Yoshio, "Carbon-coated silicon as anode material for lithium ion batteries: advantages and limitations," *Electrochimica Acta*, vol. 48, no. 11, pp. 1579–1587, 2003.
- [32] H.-Y. Lee, J.-K. Baek, S.-M. Lee, H.-K. Park, K.-Y. Lee, and M.-H. Kim, "Effect of carbon coating on elevated temperature performance of graphite as lithium-ion battery anode material," *Journal of Power Sources*, vol. 128, no. 1, pp. 61–66, 2004.

## Research Article

# Efficient Rapid Microwave-Assisted Route to Synthesize Monodispersive Pt Nanoparticles and Their Electrocatalytic Activity for Methanol Oxidation

Libin Wang,<sup>1,2</sup> Wenjun Xu,<sup>1</sup> Xiao Wu,<sup>1</sup> Qian Li,<sup>1</sup> Zhiming Wang,<sup>1</sup> and Xiuwen Zheng<sup>1,2</sup>

<sup>1</sup> School of Chemistry and Chemical Engineering, Linyi University, Linyi 276000, China

<sup>2</sup> Key Laboratory of Resources & Environmental Analytical Chemistry, University of Shandong, Linyi, Shandong 276000, China

Correspondence should be addressed to Libin Wang; wanglibin@lyu.edu.cn and Xiuwen Zheng; xwzheng1976@gmail.com

Received 15 November 2013; Accepted 13 April 2014; Published 4 May 2014

Academic Editor: Alireza Talebitahter

Copyright © 2014 Libin Wang et al. This is an open access article distributed under the Creative Commons Attribution License, which permits unrestricted use, distribution, and reproduction in any medium, provided the original work is properly cited.

High monodispersive Pt nanoparticles (NPs) have been prepared via two facile and environmentally-friendly procedures, either through a traditional solvothermal route (T-Pt NPs) or via a microwave-assisted route (M-Pt NPs). The transmission electron microscopy (TEM) shows the high Monodispersity for T-Pt NPs with the average diameter being ca.2.79 nm and the pod-like nanostructure for M-Pt NPs, which indicate the efficiency of both methods. An optimal choice of protocol allows reducing the reaction time from 2 hours (T-Pt NPs) to 20 minutes (M-Pt NPs). The electrocatalytic activities of as-prepared Pt NPs were investigated by cyclic voltammetry, showing very high catalytic activity for a methanol oxidation reaction.

## 1. Introduction

Recently, synthesis of platinum NPs with controlled sizes and shapes has stimulated extensive research owing to its unusual physical and chemical properties in developing highly active Pt NPs for fuel cell reactions [1, 2], bioimaging [3], chemical sensors [4], drug carrier for drug delivery systems (DDS) [5], and so forth. Because of the high surface area, a large number of edges and corner atoms for Pt NPs, it is generally accepted that both catalytic efficiency and selectivity are highly dependent on the size and shape of the platinum material [6–8]. For instance, due to the high surface area and enough absorption sites, the three-dimensional (3D) dendritic platinum display high active as nanoelectrocatalyst for the reduction of dioxygen and oxidation of methanol [9]. Both Pt cubic nanoboxes and hollow spheres exist higher activity than their solid particles in oxygen reduction reaction or methanol oxidation reaction, indicating a strong shape-dependent catalytic property [2, 10]. Therefore, it is imperative to develop synthetic routes to prepare nonagglomerated, uniform Pt NPs with a well-controlled size and a narrow size distribution. Up to date, serials methods have been developed to synthesize Pt NPs with desired

morphologies in cube [2, 5], multioctahedral [11], dendritic [12], flower [13], and one-dimensional nanostructure [14]. Recently, the mesoporous structure of Pt NPs becomes one of the hot research topics and obtains considerable progresses by Yamauchi group [15–17]. And also, serials of alloy or core-shell Pt NPs have also been synthesized [18, 19]. Despite this, developing a reliable, facile, and environmentally-friendly strategy for the production of high monodispersive Pt NPs still remains a challenge.

Herein, two facile and environmentally-friendly procedures were proposed to synthesize high monodispersive Pt NPs, either through a traditional solvothermal route (T-Pt NPs) or via a microwave-assisted route (M-Pt NPs). Microwave-assisted synthesis is a relatively new chemical method to accelerate chemical reactions, which have been widely applied in the nanomaterials preparation [20–23]. The use of the microwave-assisted route has several advantages over other existing methods in terms of energy efficiency and shorter reaction time from hours to minutes. Compared to the previous polyol synthesis route, the water-based system can provide a more environmentally benign route to the synthesis of Pt NPs, because it does not involve toxic organic solvents.

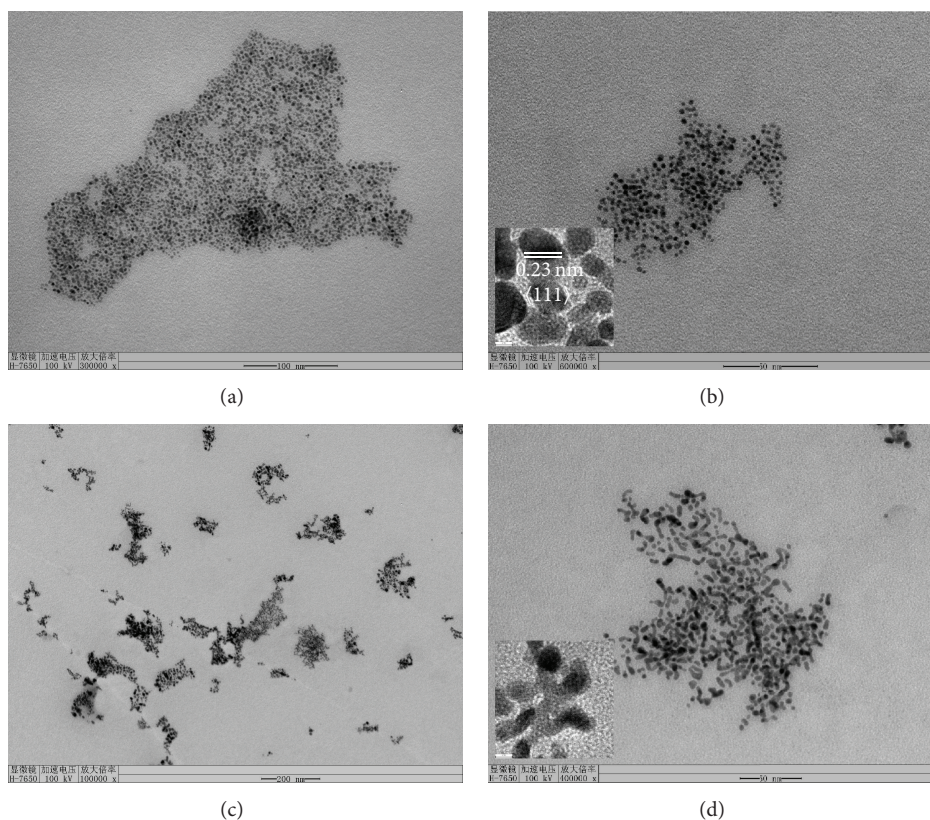


FIGURE 1: TEM images of as-prepared Pt NPs with different magnification for (a-b) T-Pt NPs and (c-d) M-Pt NPs.

## 2. Experimental Section

In a typical synthesis, PVP (~0.0025 mmol) was completely dispersed into 15 mL distilled water with the assistance of ultrasound irradiation. After that,  $\text{H}_2\text{PtCl}_6 \cdot 6\text{H}_2\text{O}$  dispersed in ethylene glycol (EG) solution (7 mL,  $9.65 \times 10^{-6}$  mol/mL) was added into the aforementioned aqueous solution under the sonication. For solvothermal route, the mixed solution was loaded into the 50 mL Teflon lined autoclave, which was maintained at  $200^\circ\text{C}$  for 2 h. For microwave-assisted route, the microwave-assisted reactions were carried out in a focused single-mode microwave synthesis system (Discover, CEM, 2.45 GHz, 300 W). Reactions at elevated pressure and temperature were performed in 10 mL vial, and the temperature was accurately controlled by automatic adjusting of microwave power at  $200^\circ\text{C}$  for 20 min. After reactions, the products were cooled down to room temperature. The final products were collected by centrifugation, washed several times with water and ethanol, and dried at  $50^\circ\text{C}$  under vacuum condition. The samples are designated as T-Pt NPs for solvothermal procedures and M-Pt NPs for microwave-assisted reaction.

The morphology and composition of the products were analyzed by transmission electron microscopy (TEM) and X-ray powder diffraction patterns (XRD), which were conducted on an H-7650 and Bruker D8 ADVANCE X-ray powder diffractometer with GADDS HTS and  $\text{Cu K}\alpha$  radiation ( $\lambda = 0.154184$  nm). Electrochemical measurements are per-

formed on an Epsilon/100BWBAS electrochemical working system. A glassy carbon electrode modified with Pt NPs is employed as working electrode. A platinum foil is served as the counter electrode and a saturated calomel electrode (SCE) is used as the reference electrode.

## 3. Results and Discussion

Figures 1(a) and 1(b) are the typical TEM images for T-Pt NPs with different magnification, indicating the high monodispersity for as-prepared products. Inserted is the high resolution TEM (HRTEM) image of a single Pt NPs, displaying a single crystal nature for T-Pt NPs. The fringes with lattice spacing of 0.23 nm can be indexed as {111} of face-centered cubic (fcc) Pt. Figures 1(c) and 1(d) are the TEM images for M-Pt NPs, showing the pod-like nanostructure. A few NPs display the multiarm nanostructure. HRTEM studies (Figure 1(d), inserted) show that these nanoparticles have lattice fringes of 0.23 nm, corresponding to the interplane distance of {111} planes in fcc-Pt. The crystalline nature of the Pt nanoparticles suggests that these nanocrystals were formed through an overgrowth mechanism rather than the random aggregation of small nanocrystals [10], which is due to the rapid heating and shorter reaction time function of microwave irradiation. The mean diameter for T-Pt NPs is 2.79 nm (Figure 2(a)), which is consistent with the HRTEM results (Figure 1(b), inserted). Based on Figure 1,

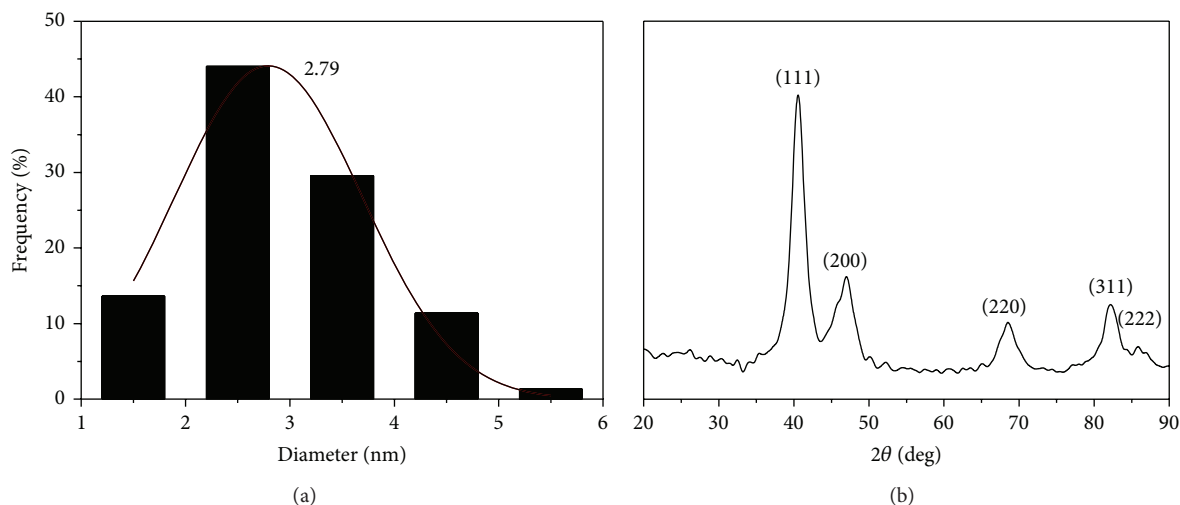


FIGURE 2: (a) The statistical result of size distribution for T-Pt NPs, (b) XRD pattern for as-prepared T-Pt NPs.

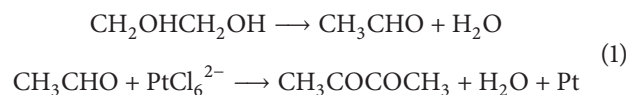
one could find that both the traditional solvothermal route and microwave-assisted route are effective routes for the synthesis of high monodisperse Pt nanoparticles via the given experimental conditions. However, for microwave-assisted route, the reaction time was reduced from 2 hours (T-Pt NPs) to 20 minutes (M-Pt NPs), indicating the reduced energy consumption. The XRD pattern of as-prepared Pt NPs is shown in Figure 2(b). The diffraction peaks at 39.8, 46.2, 67.5, 81.3, and 85.88 can be assigned to reflections from the (111), (200), (220), (311), and (222) planes of the face-centered cubic (fcc) Pt. The average size of the Pt NPs is 3.1 nm, calculated by the Debye-Scherrer formula on the basis of the Pt (111) plane, which coincides with the result from the Pt NPs size distribution histogram in the error (Figure 2(a)).

In the water-based system, contrast experiments were carried out in detail to obtain universal protocols for high monodisperse Pt NPs. Keeping the other experimental conditions constant, it is not easy to obtain the ideal result using sodium oleate instead of PVP. However, high monodisperse Pt NPs could be obtained using ascorbic acid as reducing agent at appropriate sodium oleate concentration. For this system,  $\text{H}_2\text{PtCl}_6 \cdot 6\text{H}_2\text{O}$  was firstly dispersed in distilled water rather than EG solution ( $9.65 \times 10^{-6}$  mol/mL). At optimal conditions ( $2.7 \times 10^{-5}$  mol/mL for sodium oleate,  $6.7 \times 10^{-7}$  mol/mL for ascorbic acid), both samples show high monodisperse nature with average ca. 3 nm for T-Pt (Figures 3(a) and 3(b)) NPs and ca. 2.4 nm for M-Pt NPs (Figures 3(c) and 3(d)), respectively. Based on Figure 3, one could see that there is no obvious difference for the as-prepared Pt NPs via the solvothermal (T-Pt NPs) and microwave-assisted routes. In order to further understand the influence of concentration of surfactants on Pt NPs growth, the process was carried out with different sodium oleate concentrations. It is found that the aggregative Pt NPs (not shown here) could be obtained if the surfactant concentration was decreased down to  $2.7 \times 10^{-6}$  mol/mL.

Electrocatalytic activity of the Pt NPs toward methanol oxidation reaction (MOR) was studied by cyclic voltammetry in a nitrogen-saturated 0.5 M  $\text{CH}_3\text{OH}$ -0.5 M  $\text{H}_2\text{SO}_4$  solution

at a scan rate of  $50 \text{ mV s}^{-1}$ , and the CV curves are shown in Figure 4. Line a is the cure on behalf of the bare glassy carbon electrode in 0.5 M  $\text{H}_2\text{SO}_4$  solution. Line b is representative of bare glassy carbon electrode in 0.5 M  $\text{H}_2\text{SO}_4$  and 0.5 M  $\text{CH}_3\text{OH}$  mixed solution. Line c stands for Pt NPs modified glassy carbon electrode in 0.5 M  $\text{H}_2\text{SO}_4$  and 0.5 M  $\text{CH}_3\text{OH}$  mixed solution. Compared with lines a and b, it can be seen from line c that there is a strong peak at 0.68 V, which is the oxidation peak of  $\text{CH}_3\text{OH}$  oxidized to  $\text{HCHO}$ . The peak at 0.39 V should be primarily attributed to the removal of the residual carbon species, such as  $\text{CO}_{\text{ads}}$ , formed in the forward scan. The peak ratios between positive and negative scans are ca. 1.8, indicating relatively complete oxidation of methanol to carbon dioxide [24]. All these results confirmed the high catalytic activity of as-prepared Pt NPs for MOR.

Here, the efficiencies of two methods of synthesizing monodisperse Pt NPs are compared using the ethylene glycol as reducing agent, either through a traditional solvothermal procedure or via microwave-assisted method. It is well known that microwave irradiation provides rapid and uniform heating of reagents, solvents, and intermediates. This rapid MW heating also provides uniform nucleation and growth conditions, leading to homogeneous nanomaterials with smaller sizes [20–23]. In the polyol reactions, EG was as a sacrificial reductant of Pt ions according to the following mechanism [25]:



Firstly, EG was rapidly changed into  $\text{CH}_3\text{CHO}$  up to given temperature; simultaneously the Pt metallic ions are reduced to metallic Pt NPs by  $\text{CH}_3\text{CHO}$ .

#### 4. Conclusion

A universal water-based protocol was developed to synthesize high monodisperse Pt NPs with spherical or pod-like shape, using a traditional solvothermal route or via a

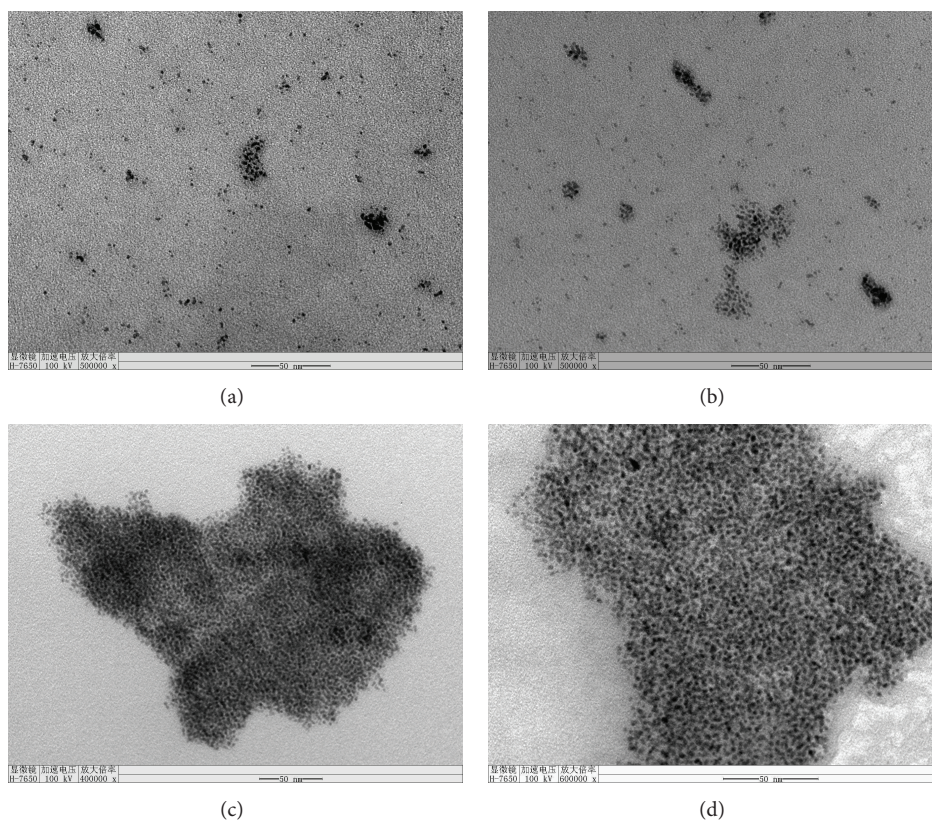


FIGURE 3: TEM images of as-prepared Pt NPs with different magnification for (a-b) M-Pt NPs and (c-d) T-Pt NPs using sodium oleate as surfactant and ascorbic acid as reducing agent.

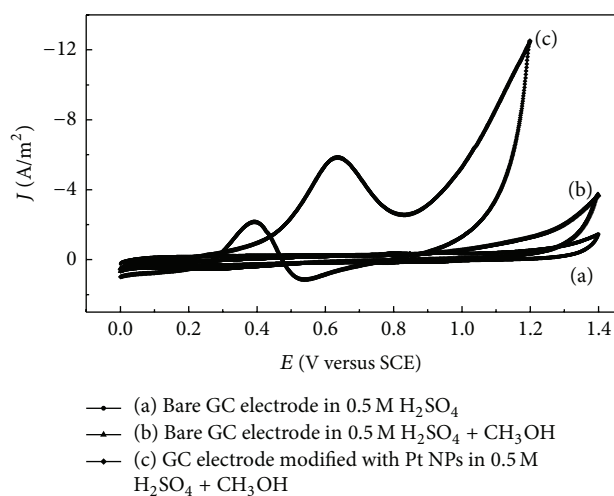


FIGURE 4: CVs of the Pt NPs (the potential was applied with a scanning rate of  $50 \text{ mVs}^{-1}$ ).

microwave-assisted route. Due to the rapid heating from microwave irradiation, the overgrowth of Pt nanocrystals results in the pod-like morphology for M-Pt NPs. However, the microwave-assisted route is the more efficient method to overcome tedious and time-consuming process and reduces the reaction time from several hours to several minutes. CVs confirmed the high catalytic activity of as-prepared Pt NPs for MOR.

## Conflict of Interests

The authors declare that there is no conflict of interests regarding the publication of this paper.

## Acknowledgment

This work was supported by the National Natural Science Foundation of China (nos. 21101087, 21375057, and 21205057) and Shandong Province Natural Science Foundation (no. ZR2010BQ030).

## References

- [1] Y. J. Kang, J. B. Pyo, X. C. Ye, T. R. Gordon, and C. B. Murray, "Synthesis, shape control, and methanol electro-oxidation properties of Pt-Zn alloy and Pt<sub>3</sub>Zn intermetallic nanocrystals," *ACS Nano*, vol. 6, pp. 5642–5647, 2012.
- [2] Z. M. Peng, H. J. You, J. B. Wu, and H. Yang, "Electrochemical synthesis and catalytic property of sub-10 nm platinum cubic nanoboxes," *Nano Letters*, vol. 10, pp. 1492–1496, 2010.
- [3] S.-I. Tanaka, J. Miyazaki, D. K. Tiwari, T. Jin, and Y. Inouye, "Fluorescent platinum nanoclusters: synthesis, purification, characterization, and application to bioimaging," *Angewandte Chemie*, vol. 50, no. 2, pp. 431–435, 2011.
- [4] S. Guo, D. Wen, Y. Zhai, S. Dong, and E. Wang, "Platinum nanoparticle ensemble-on-graphene hybrid nanosheet: one-pot, rapid synthesis, and used as new electrode material for electrochemical sensing," *ACS Nano*, vol. 4, no. 7, pp. 3959–3968, 2010.

- [5] C. Y. Hong, Y. Yamauchi, and K. C. W. Wu, "In vitro cytotoxicity and intracellular bioimaging of dendritic platinum nanoparticles by differential interference contrast (DIC)," *Chemistry Letters*, vol. 40, pp. 408–409, 2011.
- [6] M. N. Mankin, V. Mazumder, and S. Sun, "One-pot synthesis of Pt nanocubes and nanopods via burst nucleation and controlled secondary growth," *Chemistry of Materials*, vol. 23, no. 2, pp. 132–136, 2011.
- [7] C. Wang, H. Daimon, T. Onodera, T. Koda, and S. Sun, "A general approach to the size- and shape-controlled synthesis of platinum nanoparticles and their catalytic reduction of oxygen," *Angewandte Chemie*, vol. 47, no. 19, pp. 3588–3591, 2008.
- [8] C. Koenigsmann, W.-P. Zhou, R. R. Adzic, E. Sutter, and S. S. Wong, "Size-dependent enhancement of electrocatalytic performance in relatively defect-free, processed ultrathin platinum nanowires," *Nano Letters*, vol. 10, no. 8, pp. 2806–2811, 2010.
- [9] L. Wang and Y. Yamauchi, "Facile synthesis of three-dimensional dendritic platinum nanoelectrocatalyst," *Chemistry of Materials*, vol. 21, no. 15, pp. 3562–3569, 2009.
- [10] S. J. Guo, S. J. Dong, and E. Wang, "A general method for the rapid synthesis of hollow metallic or bimetallic nanoelectrocatalysts with urchinlike morphology," *Chemistry*, vol. 14, pp. 4689–4695, 2008.
- [11] B. Lim, X. Lu, M. Jiang et al., "Facile synthesis of highly faceted multioctahedral Pt nanocrystals through controlled overgrowth," *Nano Letters*, vol. 8, no. 11, pp. 4043–4047, 2008.
- [12] L. Wang, H. Wang, Y. Nemoto, and Y. Yamauchi, "Rapid and efficient synthesis of platinum nanodendrites with high surface area by chemical reduction with formic acid," *Chemistry of Materials*, vol. 22, no. 9, pp. 2835–2841, 2010.
- [13] J. N. Tiwari, F.-M. Pan, and K.-L. Lin, "Facile approach to the synthesis of 3D platinum nanoflowers and their electrochemical characteristics," *New Journal of Chemistry*, vol. 33, no. 7, pp. 1482–1485, 2009.
- [14] L. C. Liu, S. H. Yoo, and S. Park, "Synthesis of vertically aligned hollow platinum nanotubes with single crystalline nanoflakes," *Chemistry of Materials*, vol. 22, pp. 2681–2684, 2010.
- [15] Y. Yamauchi, "Field-Induced alignment controls of one-dimensional mesochannels in mesoporous materials," *Journal of the Ceramic Society of Japan*, vol. 121, no. 1417, pp. 831–840, 2013.
- [16] H. Wang, H. Y. Jeong, M. Imura et al., "Shape- and size-controlled synthesis in hard templates: sophisticated chemical reduction for mesoporous monocrystalline platinum nanoparticles," *Journal of the American Chemical Society*, vol. 133, no. 37, pp. 14526–14529, 2011.
- [17] H. J. Wang, L. Wang, T. Sato et al., "Synthesis of mesoporous Pt films with tunable pore sizes from aqueous surfactant solutions," *Chemistry of Materials*, vol. 24, pp. 1591–1598, 2012.
- [18] C. L. Li and Y. Yamauchi, "Facile solution synthesis of Ag@Pt core-shell nanoparticles with dendritic Pt shells," *Physical Chemistry Chemical Physics*, vol. 15, pp. 3490–3496, 2013.
- [19] L. Wang and Y. Yamauchi, "Controlled aqueous solution synthesis of platinum-palladium alloy nanodendrites with various compositions using amphiphilic triblock copolymers," *Chemistry*, vol. 5, no. 12, pp. 2493–2498, 2010.
- [20] X. W. Zheng, Q. T. Hu, and C. H. Sun, "Efficient rapid microwave-assisted route to synthesize InP micrometer hollow spheres," *Materials Research Bulletin*, vol. 44, pp. 216–219, 2009.
- [21] R. Eluri and B. Paul, "Microwave assisted greener synthesis of nickel nanoparticles using sodium hypophosphite," *Materials Letters*, vol. 76, pp. 36–39, 2012.
- [22] K. D. Bhatte, D. N. Sawant, R. A. Watile, and B. M. Bhanage, "A rapid, one step microwave assisted synthesis of nanosize zinc oxide," *Materials Letters*, vol. 69, pp. 66–68, 2012.
- [23] H. Wang, L. Wang, Y. Nemoto, N. Suzuki, and Y. Yamauchi, "Microwave-assisted rapid synthesis of platinum nanoclusters with high surface area," *Journal of Nanoscience and Nanotechnology*, vol. 10, no. 10, pp. 6489–6494, 2010.
- [24] Y. Lin, X. Cui, C. H. Yen, and C. M. Wai, "PtRu/carbon nanotube nanocomposite synthesized in supercritical fluid: a novel electrocatalyst for direct methanol fuel cells," *Langmuir*, vol. 21, no. 24, pp. 11474–11479, 2005.
- [25] R. Harpeness and A. Gedanken, "Microwave synthesis of core-shell gold/palladium bimetallic nanoparticles," *Langmuir*, vol. 20, no. 8, pp. 3431–3434, 2004.

## Research Article

# Radiolytic Preparation of Electrocatalysts with Pt-Co and Pt-Sn Nanoparticles for a Proton Exchange Membrane Fuel Cell

Sang Kyum Kim,<sup>1</sup> Ji Yun Park,<sup>2</sup> Soon Choel Hwang,<sup>1</sup> Do Kyun Lee,<sup>2</sup> Sang Heon Lee,<sup>2</sup> Moon Hee Han,<sup>1</sup> and Young Woo Rhee<sup>1</sup>

<sup>1</sup> Graduate School of Energy Science and Technology, Chungnam National University, 99 Daehak-ro, Yuseong-gu, Daejeon 305-764, Republic of Korea

<sup>2</sup> Department of Applied Chemistry and Biological Engineering, Chungnam National University, Daejeon 305-764, Republic of Korea

Correspondence should be addressed to Young Woo Rhee; ywrhee@cnu.ac.kr

Received 30 December 2013; Accepted 10 April 2014; Published 4 May 2014

Academic Editor: Ajay Soni

Copyright © 2014 Sang Kyum Kim et al. This is an open access article distributed under the Creative Commons Attribution License, which permits unrestricted use, distribution, and reproduction in any medium, provided the original work is properly cited.

Nanosized Pt-Sn/VC and Pt-Co/VC electrocatalysts were prepared by a one-step radiation-induced reduction (30 kGy) process using distilled water as the solvent and Vulcan XC72 as the supporting material. While the Pt-Co/VC electrodes were compared with Pt/VC (40 wt%, HiSpec 4000), in terms of their electrocatalytic activity towards the oxidation of H<sub>2</sub>, the Pt-Co/VC electrodes were evaluated in terms of their activity towards the hydrogen oxidation reaction (HOR) and compared with Pt/VC (40 wt%, HiSpec 4000), Pt-Co/VC, and Pt-Sn/VC in a single cell. Additionally, the prepared electrocatalyst samples (Pt-Co/VC and Pt-Sn/VC) were characterized by transmission electron microscopy (TEM), scanning electron microscope (SEM), thermogravimetric analysis (TGA), X-ray diffraction (XRD), X-ray photoelectron spectroscopy (XPS), electrochemical surface area (ECSA), and fuel cell polarization performance.

## 1. Introduction

Fuel cells have garnered global attention in recent decades due to their high efficiency and environmental compatibility [1, 2]. Among various types of fuel cells, proton exchange membrane fuel cells (PEMFC) have shown great promise as an alternative source of power generation for transportation applications due to their low operating temperature, fast startup, high power density, and low emission of pollutants [1–5]. However, to make PEMFCs commercially viable, some technical and economical challenges have to be overcome, including the poor kinetics of the anodic reaction, the complicated catalyst loading process, and the high cost of electrocatalysts [6–9].

In a standard H<sub>2</sub> fuel cell, the PEMFC anode catalyst facilitates the following hydrogen oxidation reaction (HOR):



Currently, the best electrocatalyst for the HOR is platinum (Pt). The extremely high activity of Pt is believed to be

due to the nearly optimal bonding affinity that exists between Pt and hydrogen. The bonding is strong enough to promote facile absorption of H<sub>2</sub> from the gas phase onto a Pt surface and the subsequent electron transfer, but the bonding is weak enough to allow desorption of the resultant H<sup>+</sup> ion into the electrolyte [10–14]. In contrast, the bond between H<sub>2</sub> and metals like W, Mo, Nb, and Ta is too strong, resulting in a stable hydride phase. On the other hand, the bond between H<sub>2</sub> and metals like Co, Pb, Sn, Zn, Ag, Cu, and Au is too weak, resulting in little or no absorption [15–21].

Although Pt is expensive, it proves to be an exceptionally effective catalyst for the HOR. Using the well-developed Pt/VC catalyst approach, whereby ultrasmall (2–3 nm) Pt particles are supported on a high-surface-area carbon powder, only an extremely small amount of Pt catalyst is required. Thus, typical Pt loadings in PEMFC anodes have been successfully reduced to around 0.05 mg Pt/cm<sup>2</sup>. At these levels, the anode Pt catalyst expense is relatively modest compared to the expense associated with other components in the fuel cell. For example, a 50 kW automotive fuel cell stack,

operating at a power density of  $1.0 \text{ W/cm}^2$ , would require about 2.5 grams of Pt for the anode catalyst. At a price of \$42/g, this represents a Pt material cost of approximately \$100 [1–3, 14, 16].

In this study, we prepared the Pt-Co/VC (Vulcan XC72) and Pt-Sn/VC electrocatalysts by one-step radiation-induced reduction. The obtained electrocatalysts have overcome the disadvantages of the PEMFC (e.g., high cost and a weak bond with  $\text{H}_2$ ). Pt-Co/VC and Pt-Sn/VC electrocatalysts were then characterized by transmission electron microscopy (TEM), scanning electron microscope-energy dispersive spectroscopic (SEM-EDS), thermogravimetric analysis (TGA), X-ray diffraction (XRD), X-ray photoelectron spectroscopy (XPS), electrochemical surface area (ECSA), and fuel cell polarization performance [17, 18].

## 2. Experimental

**2.1. Chemicals.** In this experiment, the  $\text{H}_2\text{PtCl}_6 \cdot \text{H}_2\text{O}$  (37.5% Pt),  $\text{CoCl}_2 \cdot \text{H}_2\text{O}$  (47.4% Co), and  $\text{SnCl}_2 \cdot \text{H}_2\text{O}$  (52.0% Sn) were of analytical reagent grade (Sigma-Aldrich, USA) and were used without further purification. Carbon black (Vulcan XC72) was purchased from CABOT Co., Ltd. (USA). Nafion (perfluorinated ion-exchange resin, 5% (w/v) solution in a solution of 90% aliphatic alcohol/10% water mixture) was also purchased from Sigma-Aldrich (USA). Solutions for the experiments were prepared with water purified in an aquaMAX-Basic 360 series plus water purification system (YL Instruments Co., Ltd., Korea). The final resistance of the water was  $18.2 \text{ M}\Omega\text{cm}^{-1}$  and the solutions were degassed prior to each measurement. The other chemicals used in the experiment were of reagent grade.

**2.2. One-Step Preparation of Electrocatalysts by Radiation-Induced Reduction.** First, VC (Vulcan XC72) was purified to remove the noncrystallized carbon impurities. VC was treated with a mixture of  $\text{H}_2\text{SO}_4/\text{H}_2\text{O}$  (2:8 vol%) and, in the process, VC was purified. The purified VC was used as the supporting material for deposition of the catalysts. The Pt-Co/VC catalyst was prepared as follows:  $\text{H}_2\text{PtCl}_6 \cdot \text{H}_2\text{O}$  (0.43 g) and  $\text{CoCl}_2 \cdot \text{H}_2\text{O}$  (0.37 g) were dissolved in a mixture of deionized water (188 mL) and 2-propanol (12.0 mL) was added as a radical scavenger. Next, 1.0 g of the purified VC support was added to the previously mentioned solution. The PH of the reaction solution was adjusted to 10.0 using NaOH. Nitrogen was bubbled through the solution for 30 min to remove oxygen and then the solution was irradiated under atmospheric pressure and ambient temperature. A total irradiation dose of 30 kGy (dose rate =  $6.48 \times 10^5/\text{h}$ ) was applied. Pt-Co nanoparticle-deposited VC catalysts were precipitated after  $\gamma$ -irradiation. The Pt-Sn/VC electrocatalysts were prepared as described above. The molar ratios of the input metal ions are Pt-Co/VC (Pt/Co = 0.6/0.4) and Pt-Sn/VC (Pt/Sn = 0.6/0.4).

**2.3. Characterization of Electrocatalysts Surface.** The particle size and morphology of the electrocatalysts were analyzed by SEM-EDS images obtained with a Hitachi S-4800 microscope

operated at 30 kV. The HR-TEM images were obtained using a JEOL JEM-2100 microscope operated at 200 kV. The TGA of the PEM was made on the TA instruments of the TGA S-1000 model with a heating rate of  $10^\circ\text{C}/\text{min}$ , in a temperature range of  $0\text{--}800^\circ\text{C}$ . XRD was conducted using a Japanese Rigaku D/max  $\gamma\text{A}$  XRD, equipped with graphite monochromatized  $\text{Cu K}\alpha$  radiation ( $\lambda = 0.15414 \text{ nm}$ ). The XPS analyses were carried out with a MultiLab 2000 (Thermo) XPS using a monochromated Al K $\alpha$  source under a base pressure of  $2.6 \times 10^{-9}$  torr.

**2.4. Characterization of Electrochemical Performance Measurement.** Electrochemical measurements were carried out at room temperature in a three-electrode cell connected to an electrochemical analysis. A glassy carbon, coated with a catalyst, was used as the working electrode. An Ag/AgCl electrode and a Pt electrode were used as a reference electrode and as a counter electrode, respectively. Unless otherwise stated, all potentials were relative to the Ag/AgCl. HOR activity tests can be conducted by cyclic voltammogram (CV). With the CV, the HOR was measured in oxygen-saturated  $0.5 \text{ M H}_2\text{SO}_4$  at  $25^\circ\text{C}$  with the scan rate of  $0.1 \text{ V s}^{-1}$ , in the potential ranging from  $-0.2 \text{ V}$  to  $+0.3 \text{ V}$ .

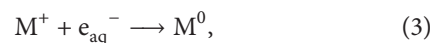
Single cells were constructed to evaluate the fuel cell polarization performance of the Pt-Co and Pt-Sn catalyst electrodes. Membrane electrode assembly (MEA), with an area of  $10 \text{ cm}^2$ , was used to construct a single cell, which had been fabricated by hot-pressing a pretreated Nafion 112 membrane (DuPont) between the anode and the cathode. The catalyst loadings were 0.2 mg of Pt at the cathode and 0.4 mg of Pt-Co, Pt-Sn at the anode. For all the tests, Pt (40 wt%)/VC (HiSpec 4000) was used as the anode catalyst. The catalyst inks were prepared in a mixture solution composed of an appropriate amount of DI water and the required amount of 5 wt% Nafion ionomer solution (Aldrich). The Nafion ionomer content was 20 wt% in the anode catalyst layer and 25 wt% in the cathode catalyst layer. The appropriate amount of catalyst inks was painted uniformly on Teflon-coated carbon paper (TGPH-090) and dried at  $80^\circ\text{C}$  overnight. Fuel cell polarization performance tests were conducted at  $60^\circ\text{C}$  with a WFCTS fuel cell test station.

## 3. Results and Discussion

Pt-M/VC catalysts were successfully prepared by a one-step radiation-induced reduction (RIR) process. Diverse papers have reported that the mechanism of RIR could be generally proven by the following equation [22–28]:



Among these, free radical ( $\text{H}^\bullet$ ) and solvated electrons ( $\text{e}_{\text{aq}}^-$ ) were used as strong reducing agents to reduce the metal ions up to the zero-valence state, as shown in



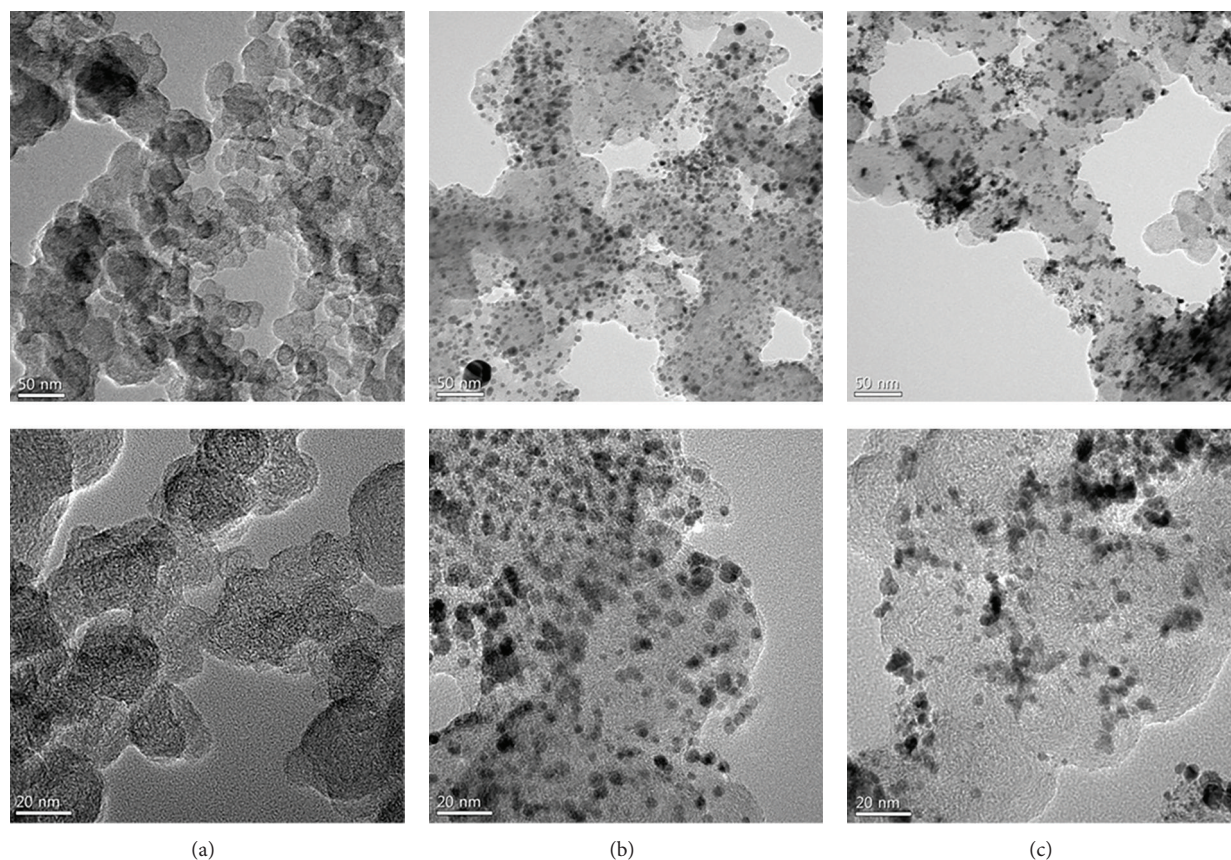
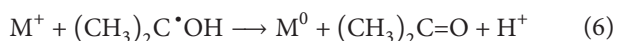
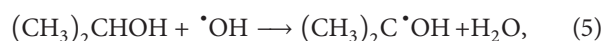


FIGURE 1: TEM image of original VC (a), Pt-Co/VC (b), and Pt-Sn/VC (c) prepared by RIR.

Similarly, multivalent ions, such as  $\text{Pt}^{4+}$ ,  $\text{Co}^{2+}$ , and  $\text{Sn}^{2+}$ , are reduced by a multistep reaction. On the other hand, the hydroxyl radical ( $\text{OH}^{\bullet}$ ) has a high oxidizing capacity and metal atoms and ions can be oxidized by hydroxyl radical. In order to protect the oxidizing agent ( $\text{OH}^{\bullet}$ ), 2-propanol was added to the reaction solution. The  $\text{OH}^{\bullet}$  radical reacted with 2-propanol, as shown in (5). As a result, the metal ion was then reduced to a zero-valence metal atom by 2-propanol radical, as shown in (6):



Similar to the findings of Choi et al. [24, 26, 28], various metal and vinyl monomers were grafted onto the surface of MWNT via trapped radicals. The results showed that RIR was an effective metal deposition method on the surface of the VC-supported electrocatalysts.

Figure 1 shows the HR-TEM images of the VC-supported electrocatalysts prepared by one-step radiation reaction. They are (a) purified VC, (b) Pt-Co/VC, and (c) Pt-Sn/VC catalysts, respectively. As shown in Figure 1(a), there are no metallic nanoparticles on the surface of the VC. Figures 1(b) and 1(c) show that the HR-TEM images of the Pt-M/VC ( $\text{M} = \text{Co}, \text{Sn}$ ) catalyst clearly provide evidence for more deposition of Pt-M alloy nanoparticles on the surface of VC composites

compared to the surface of pristine VC. The mean particle size of the metallic nanoparticles was in 10 nm under.

Figure 2 shows SEM images of the VC-supported electrocatalysts prepared by one-step radiation reaction. They are (a) Pt-Co/VC and (b) Pt-Sn/VC catalysts, respectively. As shown in Figures 2(a) and 2(b), the SEM images of the Pt-M/VC catalyst clearly provide evidence for more deposition of Pt-M alloy nanoparticles on the surface of the VC composites compared to the surface of the pristine VC. The mean particle size of the metallic nanoparticles were 10 nm under. This also indicates that the RIR is capable of preparing a stoichiometric Pt-M/VC electrocatalyst.

Although various strategies were used for synthesis of the Pt-Co/VC and Pt-Sn/VC catalysts, the TGA data shown in Figure 3 reveals that the actual metal loadings in all the Pt-Co/VC and Pt-Sn/VC electrocatalysts are very close to the normal value of 57~62 wt%. This suggests that Pt-Co/VC and Pt-Sn/VC of the synthesis strategies are efficient for preparation of high metal loading Pt-M catalysts [29].

Figure 4 shows the XRD patterns for the Pt-Co/VC and Pt-Sn/VC electrocatalysts prepared by one-step radiation-induced reduction. The Pt-Co/VC and Pt-Sn/VC electrocatalysts exhibit characteristics of a Pt face-centered cubic (fcc) structure [29, 30]. The average particle sizes were calculated using a Debye-Scherrer equation from the broadening of the Pt (220) reflection [27, 28] as ca. 2.8 nm and 3.7 nm

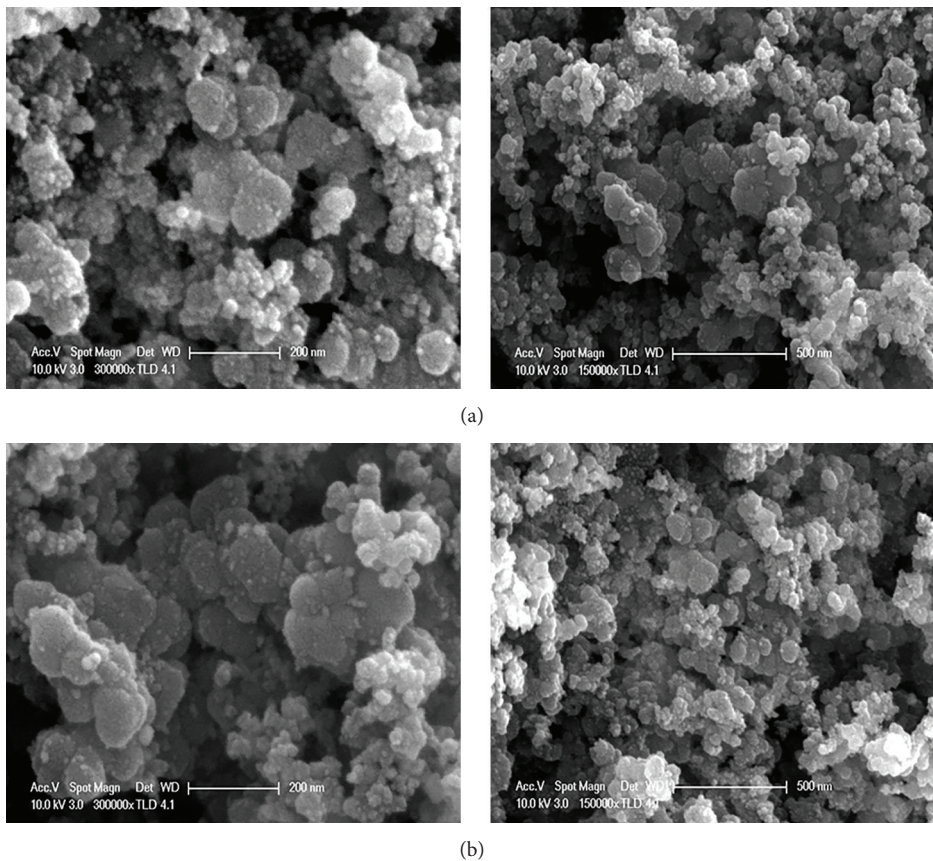


FIGURE 2: SEM images of the Pt-Co/VC and Pt-Sn/VC prepared by RIR.

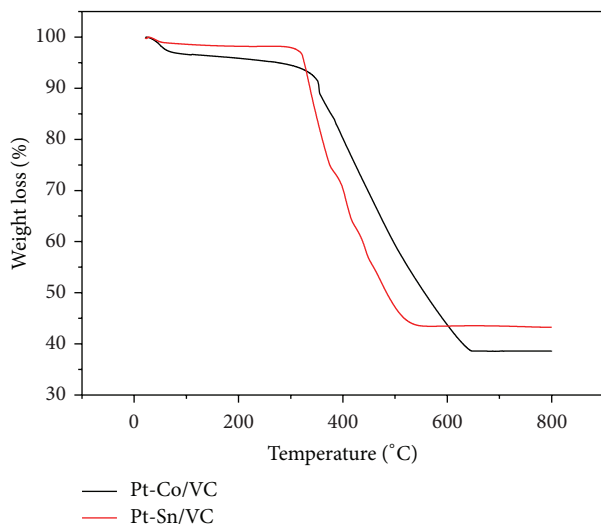


FIGURE 3: TGA data of Pt-Co/VC and Pt-Sn/VC by RIR.

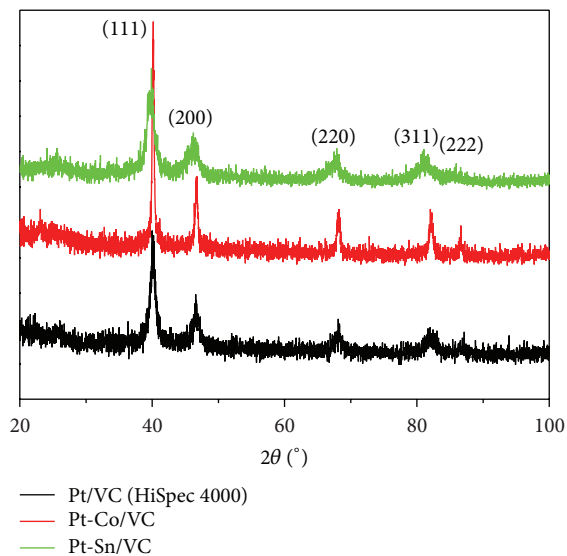


FIGURE 4: X-ray diffraction patterns of Pt/VC, Pt-Co/VC, and Pt-Sn/VC by RIR.

for Pt-Co/VC and Pt-Sn/VC, respectively. The particle sizes calculated from the XRD data for Pt-Co nanoparticles are generally in good agreement with the randomly measured particle sizes from the HR-TEM and HR-SEM images shown in Figures 1 and 2.

As shown in Figure 5, the XPS data was employed to analyze the valence state and the surface composition of the metal catalyst nanoparticles. Figures 5(b) shows the Cls,

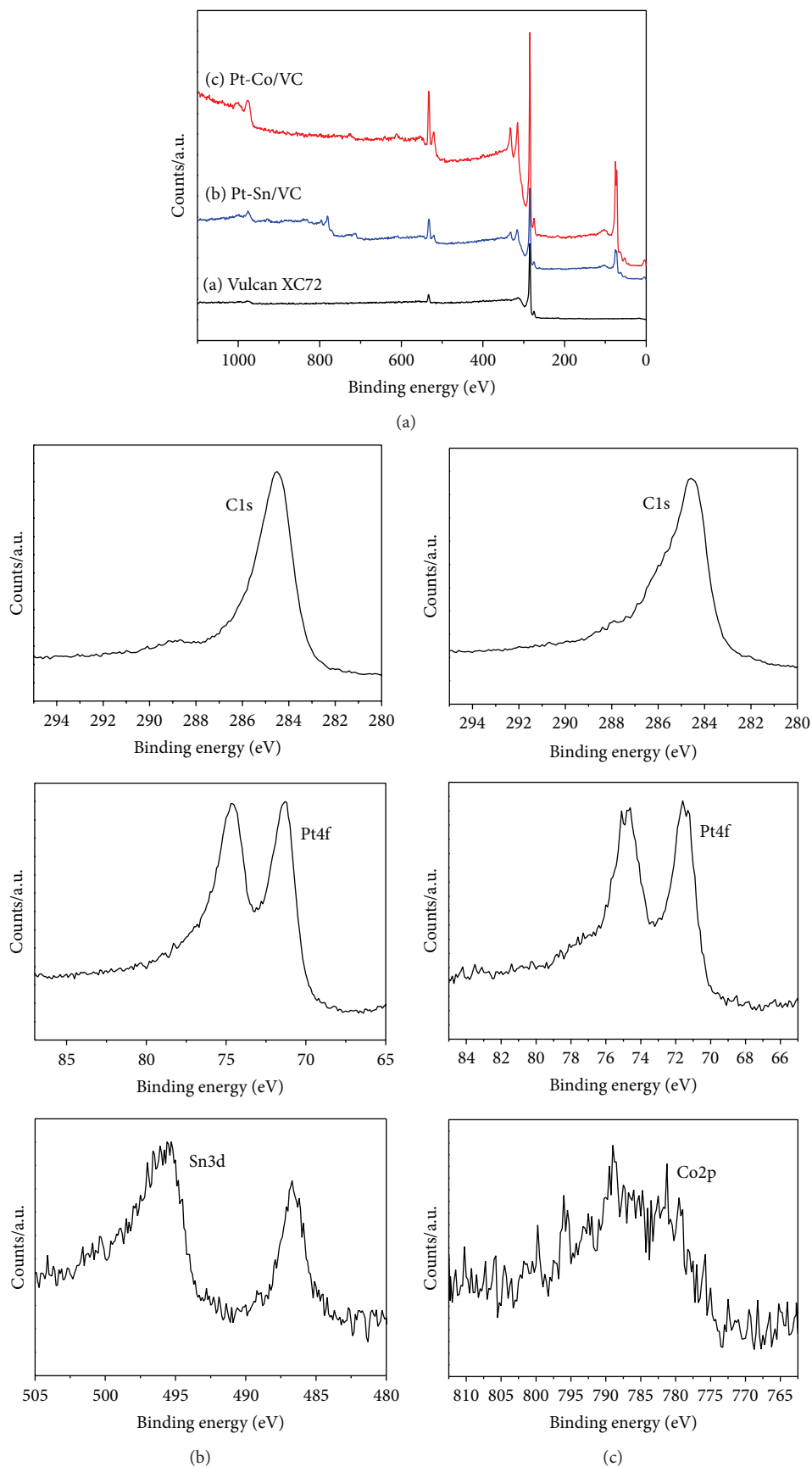


FIGURE 5: XPS spectra of original VC (a), Pt-Sn/VC (b), and Pt-Co/VC (c) by RIR.

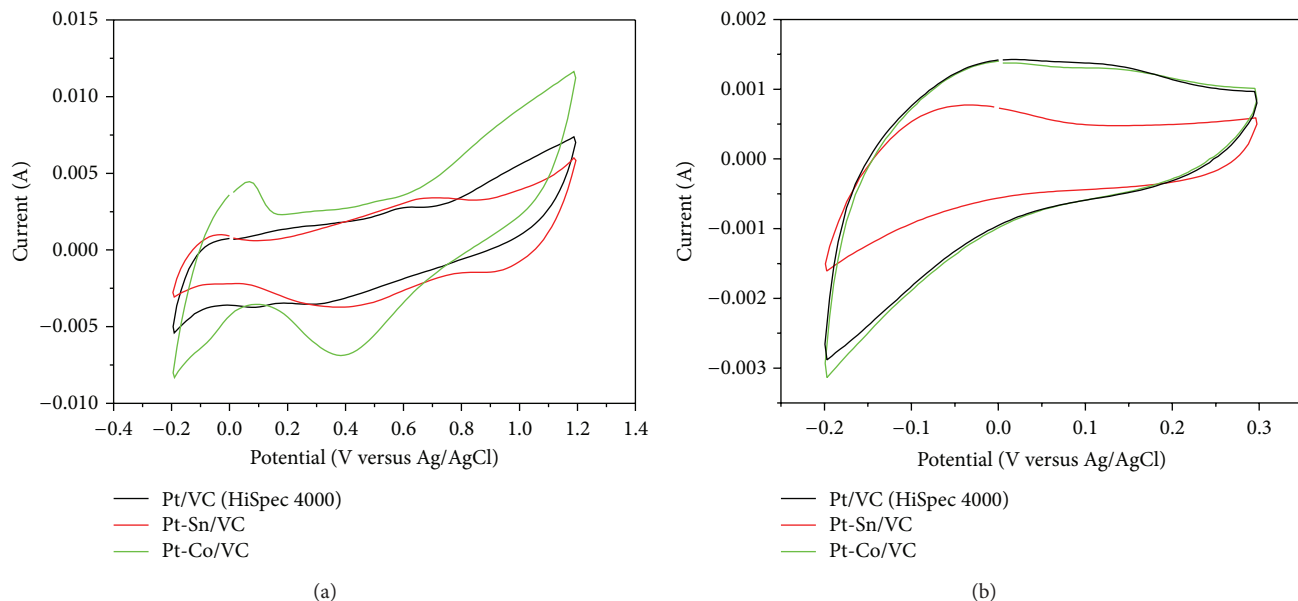


FIGURE 6: Cyclic voltammograms of the Pt-Co/C, Pt-Sn/VC, and Pt/VC (HiSpec 4000) electrodes in 0.5 M  $\text{H}_2\text{SO}_4$ ; room temperature, scan rate 0.1 V/s.

Pt4f, and Sn3d peaks of the commercial Pt-Sn/VC catalysts prepared by RIR methods, respectively. The Cls peaks appear at 285 eV. The Pt4f peaks and Sn3d of the Pt-Sn/VC appear at 74, 71 eV, and 496 eV respectively. Figures 5(b) shows the Cls, Pt4f, and Co2P peaks of the commercial Pt-Sn/VC catalysts. The Pt4f peaks and the Co2p of the Pt-Co/VC appear at 74, 71 eV, and 785 eV, respectively [31–33]. As a result, the Pt-Co and Pt-Sn were successfully deposited onto the VC-supported electrocatalyst by RIR.

Catalyst utilization efficiency is a very crucial factor which reflects the properties of catalysts, which is generally determined by dividing the electrochemical active surface area (ECSA) by the chemical surface area (CSA). Electrochemical surface area (ECSA) represents intrinsic electrocatalytic activity of electrocatalysts. The ECSA can be estimated from the integrated charge (after subtraction of capacitance contribution) in the hydrogen adsorption region of the steady-state CV in 0.5 mol  $\text{H}_2\text{SO}_4$  under  $\text{N}_2$  atmosphere, based on a monolayer hydrogen adsorption charge of  $0.2 \text{ mC/cm}^2$  on crystalline Pt, Pt-Co, and Pt-Sn. Well-defined hydrogen adsorption/desorption characteristics were observed for Pt-M/VC electrocatalysts.

Figure 6 shows the cyclic voltammograms (CV) curves of the Pt/C (HiSpec 4000), Pt-Co/VC, and Pt-Sn/VC electrocatalysts in 0.5 M  $\text{H}_2\text{SO}_4$  at room temperature under  $\text{N}_2$  atmosphere for the ECSA. The measured ECSA for the Pt-Co/VC was found to be  $92 \text{ m}^2 \text{ g}^{-1}$ , which is much higher than the measured ECSA of Pt-Sn/VC and Pt/C (HiSpec 4000), which were  $67 \text{ m}^2 \text{ g}^{-1}$  and  $72 \text{ m}^2 \text{ g}^{-1}$ , respectively. Compared with Pt/VC and Pt-Sn/VC catalysts, higher ECSA for the Pt-Co/VC catalysts suggests better utilization efficiency due to smaller Pt-Co nanoparticles and better particle distribution [34–36].

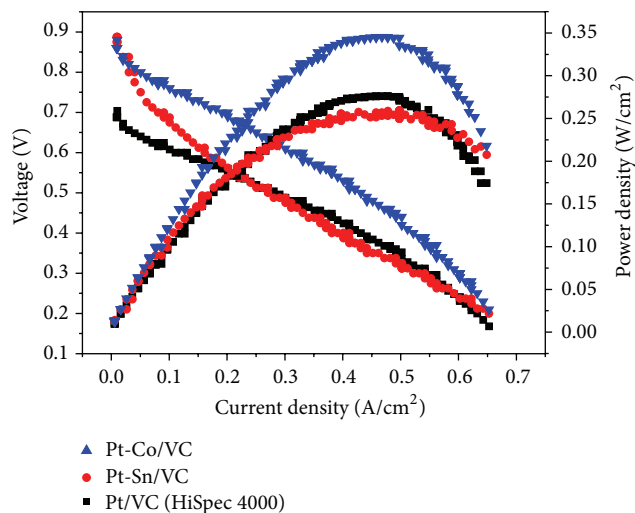


FIGURE 7: Polarization and power density plots at  $60^\circ\text{C}$  for PEMFCs using Pt-Co/VC, Pt-Sn/VC, and Pt/VC (HiSpec 4000) anode catalysts prepared by RIR. Test conditions: back pressure,  $\text{PO}_2 = 0 \text{ kPa}$ ,  $\text{PH}_2 = 0 \text{ kPa}$ ;  $\text{O}_2$  and  $\text{H}_2$  gases flowing at 200 SCCM and 400 SCCM; the catalyst loading was  $0.2 \text{ mg of Pt}$  at the cathode and  $0.4 \text{ mg of Pt-M or Pt/cm}^2$  at the anode;  $T_{\text{cell}} = 60^\circ\text{C}$ .

Figure 7 shows the polarization performance and power density curves of PEMFCs at  $60^\circ\text{C}$  using Pt-Co/VC and Pt-Sn/VC electrocatalysts. The  $\text{H}_2$ -fueled fuel cell polarization at low current density is electrochemical-activation controlled and mainly attributed to the sluggish HOR at the anode surface. The lowest loss in polarization voltage was observed for the Pt-Co/VC catalyst compared to the Pt-Sn/VC catalyst,

indicating that the highest catalytic activity was toward the HOR. The maximum power density is  $345 \text{ mW cm}^{-2}$  for the Pt-Co/VC catalyst, which is much higher than the maximum power density observed for the Pt-Sn/VC ( $275 \text{ mW cm}^{-2}$ ) and Pt/VC ( $252 \text{ mW cm}^{-2}$ ) catalysts. Once more, this illustrates that the Pt-Co/VC catalyst exhibits better fuel cell performance compared to those other catalysts (HiSpec 4000, Pt-Sn/VC), which is in full agreement with electron microscopy (HR-TEM, HR-SEM) data and the XRD data. The Pt-Co/VC catalysts exhibited a power density that was similar to the HiSpec 4000 Pt (40 wt%)/VC catalysts [34, 35], respectively. Surprisingly, the Pt-Co catalysts outperformed the state-of-the-art commercial Pt/VC (HiSpec 4000), having half as much Pt loading. Higher HOR electrocatalytic activity and better fuel cell performance are attributable to its larger ECSA, which is closely related to the smaller nanoparticles and the greater uniform particle dispersion of the Pt-Co catalyst (one-step radiation-induced reaction) on the VC-supported electrocatalyst [35–37].

#### 4. Conclusions

In this study, VC-supported electrocatalysts were synthesized by a one-step radiation-induced reaction process in aqueous solution at room temperature without reducing agents. The efficiency of the prepared electrocatalysts was evaluated. The following conclusions were drawn based on the experimental results. In spite of the low metallic contents of Pt-Co/VC electrocatalysts, their efficiencies for hydrogen oxidation reaction and power density were higher than those of the Pt/VC and Pt-Sn/VC electrocatalysts. The resulting Pt-Co/VC electrocatalyst has demonstrated its possibility as a promising electrocatalyst in PEMFC.

#### Conflict of Interests

The authors declare that there is no conflict of interests regarding the publication of this paper.

#### References

- [1] T. E. Springer, T. A. Zawodzinski, and S. Gottesfeld, "Polymer electrolyte fuel cell model," *Journal of the Electrochemical Society*, vol. 138, no. 8, pp. 2334–2342, 1991.
- [2] R. L. Borup and N. E. Vanderborgh, "Design and testing criteria for bipolar plate materials for PEM fuel cell applications," in *Materials Research Society Symposium Proceedings*, vol. 393, pp. 151–155, April 1995.
- [3] P. Adcock, *Development of Cost Effective, High Performance PEM Fuel Cells for Automotive Applications*, IQPC, London, UK, 1998.
- [4] P. L. Hentall, J. Barry Lakeman, G. O. Mepsted, P. L. Adcock, and J. M. Moore, "New materials for polymer electrolyte membrane fuel cell current collectors," *Journal of Power Sources*, vol. 80, no. 1, pp. 235–241, 1999.
- [5] H. I. Lee, C. H. Lee, T. Y. Oh, S. G. Choi, I. W. Park, and K. K. Baek, "Development of 1 kW class polymer electrolyte membrane fuel cell power generation system," *Journal of Power Sources*, vol. 107, no. 1, pp. 110–119, 2002.
- [6] L. Xiong, A. M. Kannan, and A. Manthiram, "Pt-M (M = Fe, Co, Ni and Cu) electrocatalysts synthesized by an aqueous route for proton exchange membrane fuel cells," *Electrochemistry Communications*, vol. 4, no. 11, pp. 898–903, 2002.
- [7] T. Toda, H. Igarashi, H. Uchida, and M. Watanabe, "Enhancement of the electroreduction of oxygen on Pt alloys with Fe, Ni, and Co," *Journal of the Electrochemical Society*, vol. 146, no. 10, pp. 3750–3756, 1999.
- [8] H. Yano, M. Kataoka, H. Yamashita, H. Uchida, and M. Watanabe, "Oxygen reduction activity of carbon-supported Pt-M (M = V, Ni, Cr, Co, and Fe) alloys prepared by nanocapsule method," *Langmuir*, vol. 23, no. 11, pp. 6438–6445, 2007.
- [9] T. Tadaki, K. Kifune, Y. Kubota, and H. Yamaoka, "Stabilization of the gamma phase in Fe-Pt alloy nanoparticles with low Pt contents prepared by chemical synthesis method," *Materials Science and Engineering A*, vol. 438–440, pp. 407–410, 2006.
- [10] D. L. Wood III, J. S. Yi, and T. V. Nguyen, "Effect of direct liquid water injection and interdigitated flow field on the performance of proton exchange membrane fuel cells," *Electrochimica Acta*, vol. 43, no. 24, pp. 3795–3809, 1998.
- [11] J. S. Yi and T. Van Nguyen, "Multicomponent transport in porous electrodes of proton exchange membrane fuel cells using the interdigitated gas distributors," *Journal of the Electrochemical Society*, vol. 146, no. 1, pp. 38–45, 1999.
- [12] A. Kumar and R. G. Reddy, "Effect of channel dimensions and shape in the flow-field distributor on the performance of polymer electrolyte membrane fuel cells," *Journal of Power Sources*, vol. 113, no. 1, pp. 11–18, 2003.
- [13] E. Hontañón, M. J. Escudero, C. Bautista, P. L. García-Ybarra, and L. Daza, "Optimization of flow-field in polymer electrolyte membrane fuel cells using computational fluid dynamics techniques," *Journal of Power Sources*, vol. 86, no. 1, pp. 363–368, 2000.
- [14] V. Gurau, F. Barbir, and H. Liu, "Analytical solution of a half-cell model for PEM fuel cells," *Journal of the Electrochemical Society*, vol. 147, no. 7, pp. 2468–2477, 2000.
- [15] N. P. Lebedeva and G. J. M. Janssen, "On the preparation and stability of bimetallic PtMo/C anodes for proton-exchange membrane fuel cells," *Electrochimica Acta*, vol. 51, no. 1, pp. 29–40, 2005.
- [16] B. Moreno, J. R. Jurado, and E. Chinarro, "Pt-Ru-Co catalysts for PEMFC synthesized by combustion," *Catalysis Communications*, vol. 11, no. 2, pp. 123–126, 2009.
- [17] M. Mirdamadi-Esfahani, M. Mostafavi, B. Keita, L. Nadjo, P. Kooyman, and H. Remita, "Bimetallic Au-Pt nanoparticles synthesized by radiolysis: application in electro-catalysis," *Gold Bulletin*, vol. 43, no. 1, pp. 49–56, 2010.
- [18] A. Henglein, "Physicochemical properties of small metal particles in solution: "Microelectrode" reactions, chemisorption, composite metal particles, and the atom-to-metal transition," *The Journal of Physical Chemistry*, vol. 97, no. 21, pp. 5457–5471, 1993.
- [19] D. Lee, S. Hwang, and I. Lee, "A study on composite PtRu(1:1)-PtSn(3:1) anode catalyst for PEMFC," *Journal of Power Sources*, vol. 145, no. 2, pp. 147–153, 2005.
- [20] L. Ma, H. Zhang, Y. Liang et al., "A novel carbon supported PtAuFe as CO-tolerant anode catalyst for proton exchange membrane fuel cells," *Catalysis Communications*, vol. 8, no. 6, pp. 921–925, 2007.
- [21] L. G. S. Pereira, V. A. Paganin, and E. A. Ticianelli, "Investigation of the CO tolerance mechanism at several Pt-based

- bimetallic anode electrocatalysts in a PEM fuel cell," *Electrochimica Acta*, vol. 54, no. 7, pp. 1992–1998, 2009.
- [22] S.-H. Choi, M.-S. Choi, K.-P. Lee, and H.-D. Kang, "Preparation and characterization of CdS and CdS/polyacrylonitrile nanocomposites by  $\gamma$ -irradiation and emulsion polymerization," *Journal of Applied Polymer Science*, vol. 91, no. 4, pp. 2335–2342, 2004.
- [23] Y.-O. Kang, S.-H. Choi, A. Gopalan, K.-P. Lee, H.-D. Kang, and Y. S. Song, "One-pot synthesis of a few nanocomposites with poly(N-vinylcarbazole) and CdS, Ag, Pd50-Ag50, and Pt50-Ru50 nanoparticles with  $\gamma$  irradiation," *Journal of Applied Polymer Science*, vol. 100, no. 3, pp. 1809–1815, 2006.
- [24] K.-D. Seo, S.-D. Oh, S.-H. Choi, S.-H. Kim, H. G. Park, and Y. P. Zhang, "Radiolytic loading of the Pt-Ru nanoparticles onto the porous carbons," *Colloids and Surfaces A: Physicochemical and Engineering Aspects*, vol. 313–314, pp. 393–397, 2008.
- [25] S.-G. Ryu, S.-W. Kim, S.-D. Oh, S.-H. Choi, H. G. Park, and Y. P. Zhang, "Preparation of Pd-PS, Pd-PSB and Pd-PSC nanoparticles by  $\gamma$ -irradiation and their catalytic efficiency in Sonogashira coupling reaction," *Colloids and Surfaces A: Physicochemical and Engineering Aspects*, vol. 313–314, pp. 224–229, 2008.
- [26] S.-J. Kim, S.-D. Oh, S. Lee, and S.-H. Choi, "Radiolytic synthesis of Pd-M (M = Ag, Ni, and Cu)/C catalyst and their use in Suzuki-type and Heck-type reaction," *Journal of Industrial and Engineering Chemistry*, vol. 14, no. 4, pp. 449–456, 2008.
- [27] S.-D. Oh, M.-R. Kim, S.-H. Choi et al., "Radiolytic synthesis of Pd-M (M = Ag, Au, Cu, Ni and Pt) alloy nanoparticles and their use in reduction of 4-nitrophenol," *Journal of Industrial and Engineering Chemistry*, vol. 14, no. 5, pp. 687–692, 2008.
- [28] S.-K. Kim, H.-D. Kwen, and S.-H. Choi, "Radiation-induced synthesis of vinyl copolymer based nanocomposites filled with reactive organic montmorillonite clay," *Radiation Physics and Chemistry*, vol. 81, no. 5, pp. 519–523, 2012.
- [29] B. Fang, N. K. Chaudhari, M.-S. Kim, H. K. Jung, and J.-S. Yu, "Homogeneous deposition of platinum nanoparticles on carbon black for proton exchange membrane fuel cell," *Journal of the American Chemical Society*, vol. 131, no. 42, pp. 15330–15338, 2009.
- [30] J. R. C. Salgado, E. Antolini, and E. R. Gonzalez, "Carbon supported Pt-Co alloys as methanol-resistant oxygen-reduction electrocatalysts for direct methanol fuel cells," *Applied Catalysis B: Environmental*, vol. 57, no. 4, pp. 283–290, 2005.
- [31] J. Llorca, N. Homs, J. León, J. Sales, J. L. G. Fierro, and P. Ramirez De La Piscina, "Supported Pt-Sn catalysts highly selective for isobutane dehydrogenation: preparation, characterization and catalytic behavior," *Applied Catalysis A: General*, vol. 189, no. 1, pp. 77–86, 1999.
- [32] A. K. Shukla, M. Neergat, P. Bera, V. Jayaram, and M. S. Hegde, "An XPS study on binary and ternary alloys of transition metals with platinized carbon and its bearing upon oxygen electroreduction in direct methanol fuel cells," *Journal of Electroanalytical Chemistry*, vol. 504, no. 1, pp. 111–119, 2001.
- [33] Z. Liu, B. Guo, L. Hong, and T. H. Lim, "Microwave heated polyol synthesis of carbon-supported PtSn nanoparticles for methanol electrooxidation," *Electrochemistry Communications*, vol. 8, no. 1, pp. 83–90, 2006.
- [34] E. V. Spinacé, M. Linardi, and A. O. Neto, "Co-catalytic effect of nickel in the electro-oxidation of ethanol on binary Pt-Sn electrocatalysts," *Electrochemistry Communications*, vol. 7, no. 4, pp. 365–369, 2005.
- [35] Y. M. Tsou, L. Cao, and E. D. Castro, "Novel high performance platinum and alloy catalysts for PEMFC & DMFC," *Preprints of Papers-American Chemical Society, Division of Fuel Chemistry*, vol. 49, no. 2, pp. 679–680, 2004.
- [36] H. Chhina, S. Campbell, and O. Kesler, "High surface area synthesis, electrochemical activity, and stability of tungsten carbide supported Pt during oxygen reduction in proton exchange membrane fuel cells," *Journal of Power Sources*, vol. 179, no. 1, pp. 50–59, 2008.
- [37] M. S. Saha, A. F. Gullá, R. J. Allen, and S. Mukerjee, "High performance polymer electrolyte fuel cells with ultra-low Pt loading electrodes prepared by dual ion-beam assisted deposition," *Electrochimica Acta*, vol. 51, no. 22, pp. 4680–4692, 2006.

## Research Article

# Optimization of the Electrodeposition Parameters to Improve the Stoichiometry of $\text{In}_2\text{S}_3$ Films for Solar Applications Using the Taguchi Method

Maqsood Ali Mughal,<sup>1</sup> M. Jason Newell,<sup>1</sup> Joshua Vangilder,<sup>1</sup> Shyam Thapa,<sup>1</sup> Kayla Wood,<sup>2</sup> Robert Engelken,<sup>1,2</sup> B. Ross Carroll,<sup>3</sup> and J. Bruce Johnson<sup>3</sup>

<sup>1</sup> Environmental Sciences Graduate Program, Arkansas State University, State University, Jonesboro, AR 72467, USA

<sup>2</sup> Electrical Engineering Program, Arkansas State University, State University, Jonesboro, AR 72467, USA

<sup>3</sup> Chemistry and Physics Program, Arkansas State University, State University, Jonesboro, AR 72467, USA

Correspondence should be addressed to Robert Engelken; [bdengens@astate.edu](mailto:bdengens@astate.edu)

Received 7 November 2013; Accepted 28 March 2014; Published 30 April 2014

Academic Editor: Alireza Talebitahter

Copyright © 2014 Maqsood Ali Mughal et al. This is an open access article distributed under the Creative Commons Attribution License, which permits unrestricted use, distribution, and reproduction in any medium, provided the original work is properly cited.

Properties of electrodeposited semiconductor thin films are dependent upon the electrolyte composition, plating time, and temperature as well as the current density and the nature of the substrate. In this study, the influence of the electrodeposition parameters such as deposition voltage, deposition time, composition of solution, and deposition temperature upon the properties of  $\text{In}_2\text{S}_3$  films was analyzed by the Taguchi Method. According to Taguchi analysis, the interaction between deposition voltage and deposition time was significant. Deposition voltage had the largest impact upon the stoichiometry of  $\text{In}_2\text{S}_3$  films and deposition temperature had the least impact. The stoichiometric ratios between sulfur and indium (S/In: 3/2) obtained from experiments performed with optimized electrodeposition parameters were in agreement with predicted values from the Taguchi Method. The experiments were carried out according to Taguchi orthogonal array  $L_{27}(3^4)$  design of experiments (DOE). Approximately 600 nm thick  $\text{In}_2\text{S}_3$  films were electrodeposited from an organic bath (ethylene glycol-based) containing indium chloride ( $\text{InCl}_3$ ), sodium chloride (NaCl), and sodium thiosulfate ( $\text{Na}_2\text{S}_2\text{O}_3 \cdot 5\text{H}_2\text{O}$ ), the latter used as an additional sulfur source along with elemental sulfur (S). An X-ray diffractometer (XRD), energy dispersive X-ray spectroscopy (EDS) unit, and scanning electron microscope (SEM) were, respectively, used to analyze the phases, elemental composition, and morphology of the electrodeposited  $\text{In}_2\text{S}_3$  films.

## 1. Introduction

During the last few decades solar energy has received attention due to increased environmental concerns over traditional energy resources such as coal, oil, and natural gas. Fossil fuel prices will rise over time and resources may eventually deplete. Hence, the world's current electricity supply is facing government, businesses, and consumer pressures to support development of alternative energy resources such as solar cells. The solar industry has come of age lately and the world's most efficient solar cell from Sharp can convert an impressive 44.4% of incoming photon energy into electrical energy [1]. Prices of solar panels have continued to drop while the market size of the US solar industry grew 34% between 2011 (\$8.6 billion, 1,187 MW) and 2013 (\$11.5 billion,

3,317 MW) [2]. However, scientists continue to research novel semiconductor materials and deposition techniques that can provide higher efficiencies and low-cost solar panels with less environmental impact upon the Earth.

In this paper, we report studies on electrodeposition of  $\text{In}_2\text{S}_3$ , an environmentally friendly replacement to CdS for solar cell applications as a buffer layer.  $\text{In}_2\text{S}_3$  films were electrodeposited onto molybdenum-coated glass substrates. Electrodeposition is a low-cost, nonvacuum, and large industrial scale-based deposition technique to deposit material efficiently and uniformly. However, the electrochemistry behind it is complex due to multiple deposition parameters that may have individually and in tandem an impact upon the properties of the material [3, 4]. The Taguchi Method was used to optimize electrodeposition parameters in order to

improve the stoichiometry of  $\text{In}_2\text{S}_3$  films, which is one of the most important properties of any photovoltaic material and critical to obtaining the desired band gap and performance. Therefore, in the present study, the primary goal was to improve the stoichiometry while avoiding nonuniformity and nonadherency in the electrodeposited  $\text{In}_2\text{S}_3$  films. Taguchi analysis helped us to analyze the effect of each deposition parameter upon the stoichiometry of  $\text{In}_2\text{S}_3$  films.

## 2. Materials and Methods

**2.1. Indium Sulfide ( $\text{In}_2\text{S}_3$ ).**  $\text{In}_2\text{S}_3$  is an important member of III–VI group of midgap semiconducting sulfides, applicable for optoelectronics, solar cells, and photoelectric devices [2].  $\text{In}_2\text{S}_3$  is an indirect band gap semiconductor with potential to become a nontoxic alternative to CdS as a buffer layer in copper indium gallium selenide/sulfide- (CIGS-) based solar cells [5, 6]. It is a promising buffer material for photovoltaic applications because of its stability, reasonably wide band gap (2.3 eV) [7, 8], and photoconductive behavior [9]. Several reports have been published on deposition of  $\text{In}_2\text{S}_3$  by different deposition techniques (both wet and dry), in thin film and powder form, with diverse morphologies [7, 10, 11]. In CIGS-based solar cells buffered with  $\text{In}_2\text{S}_3$ , efficiencies of 15.7% [12] have been achieved, which is slightly less than the 16% efficiency reported for CdS-based solar cells deposited by chemical bath deposition (CBD) [13]. Electrodeposited  $\text{In}_2\text{S}_3$ -buffered CIGSe solar cells have yielded 10.2% efficiency [14]. However, the use of ethylene glycol as an organic electrolyte for the electrochemical synthesis of  $\text{In}_2\text{S}_3$  films has not been reported previously, with the exception of IEEE conference proceedings [3] regarding our work at the Optoelectronic Materials Research Laboratory (OMRL), Arkansas State University, Jonesboro, AR.

**2.2. Electrodeposition.** Electrodeposition is widely used in the coating industry and is considered to be a low-cost technique for large surface coatings with full coverage and high growth yield [15]. It was introduced by Kröger in the field of semiconductors in 1978, while working on cathodic deposition of CdTe, an absorber material [16]. Since then, electrodeposition has emerged as a method for the synthesis of semiconductor thin films and manufacturing of nanostructures such as chalcogenides [17]. Electrodeposition takes place when voltage is applied across the electrodes (anode and cathode) immersed in an electrolyte. The anode is anodized and the cations in the solution start moving towards the cathode with the help of the electric field created in the electrochemical cell. The reduction reaction takes place at the surface of the cathode and leads to deposition of the desired material. The process provides high material transfer/utilization efficiency, *in situ* measurements [18], precision control with proper bath chemistry, and environmental safety in terms of solvent emissions [14]. However, most of the work on semiconductor electrodeposition is limited to a few technologically important semiconductors. There are several deposition parameters which can affect the properties of the semiconductor material [19]. Many fundamental aspects of

the electrodeposition of semiconductors are still misunderstood and not clearly defined. Since  $\text{In}_2\text{S}_3$  shows promise and has not been studied as extensively as some semiconductors, in this work we determine the optimal deposition parameters for the electrodeposition of  $\text{In}_2\text{S}_3$  thin films to obtain proper stoichiometry, crystalline structure, and morphology.

**2.3. Taguchi Method.** The “Taguchi Method” is a powerful tool developed by Genichi Taguchi in 1966 to improve the quality of industrially manufactured products [20]. It is a simple and effective technique that aims to optimize manufacturing processes in order to obtain the optimal performance. Today, this statistical tool is frequently applied to engineering, pharmaceutical, and biotechnology industries [21, 22].

Taguchi believed that this robust design could help to minimize (if not eliminate) a loss of quality which ultimately results in cost to society [23]. He defined the sensitivity (signal-to-noise ratio,  $S/N$ ) as the logarithmic function for the response analysis (the characteristic performance that could be “stoichiometry” as it is in our case) of chosen deposition parameters to generate optimal design [22]. This analysis helps to compare the performance of a product with changing  $S/N$  ratios depending upon experimental procedures. The  $S/N$  ratio can integrate with the Taguchi orthogonal array (TOA) design of experiments and predict values (optimal) to achieve improved performance in the product and the process [21]. It is a suitable method to statistically analyze thin films since there are so many electrodeposition parameters that may have an impact upon the properties of semiconductor thin films. In the past, the Taguchi Method has been applied to various thin films (CuInSe<sub>2</sub>, TiN, and Ni) [21–24]. Figure 1 depicts the flowchart of the steps involved in the Taguchi Method.

### 2.4. Steps

**(1) Select Characteristic Performance.** The initial step in the Taguchi Method involves selecting a characteristic performance that is affected by different parameters in the manufacturing process. The stoichiometric ratio between sulfur and indium was chosen as a characteristic performance in this study. The Taguchi Method will allow investigating how different parameters affect the means and variances of the stoichiometry of  $\text{In}_2\text{S}_3$  films. Furthermore, this will help improve the functioning of the process and quality of the product.

**(2) Select Deposition Parameters and Their Levels.** Based upon the preliminary experiments and results, deposition parameters significantly affecting the stoichiometry of  $\text{In}_2\text{S}_3$  films were selected. These deposition parameters include voltage, time, composition of solution, and temperature at three different levels, as specified in Table 1. The values of the levels were changed to study the effects of individual deposition parameters, as well as their interactions, upon the responses, with the least number of experimental runs.

The levels for each deposition parameter were chosen such as to cover the combinations where optimal conditions could potentially exist.

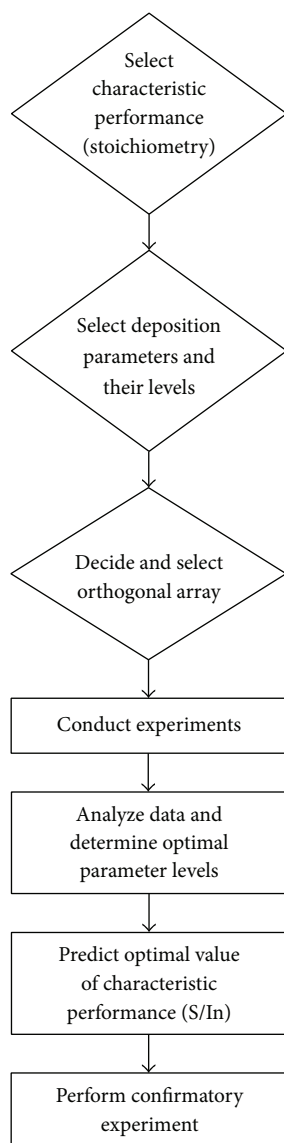


FIGURE 1: Steps in the Taguchi Method for design of experiments.

(3) *Select Orthogonal Array Taguchi Design of Experiments (DOE)*. Taguchi orthogonal array  $L_{27}$  ( $3^4$ ) design of experiments (DOE) (see Table 2) was applied to identify the critical deposition parameters. An orthogonal array of  $L_{27}$  was selected for conducting experiments at three levels for four deposition parameters, as mentioned above. In Table 2, Columns 1, 2, 5, and 9 represent deposition parameters A, B, C, and D. The design speeds up the process of experimentation and additionally saves time and resources.

(4) *Conduct Experiments*. According to  $L_{27}$  DOE, there are a total of 27 experiments needed to complete this study. For each experiment, three trials were performed to gain balance in the DOE and achieve high accuracy in the data. Hence, a total number of **81** experiments were performed.

(5) *Analyze Data and Determine Optimal Parameter Levels*. With the Taguchi Method, the analysis consisted of analysis

of means (ANOM) and analysis of variance (ANOVA) for  $S/N$  ratios. The effect of each deposition parameter at a given level upon the quality of  $\text{In}_2\text{S}_3$  films can be best estimated using ANOM. The basic goal of ANOVA is to estimate the variance in the film quality, owing to the deposition parameters in terms of  $S/N$  ratios.

A main effect plot for  $S/N$  ratios helped us to determine the optimal value for each deposition parameter.

(6) *Predict Optimal Values: Orthogonal Regression Analysis*. Orthogonal regression analysis helped improve the mean characteristic performance value and drive it closer to the target value, thus improving the quality of the product. It narrows down the scope of the manufacturing process and identifies the problem with the help of data already in existence.

(7) *Perform Confirmatory Experiment*. The final step in the Taguchi Method involves the validation of experiment and results from optimal deposition parameters to acquire the targeted value of the characteristic performance, that is, the stoichiometric ratio between sulfur and indium.

### 3. Experimental Details

A three-electrode electrochemical cell (see Figure 2) containing an ethylene glycol (organic solvent) bath of sulfur S (precipitated, 99.5%), sodium thiosulfate  $\text{Na}_2\text{S}_2\text{O}_3 \cdot 5\text{H}_2\text{O}$  (99+%), indium chloride  $\text{InCl}_3$  (anhydrous, 99.99%, metal basis), and sodium chloride  $\text{NaCl}$  (metal basis, 99.99%) from Alfa Aesar was used to conduct experiments with three different compositions as shown in Table 1.

A Ag/AgCl reference electrode from Fisher Scientific filled with potassium chloride (KCl) and ethylene glycol ( $\text{C}_2\text{H}_6\text{O}_2$ ), a Mo-coated glass substrate (Mo sputtered onto 0.12-inch thick soda lime glass, 1 inch  $\times$  1 inch) as the working electrode (cathode), and graphite (1.25 inch  $\times$  1.25 inch) as a counter electrode (anode) were used to perform experiments. A digital potentiostat (WaveNow) from Pine Research Instrument Company was used for supplying voltage. A digital hotplate from Fisher Scientific (Isotemp 11-400-49SHP) was used to heat and stir the solution. Magnetic agitation of the organic bath was produced with a commercial Teflon-coated magnetic stir bar centered at the bottom of the glass beaker. The stir rate was kept constant at 300 rpm.

Molybdenum-coated glass substrates were cleaned in an acetone solution in an ultrasonic bath (Cole-Parmer 8890) and vibrated for 15 min. The organic electrolytic solution was prepared by dissolving elemental S in 150 mL of ethylene glycol and heating the solution at  $150^\circ\text{C}$ . Once the S was fully dissolved, the solution was cooled to  $80^\circ\text{C}$ , and then  $\text{InCl}_3$  (0.05 M) and  $\text{NaCl}$  (0.1 M) were added.  $\text{Na}_2\text{S}_2\text{O}_3 \cdot 5\text{H}_2\text{O}$  (used as an additional source for sulfur) was then added. The solution was continuously stirred and uniformly heated to avoid precipitation of sulfur in the cell and aging of the  $\text{In}_2\text{S}_3$  colloid (small size chemical traces/species that stand idle at the walls or bottom of the beaker) formed by trace reduction and chemical precipitation of the solutes. The solution was then used for electroplating  $\text{In}_2\text{S}_3$  onto the substrate.  $\text{In}_2\text{S}_3$  films were first slowly cooled to room

TABLE 1: Control deposition parameters and levels for the electrodeposition of  $\text{In}_2\text{S}_3$  thin films.

Level	“A,” deposition voltage (V)	“B,” deposition time (min)	“C,” composition of solution	“D,” deposition temperature ( $^{\circ}\text{C}$ )
1	-0.6	3	0.1 M S + 0.05 M $\text{InCl}_3$ + 0.1 M NaCl	150
2	-0.7	6	0.1 M S + 0.1 M $\text{Na}_2\text{S}_2\text{O}_3 \cdot 5\text{H}_2\text{O}$ + 0.05 M $\text{InCl}_3$ + 0.1 M NaCl	160
3	-0.8	9	0.2 M S + 0.05 M $\text{InCl}_3$ + 0.1 M NaCl	170

TABLE 2: Taguchi orthogonal array  $L_{27}(3^4)$  design of experiments with interactions.

Exp. number	1 (A)	2 (B)	3 (A $\times$ B)	4 (A $\times$ B)	5 (C)	6 (A $\times$ C)	7 (A $\times$ C)	8 (B $\times$ C)	9 (D)	10	11 (B $\times$ C)	12	13
1	1	1	1	1	1	1	1	1	1	1	1	1	1
2	1	1	1	1	2	2	2	2	2	2	2	2	2
3	1	1	1	1	3	3	3	3	3	3	3	3	3
4	1	2	2	2	1	1	1	2	2	2	3	3	3
5	1	2	2	2	2	2	2	3	3	3	1	1	1
6	1	2	2	2	3	3	3	1	1	1	2	2	2
7	1	3	3	3	1	1	1	3	3	3	2	2	2
8	1	3	3	3	2	2	2	1	1	1	3	3	3
9	1	3	3	3	3	3	3	2	2	2	1	1	1
10	2	1	2	3	1	2	3	1	2	3	1	2	3
11	2	1	2	3	2	3	1	2	3	1	2	3	1
12	2	1	2	3	3	1	2	3	1	2	3	1	2
13	2	2	3	1	1	2	3	2	3	1	3	1	2
14	2	2	3	1	2	3	1	3	1	2	1	2	3
15	2	2	3	1	3	1	2	1	2	3	2	3	1
16	2	3	1	2	1	2	3	3	1	2	2	3	1
17	2	3	1	2	2	3	1	1	2	3	3	1	2
18	2	3	1	2	3	1	2	2	3	1	1	2	3
19	3	1	3	2	1	3	2	1	3	2	1	3	2
20	3	1	3	2	2	1	3	2	1	3	2	1	3
21	3	1	3	2	3	2	1	3	2	1	3	2	1
22	3	2	1	3	1	3	2	2	1	3	3	2	1
23	3	2	1	3	2	1	3	3	2	1	1	3	2
24	3	2	1	3	3	2	1	1	3	2	2	1	3
25	3	3	2	1	1	3	2	3	2	1	2	1	3
26	3	3	2	1	2	1	3	1	3	2	3	2	1
27	3	3	2	1	3	2	1	2	1	3	1	3	2

temperature to avoid thermal shock by immersing in warmed ethylene glycol and then rinsed with distilled water and acetone. The samples were stored in airtight plastic boxes.

## 4. Results and Discussions

**4.1. Energy Dispersive X-Ray Spectroscopy (EDS).** After conducting all 81 experiments, the elemental compositions for the electrodeposited  $\text{In}_2\text{S}_3$  films were determined using EDS on the scanning electron microscope (SEM) from Tescan (Model VEGA TS 5136 XM). The INCA X-Sight (Model 7378) from Oxford Instruments is integrated with the SEM for EDS

to function. The films were scratched off of the Mo-coated glass substrates because sulfur peaks (K lines) in EDS overlap with molybdenum peaks (L lines) from the substrates during acquisition at about 2.3 keV.

Following removal, the film was collected on an aluminum stub in powder form with the help of adhesive tabs. EDS was performed on three different areas over the surface distribution of the scratched- $\text{In}_2\text{S}_3$  film collected on the stub to calculate the mean S/In molar ratio for each film (see Figure 3 and Table 3). The  $\text{In}_2\text{S}_3$  films may contain oxygen, carbon, aluminum, and molybdenum, as is evident from Table 3 (see Spectra 1 and 2). The  $\text{In}_2\text{S}_3$  films may oxidize

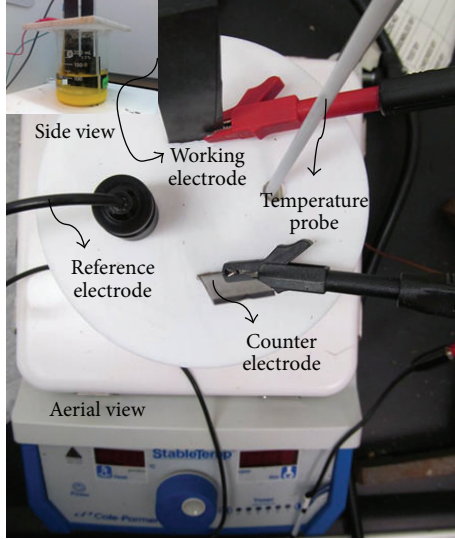


FIGURE 2: Three-electrode electrochemical cell.

TABLE 3: EDS analysis (Experiment Number 5, Trial 2).

Spectrum	Atomic %						
	O	C	S	Mo	Al	In	S/In
Spectrum 1	16.7	21.27	37.41	0	0	24.62	1.519
Spectrum 2	1.05	20	44.45	3.21	0	31.29	1.421
Spectrum 3	0	0	60.32	0	0	39.68	1.520
Mean	5.91	13.75	47.39	1.07	0	31.86	<b>1.487</b>

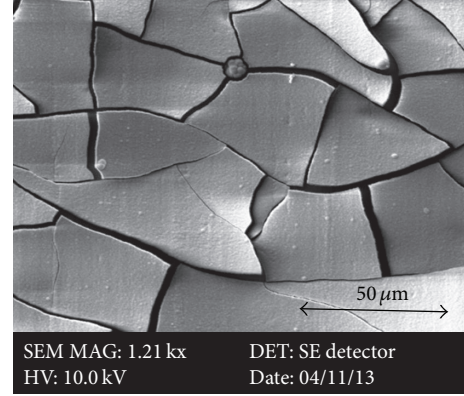
over a period of time, especially if not properly/immediately stored. Since the adhesive on the aluminum stub used to collect the scratched- $\text{In}_2\text{S}_3$  film contains carbon, EDS may detect carbon and also aluminum, as a part of the composition of the film. Molybdenum may also be detected by EDS as films were scratched off of the molybdenum-coated glass substrate. However, the stoichiometric ratios between sulfur and indium were close to optimal values, which is also evident from Table 3.

Hence, the  $S/\text{In}$  ratio calculated for each experiment was the mean of the mean  $S/\text{In}$  ratios determined from all three trials for the same experiment. The  $S/\text{In}$  ratios determined for all 27 experiments are listed in Table 4.

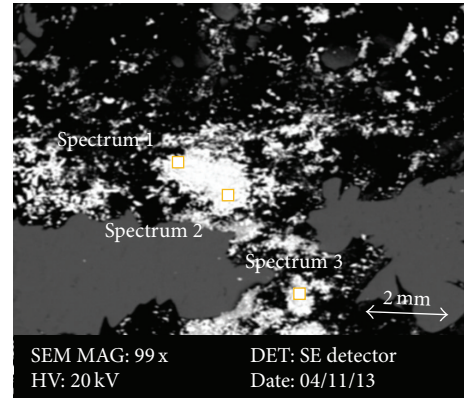
**4.2. Signal-to-Noise Ratio (S/N) Analysis.** Signal-to-noise ratio (S/N) was calculated using Minitab 16 in response to these stoichiometric ratios to measure the quality characteristic. The average S/N ratio was an average of all S/N ratios of a deposition parameter at a given level.

The formula used to calculate the S/N ratio is given by the following equation (“ $y$ ” is the mean value of the performance characteristic for a given experiment and “ $s$ ” is the variance):

$$S/N = 10 \log \frac{\bar{y}_i^2}{s_i^2}, \quad (1)$$



(a)



(b)

FIGURE 3: E5,2 (Experiment Number 5 and Trial Number 2): (a) SEM image of  $\text{In}_2\text{S}_3$  film at 1.21 kX. (b) SEM image of scratched off film on an aluminum stub at 99 X with selected surface area (squares) for EDS analysis.

where

$$s_i^2 = \frac{1}{N_i - 1} \sum_{u=1}^{N_i} (y_{i,u} - \bar{y}_i)^2 \quad (2)$$

$$\bar{y}_i = \frac{1}{N_i} \sum_{u=1}^{N_i} y_{i,u}, \quad (3)$$

where  $i$  is the experiment number,  $u$  is the trial number, and  $N_i$  is the number of trials for experiment  $i$ .

Using the above mathematical expressions, S/N ratios response for each deposition parameter and its level were calculated and are given in Table 5.

The response table includes ranks based upon delta statistics ( $\blacktriangle$ ), which compare the relative magnitude of effects for each deposition parameter. The symbol  $\blacktriangle$  is the highest average S/N ratio for each parameter minus the lowest average S/N ratio for the same (e.g., in case of parameter “A,”  $\blacktriangle = 34.79 - 23.21 = 11.58$ ). Ranks are assigned based on  $\blacktriangle$  values; Rank 1 is assigned to the highest  $\blacktriangle$  value, Rank 2 to the second highest  $\blacktriangle$  value, and so on. Therefore, deposition voltage had the most significant impact upon the stoichiometry of the  $\text{In}_2\text{S}_3$  films, and deposition temperature

TABLE 4: Sulfur to indium (S/In) molar ratios from EDS.

Uniformity	L <sub>27</sub> orthogonal array experiment	S/In molar ratio
■	1	1.1556
■	2	1.2567
■	3	1.2313
■	4	1.3697
■	5	1.3132
■	6	1.3196
■	7	1.6671
■	8	1.4445
■	9	1.4097
■	10	1.2559
■	11	1.3510
■	12	1.3297
■	13	1.3818
□	14	1.3910
□	15	1.4462
□	16	1.3684
□	17	1.4012
□	18	1.46
□	19	1.2894
□	20	1.2354
□	21	1.4032
□	22	1.3520
□	23	1.2807
□	24	1.4150
□	25	1.4108
□	26	1.2442
□	27	1.4221

■ Uniform In<sub>2</sub>S<sub>3</sub> films.

□ Nonuniform In<sub>2</sub>S<sub>3</sub> films.

TABLE 5: Response table for signal-to-noise ratios.

Levels	A, deposition voltage (V)	B, deposition time (min)	C, composition of solution	D, deposition temperature (°C)
1	34.79	31.61	24.68	25.04
2	23.21	25.73	30.92	30.13
3	23.63	24.52	26.15	27.18
▲	11.58	7.08	6.23	5.10
Rank	1	2	3	4

had the least significant impact. The corresponding main effects and interaction plots between the parameters are also shown in Figures 4 and 5, respectively.

In the main effects plot, if the line (represents the grand mean of *S/N* ratios with respect to response) for a particular deposition parameter is nearly horizontal, the parameter has no significant effect. The highest average *S/N* ratio defines the optimal level (encircled) for that deposition

parameter. Therefore, the optimal deposition parameters for the electrodeposition of In<sub>2</sub>S<sub>3</sub> films are A1, B1, C2, and D2. On the other hand, a deposition parameter for which the line has the largest slope has the most significant effect. It is clear from the main effects plot that deposition parameter A (deposition voltage) was the most significant parameter while parameter D (deposition temperature) was the least significant. In the interaction plots, if the lines are nonparallel, then there is an interaction between parameters and if the lines cross, strong interaction occurs. From Figure 5, it can be seen that there is a strong interaction between parameters A and B, and there is a moderate interaction between parameters A and C and A and D.

**4.3. Orthogonal Regression Analysis.** Orthogonal regression equations were formulated for estimating predicted values to improve stoichiometry over a specified range of deposition voltage, the most significant factor of all, as shown in Figure 6. The In<sub>2</sub>S<sub>3</sub> films deposited with these predicted values produced uniform In<sub>2</sub>S<sub>3</sub> thin films with an average S/In molar ratio of 1.493 (see Table 6).

Confirmatory experiments with optimal and predicted values (from the main effect plot for *S/N* ratios and the orthogonal regression plot) from Taguchi analysis were repeatedly performed to verify stoichiometric ratios between sulfur and indium. The In<sub>2</sub>S<sub>3</sub> films were grown at  $-0.685$  V for 3 min in a bath containing 0.1M each of sulfur and sodium thiosulfate, at a deposition temperature of 160°C. The films were uniform and adherent. The stoichiometric ratios between sulfur and indium from these experiments were in agreement with predicted values from the Taguchi Method. The S/In molar ratio was calculated to be 1.49, almost equal to the ideal S/In molar ratio of 3/2. Table 6 shows the EDS data for one of the confirmatory experiments. The electrodeposited In<sub>2</sub>S<sub>3</sub> films produced from these experiments were approximately 600 nm thick. The thickness of the films was measured using a surface profilometer from Veeco (Dektak Model 6M).

However, the In<sub>2</sub>S<sub>3</sub> films exhibited narrow cracks within 1 μm width (see Figure 3(a)).

**4.4. X-Ray Diffraction.** An X-ray diffractometer from the Rigaku Corporation (Model D/MAX-B System) was used for phase identification of the crystalline structure of the electrodeposited In<sub>2</sub>S<sub>3</sub> films synthesized at optimal values before and after heat treatment. Figure 7 shows the XRD plot of an as-grown and then annealed In<sub>2</sub>S<sub>3</sub> film. The film was annealed in air for 2 hours at 250°C. It is evident from the figure that the as-grown In<sub>2</sub>S<sub>3</sub> films exhibited a beta-phase crystalline structure. The In<sub>2</sub>S<sub>3</sub> peaks were slightly more narrow and intense for annealed films, which indicated that the grains were better crystallized.

## 5. Conclusion

In<sub>2</sub>S<sub>3</sub> films with nearly ideal stoichiometric ratios were successfully electrodeposited onto Mo-coated glass from an organic bath. The optimized electrodeposition parameters obtained by the Taguchi Method were as follows: deposition

TABLE 6: EDS data for  $\text{In}_2\text{S}_3$  films grown at optimal values obtained by the Taguchi Method (confirmatory results).

Spectrum	Atomic %						
	O	Si	S	Mo	In	Total	S/In
Spectrum 1	6.54	0.0	54.1	3.12	36.2	100.0	1.493
Spectrum 2	0.00	0.0	56.6	8.36	37.5	100.0	1.51
Spectrum 3	0.00	0.0	55.1	7.27	37.5	100.0	1.471
Spectrum 4	14.4	0.0	50.6	2.82	33.7	100.0	1.5
Spectrum 5	0.00	0.0	58.3	0.00	40.5	100.0	1.443
Spectrum 6	0.00	0.0	59.8	0.00	39.9	100.0	1.498
Spectrum 7	4.21	0.0	57.4	0.00	38.3	100.0	1.501
Spectrum 8	0.00	0.0	60.2	0.1	39.7	100.0	1.53
Mean	3.14	0.0	56.5	2.7	37.9	100.0	<b>1.493</b>
Max.	14.4	0.0	60.2	8.36	40.5		
Min.	0.00	0.0	50.6	0.00	33.7		

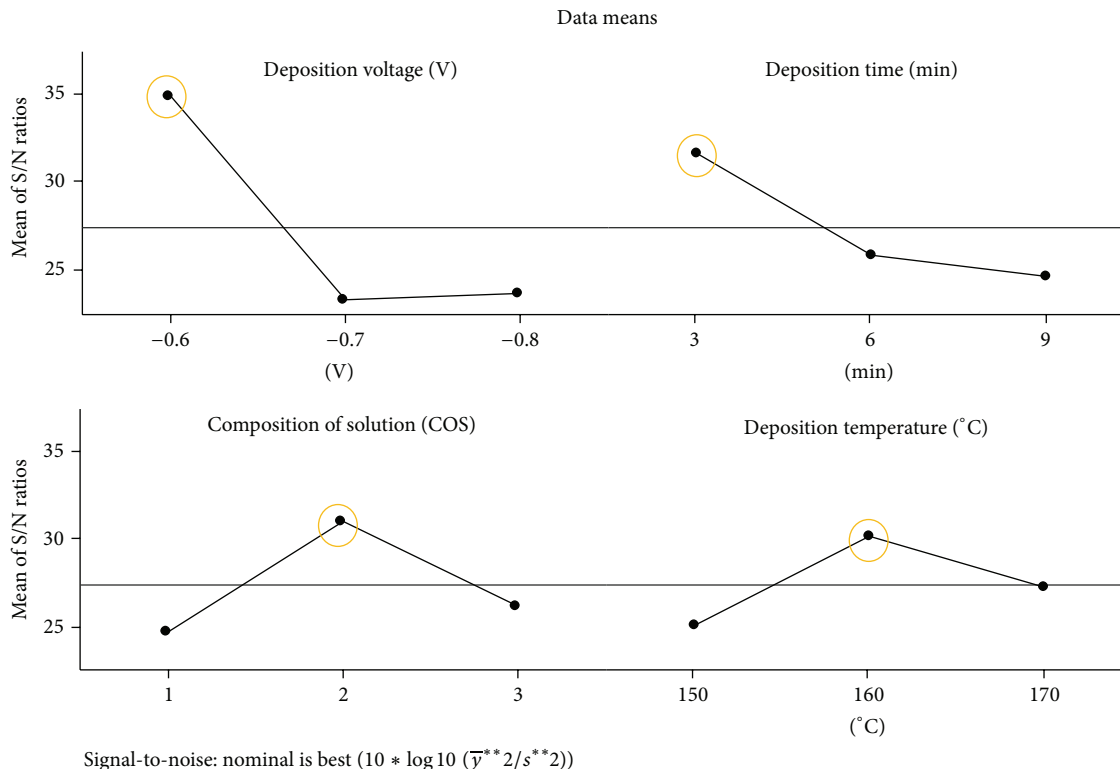


FIGURE 4: Main effect plot for S/N ratios.

voltage,  $-0.6$  V; deposition time, 3 min; composition of solution,  $0.1$  M S +  $0.1$  M  $\text{Na}_2\text{S}_2\text{O}_3 \cdot 5\text{H}_2\text{O}$  +  $0.1$  M NaCl +  $0.05$  M  $\text{InCl}_3$ ; and deposition temperature,  $160^\circ\text{C}$ . The ANOVA analysis for means and S/N ratios showed that deposition voltage had the largest impact upon the stoichiometry of the  $\text{In}_2\text{S}_3$  films, and deposition temperature had the least significant impact. Also deposition voltage and deposition time showed stronger interaction (largest impact upon the characteristic performance) between them compared to other

deposition factors. Furthermore, orthogonal regression analysis produced plots with a predicted value for deposition voltage ( $-0.685$  V). From the EDS analysis, it was clear that  $\text{In}_2\text{S}_3$  films exhibited nearly ideal stoichiometric molar ratios between sulfur and indium. The S/In molar ratio calculated was 1.49, almost equivalent to the ideal S/In molar ratio of  $3/2$ . XRD plots revealed that electrodeposited films exhibit  $\beta$ - $\text{In}_2\text{S}_3$  crystalline structures. The  $\text{In}_2\text{S}_3$  films were uniform and adherent with approximately 600 nm thickness. Eventually,

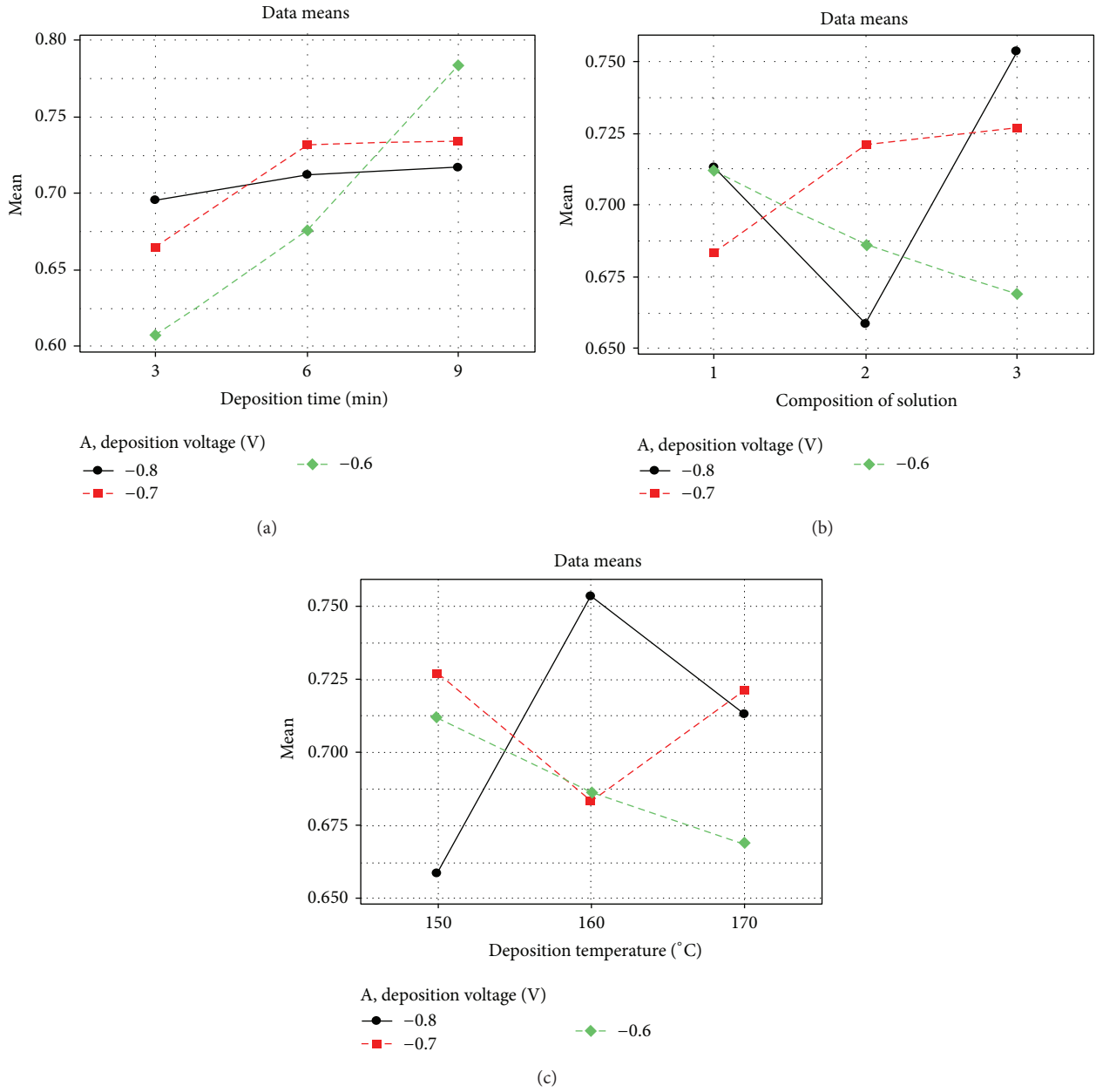


FIGURE 5: Interaction plot for deposition voltage versus (a) deposition time, (b) composition of solution, and (c) deposition temperature.

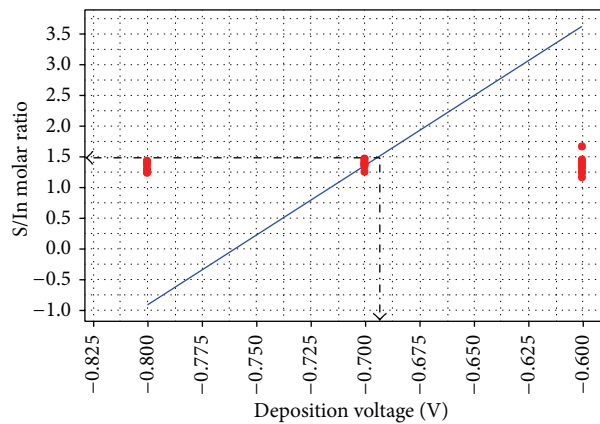


FIGURE 6: Orthogonal regression plot of S/In molar ratio versus deposition voltage with fitted line.

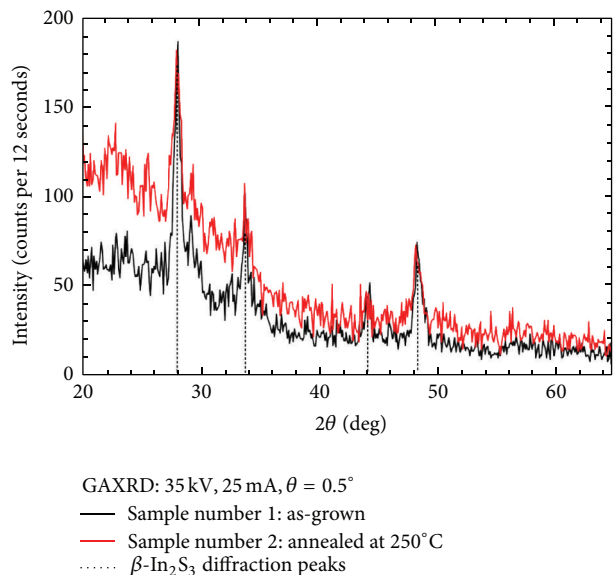


FIGURE 7: Glancing angle X-ray diffraction spectra for as-grown and annealed (in air at 250°C) In<sub>2</sub>S<sub>3</sub> film.

In<sub>2</sub>S<sub>3</sub> films will be combined with electrodeposited CuInS<sub>2</sub> or CdTe films to form heterojunction solar cells.

## Conflict of Interests

The authors declare that there is no conflict of interests regarding the publication of this paper.

## Acknowledgments

National Science Foundation Grant EPS 1003970 and NASA Grant NNX09AW22A, respectively, administered by the Arkansas Science and Technology Authority (Dr. Gail McClure, Cathy Ma, and Marta Collier) and the Arkansas Space Grant Consortium (Dr. Keith Hudson and Laura Holland) jointly funded this work. The authors also thank the Principal Investigators on the projects, respectively, Dr. Alan Mantooh (University of Arkansas-Fayetteville) with assistant Kathy Kirk and Dr. Tansel Karabacak (University of Arkansas-Little Rock). The authors also thank Dr. Stan Trauth of Arkansas State University for use of the SEM/EDS unit.

## References

- [1] D. Tom, "Sharp develops world's most efficient solar panel," TechSpot: Technology News and Analysis, June 2013.
- [2] J. Nolan, N. Rinaldi, and S. Kann, "U.S. solar market grows 76% in 2012; now an increasingly-competitive energy source for millions of Americans today," Solar Energy Industry Association, March 2013.
- [3] M. J. Newell, M. A. Mughal, R. Engelken et al., "Elemental sulfur-based electrodeposition of indium sulfide films," in *Proceedings of the 37th IEEE Photovoltaic Specialists Conference (PVSC '11)*, pp. 1322–1326, Seattle, Wash, USA, June 2011.
- [4] M. A. Mughal, M. J. Newell, R. Engelken et al., "Statistical analysis of electrodeposited indium (III) sulfide (In<sub>2</sub>S<sub>3</sub>) films, a potential buffer material for PV, (Heterojunction Solar Cell) systems, using organic electrolytes," in *Nanotechnology 2013: Bio Sensors, Instruments, Medical, Environment, and Energy*, 3. *Technical Proceedings of the 2013 NSTI Nanotechnology Conference*, pp. 523–527, Washington, DC, USA, May 2013.
- [5] I. Gurrappa and L. Binder, "Electrodeposition of nanostructured coatings and their characterization—a review," *Science and Technology of Advanced Materials*, vol. 9, no. 4, Article ID 043001, pp. 11–15, 2008.
- [6] W. Wang, W. Zhu, and L. Zhang, "A facile preparation and visible light-induced photocatalysis of indium sulfide superstructure," *Research on Chemical Intermediates*, vol. 35, no. 6-7, pp. 761–767, 2009.
- [7] A. Datta, S. K. Panda, S. Gorai, D. Ganguli, and S. Chaudhuri, "Room temperature synthesis of In<sub>2</sub>S<sub>3</sub> micro- and nanorod textured thin films," *Materials Research Bulletin*, vol. 43, no. 4, pp. 983–989, 2008.
- [8] R. Jayakrishnan, T. T. John, C. S. Kartha, K. P. Vijayakumar, T. Abe, and Y. Kashiwaba, "Defect analysis of sprayed  $\beta$ -In<sub>2</sub>S<sub>3</sub> thin films using photoluminescence studies," *Semiconductor Science and Technology*, vol. 20, no. 12, pp. 1162–1167, 2005.
- [9] M. Lajnef and H. Ezzaouia, "Structural and optical studies of indium sulfide thin films prepared by sulfurization of indium thin films," *The Open Applied Physics Journal*, vol. 2, pp. 23–26, 2009.
- [10] N. A. Allsop, A. Schönmann, H.-J. Muffler, M. Bär, M. C. Lux-Steiner, and C.-H. Fischer, "Spray-ILGAR indium sulfide buffers for Cu(In,Ga)(S,Se)<sub>2</sub> solar cells," *Progress in Photovoltaics: Research and Applications*, vol. 13, no. 7, pp. 607–616, 2005.
- [11] X. Sheng, L. Wang, G. Chen, and D. Yang, "Simple synthesis of flower-like In<sub>2</sub>S<sub>3</sub> structures and their use as templates to prepare CuS particles," *Journal of Nanomaterials*, vol. 2011, Article ID 280216, 5 pages, 2011.
- [12] D. Hariskos, M. Ruckh, U. Rühle et al., "A novel cadmium free buffer layer for Cu(In,Ga)Se<sub>2</sub> based solar cells," *Solar Energy Materials and Solar Cells*, vol. 41-42, pp. 345–353, 1996.
- [13] K. Govender, D. S. Boyle, and P. O'Brien, "Improved routes towards solution deposition of indium sulfide thin films for photovoltaic applications," *Materials Research Society*, vol. 692, pp. H9.33–H9.38, 2002.
- [14] N. Naghavia, E. Chassaing, S. Galanti et al., "Electrodeposition of In<sub>2</sub>S<sub>3</sub> buffer layer for Cu(In,Ga)Se<sub>2</sub> solar cells," in *Proceedings of the European Materials Research Society Conference Symposium, Advanced Inorganic Materials and Concepts for Photovoltaics*, Electrochemical Society, pp. 155–160, May 2011.
- [15] W. Schwarzacher, "Electrodeposition: a technology for the future," *Electrochemical Society Interface*, vol. 15, no. 1, pp. 32–33, 2006.
- [16] F. A. Kröger, "Cathodic deposition and characterization of metallic or semiconducting binary alloys or compounds," *Journal of Electrochemical Society*, vol. 125, no. 12, pp. 2028–2034, 1978.
- [17] D. Lincot, "Electrodeposition of semiconductors," in *Proceedings of the 207th Annual Meeting of the Electrochemical Society (ECS '05)*, Paris, France, 2005.
- [18] M. Krenzelo, P. Rychlovsky, M. Volny, and J. P. Matousek, "Evaluation of in situ electrodeposition technique in electrothermal atomic absorption spectrometry," *Analyst*, vol. 128, no. 3, pp. 293–300, 2003.

- [19] G. F. Fulop and R. M. Taylor, "Electrodeposition of semiconductors," *Annual Review of Material Science*, vol. 15, pp. 197–210, 1985.
- [20] I. N. Vuchkov and L. N. Boyadjieva, *Quality Improvement with Design of Experiments: A Response Surface Approach*, Kluwer Academic Publishers, Dordrecht, The Netherlands, 2001.
- [21] W.-L. Liu, S.-H. Hsieh, W.-J. Chen, P.-I. Wei, and J.-H. Lee, "Synthesis of the CuInSe<sub>2</sub> thin film for solar cells using the electrodeposition technique and Taguchi method," *International Journal of Minerals, Metallurgy and Materials*, vol. 16, no. 1, pp. 101–107, 2009.
- [22] S. T. Aruna, P. V. K. Srikanth, M. J. Ahamad, S. Latha, and K. S. Rajam, "Optimization of the properties of electrodeposited Ni-YSZ composites using Taguchi method and regression analysis," *Portugaliae Electrochimica Acta*, vol. 29, no. 1, pp. 23–37, 2011.
- [23] D. M. Steinberg and D. Burnsztytn, *Noise Factors, Dispersion Effects, and Robust Design*, vol. 107, Center for Quality and Product Improvement, University of Wisconsin, 1993.
- [24] S. H. Kang, Y.-K. Kim, D.-S. Choi, and Y.-E. Sung, "Characterization of electrodeposited CuInSe<sub>2</sub> (CIS) film," *Electrochimica Acta*, vol. 51, no. 21, pp. 4433–4439, 2006.

## Research Article

# A Novel Approach to the Fabrication of CdSe Quantum Dots in Aqueous Solution: Procedures for Controlling Size, Fluorescence Intensity, and Stability over Time

M. J. Almendral-Parra,<sup>1</sup> A. Alonso-Mateos,<sup>1</sup> J. F. Boyero-Benito,<sup>1</sup>  
S. Sánchez-Paradinas,<sup>1</sup> and E. Rodríguez-Fernández<sup>2</sup>

<sup>1</sup>Departamento de Química Analítica, Nutrición y Bromatología, Facultad de Ciencias Químicas, Universidad de Salamanca, Plaza de la Merced, s/n, 37007 Salamanca, Spain

<sup>2</sup>Departamento de Química Inorgánica, Facultad de Ciencias Químicas, Universidad de Salamanca, Plaza de la Merced, s/n, 37007 Salamanca, Spain

Correspondence should be addressed to M. J. Almendral-Parra; [almendral@usal.es](mailto:almendral@usal.es)

Received 10 October 2013; Accepted 4 April 2014; Published 24 April 2014

Academic Editor: M. Ghoranneviss

Copyright © 2014 M. J. Almendral-Parra et al. This is an open access article distributed under the Creative Commons Attribution License, which permits unrestricted use, distribution, and reproduction in any medium, provided the original work is properly cited.

This paper reports a straightforward approach for the synthesis of CdSe quantum dots (CdSe QDs) in aqueous solution. This method, performed in homogeneous phase, affords optimal sizes and high quantum yields for each application desired. It is an *a la carte* procedure for the synthesis of nanoparticles aimed at their later application. By controlling the experimental conditions, CdSe QDs of sizes ranging between 2 and 6 nm can be obtained. The best results were achieved in an ice-bath thermostated at 4°C, using mercaptoacetic acid as dispersant. Under these conditions, a slow growth of quantum nanocrystals was generated and this was controlled kinetically by the hydrolysis of  $\text{SeSO}_3^{2-}$  to generate  $\text{Se}^{2-}$  *in situ*, one of the forming species of the nanocrystal. The organic dispersant mercaptoacetate covalently binds to the  $\text{Cd}^{2+}$  ion, modifying the diffusion rate of the cation, and plays a key role in the stabilization of CdSe QDs. In optimum conditions, when kept in their own solution CdSe QDs remain dispersed over 4 months. The NPs obtained under optimal conditions show high fluorescence, which is a great advantage as regards their applications. The quantum efficiency is also high, owing to the formation under certain conditions of a *nanoshell* of  $\text{Cd}(\text{OH})_2$ , values of 60% being reached.

## 1. Introduction

Quantum dots (QDs) are semiconductor nanoparticles (NPs) that have recently attracted much interest in biological research because of their unique spectral properties [1–3]. They are composed of elements from groups II–VI, III–V, and IV–VI of the periodic table [4], having a more or less spherical shape and sizes typically ranging from 1 to 12 nm. They exhibit unique optical and electronic properties based on a strong quantum-confinement effect [5, 6]. One of the extraordinary properties of QDs is that their particle size determines most of their properties, mainly the wavelength of fluorescence emission, which can be altered by manipulating their size [7]. In comparison with traditional organic fluorophores, QDs

have considerable advantages [8], including size-dependent emission, narrow emission bands, and high luminescence. Furthermore, the high surface/volume ratio of QDs allows them to be used for the design of more complex nanosystems [9]. All the above properties make QDs good fluorescent markers for biological and biomedical applications, in particular in cellular imaging [10]. Moreover, they have attracted great interest for their potential application in electronic and optoelectronic devices [11, 12]. Strongly luminescent semiconductor nanocrystals are highly desirable for a large number of optoelectronic applications, such as light-emitting diodes (LEDs) [13]. In recent years, intense efforts have been made in the field of the synthesis and use of photoluminescent QDs as markers for biochemical applications in

bioanalysis, diagnosis, and in *in vivo* imaging. The different requirements in each case have resulted in the development of many different synthesis procedures, widely reported in the literature. Among the different semiconductor NPs, the synthesis of CdSe nanocrystals continues to be the field most widely investigated, mainly because the method of preparation used affords an exceptional degree of control over the size and shape of the nanocrystals obtained. High quality QDs are usually prepared at elevated temperatures in organic solvents such as tri-*n*-octylphosphine oxide (TOPO) or a mixture of TOPO and tri-*n*-octylphosphine (TOP). The surfaces of the QDs prepared in an organic phase are coated with a hydrophobic layer of TOP or TOPO molecules. However, these QDs cannot be applied directly in biosystems owing to the organic nature of their surfaces. Normally, it is necessary to replace the molecules coating the surface of the nanoparticle, using time-consuming methods of ligand exchange that significantly reduce the quantum yield of QDs. Additionally, it has been found that after ligand exchange these hydrophilic QDs are not sufficiently stable in aqueous solution. Some techniques of surface modification aimed at increasing the hydrophilic character and stability of QDs in aqueous solution have also been used. This change has often provided a significant increase in the diameter of the QDs to close to 20–30 nm. In contrast to organic synthesis, aqueous synthesis exhibits good reproducibility and low toxicity, and it is cheap, and—in particular—the products thus prepared have excellent water solubility, stability, and biological compatibility. Despite this, QDs prepared in aqueous phase tend to have low quantum yields (QY: 3–10%). However, perhaps owing to excessive haste in obtaining practical results that would meet the high expectations that will undoubtedly arise in relation to the use of QDs in biological media, our knowledge of their structures and chemical behavior (both of them critical aspects for optimizing the bioconjugation process) remains somewhat shallow. However, in recent years, methods for preparing luminescent QDs in aqueous solution have increased substantially in number due to the work of Zhang et al. [13, 14], who have made considerable advances in improving QY. All the results show that synthesis processes in aqueous media are an attractive alternative to the synthesis of QDs in organic media and they are now an important avenue of enquiry.

In the present work we report a simple procedure for the preparation of CdSe QDs in aqueous solution. By controlling the experimental conditions, CdSe QDs of sizes ranging between 2 and 6 nm can be obtained. The best results were achieved in an ice-bath thermostated at 4°C, using mercaptoacetic acid as dispersant. Under these conditions, a slow growth of quantum nanocrystals was generated and this was controlled kinetically by the hydrolysis of  $\text{SeSO}_3^{2-}$  to generate  $\text{Se}^{2-}$  *in situ*, one of the forming species of the nanocrystal. This homogeneous phase synthesis allows the different variables involved in the process to be controlled in order to obtain optimum sizes and high quantum yields for each application. It is an *a la carte* procedure for the synthesis of the NPs addressed here as regards their future use. The QDs obtained are stable for more than three months

under the experimental conditions used, maintaining their high fluorescence. NPs have been characterized by absorption spectroscopy, fluorescence spectroscopy, and transmission electron microscopy (TEM). These techniques have allowed in-depth studies of all the variables affecting their size and properties in aqueous solution for their possible use as biomarkers and in other applications of interest.

## 2. Experimental

**2.1. Reagents.** All chemical reagents were of analytical grade and used as purchased. Solutions were prepared with ultra-high quality deionized water. Cadmium chloride solutions were prepared by direct weighing of 99% pure anhydrous  $\text{CdCl}_2$  (Acros Organics) and dissolution in water. Aqueous solutions of anhydrous sodium sulphite,  $\text{Na}_2\text{SO}_3$  (Acros Organics), at different concentrations, were prepared at the time of use. Selenium powder, 99.99% pure (Aldrich), and 1 M sodium hydroxide, NaOH (Scharlau), were included.  $10^{-5}$  M quinine sulphate solution (Acros Organics) was prepared by direct weighing and dissolution in 0.5 M  $\text{H}_2\text{SO}_4$ . Buffer solutions of pH = 4.00 and pH = 7.00 (Scharlau). Mercaptoacetic acid (MAA),  $\text{HSCH}_2\text{COOH}$ , 98% (Acros Organics) was included.

**2.2. Instrumentation.** Fluorescence spectra were measured using a Shimadzu Model RF-5000 spectrofluorophotometer, with a Model DR-15 controller unit and a 150 W Xenon lamp as a light source. The slits for the excitation and emission widths were both 3 nm. The UV-visible absorption measurements of the samples were performed on a Shimadzu UV/Vis-160 spectrophotometer. The pH value of the solutions was measured with a Crison 501 pHmeter. TEM images were performed on a ZEISS EM-900 device.

### 2.3. Synthesis of CdSe Quantum Dots in Aqueous Medium

**2.3.1. Preparation and Determination of the Concentration of Sodium Selenosulphate Solutions.** As the  $\text{Se}^{2-}$  ion source, solutions of selenosulphate prepared from selenium powder and sodium sulphite were used and were prepared as follows. Briefly, 2.5 g of  $\text{Na}_2\text{SO}_3$  was added to 100 mL of deoxygenated water. Then, 0.4 g of selenium powder was added, allowing the reaction to take place at 80°C in sealed containers overnight. After this time, the solution was filtered and a reddish working stock solution was obtained. The final concentration of  $\text{SeSO}_3^{2-}$  was determined gravimetrically by weighing the solid selenium precipitated in acid medium. The stability of the  $\text{SeSO}_3^{2-}$  solutions over time was found to persist for at least one month, their concentrations remaining constant. In the experiments carried out during this work, when the  $\text{SeSO}_3^{2-}$  solution reached one month of life, a new solution was prepared and its concentration was determined.

**2.3.2. General Method for the Synthesis of CdSe NPs in Aqueous Medium.** The general procedure for obtaining CdSe nanoparticles in aqueous medium, without specifying the values of the variables set in each experimental study,

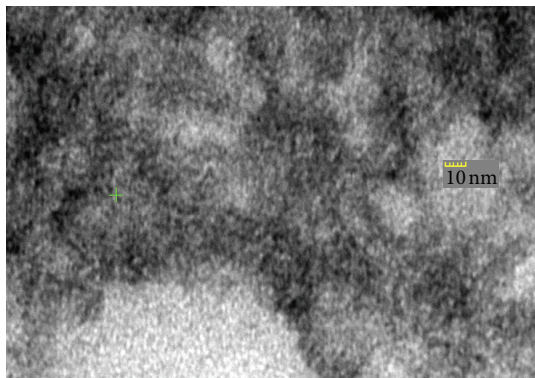
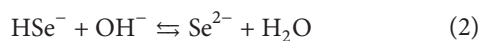


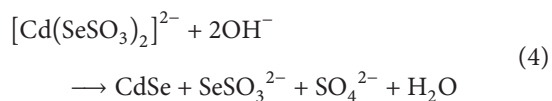
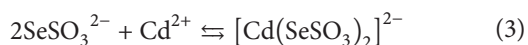
FIGURE 1: Characteristic TEM image of CdSe nanoparticles.

employed the following steps: 100 mL of a  $\text{Cd}^{2+}$  ion solution was placed in a topaz flask. Under stirring, the desired amount of a solution of 1.14 M mercaptoacetic acid was added. Then, the pH of the solution was adjusted with 1 M NaOH. When it was necessary to work at temperatures higher than the ambient temperature, this was achieved by controlled heating. Temperatures lower than ambient temperature were achieved by introducing the flask with the solution in an ice-bath ( $4^\circ\text{C}$ ) and keeping it there during the procedure. After the working temperature had been reached and  $\text{N}_2$  had been bubbled through the solution, the desired amount of  $\text{SeSO}_3^{2-}$  was added slowly, with stirring, to control the concentration of  $\text{Se}^{2-}$  in solution and to avoid supersaturation. The time of the addition of this reagent ranged between 8 and 10 min, considering this moment as  $t = 0$  for the kinetic studies. The final pH was checked to control for possible modifications. Periodically, the absorption spectra and the fluorescence excitation and emission spectra were recorded.

The  $\text{Se}^{2-}$  ion contribution to the formation of nanoparticles may come from two different routes. One of them involves the decomposition in basic medium of selenosulphate in two stages:



The second one involves the hydrolysis in basic medium of a complex formed by  $\text{Cd}^{2+}$  and selenosulphate:



Either way, or both, the fact is that the formation of nanoparticles is controlled by a slow kinetic chemical process similar to homogeneous phase precipitation processes.

The morphology of the CdSe nanoparticles was studied with TEM (Figure 1).

**2.3.3. Absorption Spectrum.** It is possible to obtain the mean value of the diameter of QDs by applying the Henglein equation (5), which relates it to the extrapolated wavelength,  $\lambda_e$ , and it is obtained by tracing the tangent to the absorption curve on the ascending segment, and it is clearly differentiated from the zero absorbance value:

$$2\bar{R} = \bar{d} = \frac{0.1}{(0.138 - 0.0002345 \cdot \lambda_e)}. \quad (5)$$

Figure 2 shows the procedure. Obtaining the value of  $\lambda_e$  is simple for times exceeding 95 min, when there is no turbidity in the solution, and above 500 nm the base line coincides with  $A = 0$ , but for lower times turbidity alters the baseline so the  $\lambda_e$  value must be obtained from the cut between the line tangent to the ascending part of the spectrum and the constant baseline drawn by the value of absorbance at 600 nm, as shown in Figure 2(a).

There is also a procedure for calculating the concentration of nanoparticles from the absorption spectral data. This method involves obtaining data by studying the region of wavelengths where the nanoparticles do not absorb radiation for excitonic processes and behave merely as colloids, dispersing the radiation as a function of size. In this region of the spectrum, the molar absorption coefficient of the nanoparticles,  $\epsilon_{\text{CdSe}}$ , is independent of their size.

The concentration of colloidal particles and thus nanoparticles can be determined by measuring absorbance at 350 nm (or lower wavelengths) as an indirect measurement of scattered light, using a relationship between two variables that is dependent on the size. This relationship, previously used by other researchers [13, 14], which is derived empirically and is related to the Rayleigh expression (intensity of light scattered by colloidal particles with a diameter less than the wavelength of the incident light  $\lambda$ ) is expressed in the following:

$$C_{\text{CdSe}} = \frac{A_{350}}{1.438 \times 10^{29} \cdot (2R)^3}, \quad (6)$$

where  $C_{\text{CdSe}}$  is the concentration of nanoparticles in moles  $\text{L}^{-1}$ ;  $A_{350}$  is the absorbance value measured at 350 nm; and  $R$  is the radius of the nanoparticle with a spherical shape.

Assuming the spherical shape of CdSe nanoparticles and taking into account their diameter the number of molecules that constitute a single CdSe nanocrystal at each instant can be calculated with the following expression:

$$N_{\text{CdSe}} = \frac{4\pi R^3}{3} \cdot \frac{\rho_{\text{CdSe}} \cdot N_0}{M_{\text{CdSe}}}, \quad (7)$$

where  $N_{\text{CdSe}}$  is the number of CdSe molecules on each nanoparticle;  $R$  is the radius of the NP in centimeters;  $\rho_{\text{CdSe}}$  is the density of CdSe in  $\text{g cm}^{-3}$ ;  $N_0$  is the Avogadro constant ( $6.023 \times 10^{23} \text{ mol}^{-1}$ ), and  $M$  is the molecular weight of CdSe ( $191.36 \text{ g mol}^{-1}$ ).

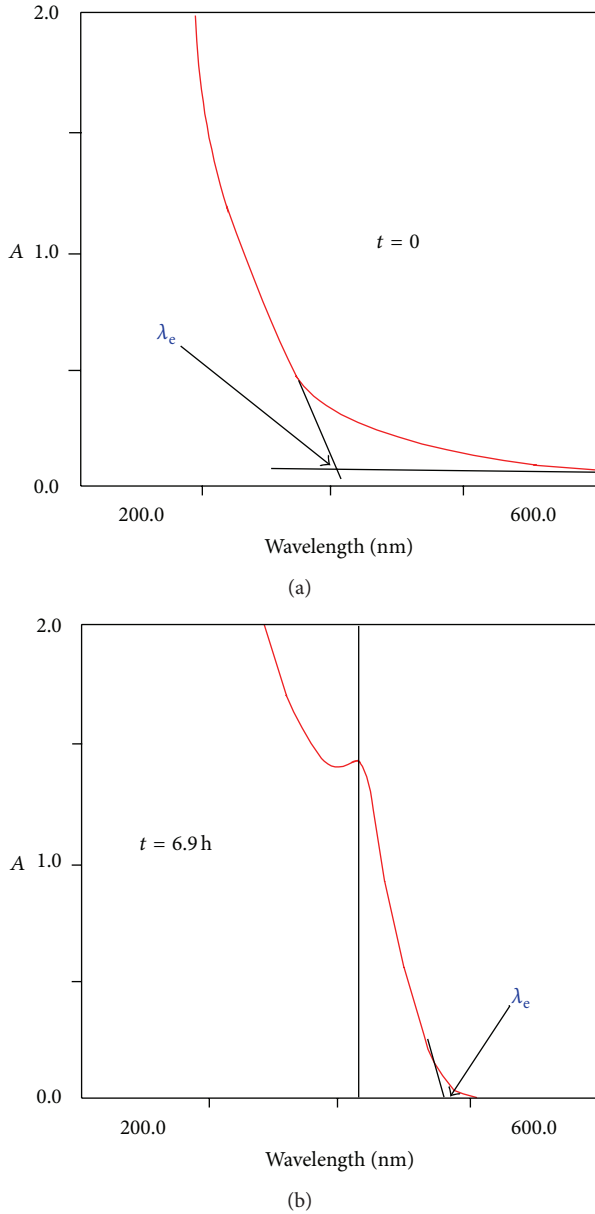


FIGURE 2: Absorption spectra of the CdSe quantum dots in aqueous solution. Calculating the value  $\lambda_e$  for a cloudy solution (a) and a solution without turbidity (b).

By multiplying (6) and (7) it is possible to obtain an equation to calculate the molar concentration of CdSe forming the nanoparticles:

$$\begin{aligned}
 (6) \cdot (7) &= [\text{CdSe}] \\
 &= \frac{A_{350}}{1.438 \times 10^{29} \cdot R^3} \frac{4\pi R^3}{3} \frac{\rho_{\text{CdSe}} \cdot N_0}{M_{\text{CdSe}}} \quad (8) \\
 &= 0.667 \times 10^{-4} MA_{350}.
 \end{aligned}$$

**2.3.4. Luminescence Spectrum.** An important aspect of nanoparticles is their luminescence behavior. To study this

feature, once the addition of  $\text{Na}_2\text{SeSO}_3$  is finished, aliquots of the solution were collected and placed in the spectrofluorometer. The shape of the excitation spectrum affords information about the state of the surface of the nanoparticles and its changes with time. The emission spectrum provides information about the fluorescence emission intensity of the nanoparticle and the size distribution of nanoparticles around the average diameter ( $d$ ), which is related to the full width at half maximum (FWHM), also called  $\Delta$ .

Based on measurement of the parameters mentioned above, a detailed study of the effect of several variables on the nanoparticle collection process was performed.  $\text{N}_2$  must be bubbled through the solution prior to the addition of  $\text{SeSO}_3^{2-}$ . If this is performed during the formation of the CdSe nanoparticles, their size would increase and therefore their concentration in solution would reduce and, as a result, the fluorescence emission intensity would also decline. The rate of addition of the  $\text{SeSO}_3^{2-}$  solution also affects the size of the nanoparticles: the higher this rate, the greater the size. Maintaining stirring after the addition of  $\text{SeSO}_3^{2-}$  modifies the composition of the nanoparticle surface, adversely affecting their luminescence properties. Besides depending on the concentration of nanoparticles, the fluorescence emission intensity depends on a process that occurs simultaneously at the surface. This process may involve the formation of hydroxylated complexes of cadmium, the formation of a film or nanoshell of cadmium hydroxide, or both, all of them affecting the luminescence quantum yield. Maximum fluorescence intensity is reached when the thickness of the nanoshell reaches a specific value, related to the mean diameter of the nanoparticles, there being an optimum ratio between nanoshell size and the size of the nanoparticle.

### 3. Results and Discussion

A profound knowledge of all the variables allows choice of the optimal conditions necessary to achieve the desired property in the nanoparticles for a particular application. Thus, what type of nanoparticles are we looking for?

In some cases, highly stable nanoparticles, preserved in their own solution, will be desirable. In other cases, highly fluorescent nanoparticles will be what we are interested in. Finally, nanoparticles with a size as small as possible will find other applications. Here we describe three synthesis methods that achieve these three objectives individually.

**3.1. Synthesis of Highly Stable CdSe Nanoparticles.** In this case, the specific experimental conditions were as follows: 8 mL of  $5 \times 10^{-2} \text{ M}$   $\text{CdCl}_2$  was diluted with bidistilled water up to 100 mL. Then,  $160 \mu\text{L}$  of mercaptoacetic acid solution 1.41 M was added. The pH of the solution was adjusted to 4.6 with NaOH and the flask was placed in an ice-bath until the solution reached  $4^\circ\text{C}$ . At this point,  $\text{N}_2$  was bubbled through for 15 min with constant stirring, after which 2.5 mL of 0.0892 M  $\text{SeSO}_3^{2-}$  was added over another 15 min. The solution obtained was stored at  $4^\circ\text{C}$ . Under these conditions, the final molar ratios were  $[\text{Cd}^{2+}]_F/[\text{Se}^{2-}]_F = 1.79$ ;  $[\text{Cd}^{2+}]_F/[\text{MAA}]_F = 1.77$ . The

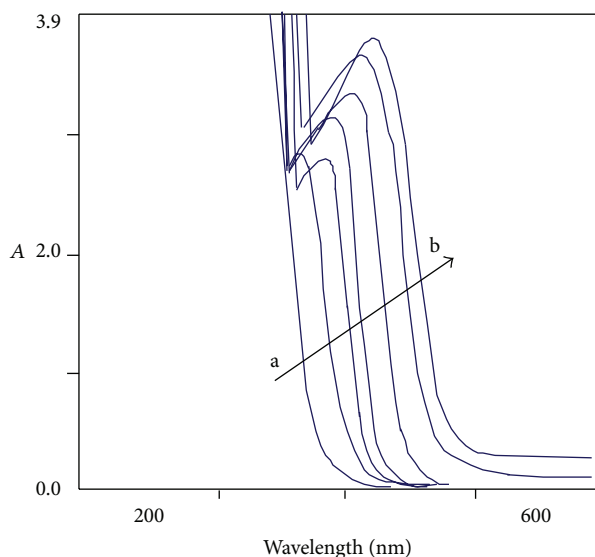


FIGURE 3: Evolution with time of the absorption spectrum of the highly stable CdSe QDs. From a ( $t = 0$ ) to b ( $t = 114$  days).

absorption spectra were measured at room temperature and are plotted in Figure 3.

Figure 3 shows the absorption spectrum of the aqueous solution from which the nanoparticles were obtained and its evolution with time. The appearance of an absorption band can be seen, manifesting initially with an inflection zone at around 350 nm and thereafter evolving to a clear peak at 443.5 nm at 22 hours. This absorption band is due to the presence of CdSe nanoparticles in which the electrons are confined quantumly, being able to absorb electromagnetic waves of a given energy to perform electronic transitions through the hollow bands of the semiconductor. With time, the absorption band is displaced towards higher wavelength values and the absorption value of the maximum of the band does so in the same sense. Both phenomena are related to the fact that the CdSe nanoparticles evolve with time, as seen from the increase in their mean diameter and in their concentration in solution.

The mean diameter changed from 2.1 nm at  $t = 0$  to 2.9 nm at  $t = 6$  days (Figure 4). This slow evolution was mainly due to kinetic control of the growth rate by the hydrolysis process at 4°C. Following this, there was a period of more than 70 days during which the CdSe nanoparticles maintained a fairly constant size. From day 103 the presence of a small yellow precipitate was observed, and when the solution was homogenized the absorbance value at the baseline was increased. This phenomenon is due to the rearrangement of nanoparticles to create insoluble aggregates, a process that leads to an increase in nanoparticle size. The fluorescence intensity values are plotted against time in Figure 4.

As can be seen, the maximum value of fluorescence intensity was reached on day 29 and remained practically constant until about day 90, thereafter starting to decline. In addition to their stability over a long period of time the CdSe

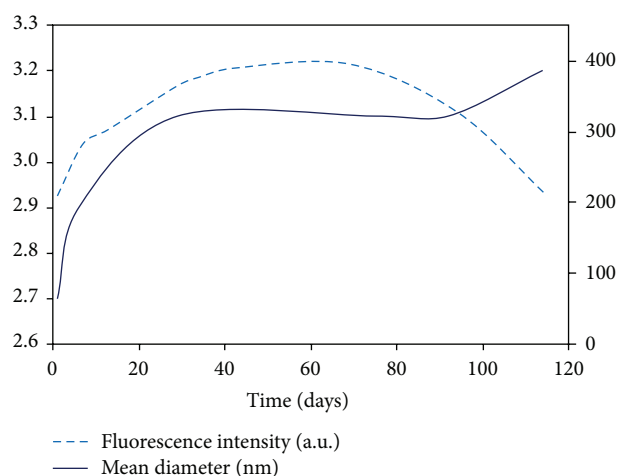


FIGURE 4: Evolution with time of the mean diameter (bold line) and the luminescence intensity (broken line) of the highly stable CdSe NPs.  $[\text{Cd}^{2+}]_{\text{F}}/[\text{Se}^{2-}]_{\text{F}} = 1.79$ ;  $[\text{Cd}^{2+}]_{\text{F}}/[\text{MAA}]_{\text{F}} = 1.77$ , pH = 4.6; temperature: 4°C;  $[\text{Cd}^{2+}]_{\text{F}} = 3.9 \times 10^{-3}$ ; *rendija*: 3 nm.

nanoparticles obtained under these experimental conditions had a relatively high and perfectly measurable fluorescence.

**3.2. Obtaining Highly Fluorescent CdSe Nanoparticles.** One of the possible applications of CdSe nanoparticles is their use in *in vivo* studies as carriers of molecules of biochemical interest, in which case their effectiveness must be followed through their luminescence properties. To ensure the sensitivity of the measurements it is useful to have highly fluorescent nanoparticles.

In this part of the study, the same synthesis procedure as that described above was followed, with one difference: the final concentration of  $\text{SeSO}_3^{2-}$  was  $1.06 \times 10^{-3}$  M. The molar ratios of the reagents were as follows:  $[\text{Cd}^{2+}]_{\text{F}}/[\text{Se}^{2-}]_{\text{F}} = 3.74$ ;  $[\text{Cd}^{2+}]_{\text{F}}/[\text{MAA}]_{\text{F}} = 1.77$ . Because of the excess of  $\text{Cd}^{2+}$  ions in solution (compared to selenium ions) in this case the nucleation rate was higher than the growth rate.

The aim of this experiment was to obtain CdSe nanoparticles that would be as fluorescent as possible and would retain this property for as long as possible. Accordingly, below we focus our comments on the luminescence properties of nanoparticles obtained.

As can be seen in Figure 5, these nanoparticles had a very high fluorescence intensity, which remained practically constant between days 22 and 37. It was at this time when the optimal nanoparticle size/nanoshell size ratio was reached and when the quantum efficiency of the luminescence process was maximum.

**3.3. Preparation of the Smallest Nanoparticles Possible.** Size is an important factor in the ability of nanoparticles to cross the cell membrane and be effective in their role as drug carriers. When desired, by controlling the experimental conditions it is possible to obtain small nanoparticles that will remain small for long periods of time. As shown previously, the growth rate of nanoparticles can be controlled kinetically

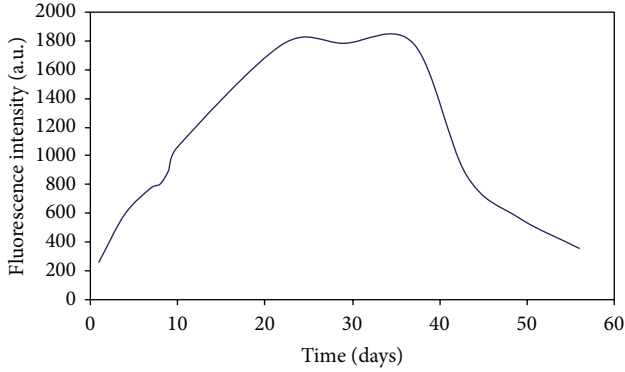


FIGURE 5: Evolution with time of the luminescence intensity of the highly fluorescent CdSe nanoparticles:  $[\text{Cd}^{2+}]_{\text{F}}/[\text{Se}^{2-}]_{\text{F}} = 3.74$ ;  $[\text{Cd}^{2+}]_{\text{F}}/[\text{MAA}]_{\text{F}} = 1.77$ , pH = 4.6; temperature: 4°C;  $[\text{Cd}^{2+}]_{\text{F}} = 3.9 \times 10^{-3}$ ; rendija: 3 nm.

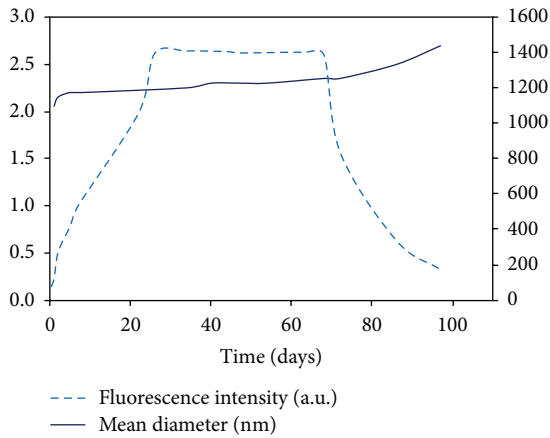


FIGURE 6: Evolution with time of the mean diameter (bold line) and the luminescence intensity (broken line) of the smallest CdSe nanoparticles possible:  $[\text{Cd}^{2+}]_{\text{F}}/[\text{Se}^{2-}]_{\text{F}} = 5.60$ ;  $[\text{Cd}^{2+}]_{\text{F}}/[\text{MAA}]_{\text{F}} = 1.77$ , pH = 4.6; temperature: 4°C;  $[\text{Cd}^{2+}]_{\text{F}} = 3.9 \times 10^{-3}$ ; rendija: 3 nm.

by fixing the synthesis temperature at 4°C and the solution pH at 4.6. Additionally, the greater the excess of  $\text{Cd}^{2+}$  in solution over  $\text{SeSO}_3^{2-}$ , the higher the nucleation rate and the lower the growth rate. To check these theoretical aspects, CdSe nanoparticles were obtained under the experimental conditions of the two previous assays, but with the following molar ratios:  $[\text{Cd}^{2+}]_{\text{F}}/[\text{Se}^{2-}]_{\text{F}} = 5.60$ ;  $[\text{Cd}^{2+}]_{\text{F}}/[\text{MAA}]_{\text{F}} = 1.77$ . The size of CdSe nanoparticles increased from 1.9 nm at  $t = 0$  to 2.2 nm at 5 days, but then their size remained smaller than 2.3 nm for more than 60 days (Figure 6).

Figure 6 shows that the maximum value of fluorescence intensity was reached at about the same time as in the previous experiment. In this experiment, the maximum fluorescence value was slightly lower but remained constant over a longer period of time. This difference can be attributed to the amount of mercaptoacetate surrounding the nanoparticles, depending on their size and affecting the stability of the colloidal system. Apparently, the number of MAA molecules

TABLE 1: Spectral characteristics of the CdSe nanoparticles from two different experiments performed under the same experimental conditions (Experiment A: bold; Experiment B, 23 h later: not bold).

Time	A	$\lambda_{\text{abs}}$	$d$	FI	$\lambda_{\text{ex}}$	$\lambda_{\text{em}}$	
1 hour	<b>2.503</b>	<b>362</b>	<b>2.2</b>	<b>27.64</b>	<b>395</b>	<b>492</b>	<b>A</b>
	2.489	360	2.2	22.52	401	491	B
12 days	<b>2.826</b>	<b>388</b>	<b>2.7</b>	<b>168.64</b>	<b>425</b>	<b>497</b>	<b>A</b>
	2.853	393	2.7	172.73	425	497	B
62 days	<b>2.937</b>	<b>398</b>	<b>2.8</b>	<b>94.91</b>	<b>432</b>	<b>502</b>	<b>A</b>
	2.940	402	2.8	113.28	438	505	B

A: absorption;  $\lambda_{\text{abs}}$ : absorption wavelength in nm;  $d$ : mean diameter in nm; FI: fluorescence intensity in arbitrary units;  $\lambda_{\text{ex}}$ : excitation wavelength in nm;  $\lambda_{\text{em}}$ : emission wavelength in nm.

surrounding one nanoparticle was higher in this experiment (because of the lower mean diameter), and hence stability was also higher.

**3.4. Reproducibility in the Synthesis Process.** One of the strongest criticisms usually made concerning the methods used for obtaining crystals, colloids, and nanoparticles is the lack of reproducibility due to the amount of variables that influence their synthesis, some of them uncontrolled. In order to check the reproducibility of the proposed method for the synthesis of CdSe nanoparticles in aqueous media, two experiments (A and B) were prepared and carried out under the same experimental conditions, but one of them 23 h later (B).

After studying the absorption spectra, it was found that there were no significant differences between the spectra of either experiment at similar times (Table 1). The size of the nanoparticles, the wavelength at which the inflection points appeared, and the maximum absorption value were similar for similar times.

However, reproducibility in the size and concentration of the  $C_{\text{CdSe}}$  nanoparticles obtained in two similar and parallel experiences is not sufficient to demonstrate the reproducibility of the method of synthesis. As demonstrated previously, the state of the surface of the nanoparticles is critical for explaining the luminescence properties. The only way to check that the surface is reproducible is to record the luminescence properties of the nanoparticles. By comparing the emission spectra of the nanoparticles for similar times, it is possible to check the reproducibility of the surface. Neither the optimal  $\lambda_{\text{em}}$  nor the value of fluorescence intensity differed significantly (Table 1).

The proposed method for preparing CdSe nanoparticles in aqueous medium showed good reproducibility.

## 4. Conclusions

We have developed a simple, easy, and cheap method for obtaining CdSe nanoparticles. Synthesis is performed in an aqueous medium and this solves one of the drawbacks of synthesis in organic media, namely, the later stage of solubilization in aqueous media, which sometimes alters not

only the size of the nanoparticles but also their luminescence properties. By controlling the experimental conditions, CdSe quantum dots of sizes ranging between 2 and 6 nm can be obtained.

We achieved a very slow nanocrystal growth rate due to the kinetic control of the low temperature (4°C), which controls  $\text{SeSO}_3^{2-}$  hydrolysis to generate  $\text{Se}^{2-}$ . Thus, the method can be referred to as the *in situ* and homogeneous phase generation of nanocrystal-forming  $\text{Se}^{2-}$  species.

## Conflict of Interests

The authors declare that there is no conflict of interests regarding the publication of this paper.

## Acknowledgment

The authors thank the Council for Education and Culture of the Regional Government of Castilla y León for financial support.

## References

- [1] D. Ramadurai, D. Geerpuram, D. Alexson et al., “Electrical and optical properties of colloidal semiconductor nanocrystals in aqueous environments,” *Superlattices and Microstructures*, vol. 40, no. 1, pp. 38–44, 2006.
- [2] S. Pathak, M. C. Davidson, and G. A. Silva, “Characterization of the functional binding properties of antibody conjugated quantum dots,” *Nano Letters*, vol. 7, no. 7, pp. 1839–1845, 2007.
- [3] R. S. Chouhan, A. C. Vinayaka, and M. S. Thakur, “Thiol-stabilized luminescent CdTe quantum dot as biological fluorescent probe for sensitive detection of methyl parathion by a fluoroimmunochemical technique,” *Analytical and Bioanalytical Chemistry*, vol. 397, no. 4, pp. 1467–1475, 2010.
- [4] W. W. Yu, L. Qu, W. Guo, and X. Peng, “Experimental determination of extinction coefficient of CdTe, CdSe, and CdS nanocrystals,” *Chemical Materials*, vol. 15, no. 14, pp. 2854–2860, 2003.
- [5] A. P. Alivisatos, “Semiconductor clusters, nanocrystals, and quantum dots,” *Science*, vol. 271, no. 5251, pp. 933–937, 1996.
- [6] C. J. Murphy and J. L. Coffey, “Quantum dots: a primer,” *Applied Spectroscopy*, vol. 56, no. 1, pp. 16A–27A, 2002.
- [7] W. W. Yu, E. Chang, R. Drezek, and V. L. Colvin, “Water-soluble quantum dots for biomedical applications,” *Biochemical and Biophysical Research Communications*, vol. 348, no. 3, pp. 781–786, 2006.
- [8] F. Pinaud, X. Michalet, L. A. Bentolila et al., “Advances in fluorescence imaging with quantum dot bio-probes,” *Biomaterials*, vol. 27, no. 9, pp. 1679–1687, 2006.
- [9] T. Jamieson, R. Bakhshi, D. Petrova, R. Pocock, M. Imani, and A. M. Seifalian, “Biological applications of quantum dots,” *Biomaterials*, vol. 28, no. 31, pp. 4717–4732, 2007.
- [10] P. Alivisatos, “The use of nanocrystals in biological detection,” *Nature Biotechnology*, vol. 22, no. 1, pp. 47–52, 2004.
- [11] P. T. Tran, E. R. Goldman, G. P. Anderson, J. M. Mauro, and H. Mattoussi, “Use of luminescent CdSe-ZnS nanocrystal bioconjugates in quantum dot-based nanosensors,” *Physica Status Solidi (B)*, vol. 229, pp. 427–432, 2002.
- [12] D. Gerion, F. Pinaud, S. C. Williams et al., “Synthesis and properties of biocompatible water-soluble silica-coated CdSe/ZnS semiconductor quantum dots,” *Journal of Physical Chemistry B*, vol. 105, no. 37, pp. 8861–8871, 2001.
- [13] H. Zhang, Z. Cui, Y. Wang et al., “From water-soluble CdTe nanocrystals to fluorescent nanocrystal-polymer transparent composites using polymerizable surfactants,” *Advanced Materials*, vol. 15, no. 10, pp. 777–780, 2003.
- [14] J. Weng, X. Song, L. Li et al., “Highly luminescent CdTe quantum dots prepared in aqueous phase as an alternative fluorescent probe for cell imaging,” *Talanta*, vol. 70, no. 2, pp. 397–402, 2006.

## Research Article

# Sm:HAp Nanopowders Present Antibacterial Activity against *Enterococcus faecalis*

Carmen Steluta Ciobanu,<sup>1</sup> Cristina Liana Popa,<sup>1,2</sup> and Daniela Predoi<sup>1</sup>

<sup>1</sup> National Institute of Materials Physics, P.O. Box MG 07, 76900 Bucharest, Romania

<sup>2</sup> Faculty of Physics, University of Bucharest, 405 Atomistilor, P.O. Box MG-1, 077125 Bucharest, Romania

Correspondence should be addressed to Daniela Predoi; [dpredoi@gmail.com](mailto:dpredoi@gmail.com)

Received 22 January 2014; Accepted 24 February 2014; Published 17 April 2014

Academic Editor: Necdet Aslan

Copyright © 2014 Carmen Steluta Ciobanu et al. This is an open access article distributed under the Creative Commons Attribution License, which permits unrestricted use, distribution, and reproduction in any medium, provided the original work is properly cited.

The synthesis of nanoparticles with inhibitory and bactericidal effects represents a great interest in development of new materials for biological applications. In this paper we present for the first time the synthesis of  $\text{Ca}_{10-x}\text{Sm}_x(\text{PO}_4)_6(\text{OH})_2$  nanoparticles at low temperature and primary tests concerning the adherence of *Enterococcus faecalis* ATCC 29212 (gram-positive bacteria). All the XRD peaks were indexed in accordance with the hexagonal HAp in P63m space group. The EDAX spectrum and elemental mapping of O, P, Ca, and Sm demonstrate that all the elements were homogeneously distributed in  $\text{Ca}_{10-x}\text{Sm}_x(\text{PO}_4)_6(\text{OH})_2$  with  $x_{\text{Sm}} = 0.03$ . The peaks at 347.3 eV, 532.1 eV, and 133.8 eV in the XPS spectra can be attributed to the binding energy of Ca 2p, O 1s, and P 2p. The peak at 1084.4 eV observed in  $\text{Ca}_{10-x}\text{Sm}_x(\text{PO}_4)_6(\text{OH})_2$  was attributed to the Sm 3d<sub>5/2</sub>. Bacterial adhesion was reduced on  $\text{Ca}_{10-x}\text{Sm}_x(\text{PO}_4)_6(\text{OH})_2$  sample when compared to pure HAp ( $x_{\text{Sm}} = 0$ ) and significant differences in bacterial adhesion on pure HAp ( $x = 0$ ) and Sm:HAp ( $x_{\text{Sm}} = 0.01$ ,  $x_{\text{Sm}} = 0.03$ , and  $x_{\text{Sm}} = 0.1$ ) were observed. The bacterial adhesion decreased when the samarium concentrations increased. Finally, we demonstrate that the Sm:HAp nanopowder with  $x_{\text{Sm}} > 0$  showed high antibacterial activity against *Enterococcus faecalis* ATCC 29212.

## 1. Introduction

In the past decades scientists worldwide have tried to find new solutions for improving treatments used for different bone related diseases and injuries. Their attention has been focused to the field of biomaterials in order to create and develop new and improved materials for tissue engineering [1–3]. Among these materials, hydroxyapatite (HAp) is one of the most commonly used for bone implants [4–9] or it is a drug release system [4, 10–15]. Moreover, it has been shown that it is also a good candidate for the role of adsorbent in column chromatography, in order to separate and purify nucleic acids and proteins [3, 16, 17]. It is possible to use hydroxyapatite for a large number of applications in the biomedical field due to its remarkable properties, such as biocompatibility, bioactivity, and osteoconductivity [4, 18–21]. In live tissue, HAp is the major mineral component of human bones and teeth [4, 22, 23]. Various factors, such

as grain size, morphology, surface area, and microporosity [24–26], must be taken into account when developing the biomaterial. Therefore, in order to improve the properties of HAp (for its use in different bone tissue applications), researchers have developed various methods of obtaining new compounds based on HAp doped with different rare-earth (RE) ions [24, 27]. The choice for lanthanides as doping agents has been made due to their high bioactivity and their ability to substitute calcium ions in structured molecules [24, 28–30]. It has been reported that lanthanides have been previously used in the biomedical field as contrast agents for magnetic resonance imaging and as luminescent probes for biosensors used for various *in vivo* imaging applications [24, 28, 29, 31], due to their narrow emission bands and long emission lifetime [24, 32, 33]. Among the rare-earth elements, samarium (Sm) is a good candidate for different radiation therapies used for cancer treatments. For more than a decade, <sup>153</sup>Sm isotopes have been used for cancer radiation

treatments [4, 34, 35] which are now administered clinically to patients that have symptomatic bone metastases from different types of cancer, mostly prostatic and breast carcinoma, for pain alleviation [4, 34–37]. In addition, different new studies have used  $^{153}\text{Sm}$ -hydroxyapatite particles as radiation synovectomy agent in the treatment of chronic synovitis [38–41], especially knee synovitis [38, 39]. Radiation synovectomy is a method used to alleviate the pain of patients suffering from swelling of rheumatoid arthritis [42]. Furthermore, another major problem encountered in the medical field is the inflammation of the synovial membrane caused by prosthetic joint infections (PJI) [43] which could also be treated by radiation synovectomy. The procedure involves an intra-articular injection of the beta-emitting radiopharmaceutical into the joint space. Once the radionuclide decays, the regenerating synovium starts to be irradiated [41]. Therefore, the  $^{153}\text{Sm}$ -hydroxyapatite particles are better candidates for this type of treatment than other compounds based on  $^{90}\text{Y}$  due to the shorter half-life of  $^{153}\text{Sm}$  and the lower extra-articular leakage of  $^{153}\text{Sm}$ -hydroxyapatite [39]. Furthermore, it has been shown that  $^{153}\text{Sm}$  emits  $\beta$  rays with a small tissue penetration (0.8 mm), more than 99% of the  $^{153}\text{Sm}$  being bound to the hydroxyapatite *in vivo* [44]. According to a clinical study made by Brazilian researchers after one year of treatment based on  $^{153}\text{Sm}$ -hydroxyapatite on patients suffering from haemophilic arthropathy, it was established that this treatment is effective for several types of joints. They obtained good results for 75% of elbows, 87.5% of ankles, and 40% of knees [45].

The prior studies have focused on preparation and characterization of complexes of europium (III) metal ion with organic reagents [46]. On the other hand, previous studies concerning the antibacterial and antifungal activity of ligand and its metal complexes tested against gram-positive and gram-negative bacteria, yeast, and fungi show that the complexes are more potent antimicrobials than the parent ligand [47–49].

The studies on the preparation, physicochemical characterization, and biological properties of the samarium doped hydroxyapatite (Sm:HAp) powders are absent in the literature. In this paper we present for the first time a method to synthesize the nanocrystalline hydroxyapatite doped with samarium at low temperature. Physicochemical characterization and antimicrobial studies on the Sm:HAp nanopowder are also presented for the first time. The results obtained suggest that the new obtained material,  $^{153}\text{Sm}$ -hydroxyapatite, could be a good candidate for treating the inflamed and damaged synovial membrane of the joint encountered in the case of prosthetic joint infections.

The  $\text{Ca}_{10-x}\text{Sm}_x(\text{PO}_4)_6(\text{OH})_2$  powders were synthesized by coprecipitation method at low temperature, mixing  $\text{Sm}(\text{NO}_3)_3 \cdot 6\text{H}_2\text{O}$ ,  $\text{Ca}(\text{NO}_3)_2 \cdot 4\text{H}_2\text{O}$ , and  $(\text{NH}_4)_2\text{HPO}_4$  in deionized water. The structure, morphology, and vibrational properties of the obtained samples were studied by X-ray diffraction (XRD), scanning electron microscopy (SEM), and Fourier transform infrared spectroscopy (FT-IR). In order to reveal the presence of the samarium in the Sm:HAp nanopowder with  $x_{\text{Sm}} = 0.01, 0.03, \text{ and } 0.1$ , the X-ray

photoelectron spectroscopy (XPS) results are also presented. In addition, the preliminary antibacterial activity of the  $\text{Ca}_{10-x}\text{Sm}_x(\text{PO}_4)_6(\text{OH})_2$  nanopowder with  $x_{\text{Sm}} = 0.01, 0.03, \text{ and } 0.1$  is reported.

## 2. Experimental Section

**2.1. Sample Preparation.** All the reagents used for the synthesis, including ammonium dihydrogen phosphate  $[(\text{NH}_4)_2\text{HPO}_4]$ , calcium nitrate tetrahydrate  $[\text{Ca}(\text{NO}_3)_2 \cdot 4\text{H}_2\text{O}]$ , and Samarium(III) nitrate hexahydrate  $\text{Sm}(\text{NO}_3)_3 \cdot 6\text{H}_2\text{O}$  (Sigma-Aldrich), were purchased without further purification.

Nanocrystalline hydroxyapatite doped with Sm,  $(\text{Ca}_{10-x}\text{Sm}_x(\text{PO}_4)_6(\text{OH})_2)$ , with  $x_{\text{Sm}} = 0$  to  $x_{\text{Sm}} = 0.1$  was obtained by setting the atomic ratio of  $\text{Sm}/[\text{Sm}+\text{Ca}]$  from 0% to 10% and  $[\text{Ca}+\text{Sm}]/\text{P}$  as 1.67. The  $\text{Sm}(\text{NO}_3)_3 \cdot 6\text{H}_2\text{O}$  and  $\text{Ca}(\text{NO}_3)_2 \cdot 4\text{H}_2\text{O}$  were dissolved in deionised water to obtain 300 mL  $[\text{Ca}+\text{Sm}]$  containing solution. On the other hand, the  $(\text{NH}_4)_2\text{HPO}_4$  was dissolved in deionised water to make 300 mL P-containing solution. The  $[\text{Ca}+\text{Sm}]$  containing solution was put into a Berzelius and stirred at  $100^\circ\text{C}$  for 30 minutes. Meanwhile, the pH of P-containing solution was adjusted to 10 with  $\text{NH}_3$  and stirred continuously for 30 minutes. The P-containing solution was added drop by drop into the  $[\text{Ca}+\text{Sm}]$  containing solution and stirred for 2 h, the pH being constantly adjusted and kept at 10. After the reaction, the deposited mixtures were washed several times with deionised water. The resulting material (Sm:HAp) was dried at  $100^\circ\text{C}$ . The scheme of the present study is presented in Figure 1.

**2.2. Sample Characterization.** The X-ray diffraction measurements of  $\text{Ca}_{10-x}\text{Sm}_x(\text{PO}_4)_6(\text{OH})_2$  samples were recorded using a Bruker D8 Advance diffractometer, with nickel filtered  $\text{Cu K}\alpha$  ( $\lambda = 1.5418 \text{ \AA}$ ) radiation and a high efficiency one-dimensional detector (Lynx Eye type) operated in integration mode. The diffraction patterns were collected in the  $2\theta$  range  $15^\circ$ – $140^\circ$ , with a step of  $0.02^\circ$  and 34 s measuring time per step.

The scanning electron microscopy (SEM) study was performed on a HITACHI S2600N-type microscope equipped with an energy dispersive X-ray attachment (EDAX/2001 device). Energy dispersive X-ray analysis, referred to as EDS or EDAX, was used to identify the elemental composition of materials.

The functional groups present in the prepared nanoparticles and thin films were identified by FTIR using a Spectrum BX spectrometer. In order to obtain the nanoparticles spectra, 1% of nanopowder was mixed and ground with 99% KBr. Tablets of 10 mm diameter were prepared by pressing the powder mixture at a load of 5 tons for 2 min. The spectrum was taken in the range of  $500$  to  $4000 \text{ cm}^{-1}$  with  $4 \text{ cm}^{-1}$  resolution.

X-ray photoelectron spectroscopy (XPS) studies were conducted using a VG ESCA 3 MK II XPS installation ( $E_{\text{K}\alpha} = 1486.7 \text{ eV}$ ). The vacuum analysis chamber pressure was  $P \sim 3 \times 10^{-8}$  torr. The XPS recorded spectrum involved an energy window  $w = 20 \text{ eV}$  with the resolution  $R = 50 \text{ eV}$  with 256

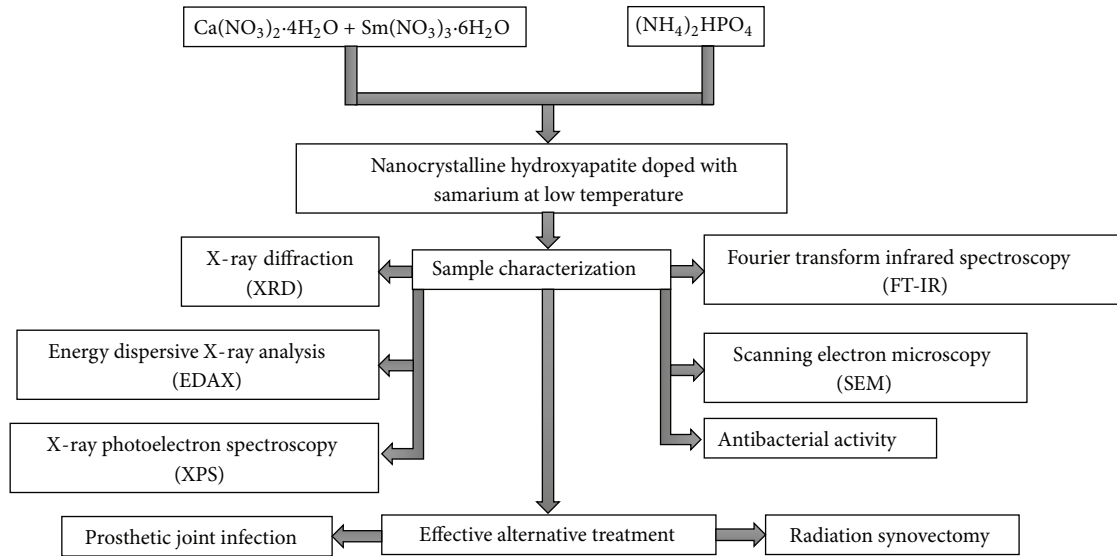


FIGURE 1: Schematic representation of preparation and evaluation of new antimicrobial Sm:HAP ceramics.

TABLE 1: Lattice parameters of Sm doped hydroxyapatite and crystallite sized.

Samples	$a$ -axis (Å)	$c$ -axis (Å)	Unit cell volume (Å <sup>3</sup> )	Crystallite size $D$ (nm)
$x_{Sm} = 0.01$	9.4195	6.8857	528.8875	18.14
$x_{Sm} = 0.03$	9.4299	6.8864	529.9895	17.53
$x_{Sm} = 0.1$	9.4398	6.8897	531.5923	12.67

recording channels. The XPS spectra were processed using Spectral Data Processor v 2.3 (SDP) software.

In order to test the *in vitro* antibacterial activity, the strains of bacteria used were *Enterococcus faecalis* ATCC 29212. The bacteria were grown overnight in Todd-Hewitt broth supplemented with 1% yeast extract at 37°C, followed by centrifuging. The supernatants were discarded and pellets were resuspended in phosphate-buffered saline (PBS) followed by a second centrifuging and resuspension in PBS. The samples to be tested were placed in 50 mL sterilized tubs followed by the addition of 2 mL of the bacterial suspension. The tubes were incubated at 3°C for 4h. At the end of the incubation period, the samples were gently rinsed three times with PBS. The nonadherent bacteria were eliminated. After washing, the samples were then put into a new tube containing 5 mL PBS and vigorously vortexed for 30 s to remove the adhering microorganisms. The viable organisms in the buffer were quantified by plating serial dilutions on yeast extract agar plates. Yeast extract agar plates were incubated for 24 h at 3°C and the colony forming units were counted visually.

### 3. Results and Discussions

In Figure 2 the XRD patterns of the synthesized  $\text{Ca}_{10-x}\text{Sm}_x(\text{PO}_4)_6(\text{OH})_2$  nanopowders with  $x_{Sm} = 0.01, 0.03,$  and  $0.1$  are shown. Good pattern fit of the synthesized Sm:HAP structures was determined using the Rietveld method implemented in the software package Materials Analysis Using

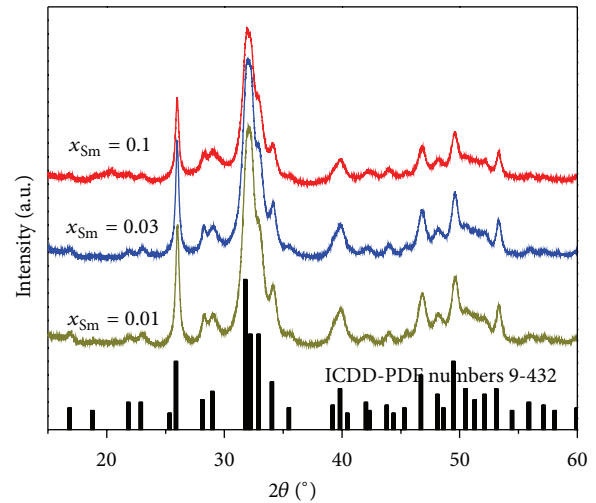


FIGURE 2: XRD patterns of  $\text{Ca}_{10-x}\text{Sm}_x(\text{PO}_4)_6(\text{OH})_2$  nanopowders with  $0.01 \leq x_{Sm} \leq 0.1$ .

Diffraction (MAUD) [50] by applying the Popa approach for the anisotropic microstructure analysis [51] implemented in the MAUD as “Popa rules.”

The XRD patterns of the Sm:HAP nanopowders with  $x_{Sm} = 0.01, 0.03,$  and  $0.1$  appeared to be identical, regardless of the Sm content in the samples. Sm doped hydroxyapatite exerted no effect on the phase composition of pure HAP.

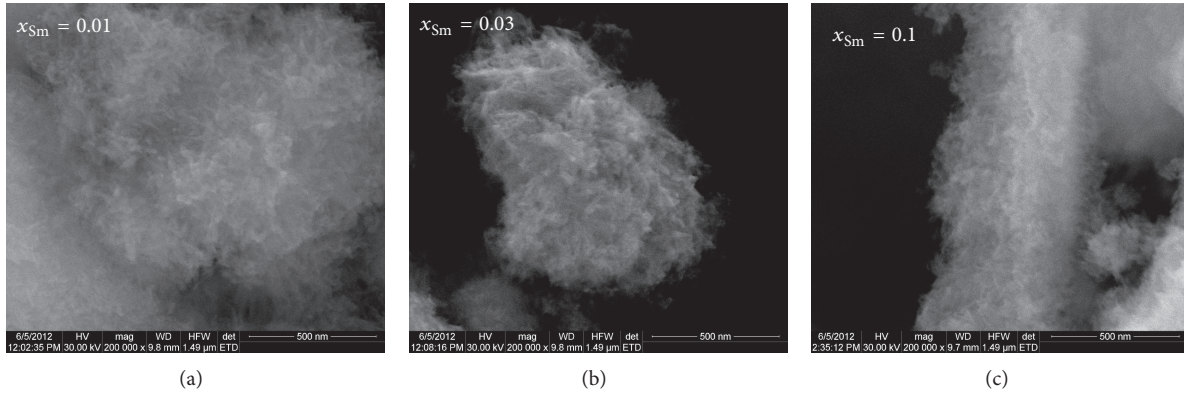


FIGURE 3: SEM images of samarium doped hydroxyapatite (Sm:HAp) powders with  $x_{\text{Sm}} = 0.01$ ,  $x_{\text{Sm}} = 0.03$ , and  $x_{\text{Sm}} = 0.1$ .

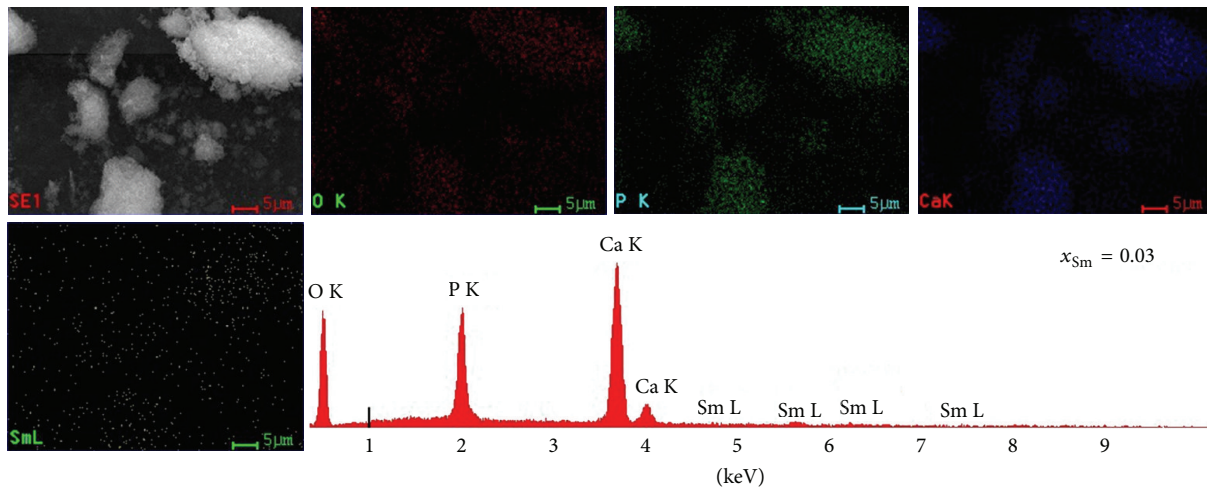


FIGURE 4: EDX spectrum and element maps of oxygen, phosphorus, calcium, and samarium (for the powders with  $x_{\text{Sm}} = 0.03$ ).

No secondary phases than those associated with HAp were detected. All the XRD peaks were indexed in accordance with the hexagonal HAp in  $P_{63m}$  space group (JCPDS card number 9-432). On the other hand, no change took place in the symmetry of the HAp crystallographic unit cell.

In the XRD spectra of the Sm:HAp powders, the diffraction peak intensities were reduced and the peak shapes were broadened when the Sm concentration increased. The broadened peaks when Sm concentration increased in the Sm:HAp samples are attributed to the small grain size. However, small variations of lattice constants and crystallite size were observed when the samarium content increases as it can be seen in Table 1.

Typical particle morphology of the Sm:HAp ( $x_{\text{Sm}} = 0.01$ ,  $x_{\text{Sm}} = 0.03$  and  $x_{\text{Sm}} = 0.1$ ) samples are shown in Figure 3. The surface morphology investigated by scanning electron microscopy reveals that the particles have a small, long morphology, coexisting with agglomerates. The results suggest that the doping of Sm has little influence on the morphology of Sm:HAp samples.

In order to investigate the uniformity of the element distribution in Sm:HAp samples, the EDX mapping technique was used. Figure 4 shows the EDAX spectrum and elemental mapping of O, P, Ca, and Sm and demonstrates that all the elements were homogeneously distributed in  $\text{Ca}_{10-x}\text{Sm}_x(\text{PO}_4)_6(\text{OH})_2$  with  $x_{\text{Sm}} = 0.03$ . On the other hand, the purity of the synthesized powders was also demonstrated. Similar results regarding the homogenous distribution of O, P, Ca, and Sm in the Sm:HAp samples were obtained for all the analysed samples.

FT-IR spectroscopy was performed in order to investigate the functional groups present in the nanohydroxyapatite,  $\text{Ca}_{10-x}\text{Sm}_x(\text{PO}_4)_6(\text{OH})_2$  ( $x_{\text{Sm}} = 0.01$ ,  $x_{\text{Sm}} = 0.03$ , and  $x_{\text{Sm}} = 0.1$ ) samples. In Figure 5 the FT-IR spectra of samarium doped hydroxyapatite with various concentration are presented.

In the FT-IR spectra, the presence of  $[\text{OH}]^-$  vibration peak at  $632\text{ cm}^{-1}$  could be observed for all the samples [52]. This band arises from stretching vibrational mode of  $[\text{OH}]^-$ . According to Markovic et al. [53], the sharpness of bands, especially sharpness of the  $632\text{ cm}^{-1}$ ,  $603\text{ cm}^{-1}$ , and

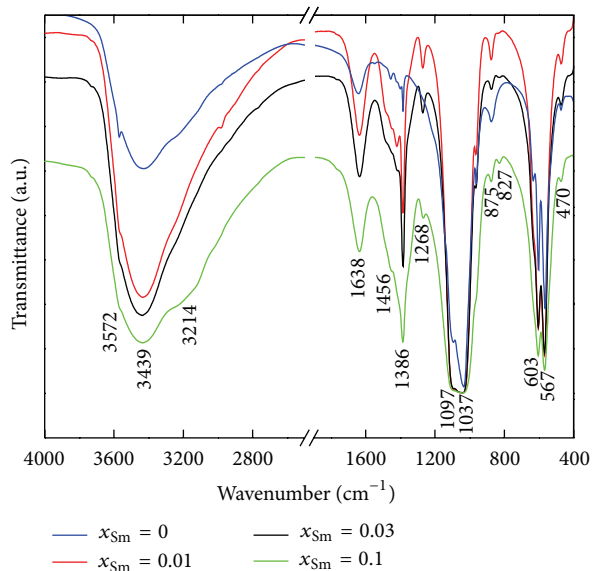


FIGURE 5: FT-IR spectra of samarium doped hydroxyapatite (Sm:HAp) with  $x_{\text{Sm}} = 0$ ,  $x_{\text{Sm}} = 0.01$ ,  $x_{\text{Sm}} = 0.03$ , and  $x_{\text{Sm}} = 0.1$ .

567  $\text{cm}^{-1}$  bands, indicates a well-crystallized HAp. The band at 470  $\text{cm}^{-1}$  is assigned to the  $\nu_2$   $[\text{PO}_4]^{3-}$  [54]. The vibration peaks in the regions 1600–1700  $\text{cm}^{-1}$  and 3200–3600  $\text{cm}^{-1}$  correspond to H–O–H bands of lattice water. The characteristic bands for carbonate are presented in the spectral regions 1400–1600  $\text{cm}^{-1}$  ( $\nu_3$ : asymmetric stretch vibration) and 873–880  $\text{cm}^{-1}$  ( $\nu_2$ : out-of-plane bend vibration). In addition, a weak band for the stretch vibration of structurally bound OH may be present in Sm:HAp samples near 3572  $\text{cm}^{-1}$ . Generally, it is difficult to distinguish between  $\text{HPO}_4^{2-}$  and  $\text{CO}_3^{2-}$  groups due to the overlapping of the characteristic peaks around 870  $\text{cm}^{-1}$  [55, 56].

The bands at around 1097  $\text{cm}^{-1}$  and about 1037  $\text{cm}^{-1}$  can be attributed to the  $\nu_3$   $[\text{PO}_4]^{3-}$ , while the band at 962 arises from  $\nu_1$   $[\text{PO}_4]^{3-}$ . The 603  $\text{cm}^{-1}$  and 567  $\text{cm}^{-1}$  bands appear from  $\nu_4$   $[\text{PO}_4]^{3-}$  [57, 58]. In the FT-IR spectrum (Figure 5) the bands corresponding to the  $\nu_3$  vibration of C–O were observed at 1456  $\text{cm}^{-1}$ , characteristic of the carbonate group [59, 60].

Also, in Figure 5 we observed that the contribution of the area that corresponds to the phosphate bands decreases when the samarium concentration in the samples increases. The bands at 632 and 962  $\text{cm}^{-1}$  progressively disappear with the increase of samarium concentration. When  $x_{\text{Sm}} = 0.1$  these bands are almost absent.

Furthermore, in agreement with the results already reported in the literature, it can be observed that the use of samarium as doping agent does not induce the appearance of other peaks [61–63].

The XPS analysis has been used to obtain the qualitative determination of the surface components and composition of the samples. Figure 6 shows the survey of XPS narrow scan spectra of the as-prepared  $\text{Ca}_{10-x}\text{Sm}_x(\text{PO}_4)_6(\text{OH})_2$  with  $x_{\text{Sm}} = 0.01$  (a),  $x_{\text{Sm}} = 0.03$  (b), and  $x_{\text{Sm}} = 0.1$  (c) nanopowder

samples. Concerning the binding energies in the pure HAp, the peaks at 347.3 eV, 532.1 eV and 133.8 eV can be attributed to the binding energy of Ca 2p, O 1s and P 2p, confirming the presence of apatite groups [64–66]. The peak at 1084.4 eV observed in  $\text{Ca}_{10-x}\text{Sm}_x(\text{PO}_4)_6(\text{OH})_2$  was attributed to the Sm 3d<sub>5/2</sub>, consistent with the normal oxidation state of Sm<sup>3+</sup>, because the binding energy of core level for Sm<sub>2</sub>O<sub>3</sub> is generally observed at 1083.2 eV [65].

The peaks associated to Ca, P, and O states presented in Figure 6 were the same in the Sm:HAp samples with different Sm<sup>3+</sup> concentrations ( $x_{\text{Sm}} = 0.01$  (a),  $x_{\text{Sm}} = 0.03$  (b), and  $x_{\text{Sm}} = 0.1$  (c)). This showed that the increasing of the concentration of Sm did not change the binding energy assigned to Ca 2p, O 1s, and P 2p presented in Sm:HAp samples. For XPS analysis, the binding energies were calibrated with reference C 1s at 285 eV. By combination of XRD results, it can be concluded that these signals can be assigned to Sm:HAp nanopowder. XPS results provided the additional evidence for the successful doping with Sm<sup>3+</sup> in Sm:HAp.

In agreement with previous studies [52, 57, 67], the luminescence, magnetic, and nuclear properties of the ceramics can be improved by doping them with lanthanides. According to [68], the biocompatibility and valuable biological properties of samarium were proved by their use in drugs to regulate blood clotting present during the process of wound healing. Knowing that lanthanides (III) have an interesting biological role but not well known, preliminary antimicrobial tests were performed on samples of hydroxyapatite doped with samarium.

Figure 7 shows the results of viable bacteria adhering to the 5, 15, 25, and 50  $\mu\text{g}/\text{mL}$  of  $\text{Ca}_{10-x}\text{Sm}_x(\text{PO}_4)_6(\text{OH})_2$  ( $x_{\text{Sm}} = 0.01$ ,  $x_{\text{Sm}} = 0.03$ , and  $x_{\text{Sm}} = 0.1$ ) when exposed to *Enterococcus faecalis* ATCC 29212. Bacterial adhesion was reduced on  $\text{Ca}_{10-x}\text{Sm}_x(\text{PO}_4)_6(\text{OH})_2$  sample when compared to pure HAp ( $x_{\text{Sm}} = 0$ ) and significant differences in bacterial adhesion on pure HAp ( $x = 0$ ) and Sm:HAp ( $x_{\text{Sm}} = 0.01$ ,  $x_{\text{Sm}} = 0.03$ , and  $x_{\text{Sm}} = 0.1$ ) were observed. We observed that the bacterial adhesion decreased when the samarium concentrations increased.

In this preliminary antimicrobial studies we observed that the Sm:HAp nanopowders have significantly lower adhesion of *Enterococcus faecalis* ATCC 29212, suggesting that the Sm:HAp nanopowders are antibacterial. In the future, the effect of samarium doped hydroxyapatite on other bacterial strains will be evaluated and these strains will be selected depending on the field of applications. The influence of the size of Sm:HAp nanoparticles on bacterial strains will be also studied.

The recent studies [69, 70] suggest that risk of infections in actual treatment of prosthetic infections is a major problem. In the patient treatment with hip or knee prosthetic infections it is noteworthy that infections with gram-negative bacilli or a fungus are contraindications. In this context, to optimize patient treatment with prosthetic infections the creation of new materials with antimicrobial properties is very important [71, 72]. In conclusion, it can be said that

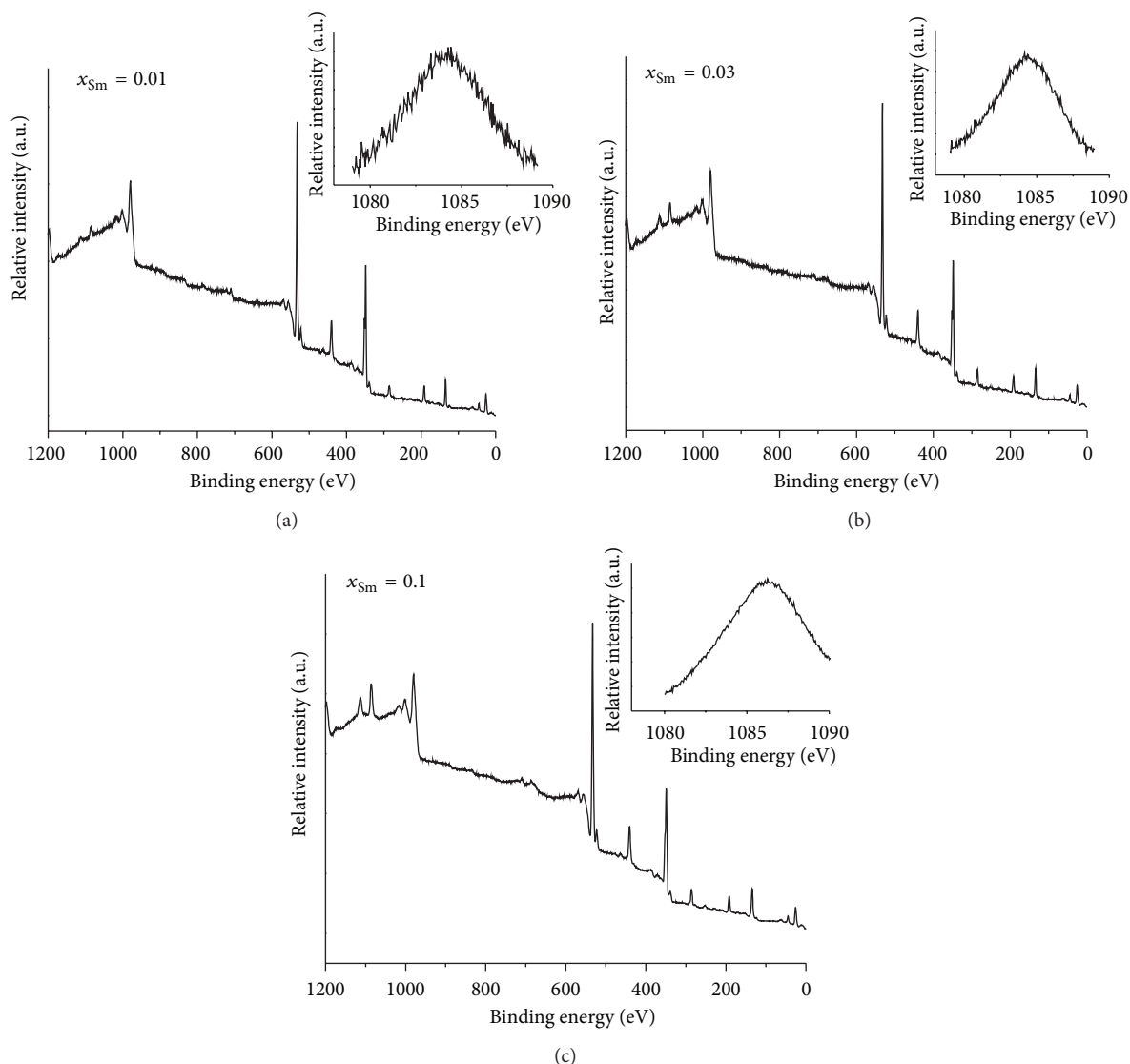


FIGURE 6: XPS general spectrum of  $\text{Ca}_{10-x}\text{Sm}_x(\text{PO}_4)_6(\text{OH})_2$  with  $x_{\text{Sm}} = 0.01$  (a),  $x_{\text{Sm}} = 0.03$  (b), and  $x_{\text{Sm}} = 0.1$  (c) powders. XPS narrow scan spectra of Sm element are presented for all the samples.

the new bioceramic Sm:HAP with antimicrobial properties may be a candidate with a good outcome in prosthetic joint infection and bone-targeting drug delivery system.

#### 4. Conclusions

In this short work, the emphasis was placed on the synthesis at low temperature by a simple method of pure Sm:HAP nanopowder with efficient antimicrobial activity.

The XRD studies have shown that the characteristic peaks of Sm:HAP nanopowders appeared to be identical regardless of the Sm content in the samples. All the XRD peaks were indexed in accordance with the hexagonal HAP in  $P_{63m}$  space group (JCPDS card number 9-432) and no other secondary phases were detected. The functional groups present in nanohydroxyapatite samples,  $\text{Ca}_{10-x}\text{Sm}_x(\text{PO}_4)_6(\text{OH})_2$  ( $x_{\text{Sm}}$

$= 0.01$ ,  $x_{\text{Sm}} = 0.03$ , and  $x_{\text{Sm}} = 0.1$ ), were investigated by FT-IR spectroscopy. It has been observed that the use of samarium as doping agent does not induce the appearance of other peaks. FTIR spectra of the Sm:HAP samples show only the absorption bands characteristic to hydroxyapatite. A small long morphology was remarked for all the Sm:HAP nanopowder samples by SEM. The doping of Sm has little influence on the morphology of Sm:HAP samples. The presence and uniform distribution of samarium in the nanopowder samples were confirmed by elemental maps. The EDX spectrum of Sm:HAP confirms the presence of calcium (Ca), phosphorus (P), oxygen (O), and samarium (Sm) in all the synthesized samples. The successful doping of  $\text{Sm}^{3+}$  in Sm:HAP was also emphasized by XPS results.

The inhibition of *Enterococcus faecalis* ATCC 29212 bacteria increased when the samarium concentrations in

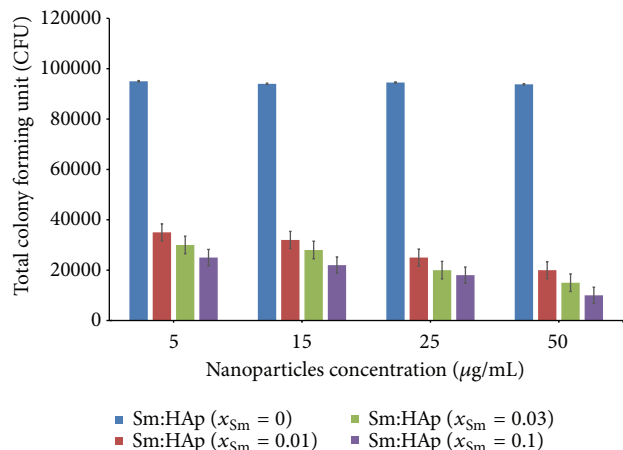


FIGURE 7: Adherence of *Enterococcus faecalis* ATCC 29212 on different concentrations of  $\text{Ca}_{10-x}\text{Sm}_x(\text{PO}_4)_6(\text{OH})_2$  ( $x_{\text{Sm}} = 0.01$ ,  $x_{\text{Sm}} = 0.03$ , and  $x_{\text{Sm}} = 0.1$ ) nanopowders compared to pure HAp ( $x_{\text{Sm}} = 0$ ) nanopowders.

$\text{Ca}_{10-x}\text{Sm}_x(\text{PO}_4)_6(\text{OH})_2$  increased from  $x_{\text{Sm}} = 0.01$  to  $x_{\text{Sm}} = 0.1$ . Our studies have shown that the  $\text{Ca}_{10-x}\text{Sm}_x(\text{PO}_4)_6(\text{OH})_2$  ( $x_{\text{Sm}} = 0.01$ ,  $x_{\text{Sm}} = 0.03$  and  $x_{\text{Sm}} = 0.1$ ) exhibited greater antimicrobial activity compared to the pure HAp ( $x_{\text{Sm}} = 0$ ). This will be significant for further antimicrobial studies of  $\text{Ca}_{10-x}\text{Sm}_x(\text{PO}_4)_6(\text{OH})_2$  on various gram-positive and gram-negative bacteria as well as fungi.

In conclusion, this study on new bioceramic Sm:HAp with antimicrobial properties may present a solution in bone-targeting drug delivery system and prosthetic joint infection. On the other hand, Sm:HAp bioceramics can be used as antimicrobial coatings in various applications.

## Conflict of Interests

The authors declare that there is no conflict of interests regarding the publication of this paper.

## Acknowledgments

The financial and encouraging support provided by the Ministry of Education of Romania under the Project IFA-CEA, no. C2-06, is acknowledged. The authors are grateful to Dr. Florica Frumosu, for XPS measurements. The authors also wish to thank Dr. Alina Mihaela Prodan for assistance with antibacterial assays.

## References

- [1] J. Hao, Y. Liu, S. Zhou, Z. Li, and X. Deng, "Investigation of nanocomposites based on semi-interpenetrating network of [L-poly ( $\epsilon$ -caprolactone)]/[net-poly ( $\epsilon$ -caprolactone)] and hydroxyapatite nanocrystals," *Biomaterials*, vol. 24, no. 9, pp. 1531–1539, 2003.
- [2] C. R. Safinya and L. Addadi, "Biomaterials," *Current Opinion in Solid State and Materials Science*, vol. 2, no. 3, pp. 325–329, 1997.
- [3] A. Groza, "Review of the processes identified during the polymerization of organic and organosilicon liquid films in atmospheric pressure air corona discharges," *Romanian Reports in Physics*, vol. 64, pp. 1227–1242, 2012.
- [4] Y. J. Han, S. C. J. Loo, N. T. Phung, F. Boey, and J. Ma, "Controlled size and morphology of EDTMP-doped hydroxyapatite nanoparticles as model for  $^{153}\text{Sm}$ -EDTMP doping," *Journal of Materials Science: Materials in Medicine*, vol. 19, no. 9, pp. 2993–3003, 2008.
- [5] D. A. Wahl and J. T. Czernuszka, "Collagen-hydroxyapatite composites for hard tissue repair," *European Cells and Materials*, vol. 11, pp. 43–56, 2006.
- [6] J. Dumbleton and M. T. Manley, "Hydroxyapatite-coated prostheses in total hip and knee arthroplasty," *Journal of Bone and Joint Surgery A*, vol. 86, no. 11, pp. 2526–2540, 2004.
- [7] P. Budrugaec, V. Trandafir, and M. G. Albu, "The effect of the hydration degree on the hydrothermal and thermo-oxidative stability of some collageneous matrices," *Journal of Thermal Analysis and Calorimetry*, vol. 72, no. 2, pp. 581–585, 2003.
- [8] M. V. Ghica, M. G. Albu, M. Leca, L. Popa, and S. T. Moiescu, "Design and optimization of some collagen-minocycline based hydrogels potentially applicable for the treatment of cutaneous wound infections," *Pharmazie*, vol. 66, no. 11, pp. 853–861, 2011.
- [9] J. S. Grimes, T. J. Bocklage, and J. D. Pitcher, "Collagen and biphasic calcium phosphate bone graft in large osseous defects," *Orthopedics*, vol. 29, no. 2, pp. 145–148, 2006.
- [10] W. Paul and C. P. Sharma, "Ceramic drug delivery: a perspective," *Journal of Biomaterials Applications*, vol. 17, no. 4, pp. 253–264, 2003.
- [11] T. Matsumoto, M. Okazaki, M. Inoue et al., "Hydroxyapatite particles as a controlled release carrier of protein," *Biomaterials*, vol. 25, no. 17, pp. 3807–3812, 2004.
- [12] A. Uchida, Y. Shinto, N. Araki, and K. Ono, "Slow release of anti-cancer drugs from porous calcium hydroxyapatite ceramic," *Journal of Orthopaedic Research*, vol. 10, no. 3, pp. 440–445, 1992.
- [13] Y. Shinto, A. Uchida, F. Korkusuz, N. Araki, and K. Ono, "Calcium hydroxyapatite ceramic used as a delivery system for antibiotics," *Journal of Bone and Joint Surgery B*, vol. 74, no. 4, pp. 600–604, 1992.
- [14] M. Itokazu, W. Yang, T. Aoki, A. Ohara, and N. Kato, "Synthesis of antibiotic-loaded interporous hydroxyapatite blocks by vacuum method and in vitro drug release testing," *Biomaterials*, vol. 19, no. 7–9, pp. 817–819, 1998.
- [15] A. Barroug and M. J. Glimcher, "Hydroxyapatite crystals as a local delivery system for cisplatin: adsorption and release of cisplatin in vitro," *Journal of Orthopaedic Research*, vol. 20, no. 2, pp. 274–280, 2002.
- [16] M. J. Gorbunoff, "Protein chromatography on hydroxyapatite columns," *Methods in Enzymology*, vol. 117, pp. 370–380, 1985.
- [17] S. Doonan, "Chromatography on hydroxyapatite," *Methods in Molecular Biology*, vol. 244, pp. 191–194, 2004.
- [18] M. Vallet-Regí, "Ceramics for medical applications," *Journal of the Chemical Society*, vol. 2, pp. 97–108, 2001.
- [19] L. Hermansson, L. Kraft, and H. Engqvist, "Chemically bonded ceramics as biomaterials," *Key Engineering Materials*, vol. 247, pp. 437–442, 2003.
- [20] T. Kokubo, H. Kim, and M. Kawashita, "Novel bioactive materials with different mechanical properties," *Biomaterials*, vol. 24, no. 13, pp. 2161–2175, 2003.

- [21] M. Shirkhazadeh, "Microneedles coated with porous calcium phosphate ceramics: effective vehicles for transdermal delivery of solid trehalose," *Journal of Materials Science: Materials in Medicine*, vol. 16, no. 1, pp. 37–45, 2005.
- [22] K. Shigeru, T. Oku, and S. Takagi, "Hydraulic property of hydroxyapatite thermal decomposition product and its application as biomaterial," *Journal of the Ceramic Society of Japan. International Edition*, vol. 97, pp. 96–101, 1989.
- [23] M. Jarcho, C. H. Bolen, M. B. Thomas, J. Bobick, J. F. Kay, and R. H. Doremus, "Hydroxylapatite synthesis and characterization in dense polycrystalline form," *Journal of Materials Science*, vol. 11, no. 11, pp. 2027–2035, 1976.
- [24] J. Coelho, N. S. Hussain, P. S. Gomes et al., "Development and characterization of lanthanides doped hydroxyapatite composites for bone tissue application," in *Current Trends on Glass and Ceramic Materials*, pp. 87–115, Scopus, 2013.
- [25] D. Veljović, R. Jančić-Hajneman, I. Balać et al., "The effect of the shape and size of the pores on the mechanical properties of porous HAP-based bioceramics," *Ceramics International*, vol. 37, no. 2, pp. 471–479, 2011.
- [26] T. Kokubo, *Bioceramics and Their Clinical Applications*, Woodhead Publishing Limited and CRC Press, 2008.
- [27] A. Aissa, M. Debbabi, M. Gruselle et al., "Sorption of tartrate ions to lanthanum (III)-modified calcium fluor- and hydroxyapatite," *Journal of Colloid and Interface Science*, vol. 330, no. 1, pp. 20–28, 2009.
- [28] S. P. Fricker, "The therapeutic application of lanthanides," *Chemical Society Reviews*, vol. 35, no. 6, pp. 524–533, 2006.
- [29] K. H. Thompson and C. Orvig, "Lanthanide compounds for therapeutic and diagnostic applications," *Chemical Society Reviews*, vol. 35, no. 6, p. 499, 2006.
- [30] T. Matsuda, C. Yamanaka, and M. Ikeya, "ESR study of  $Gd^{3+}$  and  $Mn^{2+}$  ions sorbed on hydroxyapatite," *Applied Radiation and Isotopes*, vol. 62, no. 2, pp. 353–357, 2005.
- [31] Y. Fan, S. Huang, J. Jiang et al., "Luminescent, mesoporous, and bioactive europium-doped calcium silicate (MCS:  $Eu^{3+}$ ) as a drug carrier," *Journal of Colloid and Interface Science*, vol. 357, no. 2, pp. 280–285, 2011.
- [32] M. Neumeier, L. A. Hails, S. A. Davis, S. Mann, and M. Epple, "Synthesis of fluorescent core-shell hydroxyapatite nanoparticles," *Journal of Materials Chemistry*, vol. 21, no. 4, pp. 1250–1254, 2011.
- [33] I. A. Appavoo and Y. Zhang, "Upconverting fluorescent nanoparticles for biological applications," in *Emerging Nanotechnologies for Manufacturing*, A. Waqar and J. J. Mark, Eds., pp. 159–175, William Andrew, Boston, Mass, USA, 2010.
- [34] J. H. Turner, P. G. Claringbold, E. L. Hetherington, P. Sorby, and A. A. Martindale, "A phase I study of samarium-153 ethylenediaminetetramethylene phosphonate therapy for disseminated skeletal metastases," *Journal of Clinical Oncology*, vol. 7, no. 12, pp. 1926–1931, 1989.
- [35] J. H. Turner and P. G. Claringbold, "A phase II study of treatment of painful multifocal skeletal metastases with single and repeated dose samarium-153 ethylenediaminetetramethylene phosphonate," *European Journal of Cancer*, vol. 27, no. 9, pp. 1084–1086, 1991.
- [36] J. F. Eary, C. Collins, M. Stabin et al., "Samarium-153-EDTMP biodistribution and dosimetry estimation," *Journal of Nuclear Medicine*, vol. 34, no. 7, pp. 1031–1036, 1993.
- [37] D. A. Podoloff, L. P. Kasi, E. E. Kim, F. Fossella, and V. A. Bhadkumar, "Evaluation of Sm-153-EDTMP as a bone imaging agent during a therapeutic trial," *Journal of Nuclear Medicine*, vol. 32, p. A918, 1991.
- [38] M. F. dos Santos, R. N. V. Furtado, M. S. Konai, M. L. V. Castiglioni, R. R. Marchetti, and J. Natour, "Effectiveness of radiation synovectomy with samarium-153 particulate hydroxyapatite in rheumatoid arthritis patients with knee synovitis: a controlled randomized double-blind trial," *Clinics*, vol. 64, no. 12, pp. 1187–1193, 2009.
- [39] E. K. O'Duffy, F. J. Oliver, S. J. Chatters et al., "Chromosomal analysis of peripheral lymphocytes of patients before and after radiation synovectomy with samarium-153 particulate hydroxyapatite," *Rheumatology*, vol. 38, no. 4, pp. 316–320, 1999.
- [40] E. K. O'Duffy, G. P. R. Clunie, D. Lui, J. C. W. Edwards, and P. J. Ell, "Double blind glucocorticoid controlled trial of samarium-153 particulate hydroxyapatite radiation synovectomy for chronic knee synovitis," *Annals of the Rheumatic Diseases*, vol. 58, no. 9, pp. 554–558, 1999.
- [41] P. Pusuwan, P. Asavatanabodee, and P. Chaudakshetrin, "Radiation synovectomy with Samarium-153 particulate hydroxyapatite: a preliminary report," in *Proceedings of the International Atomic Energy Agency-Publications-Iaea SR, 209, SR-209/52 Therapeutic Applications of Radiopharmaceuticals International Seminar, Therapeutic Applications of Radiopharmaceuticals*, International Atomic Energy, Agency, 1999.
- [42] G. Clunie, D. Lui, I. Cullum, J. C. W. Edwards, and P. J. Ell, "Samarium-153-particulate hydroxyapatite radiation synovectomy: biodistribution data for chronic knee synovitis," *Journal of Nuclear Medicine*, vol. 36, no. 1, pp. 51–57, 1995.
- [43] International Consensus on Periprosthetic Joint Infection, The Musculoskeletal Infection Society, <http://www.msisa-na.org/international-consensus/>.
- [44] M. Chinol, S. Vallabhajosula, S. J. Goldsmith et al., "Chemistry and biological behavior of samarium-153 and rhenium-186-labeled hydroxyapatite particles: potential radiopharmaceuticals for radiation synovectomy," *Journal of Nuclear Medicine*, vol. 34, no. 9, pp. 1536–1542, 1993.
- [45] J. U. Calegari, J. C. de Paula, J. S. C. de Almeida, and L. A. Casulari, "Clinical evaluation after 1 year of 153-samarium hydroxyapatite synovectomy in patients with haemophilic arthropathy," *Haemophilia*, vol. 15, no. 1, pp. 240–246, 2009.
- [46] Y. Wang, R. Hu, D. Jiang, P. Zhang, Q. Lin, and Y. Wang, "Synthesis, crystal structure, interaction with BSA and antibacterial activity of La(III) and Sm(III) complexes with enrofloxacin," *Journal of Fluorescence*, vol. 21, no. 2, pp. 813–823, 2011.
- [47] Y. F. Zhao, H. B. Chu, F. Bai et al., "Synthesis, crystal structure, luminescent property and antibacterial activity of lanthanide ternary complexes with 2, 4, 6-tri(2-pyridyl)-s-triazine," *Journal of Organometallic Chemistry*, vol. 716, pp. 167–174, 2012.
- [48] A. M. Ajlouni, Z. A. Taha, W. Al Momani, A. K. Hijazi, and M. Ebaq'ai, "Synthesis, characterization, biological activities, and luminescent properties of lanthanide complexes with  $N,N'$ -bis(2-hydroxy-1-naphthylidene)-1,6-hexadiimine," *Inorganica Chimica Acta*, vol. 388, pp. 120–126, 2012.
- [49] K. Mohanan, B. S. Kumari, and G. Rijulal, "Microwave assisted synthesis, spectroscopic, thermal, and antifungal studies of some lanthanide(III) complexes with a heterocyclic bishydrazone," *Journal of Rare Earths*, vol. 26, no. 1, pp. 16–21, 2008.
- [50] L. Lutterotti, "Total pattern fitting for the combined size-strain-stress-texture determination in thin film diffraction," *Nuclear Instruments and Methods in Physics Research B: Beam Interactions with Materials and Atoms*, vol. 268, no. 3–4, pp. 334–340, 2010.

- [51] N. C. Popa, "The (*hkl*) dependence of diffraction-line broadening caused by strain and size for all Laue groups in Rietveld refinement," *Journal of Applied Crystallography*, vol. 31, no. 2, pp. 176–180, 1998.
- [52] C. S. Ciobanu, S. L. Iconaru, F. Massuyeau, L. V. Constantin, A. Costescu, and D. Predoi, "Synthesis, structure, and luminescent properties of europium-doped hydroxyapatite nanocrystalline powders," *Journal Nanomaterials*, vol. 2012, Article ID 942801, 9 pages, 2012.
- [53] M. Markovic, B. O. Fowler, and M. S. Tung, "Preparation and comprehensive characterization of a calcium hydroxyapatite reference material," *Journal of Research of the National Institute of Standards and Technology*, vol. 109, no. 6, pp. 553–568, 2004.
- [54] W. Jastrzbski, M. Sitarz, M. Rokita, and K. Bułat, "Infrared spectroscopy of different phosphates structures," *Spectrochimica Acta A: Molecular and Biomolecular Spectroscopy*, vol. 79, no. 4, pp. 722–727, 2011.
- [55] J. C. Elliott, *Structure and Chemistry of the Apatites and Other Calcium, Orthophosphates*, Elsevier Science, Amsterdam, The Netherlands, 1994.
- [56] R. Z. LeGeros, *Calcium Phosphates in Oral Biology and Medicine. Monographs in Oral Sciences*, Karger, Basel, Switzerland, 1991.
- [57] C. S. Ciobanu, E. Andronescu, B. S. Vasile, C. M. Valsangiacom, R. V. Ghita, and D. Predoi, "Looking for new synthesis of hydroxyapatite doped with europium," *Optoelectronics and Advanced Materials, Rapid Communications*, vol. 4, no. 10, pp. 1515–1519, 2010.
- [58] X. Bai, K. More, C. M. Rouleau, and A. Rabiei, "Functionally graded hydroxyapatite coatings doped with antibacterial components," *Acta Biomaterialia*, vol. 6, no. 6, pp. 2264–2273, 2010.
- [59] K. Nakamoto, *Infrared and Raman Spectra of Inorganic and Coordination Compounds*, Wiley, New York, NY, USA, 1978.
- [60] R. Z. LeGeros, G. Bonel, and R. Legros, "Types of "H<sub>2</sub>O" in human enamel and in precipitated apatites," *Calcified Tissue Research*, vol. 26, no. 1, pp. 111–118, 1978.
- [61] M. Eriksson, Y. Liu, J. Hu, L. Gao, M. Nygren, and Z. Shen, "Transparent hydroxyapatite ceramics with nanograin structure prepared by high pressure spark plasma sintering at the minimized sintering temperature," *Journal of the European Ceramic Society*, vol. 31, no. 9, pp. 1533–1540, 2011.
- [62] I. Cacciotti and A. Bianco, "High thermally stable Mg-substituted tricalcium phosphate via precipitation," *Ceramics International*, vol. 37, no. 1, pp. 127–137, 2011.
- [63] E. I. Get'man, S. N. Loboda, T. V. Tkachenko, N. V. Yablochkova, and K. A. Chebyshev, "Isomorphous substitution of samarium and gadolinium for calcium in hydroxyapatite structure," *Russian Journal of Inorganic Chemistry*, vol. 55, no. 3, pp. 333–338, 2010.
- [64] M. P. Casaletto, S. Kaciulis, G. Mattogno, A. Mezzi, L. Ambrosio, and F. Branda, "XPS characterization of biocompatible hydroxyapatite-polymer coatings," *Surface and Interface Analysis*, vol. 34, no. 1, pp. 45–49, 2002.
- [65] C. S. Ciobanu, S. L. Iconaru, M. C. Chifriuc, A. Costescu, P. le Coustumer, and D. Predoi, "Synthesis and antimicrobial activity of silver-doped hydroxyapatite nanoparticles," *BioMed Research International*, vol. 2013, Article ID 916218, 10 pages, 2013.
- [66] Y. Kim, H. Schleg, K. Kim, J. T. S. Irvine, and J. H. Kim, "X-ray photoelectron spectroscopy of Sm-doped layered perovskite for intermediate temperature-operating solid oxide fuel cell," *Applied Surface Science*, vol. 288, pp. 695–701, 2014.
- [67] C. S. Ciobanu, F. Massuyeau, L. V. Constantin, and D. Predoi, "Structural and physical properties of antibacterial Ag-doped nano-hydroxyapatite synthesized at 100°C," *Nanoscale Research Letters*, vol. 6, article 613, 2011.
- [68] O. Dubok, O. Shynkaruk, and E. Buzaneva, "Lanthanides oxides usage to increase radiopaque of bioactive ceramics," *Functional Materials*, vol. 20, no. 2, pp. 172–178, 2013.
- [69] I. G. Sia, E. F. Berbari, and A. W. Karchmer, "Prosthetic joint infections," *Infectious Disease Clinics of North America*, vol. 19, no. 4, pp. 885–914, 2005.
- [70] P. Hsieh, M. S. Lee, K. Hsu, Y. Chang, H. Shin, and S. W. Ueng, "Gram-negative prosthetic joint infections: risk factors and outcome of treatment," *Clinical Infectious Diseases*, vol. 49, no. 7, pp. 1036–1043, 2009.
- [71] I. Uçkay and L. Bernard, "Gram-negative versus gram-positive prosthetic joint infections," *Clinical Infectious Diseases*, vol. 50, no. 5, p. 795, 2010.
- [72] B. Zmistowski, C. J. Fedorka, E. Sheehan, G. Deirmengian, M. S. Austin, and J. Parvizi, "Prosthetic joint infection caused by gram-negative organisms," *Journal of Arthroplasty*, vol. 26, no. 6, pp. 104–108, 2011.

## Research Article

# Hydrothermal Synthesis, Characterization, and Optical Properties of Ce Doped $\text{Bi}_2\text{MoO}_6$ Nanoplates

Anukorn Phuruangrat,<sup>1</sup> Nuengruethai Ekthammathat,<sup>2</sup> Budsabong Kuntalue,<sup>3</sup> Phattranit Dumrongrojthanath,<sup>2</sup> Somchai Thongtem,<sup>4,5</sup> and Titipun Thongtem<sup>2</sup>

<sup>1</sup> Department of Materials Science and Technology, Faculty of Science, Prince of Songkla University, Hat Yai, Songkhla 90112, Thailand

<sup>2</sup> Department of Chemistry, Faculty of Science, Chiang Mai University, Chiang Mai 50200, Thailand

<sup>3</sup> Electron Microscopy Research and Service Center, Faculty of Science, Chiang Mai University, Chiang Mai 50200, Thailand

<sup>4</sup> Department of Physics and Materials Science, Faculty of Science, Chiang Mai University, Chiang Mai 50200, Thailand

<sup>5</sup> Materials Science Research Center, Faculty of Science, Chiang Mai University, Chiang Mai 50200, Thailand

Correspondence should be addressed to Anukorn Phuruangrat; phuruangrat@hotmail.com and Titipun Thongtem; tptthongtem@yahoo.com

Received 14 December 2013; Accepted 17 March 2014; Published 15 April 2014

Academic Editor: Ajay Soni

Copyright © 2014 Anukorn Phuruangrat et al. This is an open access article distributed under the Creative Commons Attribution License, which permits unrestricted use, distribution, and reproduction in any medium, provided the original work is properly cited.

Undoped and Ce doped  $\text{Bi}_2\text{MoO}_6$  samples were synthesized by hydrothermal reaction at 180°C for 20 h. Phase, morphology, atomic vibration, and optical properties were characterized by X-ray powder diffraction (XRD), X-ray photoelectron spectroscopy (XPS), Raman spectrophotometry, Fourier transform infrared (FTIR) spectroscopy, scanning electron microscopy (SEM), transmission electron microscopy (TEM), selected area electron diffraction (SAED), and UV-visible spectroscopy. In this research, the products were orthorhombic  $\text{Bi}_2\text{MoO}_6$  nanoplates with the growth direction along the [0b0], including the asymmetric and symmetric stretching and bending modes of Bi–O and Mo–O. Undoped and Ce doped  $\text{Bi}_2\text{MoO}_6$  samples show a strong absorption in the UV region.

## 1. Introduction

Aurivillius family of structurally related oxides with chemical formula of  $\text{Bi}_2\text{A}_{n-1}\text{B}_n\text{O}_{3n+3}$  ( $\text{A} = \text{Ca}, \text{Sr}, \text{Ba}, \text{Pb}, \text{Bi}, \text{Na}, \text{K}$ , and  $\text{B} = \text{Ti}, \text{Nb}, \text{Ta}, \text{Mo}, \text{W}$ , and  $\text{Fe}$ ) was originally attractive material due to its layered structure and unique properties [1, 2]. The perovskite-type blocks lead to variable layers along the  $c$ -axis due to the integer  $n$  with  $n = 0, 1, 2, 3, 4, 5$  and a typical “mica-like” two-dimensional structure [1].  $\text{Bi}_2\text{MoO}_6$  with narrow band gap of 2.9 eV is a typical Aurivillius phase with its structure consisting of perovskite layers  $(\text{A}_{n-1}\text{B}_n\text{O}_{3n+1})^{2-}$  between  $(\text{Bi}_2\text{O}_2)^{2+}$  bismuth oxide layers, with a general formula  $[\text{Bi}_2\text{O}_2] [\text{A}_{n-1}\text{B}_n\text{O}_{3n+1}]$  [3, 4].  $\text{Bi}_2\text{MoO}_6$  is an interesting material due to its unique physical properties for solar energy conversion, ion conduction, and photocatalysis for water splitting under visible-light irradiation and gas

sensors [1, 2]. Various synthetic methods for this material have been reported such as hydrothermal/solvothermal [1, 3, 5], aerosol-spraying [4], coprecipitation [6], thermal evaporation [7], and hard-template method [8]. Recently, rare earth dopants have been excessively applied to modify optical properties of nanomaterials due to their possible transition of 4f electron configuration. Among them, cerium is one of the most interesting dopants due to its different electronic structure between  $\text{Ce}^{3+}$  ( $4f^1 5d^0$ ) and  $\text{Ce}^{4+}$  ( $4f^0 5d^0$ ), leading to different optical properties. It generates oxygen vacancies and bulk oxygen species, which have relatively high mobility. Thus they are more active for oxidation processes [9, 10].

In this paper, 0–3% Ce doped  $\text{Bi}_2\text{MoO}_6$  crystallites were successfully synthesized by the hydrothermal process. Phase,

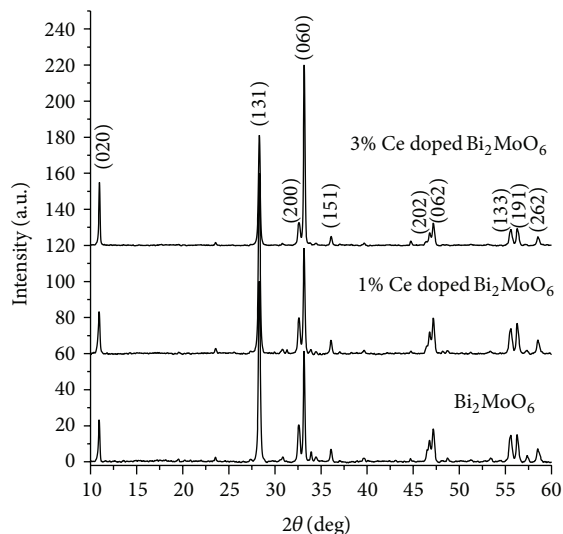


FIGURE 1: XRD patterns of the undoped, 1% Ce doped, and 3% Ce doped  $\text{Bi}_2\text{MoO}_6$  samples synthesized by hydrothermal reaction at  $180^\circ\text{C}$  for 20 h.

morphologies, and optical properties of the undoped and Ce doped  $\text{Bi}_2\text{MoO}_6$  crystallites were intensively investigated.

## 2. Experimental Procedures

All the reagents were of analytical grade and used as received without further purification. In a typical experiment, 0.5 mmol  $\text{Na}_2\text{MoO}_4 \cdot 2\text{H}_2\text{O}$  and 1 mmol  $\text{Bi}(\text{NO}_3)_3 \cdot 5\text{H}_2\text{O}$  were dissolved in 60 mL deionized water to form solution A under 20 min magnetic stirring at room temperature. Concurrently, 1 and 3% by weight  $\text{Ce}(\text{NO}_3)_3 \cdot 6\text{H}_2\text{O}$  were dissolved in 40 mL deionized water each to form solution B under 20 min magnetic stirring at room temperature. Then, solution B was slowly added to solution A to form homogeneous solutions with further stirring for 30 min. Each solution of both with and without  $\text{Ce}^{3+}$  dopants was adjusted the level of acid or alkali until reaching at the pH of 10 using 3 M NaOH, poured into each of stainless steel autoclave with a Teflon liner, and heated at  $180^\circ\text{C}$  for 20 h. At the conclusion of the process, the autoclaves were cooled to room temperature. The products were separated centrifugally, washed with deionized water and absolute ethanol several times, and dried at  $80^\circ\text{C}$  for 12 h.

The phase of the samples was characterized by X-ray diffraction (XRD) using a Philips X'Pert MPD X-ray diffractometer with  $\text{CuK}_\alpha$  irradiation at  $\lambda = 1.5406 \text{ \AA}$ . The surface morphology was investigated by field emission scanning electron microscope (FE-SEM, JEOL JSM 6335F) and transmission electron microscope (TEM, JEOL, JEM2100) operated at the accelerating voltage of 35 and 200 kV, respectively. Raman and FTIR spectra were recorded on HORIBA JOBIN YVON T64000 Raman spectrometer with 50 mW and 514.5 nm wavelength Ar green laser and BRUKER TENSOR27 Fourier transform infrared (FTIR) spectrometer with KBr as a diluting agent and operated in the ranges of  $100\text{--}1,000 \text{ cm}^{-1}$  and  $400\text{--}4,000 \text{ cm}^{-1}$ , respectively. X-ray

photoelectron spectroscopy (XPS) of the products was carried out via an Axis Ultra DLD, Kratos Analytical Ltd., with a monochromated  $\text{Al K}_\alpha$  (1486.6 eV) radiation as the excitation source at 15 kV. All obtained spectra were calibrated to a  $\text{Cl s}$  electron peak at 285.1 eV. UV-visible absorption spectra of an ethanol suspension of 0–3% Ce doped  $\text{Bi}_2\text{MoO}_6$  samples were recorded under a Lambda 25, Perkin Elmer UV-visible spectrophotometer.

## 3. Results and Discussion

The typical XRD patterns as shown in Figure 1 reveal the phase and purity of the as-obtained 0–3% Ce doped  $\text{Bi}_2\text{MoO}_6$  samples. All peaks of the undoped and Ce doped  $\text{Bi}_2\text{MoO}_6$  samples were specified as the single phase orthorhombic  $\text{Bi}_2\text{MoO}_6$  structure (JCPDS card number 73-2020 [11]). The presence of sharp and intense peaks confirmed the formation of highly crystalline nanomaterials. Furthermore, the absence of any impurity related peaks indicates that  $\text{Ce}^{3+}$  ions were successfully doped into  $\text{Bi}_2\text{MoO}_6$  nanostructure. However, the intensity ratio of the (060) peak to the (131) peak of 3% Ce doped  $\text{Bi}_2\text{MoO}_6$  sample is 1.66, obviously larger than the undoped  $\text{Bi}_2\text{MoO}_6$  which is equivalent to 0.60 [12]. This important result indicates that the crystal has special anisotropic growth along the [0b0] direction.

The morphology and particle sizes of the Ce doped  $\text{Bi}_2\text{MoO}_6$  with different contents of Ce ions were investigated by SEM as shown in Figure 2. It can be seen that the samples were comprised of a large number of nanoplates with diameters ranging between 0.1 and 0.3  $\mu\text{m}$  and <100 nm thick. The surfaces of these nanoplates are smooth. Interestingly, when the samples were doped by different Ce concentrations, Ce doped  $\text{Bi}_2\text{MoO}_6$  are still to be nanoplates. These show that Ce doping concentration had little effect on the shape of the products. Clearly, morphology and particle sizes of

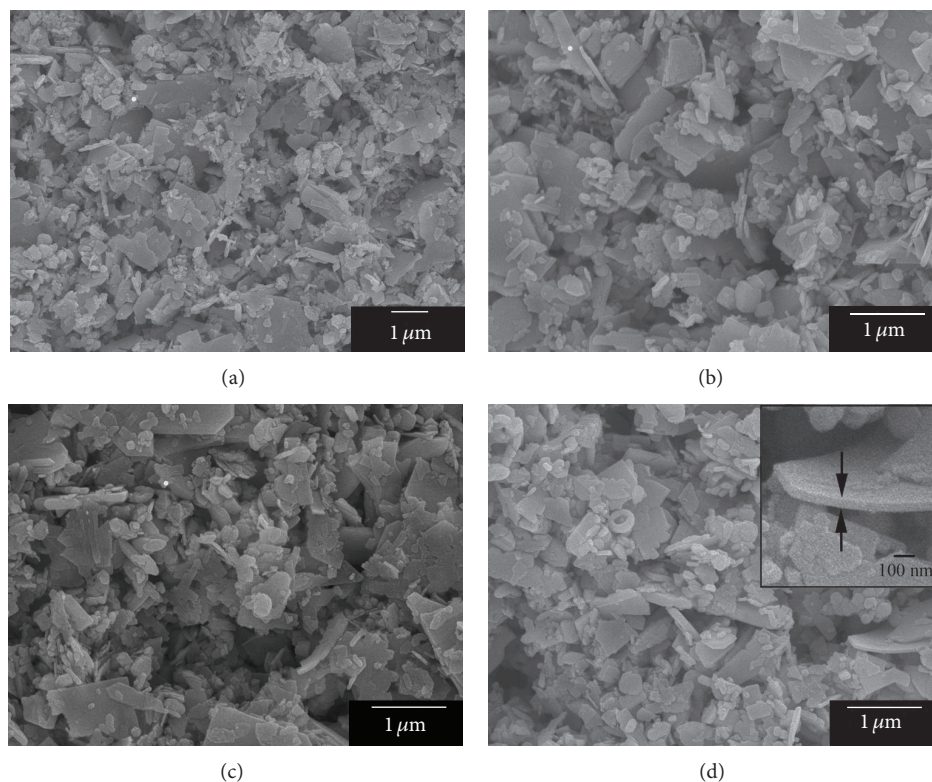


FIGURE 2: SEM images of the nanostructured ZnO of (a) undoped  $\text{Bi}_2\text{MoO}_6$ , (b) 1% Ce doped  $\text{Bi}_2\text{MoO}_6$ , and ((c), (d)) 3% Ce doped  $\text{Bi}_2\text{MoO}_6$ .

the Ce doped  $\text{Bi}_2\text{MoO}_6$  nanoplates were consistent with pure  $\text{Bi}_2\text{WO}_6$ .

More information of the structure was obtained by TEM observation as shown in Figure 3. It confirms that the undoped  $\text{Bi}_2\text{MoO}_6$  nanoplates have an average diameter of about  $0.2 \mu\text{m}$ , in accordance with the SEM analysis. Obviously, some of lighter color parts can be seen, due to the difference in the contrast in TEM, mainly related to the difference in thickness of the samples. Furthermore, the 3% Ce doped  $\text{Bi}_2\text{MoO}_6$  sample was composed of square nanoplates with  $\sim 100 \text{ nm}$  thick edge. The selected area electron diffraction (SAED) patterns clearly demonstrate the single crystalline nature of the nanoplates. Interestingly, the SAED patterns taken on the whole single nanoplate show single crystalline patterns with sharp diffraction bright spots, giving the [100] zone axis character of orthorhombic  $\text{Bi}_2\text{MoO}_6$ . Based on the above XRD results, it is reasonable to conclude that the nanoplates preferentially grew along the [010] direction.

The chemical composition of 3% Ce doped  $\text{Bi}_2\text{MoO}_6$  nanoplates was investigated by XPS spectroscopy as shown in Figure 4 and was calibrated using C1s peak at 285.1 eV. The Bi4f peaks of the 3% Ce doped  $\text{Bi}_2\text{MoO}_6$  nanoplates appear at 159.52 eV of  $4f_{7/2}$  and 164.80 eV of  $4f_{5/2}$ , corresponding to  $\text{Bi}^{3+}$  [4, 13–15]. Additional weak spin-orbit doublet peaks with binding energy of 157.92 eV for Bi  $4f_{7/2}$  and 163.40 eV for Bi  $4f_{5/2}$  are also detected, suggesting that some of bismuth exist as the  $(+3-x)$  valence state [16]. Probably, the  $\text{Bi}^{(+3-x)}$  formal oxidation state could be attributed to the substoichiometric phase within the microsized plates [16]. The production

of lower oxidation state results in the presence of oxygen vacancies inside. The Mo3d spectrum showed spin-orbit splitting of the Mo3d levels at 232.84 eV and 236.00 eV, corresponding to the  $3d_{5/2}$  and  $3d_{3/2}$  orbitals [4, 13, 17, 18]. The spin-orbit splitting between Mo $3d_{5/2}$  and Mo $3d_{3/2}$  signals of Ce doped  $\text{Bi}_2\text{MoO}_6$  nanoplates was set to 3.16 eV which are consistent with the previous reports [17]. However, single spin-orbit doublets showed peaks with binding energies of 231.3 eV (Mo $3d_{5/2}$ ) and 234.6 eV (Mo $3d_{3/2}$ ). These peaks are associated with Mo in formal (+6) oxidation state [19, 20]. The  $\text{O}_{1s}$  binding energy of 530.60 eV was in agreement with the literature value [4]. The O element might come from two kinds of chemical states: crystal lattice oxygen and adsorbed oxygen. The triple peaks of  $\text{O}_{1s}$  core at 529.30 eV, 530.45 eV, and 531.32 eV are attributed to the presence of Bi–O, Mo–O and Ce–O bonds in 3% Ce doped  $\text{Bi}_2\text{MoO}_6$  sample [13]. The  $\text{O}_{1s}$  binding energy of 532.58 eV is due to the adsorbed oxygen. The XPS Ce3d peaks of cerium compounds are well known to be complicated because of hybridization of the Ce4f orbital with ligand orbital and fractional occupancy of the valence 4f orbital. The XPS spectrum of the  $3d_{5/2}$  cerium level is therefore composed of three structures in the case of  $\text{CeO}_2$  and only two structures in the case of  $\text{Ce}_2\text{O}_3$  or other  $\text{Ce}^{3+}$  compounds [21]. The peaks at 880.73 eV, 884.34 eV, and 887.57 eV are due to  $3d_{5/2}$  spin-orbit states, and those peaks at 898.68 eV, 901.94 eV, and 905.11 eV are due to the corresponding  $3d_{3/2}$  states. The spin-orbit splitting is about 17.6 eV. The highest binding energy peaks located at about 902 eV and 884 eV are the result of a  $\text{Ce}3d^9 4f^1 \text{O}2p^6$  of Ce(III)

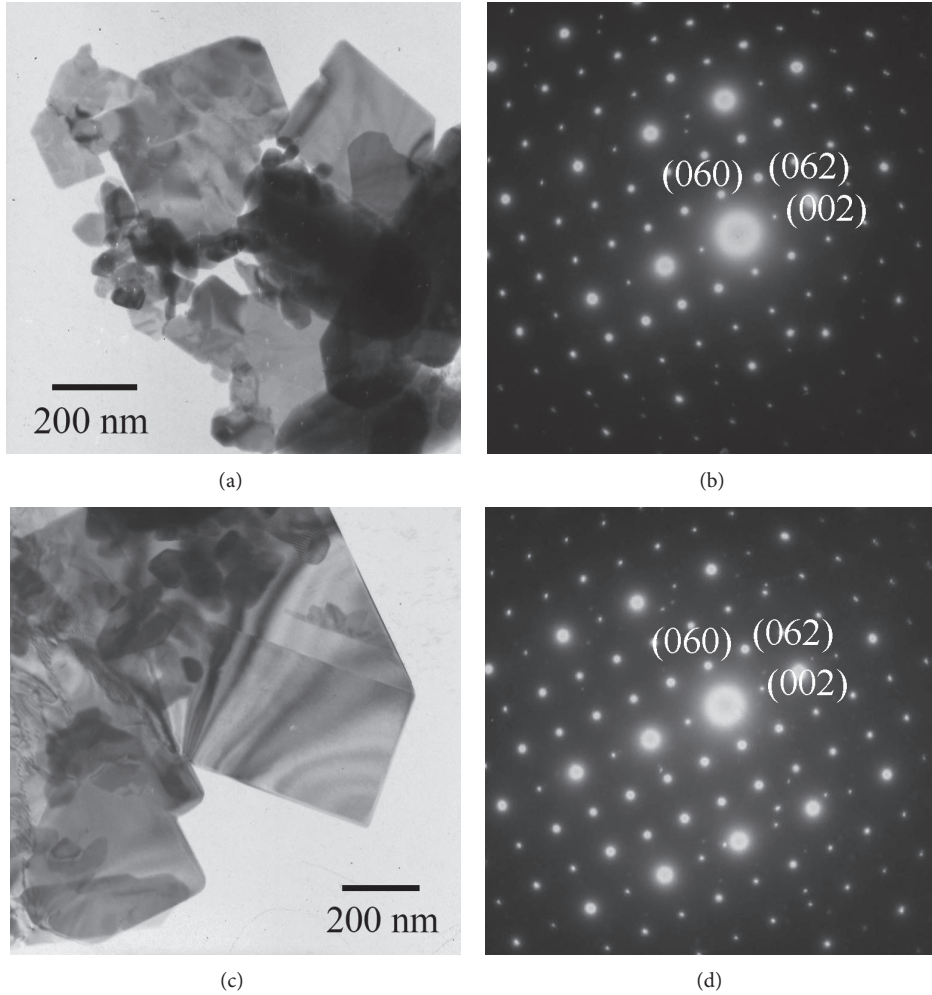


FIGURE 3: TEM images and SAED patterns of ((a), (b)) undoped  $\text{Bi}_2\text{MoO}_6$ , and ((c), (d)) 3% Ce doped  $\text{Bi}_2\text{MoO}_6$ .

in  $\text{Ce}_2\text{O}_3$  in final state. The lowest binding energies located at 898.68 eV and 880.74 eV are the result of  $\text{Ce}3d^94f^2 \text{O}2p^4$  [10, 21, 22]. The peaks at 887.57 eV and 905.11 eV are shakedown features resulting from the transfer of one or two electrons from a filled O2p orbital to an empty Ce4f orbital, that is,  $\text{Ce}3d^94f^2 \text{O}2p^4$  and  $\text{Ce}3d^94f^1 \text{O}2p^5 \text{Ce(IV)}$  in the final states. Therefore, from the above results it is quite clear that there is coexistence of  $\text{Ce}^{3+}$  and  $\text{Ce}^{4+}$  in this sample [10, 21].

$\text{Bi}_2\text{MoO}_6$  crystal is built up of perovskite-like  $(\text{MoO}_4)^{2-}$  and fluorite-like  $(\text{Bi}_2\text{O}_2)^{2+}$  layers. Its room temperature and ambient pressure structure is orthorhombic (space group symmetry  $\text{P}2_1\text{ab}$ ). A standard group theoretical analysis for the  $\text{P}2_1\text{ab}$  room temperature phase of  $\text{Bi}_2\text{MoO}_6$  unit cell leads to 108 degrees of freedom at the Brillouin zone center ( $\Gamma$  point). The optical modes are distributed among the irreducible representation of the factor group  $\text{C}_{2v}$  as  $26\text{A}_1 + 27\text{A}_2 + 26\text{B}_1 + 26\text{B}_2$ . Selection rules state that the  $\text{A}_1$ ,  $\text{B}_1$ , and  $\text{B}_2$  are both Raman and IR active whereas the  $\text{A}_2$  modes are only Raman active [23–25].

Raman spectra of 0–3% Ce doped  $\text{Bi}_2\text{MoO}_6$  samples are shown in Figure 5. It is well known that the bands in

the 180–500  $\text{cm}^{-1}$  range originated from the bending, wagging, and external modes by directly correlating the Mo–O bonds, and the 700–900  $\text{cm}^{-1}$  region originated from the stretching vibration modes of the  $\text{MoO}_6$  octahedrons. Raman peaks at 323, 345, and 400  $\text{cm}^{-1}$  corresponded to the  $E_u$  symmetry bending modes. Raman modes near 293  $\text{cm}^{-1}$  seemed to be from the  $E_g$  bending vibration. The band at 144  $\text{cm}^{-1}$  was assigned as the lattice modes of  $\text{Bi}^{3+}$  atoms mainly in the direction normal to the layers. The strong band at 792  $\text{cm}^{-1}$  was assigned to  $\text{A}_{1g}$  mode of Mo–O stretching vibration of the distorted  $\text{MoO}_6$  octahedrons. The shoulder peak at 715  $\text{cm}^{-1}$  was identified to the  $E_u$  asymmetric stretching of  $\text{MoO}_6$  octahedrons involving the vibration of the equatorial oxygen atoms within the layers. The band at 841  $\text{cm}^{-1}$  was assigned as the  $\text{A}_{2u}$  symmetric and asymmetric stretching vibrations of the  $\text{MoO}_6$  octahedrons, relating to the motion of the apical oxygen atoms normal to the layers. When the Ce was doped into the samples, the strong bands at 792  $\text{cm}^{-1}$  and two shoulder peaks at 715 and 840  $\text{cm}^{-1}$  also slightly shifted to 713, 791, and 838  $\text{cm}^{-1}$ , confirming an effective substitution

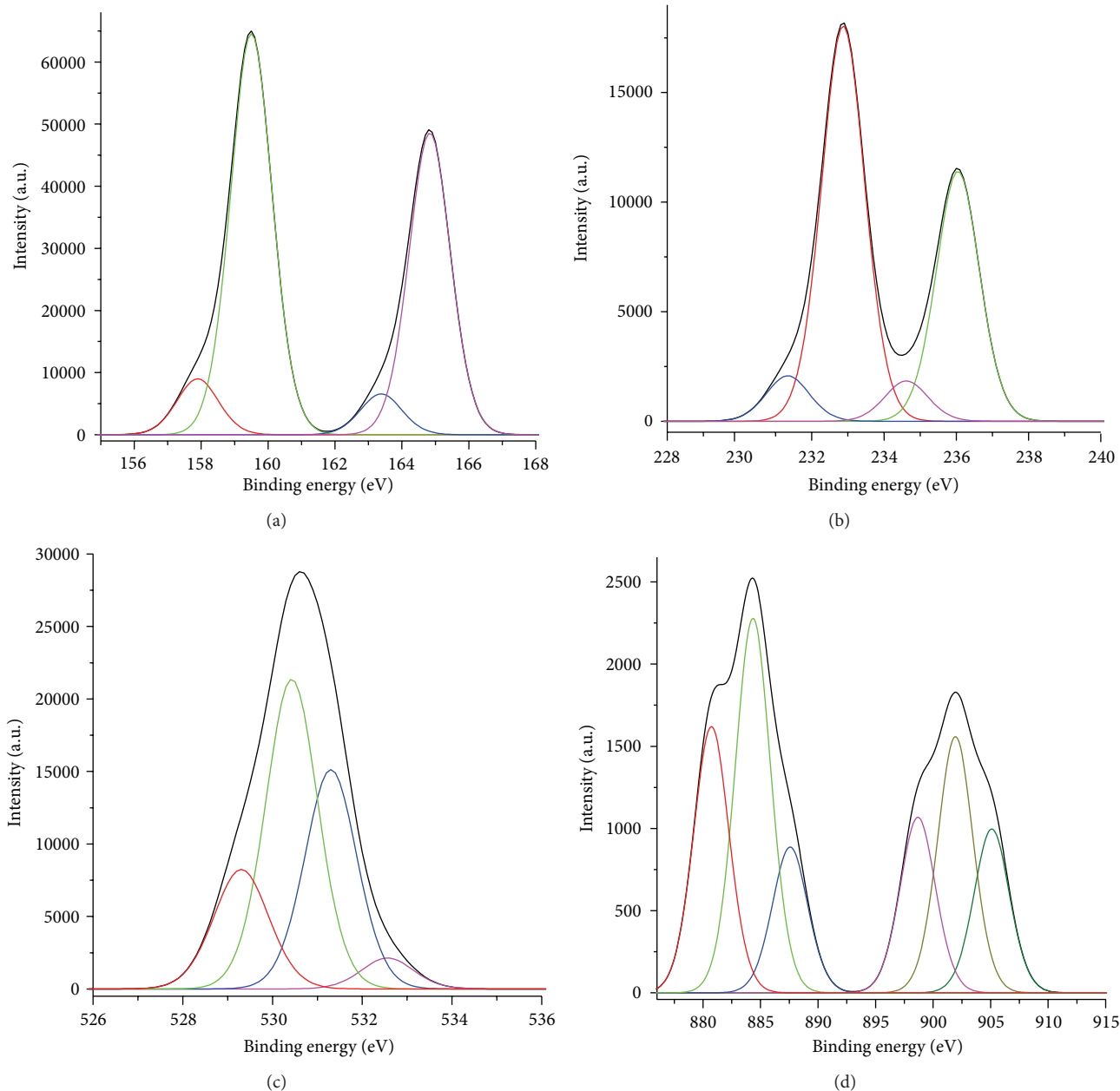


FIGURE 4: XPS spectra of the 3% Ce doped  $\text{Bi}_2\text{MoO}_6$  nanoplates for (a)  $\text{Bi}4f$ , (b)  $\text{Mo}3d$ , (c)  $\text{O}_{1s}$ , and (d)  $\text{Ce}4f$ .

of  $\text{Bi}^{3+}$  ions by  $\text{Ce}^{3+}$  ions in the as-prepared nanocrystals, as also revealed by the XRD analysis [23–26].

FTIR spectra of the samples (Figure 6) show the band in the  $400\text{--}900\text{ cm}^{-1}$  range, corresponding to Bi–O stretching and bending, Mo–O stretching, and Mo–O–Mo bridging stretching modes of  $\text{Bi}_2\text{MoO}_6$ . The bands at  $843$  and  $797\text{ cm}^{-1}$  were assigned as the asymmetric and symmetric stretching modes of  $\text{MoO}_6$  relating to vibrations of apical oxygen atoms, respectively. The  $731\text{ cm}^{-1}$  mode was attributed to the asymmetric stretching vibration of the equatorial oxygen atoms of  $\text{MoO}_6$  octahedrons. Those at  $603$  and  $570\text{ cm}^{-1}$  were specified as the bending vibrations of  $\text{MoO}_6$ . Weak bands at  $409$  and  $448\text{ cm}^{-1}$  were attributed to the stretching and bending vibrations of  $\text{BiO}_6$  octahedrons [2, 26].

The UV-visible absorption spectra of the undoped and Ce doped  $\text{Bi}_2\text{MoO}_6$  are shown in Figure 7. They show the strong absorption in the UV and visible-light regions. It should be noted that the maximum absorption was detected at  $321\text{ nm}$  for 3% Ce doped  $\text{Bi}_2\text{MoO}_6$ , obviously blue shifted compared to that of  $\text{Bi}_2\text{MoO}_6$  at  $383\text{ nm}$ . For a crystalline semiconductor, the optical absorption near the band edge follows the equation  $\alpha h\nu = A(h\nu - E_g)^{n/2}$ , where  $\alpha$ ,  $\nu$ ,  $E_g$ , and  $A$  are the absorption coefficient, photonic frequency, energy gap, and a constant, respectively [2, 3]. For  $\text{Bi}_2\text{MoO}_6$ , the value of  $n$  is 1 for the direct transition. The plot of  $(\alpha h\nu)^2$  versus photon energy ( $h\nu$ ) of undoped and Ce doped  $\text{Bi}_2\text{WO}_6$  was estimated from the intercepts of the tangents to the plots which are  $1.86\text{ eV}$  for pure  $\text{Bi}_2\text{MoO}_6$  and  $2.04\text{ eV}$  for 3%

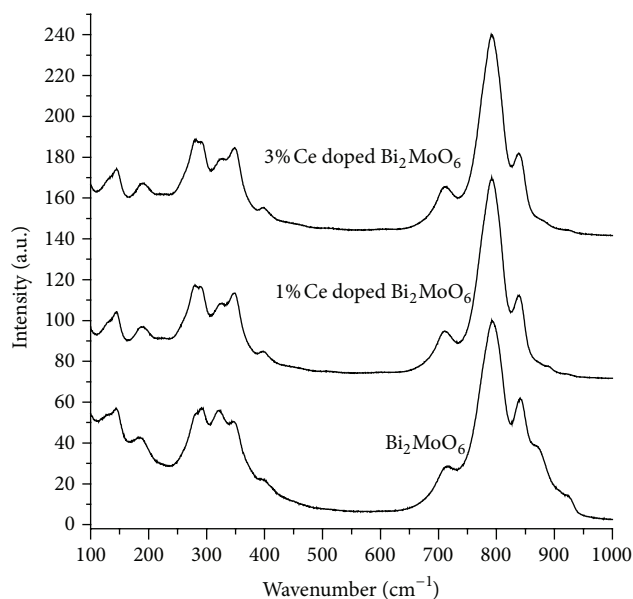


FIGURE 5: Raman spectra of undoped, 1% Ce doped, and 3% Ce doped  $\text{Bi}_2\text{MoO}_6$  samples.

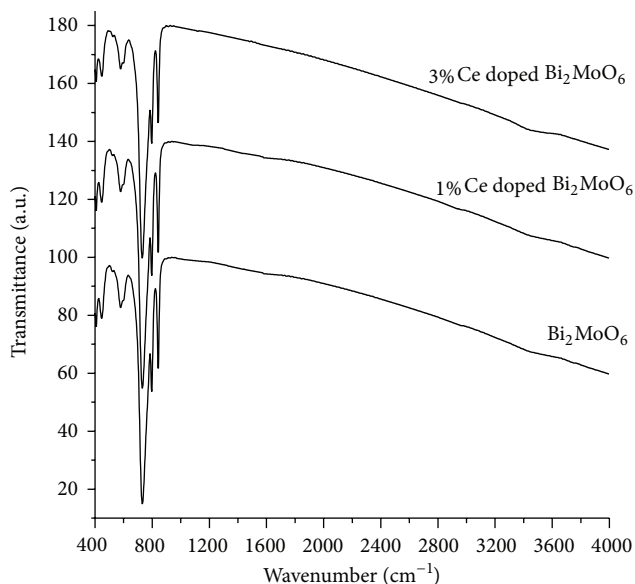
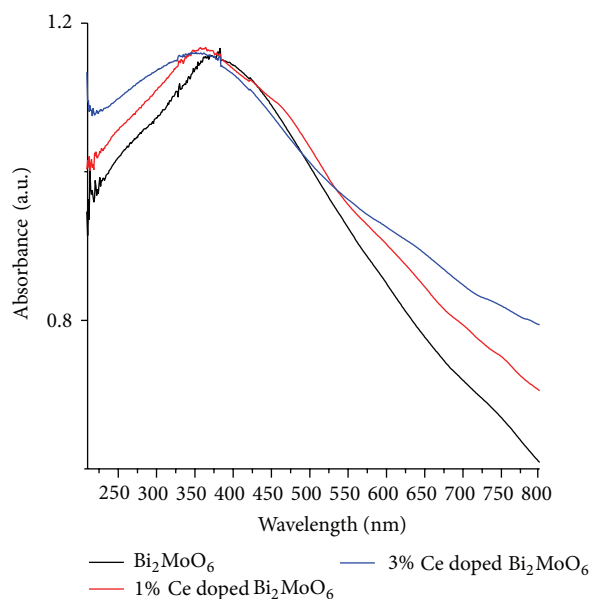


FIGURE 6: FTIR spectra of undoped, 1% Ce doped, and 3% Ce doped  $\text{Bi}_2\text{MoO}_6$  samples.

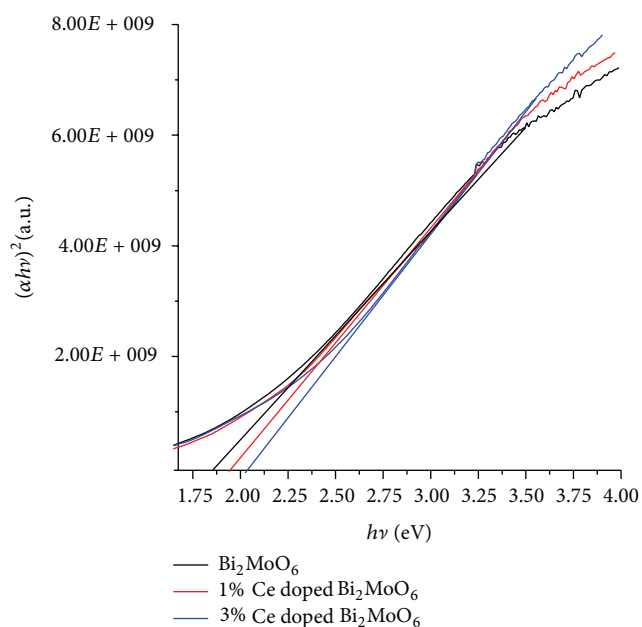
Ce doped  $\text{Bi}_2\text{MoO}_6$  which imply the possible application for visible-light photocatalysis.

#### 4. Conclusions

0–3% Ce doped orthorhombic  $\text{Bi}_2\text{MoO}_6$  nanoplates were successfully synthesized by the hydrothermal method. The experimental results presented that the as-synthesized products were orthorhombic  $\text{Bi}_2\text{MoO}_6$  with the growth along the [010] direction. UV-visible absorption spectra show strong absorption due to the intrinsic energy gap transition of  $\text{Bi}_2\text{MoO}_6$ .



(a)



(b)

FIGURE 7: (a) UV-visible absorption and (b)  $(\alpha h\nu)^2$  versus  $h\nu$  curves of undoped, 1% Ce doped, and 3% Ce doped  $\text{Bi}_2\text{MoO}_6$  samples.

#### Conflict of Interests

The authors declare that there is no conflict of interests regarding the publication of this paper.

#### Acknowledgment

The authors are extremely grateful to the Prince of Songkla University, Hat Yai, Songkhla, Thailand, for providing financial support through contract no. SCI560002S.

## References

- [1] Y. Shi, S. Feng, and C. Cao, "Hydrothermal synthesis and characterization of  $\text{Bi}_2\text{MoO}_6$  and  $\text{Bi}_2\text{WO}_6$ ," *Materials Letters*, vol. 44, no. 3, pp. 215–218, 2000.
- [2] M. Zhang, C. Shao, P. Zhang et al., " $\text{Bi}_2\text{MoO}_6$  microtubes: controlled fabrication by using electrospun polyacrylonitrile microfibers as template and their enhanced visible light photocatalytic activity," *Journal of Hazardous Materials*, vol. 225–226, pp. 155–163, 2012.
- [3] C. Xu, D. Zou, L. Wang, H. Luo, and T. Ying, " $\gamma\text{-Bi}_2\text{MoO}_6$  nanoplates: surfactant-assisted hydrothermal synthesis and optical properties," *Ceramics International*, vol. 35, no. 5, pp. 2099–2102, 2009.
- [4] Y. Miao, G. Pan, Y. Huo, and H. Li, "Aerosol-spraying preparation of  $\text{Bi}_2\text{MoO}_6$ : a visible photocatalyst in hollow microspheres with a porous outer shell and enhanced activity," *Dyes Pigments*, vol. 99, pp. 382–389, 2013.
- [5] X. Wang, F. Gu, L. Li, G. Fang, and X. Wang, "A facile mixed-solvothermal route to  $\gamma\text{-Bi}_2\text{MoO}_6$  nanoflakes and their visible-light-responsive photocatalytic activity," *Materials Research Bulletin*, vol. 48, pp. 3761–3765, 2013.
- [6] A. Martínez-de la Cruz and S. Obregón Alfaro, "Synthesis and characterization of  $\gamma\text{-Bi}_2\text{MoO}_6$  prepared by coprecipitation: photoassisted degradation of organic dyes under vis-irradiation," *Journal of Molecular Catalysis A: Chemical*, vol. 320, no. 1–2, pp. 85–91, 2010.
- [7] E. L. Cuéllar, A. Martínez-De La Cruz, K. H. L. Rodríguez, and U. O. Méndez, "Preparation of  $\gamma\text{-Bi}_2\text{MoO}_6$  thin films by thermal evaporation deposition and characterization for photocatalytic applications," *Catalysis Today*, vol. 166, no. 1, pp. 140–145, 2011.
- [8] W. Yin, W. Wang, and S. Sun, "Photocatalytic degradation of phenol over cage-like  $\text{Bi}_2\text{MoO}_6$  hollow spheres under visible-light irradiation," *Catalysis Communications*, vol. 11, no. 7, pp. 647–650, 2010.
- [9] J. Xie, D. Jiang, M. Chen et al., "Preparation and characterization of monodisperse Ce-doped  $\text{TiO}_2$  microspheres with visible light photocatalytic activity," *Colloids and Surfaces A: Physicochemical and Engineering Aspects*, vol. 372, no. 1–3, pp. 107–114, 2010.
- [10] M. Nasir, S. Bagwasi, Y. Jiao, F. Chen, B. Tian, and J. Zhang, "Characterization and activity of the Ce and N co-doped  $\text{TiO}_2$  prepared through hydrothermal method," *Chemical Engineering Journal*, vol. 236, pp. 388–397, 2014.
- [11] Powder Diffract. File, JCPDS Internat. Centre Diffract. Data, Pa, USA, 2001.
- [12] Y. Zheng, F. Duan, J. Wu, L. Liu, M. Chen, and Y. Xie, "Enhanced photocatalytic activity of bismuth molybdates with the preferentially exposed 010 surface under visible light irradiation," *Journal of Molecular Catalysis A: Chemical*, vol. 303, no. 1–2, pp. 9–14, 2009.
- [13] T. Zhou, J. Hu, and J. Li, " $\text{Er}^{3+}$  doped bismuth molybdate nanosheets with exposed 010 facets and enhanced photocatalytic performance," *Applied Catalysis B: Environmental*, vol. 110, pp. 221–230, 2011.
- [14] C. Wang, C. Shao, Y. Liu, and L. Zhang, "Photocatalytic properties  $\text{BiOCl}$  and  $\text{Bi}_2\text{O}_3$  nanofibers prepared by electrospinning," *Scripta Materialia*, vol. 59, no. 3, pp. 332–335, 2008.
- [15] B. Yuan, C. Wang, Y. Qi et al., "Decorating hierarchical  $\text{Bi}_2\text{MoO}_6$  microspheres with uniformly dispersed ultrafine Ag nanoparticles by an in situ reduction process for enhanced visible light-induced photocatalysis," *Colloids and Surfaces A*, vol. 425, pp. 99–107, 2013.
- [16] L. Wu, J. Bi, Z. Li, X. Wang, and X. Fu, "Rapid preparation of  $\text{Bi}_2\text{WO}_6$  photocatalyst with nanosheet morphology via microwave-assisted solvothermal synthesis," *Catalysis Today*, vol. 131, pp. 15–20, 2008.
- [17] Z. Li, L. Gao, and S. Zheng, "SEM, XPS, and FTIR studies of  $\text{MoO}_3$  dispersion on mesoporous silicate MCM-41 by calcination," *Materials Letters*, vol. 57, no. 29, pp. 4605–4610, 2003.
- [18] X. Zeng, X. Zhang, M. Yang, and Y. Qi, "A facile hydrothermal method for the fabrication of one-dimensional  $\text{MoO}_3$  nanobelts," *Materials Letters*, vol. 112, pp. 87–89, 2013.
- [19] B. M. Sánchez, T. Brousse, C. R. Castro, V. Nicolosi, and P. S. Grant, "An investigation of nanostructured thin film  $\alpha\text{-MoO}_3$  based supercapacitor electrodes in an aqueous electrolyte," *Electrochimica Acta*, vol. 91, pp. 253–260, 2013.
- [20] M. Rouhani, Y. L. Foo, J. Holey et al., "Photochromism of amorphous molybdenum oxide films with different initial  $\text{Mo}^{5+}$  relative concentrations," *Applied Surface Science*, vol. 273, pp. 150–158, 2013.
- [21] H. Borchert, Y. V. Frolova, V. V. Kaidiev et al., "Electronic and chemical properties of nanostructured cerium dioxide doped with praseodymium," *Journal of Physical Chemistry B*, vol. 109, no. 12, pp. 5728–5738, 2005.
- [22] M. Faisal, A. A. Ismail, A. A. Ibrahim, H. Bouzid, and S. A. Al-Sayari, "Highly efficient photocatalyst based on Ce doped ZnO nanorods: controllable synthesis and enhanced photocatalytic activity," *Chemical Engineering Journal*, vol. 229, pp. 225–233, 2013.
- [23] M. Mączka, P. T. C. Freire, C. Luz-Lima, W. Paraguassu, J. Hanuza, and J. Mendes Filho, "Pressure-induced phase transitions in ferroelectric  $\text{Bi}_2\text{MoO}_6$ —a Raman scattering study," *Journal of Physics Condensed Matter*, vol. 22, no. 1, Article ID 015901, 2010.
- [24] M. Mączka, W. Paraguassu, L. Macalik, P. T. C. Freire, J. Hanuza, and J. Mendes Filho, "A Raman scattering study of pressure-induced phase transitions in nanocrystalline  $\text{Bi}_2\text{MoO}_6$ ," *Journal of Physics Condensed Matter*, vol. 23, no. 4, Article ID 045401, 2011.
- [25] M. Mączka, L. Macalik, K. Hermanowicz, L. Kępiński, and J. Hanuza, "Synthesis and phonon properties of nanosized aurivillius phase of  $\text{Bi}_2\text{MoO}_6$ ," *Journal of Raman Spectroscopy*, vol. 41, no. 10, pp. 1289–1296, 2010.
- [26] L. Zhang, T. Xu, X. Zhao, and Y. Zhu, "Controllable synthesis of  $\text{Bi}_2\text{MoO}_6$  and effect of morphology and variation in local structure on photocatalytic activities," *Applied Catalysis B: Environmental*, vol. 98, no. 3–4, pp. 138–146, 2010.

## Research Article

# Probing Photocatalytic Characteristics of Sb-Doped TiO<sub>2</sub> under Visible Light Irradiation

Lingjing Luo, Tianfeng Li, Xia Ran, Pan Wang, and Lijun Guo

*Institute of Photobiophysics, School of Physics and Electronics, Henan University, Kaifeng, Henan 475004, China*

Correspondence should be addressed to Lijun Guo; [juneguo@henu.edu.cn](mailto:juneguo@henu.edu.cn)

Received 25 November 2013; Accepted 17 February 2014; Published 6 April 2014

Academic Editor: Necdet Aslan

Copyright © 2014 Lingjing Luo et al. This is an open access article distributed under the Creative Commons Attribution License, which permits unrestricted use, distribution, and reproduction in any medium, provided the original work is properly cited.

Sb-doped TiO<sub>2</sub> nanoparticle with varied dopant concentrations was synthesized using titanium tetrachloride (TiCl<sub>4</sub>) and antimony chloride (SbCl<sub>3</sub>) as the precursors. The properties of Sb-doped TiO<sub>2</sub> nanoparticles were characterized by X-ray diffraction (XRD), scanning electron microscope (SEM), fluorescence spectrophotometer, and Uv-vis spectrophotometer. The absorption edge of TiO<sub>2</sub> nanoparticles could be extended to visible region after doping with antimony, in contrast to the UV absorption of pure TiO<sub>2</sub>. The results showed that the photocatalytic activity of Sb-doped TiO<sub>2</sub> nanoparticles was much more active than pure TiO<sub>2</sub>. The 0.1% Sb-doped TiO<sub>2</sub> nanoparticles demonstrated the best photocatalytic activity which was better than that of the Degussa P25 under visible light irradiation using terephthalic acid as fluorescent probe. The effects of Sb dopant on the photocatalytic activity and the involved mechanism were extensively investigated in this work as well.

## 1. Introduction

In the past decade, TiO<sub>2</sub> has become a hot spot of research due to its outstanding photoelectric properties, high chemical stability, low cost, and nontoxicity and can be widely applied on photons device [1], photocatalysis [2], sensor [3], and so forth. Although TiO<sub>2</sub> has many excellent properties, the application is limited due to a relatively wide band gap (3.2 eV for the anatase) and the quick recombination of electron-hole pairs in TiO<sub>2</sub> taking place on a time scale of 10<sup>-9</sup>–10<sup>-12</sup> s [4]. Therefore, several methods have been attempted to enhance its photocatalytic activity, such as modifying TiO<sub>2</sub> with metals [5–7], nonmetals [8–10], or other semiconductors [11, 12]. In addition, the wide band gap limits the absorption of catalysts to UV light only. It has been reported that the spectral response of TiO<sub>2</sub> photocatalysts can be extended to visible light region through the doping with other elements in order to make a donor or an acceptor level [13, 14] in the forbidden band of TiO<sub>2</sub>. The doping level can either capture excited electrons of TiO<sub>2</sub> from valence band or make electrons jump to the conduction band of TiO<sub>2</sub>. As a result, the long wave photons can be absorbed and the scope of absorption spectra region is extended to lower

energy [15]. Previously, TiO<sub>2</sub> has been doped with a variety of elements, such as N [16], Fe [17], La [18], and so forth. The effect of Sb element on photocatalytic activity under visible light irradiation has also been studied by several research groups, showing high visible light absorption with UV-vis absorption spectrum measurements [19]. Although catalytic properties of Sb-doped TiO<sub>2</sub> have been found more effective, the photocatalytic mechanisms under visible light are not definitively clarified or elaborated.

In order to further study the catalytic properties of doped TiO<sub>2</sub> under visible light and the contribution of different free radicals in the catalytic reaction. In this work, pure and 0.1%–5% Sb-doped TiO<sub>2</sub> photocatalysts were prepared by coprecipitation method from TiCl<sub>4</sub> and SbCl<sub>3</sub>. Moreover, the influence of Sb dopant on the structure of TiO<sub>2</sub>, the photoabsorption properties, and catalytic activity of these samples were studied systematically. Sb doping not only expands the absorption spectra of catalysts from UV light to visible light but also improves the catalytic activity of photocatalysts. The obtained results indicate that the catalytic activity of Sb-doped TiO<sub>2</sub> is better than Degussa P25 which absorbs the UV light only [20]. Furthermore, because hydroxyl radicals (OH<sup>•</sup>) and superoxide anion radical (O<sup>2-•</sup>)

can be generated on the surface of pure and Sb-doped  $\text{TiO}_2$  under visible light irradiation ( $>420\text{ nm}$ ), the terephthalic acid was employed as the fluorescent probe to evaluate the photocatalytic activity of catalyst [21]. For the understanding of the role of two kinds of free radicals in the catalytic process and the catalytic mechanism involved, scavengers of DMSO and p-benzoquinone are used to eliminate hydroxyl radicals ( $\text{OH}^\bullet$ ) and superoxide anion radical ( $\text{O}_2^{\bullet-}$ ), respectively.

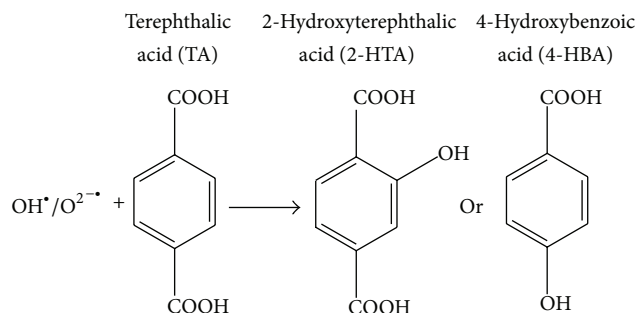
## 2. Experimental

**2.1. Materials and Catalyst Preparation.** All reagents used in the experiments were purchased from commercial sources as received, including titanium tetrachloride ( $\text{TiCl}_4$ , AR), dimethyl sulfoxide [ $(\text{CH}_3)_2\text{SO}$ , AR], n-butyl alcohol [ $\text{CH}_3(\text{CH}_2)_3\text{OH}$ , AR], and p-benzoquinone ( $\text{C}_6\text{H}_4\text{O}_2$ , CP). The distilled water from Milli-Q system was used in the preparation of materials.

Pure and 0.1%~5% Sb-doped  $\text{TiO}_2$  nanoparticles were synthesized by coprecipitation method according to the literature [19], in which the  $\text{TiCl}_4$  dissolved in diluted HCl with deionized water and the obtained mixture solution was named Solution A. Dissolving  $\text{SbCl}_3$  in  $\text{HNO}_3$  at a doping level ranging from 0.1% to 5% nominal atomic against  $\text{TiCl}_4$ , we obtained Solution B. Vigorously stirring Solution B until it is completely dissolved and then adding Solution B to Solution A under vigorous stirring at room temperature, titanium hydrous gels were precipitated upon neutralization with  $\text{NH}_4\text{OH}$  at  $\text{pH}\sim 8$ . The resulting precipitates were repeatedly washed to remove undesirable anions such as  $\text{Cl}^-$ . The coprecipitated wet gels were treated in a butanol at  $100^\circ\text{C}$  for 2 h, followed by drying at  $120^\circ\text{C}$  for 10 h. The dried precipitates were calcined at  $500^\circ\text{C}$  in air to maintain the anatase phase of  $\text{TiO}_2$  and milled with agate mortar in ethanol for 30 min.

**2.2. Characterization of Catalyst.** X-ray diffraction (XRD, DX-2700) patterns collected from  $10^\circ$  to  $80^\circ$  in  $2\theta$  with  $0.02^\circ$  steps/s were used to identify average crystallite sizes and crystallinity of the nanoparticles using a powder X-ray diffractometer ( $\lambda = 0.154056\text{ nm}$ ) with Cu  $\text{K}\alpha 1$  radiation from the monochromatized X-ray beam at 40 kV and 40 mA. The optical absorption spectra were measured using a UV-vis spectrophotometer (Shimadzu, UV-2500) equipped with an integrating sphere, a referenced against the compressed  $\text{BaSO}_4$  powders. Particle morphologies of samples were examined by scanning electron microscopy (SEM, JSM 6301F) at 15 kV. The Brunauer-Emmett-Teller (BET) surface area ( $S_{\text{BET}}$ ) of the samples was determined by nitrogen adsorption/desorption isotherm measurements at 77 K (ASAP 2010). The fluorescence emission spectrum was recorded at room temperature with excitation at 320 nm on a fluorescence spectrophotometer (Hitachi, F-4500).

**2.3. Photocatalytic Activity Test.** The fluorescence probe sensitive to the free radicals was applied to detect the photocatalytic activity of pure and 0.1%~5% Sb-doped  $\text{TiO}_2$  nanoparticles. Terephthalic acid as the fluorescent probe can readily react with hydroxyl radicals ( $\text{OH}^\bullet$ ) and superoxide anion



SCHEME 1: Reactions of hydroxyl and superoxide anion radicals with terephthalic acid to form the 2-HTA or 4-HBA.

radical ( $\text{O}_2^{\bullet-}$ ) to produce highly fluorescent products [22]. As shown in Scheme 1, the main products of terephthalic acid are 2-hydroxyterephthalic acid (2-HTA) or hydroxybenzoic acid (4-HBA), and only 2-HTA is highly fluorescent and thus can be easily determined by fluorescence spectroscopy [22, 23].

Photoreactivity experiments: 5 mg photocatalysts of P25  $\text{TiO}_2$ ; pure  $\text{TiO}_2$ ; and 0.1%, 0.5%, 1%, and 5% Sb-doped  $\text{TiO}_2$  were suspended in 20 mL aqueous solution containing 0.01 M NaOH ( $\text{pH}\sim 11.5$ ) and  $500\ \mu\text{M}$  terephthalic acid, respectively. Before exposure to visible light, the suspension was stirred in the dark for 30 min. 3 mL of the solution was then taken out after irradiation for 20 min and centrifuged for fluorescence spectroscopy measurement. The emission intensity of the 2-HTA was monitored with the excitation at 320 nm. The photoreactivity in visible region was investigated with the irradiation of light source ( $\lambda > 420\text{ nm}$ ) obtained by the cut-off filter at 420 nm from a 500 W Xe lamp.

To study the reactivity of  $\text{OH}^\bullet$  radicals formed from trapped holes solely, p-benzoquinone (0.05 mM) was used to quench  $\text{O}_2^{\bullet-}$  radicals. Similarly, for the study of  $\text{O}_2^{\bullet-}$  anion radicals, dimethyl sulfoxide (DMSO) (1 mM) was used to quench  $\text{OH}^\bullet$  radicals formed on the Sb-doped  $\text{TiO}_2$  surface. Scavenger of DMSO can react with  $\text{OH}^\bullet$  to generate methyl sulfinic acid ( $\text{CH}_3\text{SOOH}$ ) and methyl radical ( $\text{CH}_3^\bullet$ ) [24]. Detailed methods were performed as follows: 5 mg P25  $\text{TiO}_2$ ; pure  $\text{TiO}_2$ ; and 0.1%, 0.5%, 1%, and 5% Sb-doped  $\text{TiO}_2$  were suspended in 20 mL aqueous solution containing 0.01 M NaOH,  $500\ \mu\text{M}$  terephthalic acid, and (1) without scavenger, (2) 1 mM DMSO, (3) 0.01 mM p-benzoquinone, respectively. Measurement method of fluorescence spectrum is the same as photoreactivity experiments except that the irradiation time is 10 min.

In this way, we were thus able to study separately the reactivity of two radicals  $\text{h}^+/\text{OH}^\bullet$  and  $\text{e}^-/\text{O}_2^{\bullet-}$  on the surface of Sb-doped  $\text{TiO}_2$  by observing the fluorescent spectra of products.

## 3. Results and Discussion

For pure  $\text{TiO}_2$ , the absorption edge is in UV region and the bandgap is around 3.2 eV. With the Sb doping, new dopant level was formed in the forbidden band of  $\text{TiO}_2$  (Figure 1). When  $\text{TiO}_2$  is exposed to light of energy greater

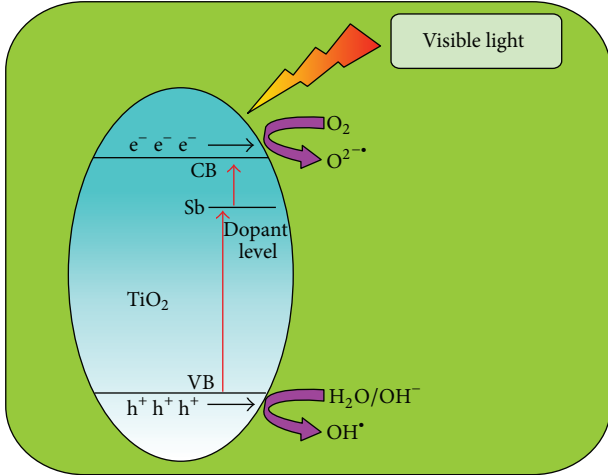


FIGURE 1: The generation of photogenerated electron-hole pairs and the formation process of two kinds of radicals on the surface of Sb-doped  $\text{TiO}_2$  catalyst.

than the bandgap energy, electrons are excited from its valence band into the conduction band to form spatially separated electron-hole ( $e^-/h^+$ ) pairs by light absorption. The photogenerated charge carriers can be transferred to the surface of the catalyst and react with electron donors or acceptors adsorbed on the surface of the photocatalyst to generate reactive oxygen species such as  $\text{OH}^\bullet$  and  $\text{O}_2^{\bullet-}$ . As shown in Figure 1, in an aqueous environment, the photogenerated electrons are trapped by adsorbed oxygen to generate radicals ( $\text{O}_2^{\bullet-}$ ), and photogenerated holes are trapped by adsorbed water or hydroxyl bound superoxide anion ( $\text{OH}^-$ ) to generate bound hydroxyl radicals ( $\text{OH}^\bullet$ ) [25].

Figure 2(A) shows the UV-vis absorption spectra of pure and 0.1%~5% Sb-doped  $\text{TiO}_2$  prepared by coprecipitation method. The pure  $\text{TiO}_2$  had strong absorption only in the UV region corresponding to its band gap energy, while Sb-doped  $\text{TiO}_2$  exhibited a new absorption band in the short wavelength region of visible light. The visible light absorption was enhanced by the dopant of pure  $\text{TiO}_2$  and increased with Sb dopant. The color of the prepared catalysts changed from yellowish-white to yellow with the increasing dopant concentration of Sb.

Figure 2(B) shows X-ray diffraction patterns of  $\text{TiO}_2$  with different Sb doping concentration; the anatase is the crystal phase of samples prepared by coprecipitation method. The average crystallite sizes of  $\text{TiO}_2$  can be estimated from XRD spectra by using the Scherrer equation [26]:

$$D = \frac{k\lambda}{\beta \cos \theta}, \quad (1)$$

where  $D$  is the crystallite size (nm),  $k$  is the Scherrer constant ( $k = 0.89$ ),  $\lambda$  is the wavelength of the X-ray radiation source ( $\lambda = 0.154056 \text{ nm}$  in this case),  $\beta$  is the full width at half maximum intensity (radians), and  $\theta$  is the angle between the incident and diffracted beams. The average crystallite sizes of  $\text{TiO}_2$  are presented in Table 1. It is found that the average crystal sizes of  $\text{TiO}_2$  with different Sb doping concentration

TABLE 1: Crystalline properties of the prepared  $\text{TiO}_2$  photocatalysts.

Samples	Different Sb doping concentration (%)				
	0%	0.1%	0.5%	1%	5%
Crystallite size (nm)	14.5	19.2	14.7	16.4	13.6
Surface area ( $\text{m}^2/\text{g}$ )	56.281	57.822	69.220	49.691	40.606

are about 13.6~19.2 nm. The  $\text{Sb}^{5+}$  species are formed in the calcination step through oxidation of the incorporated  $\text{Sb}^{3+}$  (0.0760 nm) to  $\text{Sb}^{5+}$  [27]. The ionic radii of  $\text{Ti}^{4+}$  and  $\text{Sb}^{5+}$  are 0.0600 and 0.0605 nm, respectively [28], and the ionic radius of  $\text{Sb}^{5+}$  is similar to that of  $\text{Ti}^{4+}$ . It is suggested that  $\text{Sb}^{5+}$  ions are likely to be substituted at  $\text{Ti}^{4+}$  sites within  $\text{TiO}_2$ .  $\text{Sb}^{5+}$  ions partially replace  $\text{Ti}^{4+}$  until the solubility limit is reached.

Figures 2(C) and 2(D) show the SEM images of pure and 1% Sb-doped  $\text{TiO}_2$ , respectively. They indicate that the surface morphologies of pure and 1% Sb-doped  $\text{TiO}_2$  are almost undifferentiated. All samples are irregular in shape, and the size of particles is in the range of 25~40 nm. The particle sizes of 1% Sb-doped  $\text{TiO}_2$  are almost the same as that of pure  $\text{TiO}_2$  due to the small amount of Sb [29]. There is a slight difference between the results of SEM and Scherrer formula, probably arising from aggregated particles. In addition, the specific surface area of the samples was obtained using the BET surface area measuring apparatus at the boiling point of liquid nitrogen. The specific surface area ( $S_{\text{BET}}$ ) of catalyst is among 40.606~69.220  $\text{m}^2/\text{g}$  (as shown in Table 1).

Here, on the basis of the fact that both of these radicals  $h^+/\text{OH}^\bullet$  and  $e^-/\text{O}_2^{\bullet-}$  can react oxidatively with nonfluorescent probe terephthalic acid to generate product 2-HTA (highly fluorescent) or 4-HBA (Scheme 1), the catalytic activities can be monitored by fluorescence spectroscopy. Figure 3(a) shows fluorescence spectrum of terephthalic acid solution with P25, pure, and 0.1%~5% Sb-doped  $\text{TiO}_2$ , respectively. The results indicate that the samples of 0.1%~1% Sb-doped  $\text{TiO}_2$  have better photocatalytic activity compared with pure and Degussa P25  $\text{TiO}_2$  in visible light region, and 0.1% Sb-doped  $\text{TiO}_2$  demonstrated the best photocatalytic activity. It could be suggested that Sb dopant acts as electron traps retarding electron-hole recombination and enhancing interfacial charge carriers transfer to the surface of the particles; however, the recombination rate will increase when the dopant concentration of Sb is too high [30]. Upon excitation with visible light, electrons are excited from oxygen atoms in the conduction band, probably to the Ti 3d orbitals, and are further trapped by adsorbed  $\text{O}_2$  to produce  $\text{O}_2^{\bullet-}$  radicals. The photogenerated holes are trapped by adsorbed  $\text{H}_2\text{O}$  or  $\text{OH}^-$  to produce  $\text{OH}^\bullet$  radicals bound to the surface [25]. These trapped electrons ( $e^-/\text{O}_2^{\bullet-}$ ) or holes ( $h^+/\text{OH}^\bullet$ ) react with the nearby adsorbed molecules, as shown in Figure 1.

It is known that the photocatalytic process will generate two kinds of free radical,  $e^-/\text{O}_2^{\bullet-}$  and  $h^+/\text{OH}^\bullet$ , to drive the subsequent chemical reaction. Here, on the basis of that  $e^-/\text{O}_2^{\bullet-}$  and  $h^+/\text{OH}^\bullet$  can be quenched by scavengers of p-benzoquinone and DMSO, respectively; it is expected to get more insight into the catalytic mechanism of pure and Sb-doped  $\text{TiO}_2$  by adding scavengers. As shown in Figure 3(b),

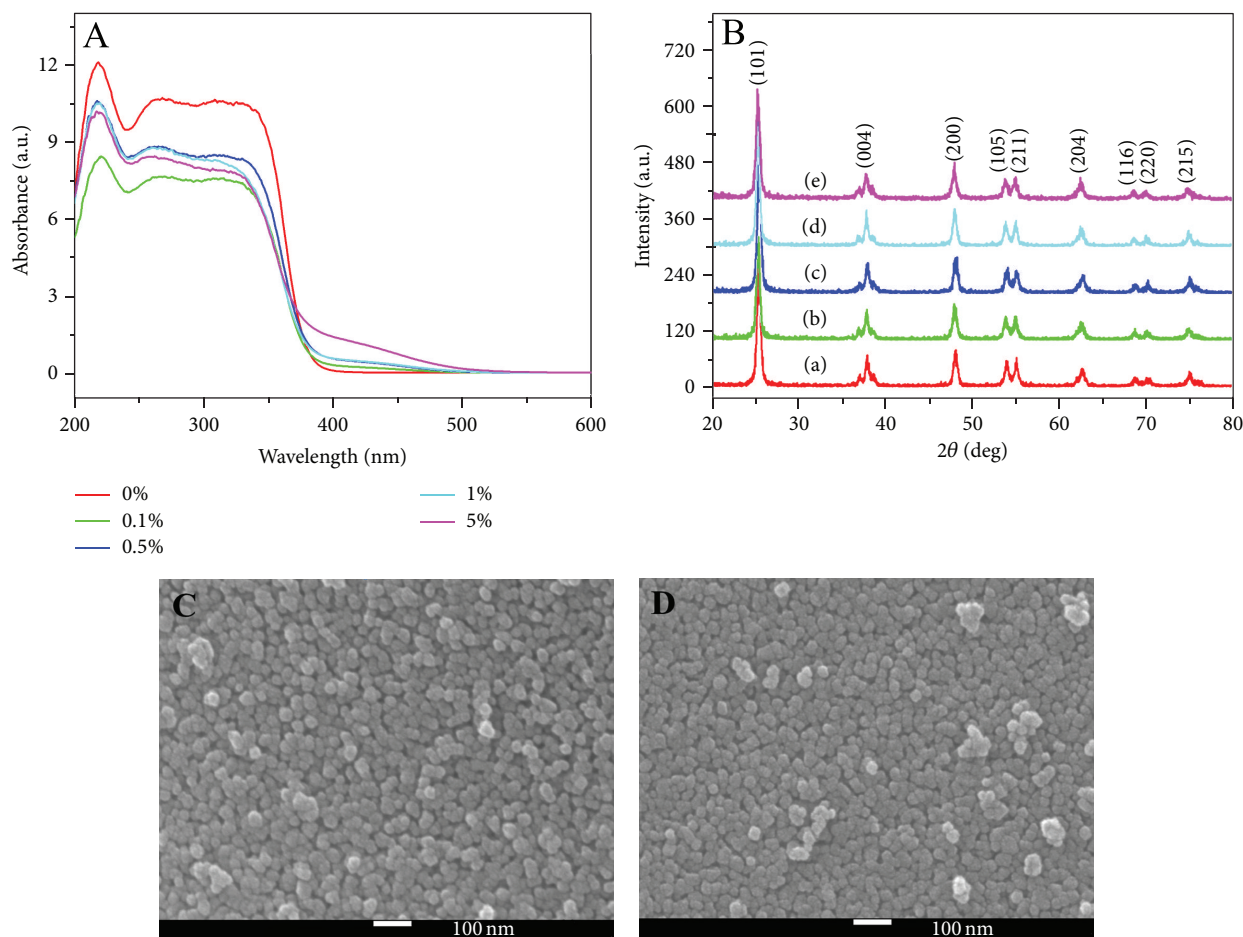


FIGURE 2: (A) UV-vis absorption spectra of pure TiO<sub>2</sub> and 0.1%~5% Sb-doped TiO<sub>2</sub>; (B) X-Ray diffraction spectra of catalysts with different Sb-doped percentage calculated at 500°C for 2 h: (a) 0%, (b) 0.1%, (c) 0.5%, (d) 1%, and (e) 5%; (C) SEM image of pure TiO<sub>2</sub>; (D) SEM image of 1% Sb-doped TiO<sub>2</sub>.

DMSO inhibited the activity of catalysts obviously, because DMSO can react with OH<sup>•</sup> and reduce the concentration of OH<sup>•</sup>. The result indicates the existence of OH<sup>•</sup> in solution and participation in the catalytic reaction of fluorescent probe. Similarly, the activity of catalysts had been also inhibited with O<sup>2-•</sup> scavenger by p-benzoquinone, showing the existence of O<sup>2-•</sup> and its involvement in the catalytic reaction at the same time. With the comparison of different Sb doping concentration, it was demonstrated that the scavengers can inhibit the photocatalytic activity of all the catalysts.

Doped TiO<sub>2</sub> demonstrates that doping Sb in TiO<sub>2</sub> can improve the photocatalytic activity of Sb-doped TiO<sub>2</sub>. The XRD results indicate that the crystalline structure of the Sb-doped TiO<sub>2</sub> is anatase with a small mean diameter. It is accepted that the anatase phase and small mean diameter are very beneficial for photocatalytic reaction [31, 32]. The Sb atoms may be substituted at some of Ti sites in TiO<sub>2</sub> and forming a narrow Sb band under the conduction band, which was determined to be responsible for visible light sensitivity. The reactive oxygen species such as OH<sup>•</sup> and O<sup>2-•</sup> on the surface of catalysts are considered beneficial for the photocatalytic process. On one hand, when the OH<sup>-</sup> or

H<sub>2</sub>O species accept h<sup>+</sup> under light irradiation, they might be oxidized to form OH<sup>•</sup>. On the other hand, the surface hydroxyl groups can also act as absorption centers for O<sub>2</sub> molecules. The e<sup>-</sup> from the conduction band can be captured by O<sub>2</sub> molecules to produce O<sup>2-•</sup>. It is OH<sup>•</sup> and O<sup>2-•</sup>, which possess high oxidizability, that oxidize terephthalic acid.

#### 4. Conclusion

The pure and Sb-doped TiO<sub>2</sub> photocatalysts have been prepared by a coprecipitation method using TiCl<sub>4</sub> and SbCl<sub>3</sub> as precursor. The influence of Sb doping concentration on the catalytic property, using terephthalic acid as fluorescent probe, has been studied in this work. Sb ions can be isomorphously substituted into the TiO<sub>2</sub> lattice to generate a new doping energy level and change the electron transition way of TiO<sub>2</sub> from valence band to conduction band. In this case, it extends the scope of TiO<sub>2</sub> absorption spectrum to the visible light region and improves photocatalytic activity of catalysts. The obtained results show that the photocatalytic activity of 0.1%~1% Sb-doped TiO<sub>2</sub> is higher than pure TiO<sub>2</sub>, and 0.1% Sb-doped TiO<sub>2</sub> presents the best photocatalytic

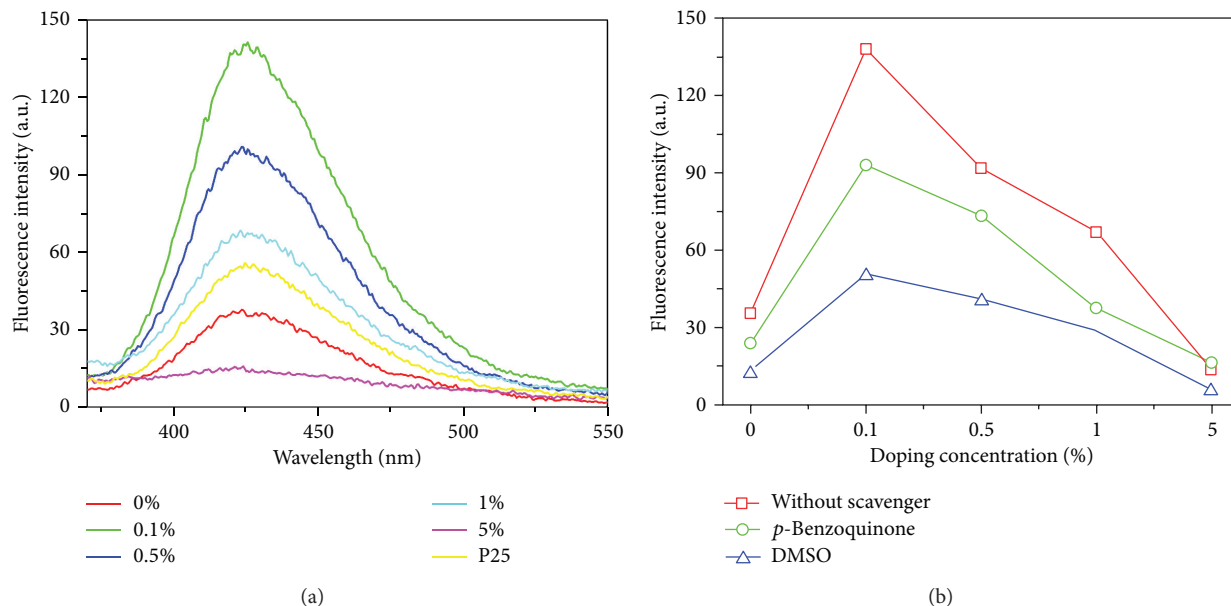


FIGURE 3: (a) Plots of the fluorescence spectral for the 500  $\mu\text{M}$  terephthalic acid on P25  $\text{TiO}_2$  and pure and 0.1%~5% Sb-doped  $\text{TiO}_2$  catalysts after visible light irradiation for 20 min. (b) The fluorescence intensity at 426 nm after irradiation 10 min for terephthalic acid on the pure and 0.1%~5% Sb-doped  $\text{TiO}_2$ , without scavenger (red), with DMSO (blue) and p-benzoquinone (green), respectively.

activity, which is much better than Degussa P25. This superior catalytic activity mainly arises from the fact that the Sb-doped  $\text{TiO}_2$  generates a new level in the forbidden band of  $\text{TiO}_2$  and contributes to the capture of carriers as well as improving the separation of photogenerated electron hole. As for the catalytic mechanism of  $\text{OH}^\bullet$  and  $\text{O}^{2-\bullet}$  in the fluorescence probe method, it can be attributed to the product fluorescence bursts from the oxidation of terephthalic acid to form 2-HTA by either one of these two radicals.

## Conflict of Interests

The authors declare that there is no conflict of interests regarding the publication of this paper.

## Acknowledgments

This work was partially supported by the National Science Foundation of China (21173068) and the Program for Innovative Research Team (Science and Technology) at the University of Henan Province (13IRTSTHN017).

## References

- [1] T. L. Thompson and J. T. Yates Jr., "Surface science studies of the photoactivation of  $\text{TiO}_2$ —new photochemical processes," *Chemical Reviews*, vol. 106, no. 10, pp. 4428–4453, 2006.
- [2] A. Kudo and Y. Miseki, "Heterogeneous photocatalyst materials for water splitting," *Chemical Society Reviews*, vol. 38, no. 1, pp. 253–278, 2009.
- [3] M. Liu, L. Piao, and W. Wang, "Fabrication and characteristics of three-dimensional flower-like titanate nanostructures," *Journal of Nanoscience and Nanotechnology*, vol. 10, no. 11, pp. 7469–7472, 2010.
- [4] M. Szostak and J. Aubé, "Chemistry of bridged lactams and related heterocycles," *Chemical Reviews*, vol. 113, no. 8, pp. 5701–5765, 2013.
- [5] A. Di Paola, G. Marci, L. Palmisano et al., "Preparation of polycrystalline  $\text{TiO}_2$  photocatalysts impregnated with various transition metal ions: characterization and photocatalytic activity for the degradation of 4-nitrophenol," *Journal of Physical Chemistry B*, vol. 106, no. 3, pp. 637–645, 2002.
- [6] W. Xue, G. Zhang, X. Xu, X. Yang, C. Liu, and Y. Xu, "Preparation of titania nanotubes doped with cerium and their photocatalytic activity for glyphosate," *Chemical Engineering Journal*, vol. 167, no. 1, pp. 397–402, 2011.
- [7] T. Morikawa, Y. Irokawa, and T. Ohwaki, "Enhanced photocatalytic activity of  $\text{TiO}_2$ -xNx loaded with copper ions under visible light irradiation," *Applied Catalysis A: General*, vol. 314, no. 1, pp. 123–127, 2006.
- [8] J. Y. Shi, W. H. Leng, W. C. Zhu, J. Q. Zhang, and C. N. Cao, "Electrochemically assisted photocatalytic oxidation of nitrite over Cr-Doped  $\text{TiO}_2$  under visible light," *Chemical Engineering and Technology*, vol. 29, no. 1, pp. 146–154, 2006.
- [9] S. Klosek and D. Raftery, "Visible light driven V-doped  $\text{TiO}_2$  photocatalyst and its photooxidation of ethanol," *Journal of Physical Chemistry B*, vol. 105, no. 14, pp. 2815–2819, 2002.
- [10] M. Sathish, B. Viswanathan, R. P. Viswanath, and C. S. Gopinath, "Synthesis, characterization, electronic structure, and photocatalytic activity of nitrogen-doped  $\text{TiO}_2$  nanocatalyst," *Chemistry of Materials*, vol. 17, no. 25, pp. 6349–6353, 2005.
- [11] T. Yamaki, T. Sumita, and S. Yamamoto, "Formation of  $\text{TiO}_2$ -xFx compounds in fluorine-implanted  $\text{TiO}_2$ ," *Journal of Materials Science Letters*, vol. 21, no. 1, pp. 33–35, 2002.
- [12] B. Mahltig, E. Gutmann, and D. C. Meyer, "Solvochemical preparation of nanocrystalline anatase containing  $\text{TiO}_2$  and

- TiO<sub>2</sub>/SiO<sub>2</sub> coating agents for application of photocatalytic treatments,” *Materials Chemistry and Physics*, vol. 127, no. 1-2, pp. 285–291, 2011.
- [13] D. Chen, H. Zhang, S. Hu, and J. Li, “Preparation and enhanced photoelectrochemical performance of coupled bicomponent ZnO-TiO<sub>2</sub> nanocomposites,” *Journal of Physical Chemistry C*, vol. 112, no. 1, pp. 117–122, 2008.
- [14] S. Stoyanov, D. Mladenova, and C. Dushkin, “Photocatalytic properties of mixed TiO<sub>2</sub>/V<sub>2</sub>O<sub>5</sub> films in water purification at varying pH,” *Reaction Kinetics and Catalysis Letters*, vol. 88, no. 2, pp. 277–283, 2006.
- [15] W. Choi, A. Termin, and M. R. Hoffmann, “The role of metal ion dopants in quantum-sized TiO<sub>2</sub>: correlation between photoreactivity and charge carrier recombination dynamics,” *Journal of Physical Chemistry*, vol. 98, no. 51, pp. 13669–13679, 1994.
- [16] H.-C. Wu, S.-W. Lin, and J.-S. Wu, “Effects of nitrogen concentration on N-doped anatase TiO<sub>2</sub>: density functional theory and Hubbard U analysis,” *Journal of Alloys and Compounds*, vol. 522, pp. 46–50, 2012.
- [17] M.-C. Wang, H.-J. Lin, C.-H. Wang, and H.-C. Wu, “Effects of annealing temperature on the photocatalytic activity of N-doped TiO<sub>2</sub> thin films,” *Ceramics International*, vol. 38, no. 1, pp. 195–200, 2012.
- [18] W. Chen, P. Yuan, S. Zhang, Q. Sun, E. Liang, and Y. Jia, “Electronic properties of anatase TiO<sub>2</sub> doped by lanthanides: a DFTU study,” *Physica B: Condensed Matter*, vol. 407, no. 6, pp. 1038–1043, 2012.
- [19] J. Moon, H. Takagi, Y. Fujishiro, and M. Awano, “Preparation and characterization of the Sb-doped TiO<sub>2</sub> photocatalysts,” *Journal of Materials Science*, vol. 36, no. 4, pp. 949–955, 2001.
- [20] Y. He, Y. Wu, H. Guo, T. Sheng, and X. Wu, “Visible light photodegradation of organics over VYO composite catalyst,” *Journal of Hazardous Materials*, vol. 169, no. 1–3, pp. 855–860, 2009.
- [21] K.-I. Ishibashi, A. Fujishima, T. Watanabe, and K. Hashimoto, “Detection of active oxidative species in TiO<sub>2</sub> photocatalysis using the fluorescence technique,” *Electrochemistry Communications*, vol. 2, no. 3, pp. 207–210, 2000.
- [22] K. Bubacz, E. Kusiak-Nejman, B. Tryba, and A. W. Morawski, “Investigation of OH radicals formation on the surface of TiO<sub>2</sub>/N photocatalyst at the presence of terephthalic acid solution. Estimation of optimal conditions,” *Journal of Photochemistry and Photobiology A: Chemistry*, vol. 261, pp. 7–11, 2013.
- [23] U. Černigoj, M. Kete, and U. L. Štangar, “Development of a fluorescence-based method for evaluation of self-cleaning properties of photocatalytic layers,” *Catalysis Today*, vol. 151, no. 1-2, pp. 46–52, 2010.
- [24] M. K. Eberhardt and R. Colina, “The reaction of OH radicals with dimethyl sulfoxide. A comparative study of Fenton’s reagent and the radiolysis of aqueous dimethyl sulfoxide solutions,” *Journal of Organic Chemistry*, vol. 53, no. 5, pp. 1071–1074, 1988.
- [25] W. Xu, P. K. Jain, B. J. Beberwyck, and A. P. Alivisatos, “Probing redox photocatalysis of trapped electrons and holes on single Sb-doped titania nanorod surfaces,” *Journal of the American Chemical Society*, vol. 134, no. 9, pp. 3946–3949, 2012.
- [26] Q. Zhang, J.-B. Joo, Z. Lu et al., “Self-assembly and photocatalysis of mesoporous TiO<sub>2</sub> nanocrystal clusters,” *Nano Research*, vol. 4, no. 1, pp. 103–114, 2011.
- [27] E. Redel, E. Arsenault, P. G. O’Brien, N. P. Kherani, and G. A. Ozin, “Growth of metal nanocrystals on nanostructured metal oxides-dramatic effect of antimony doping,” *Chemistry of Materials*, vol. 23, no. 6, pp. 1353–1355, 2011.
- [28] R. D. Shannon, “Revised effective Ionic-RadII and systematic studies of interatomic distances in halides and chalcogenides,” *Acta Crystallographica Section A*, vol. 32, pp. 751–767, 1976.
- [29] D. N. Liu, G. H. He, L. Zhu, W. Y. Zhou, and Y. H. Xu, “Enhancement of photocatalytic activity of TiO<sub>2</sub> nanoparticles by coupling Sb<sub>2</sub>O<sub>3</sub>,” *Applied Surface Science*, vol. 258, no. 20, pp. 8055–8060, 2012.
- [30] T. Ikeda, T. Nomoto, K. Eda et al., “Photoinduced dynamics of TiO<sub>2</sub> doped with Cr and Sb,” *Journal of Physical Chemistry C*, vol. 112, no. 4, pp. 1167–1173, 2008.
- [31] H. Choi, E. Stathatos, and D. D. Dionysiou, “Sol-gel preparation of mesoporous photocatalytic TiO<sub>2</sub> films and TiO<sub>2</sub>/Al<sub>2</sub>O<sub>3</sub> composite membranes for environmental applications,” *Applied Catalysis B: Environmental*, vol. 63, no. 1-2, pp. 60–67, 2006.
- [32] C. He, B. Tian, and J. Zhang, “Thermally stable SiO<sub>2</sub>-doped mesoporous anatase TiO<sub>2</sub> with large surface area and excellent photocatalytic activity,” *Journal of Colloid and Interface Science*, vol. 344, no. 2, pp. 382–389, 2010.

## Research Article

# Synthesis and Characterization of Hollow Magnetic Alloy (GdNi<sub>2</sub>, Co<sub>5</sub>Gd) Nanospheres Coated with Gd<sub>2</sub>O<sub>3</sub>

Wang Li,<sup>1</sup> Fa-gen Li,<sup>1</sup> Jun Wang,<sup>1</sup> and Guo-meng Zhao<sup>2</sup>

<sup>1</sup> Department of Physics, Faculty of Science, Ningbo University, Ningbo, China

<sup>2</sup> Department of Physics and Astronomy, California State University at Los Angeles, Los Angeles, CA 90032, USA

Correspondence should be addressed to Jun Wang; [wjnaf@ustc.edu](mailto:wjnaf@ustc.edu)

Received 30 October 2013; Accepted 15 January 2014; Published 24 February 2014

Academic Editor: Ajay Soni

Copyright © 2014 Wang Li et al. This is an open access article distributed under the Creative Commons Attribution License, which permits unrestricted use, distribution, and reproduction in any medium, provided the original work is properly cited.

Uniform magnetic hollow nanospheres (GdNi<sub>2</sub>, Co<sub>5</sub>Gd) coated with Gd<sub>2</sub>O<sub>3</sub> have been successfully prepared on a large scale via a urea-based homogeneous precipitation method using silica (SiO<sub>2</sub>) spheres as sacrificed templates, followed by subsequent heat treatment. Nitrogen sorption measurements and scanning electron microscope reveal that these hollow-structured magnetic nanospheres have the mesoporous shells that are composed of a large amount of uniform nanoparticles. After reduction treatment, these nanoparticles exhibit superparamagnetism that might have potential applications in medicine. Furthermore, the developed synthesis route may provide an important guidance for the preparation of other multifunctional hollow spherical materials.

## 1. Introduction

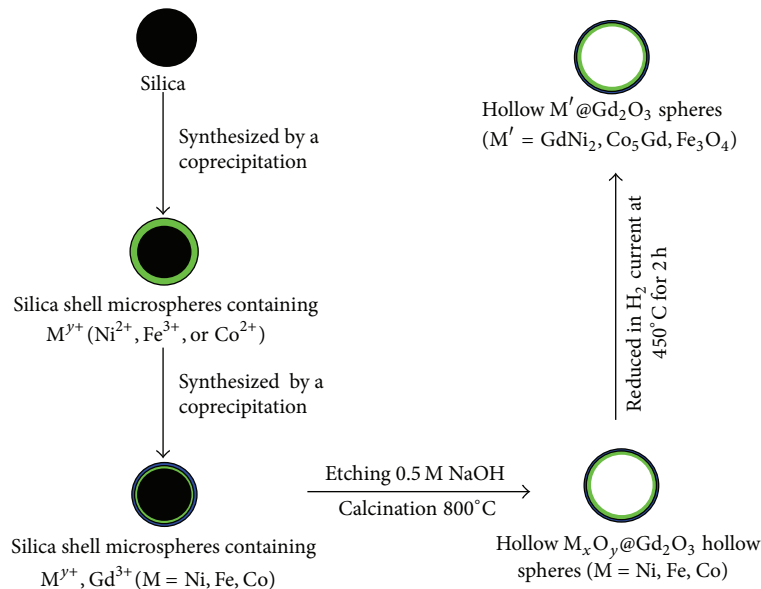
Hollow nanospheres with tailored structures have attracted tremendous interest due to their higher specific surface area, better permeation, lower density than their bulk counterparts, and their extensive potential applications in magnetic, catalysis, chemical reactors, drug delivery, and optical materials [1–10]. Generally, templating methods are to coat nanocrystals on the hard or soft templates [11–15] followed by removing the templates through etching or calcinations [16]. Moreover, the diameter of the hollow spheres and the thickness of shells can also be tuned by varying the size of cores and the times of the precipitation procedure. Importantly, the shell-shell structure of hollow spheres is involved in immobilizing desired materials on template surfaces due to potential incompatibilities between materials [17], which are well exhibited without affecting the others. It is known that RE<sub>2</sub>O<sub>3</sub> (where RE is the rare-earth element) compounds have been widely used as heat-resistant materials, high-performance luminescent devices, and catalysts based on the electrical and optical properties of their 4f electrons of lanthanide [18]. Among different RE<sub>2</sub>O<sub>3</sub> materials, gadolinium oxide (Gd<sub>2</sub>O<sub>3</sub>) is promising as host

matrix for down- and upconversion luminescence due to its good chemical durability and low phonon energy [19]. Meanwhile, magnetic microspheres were introduced into the area of biosciences in the 1970s [20]; the synthesis of micro- (or nano) magnetic carriers has received increasing interest due to their wide promising applications.

As a form of nanocomposites, the particles combine magnetic materials and gadolinium oxide to integrate the functions of magnetic and optical responses of the individual components. In particular, shell/shell nanocomposites of magnetic materials and Gd<sub>2</sub>O<sub>3</sub> combine the advantages of individual shells to enhance space utilization of the capsules and greatly extend the application. However, few studies have been involved in preparation of such shell/shell nanocomposites. Recently, template-directed synthesis, with soft templates and hard templates, has been demonstrated to be an effective approach to prepare inorganic hollow spheres. Up to now, using carboxylate silica particles [17], melamine formaldehyde (MF) [21], and silica colloidal particles as sacrificial templates has become the mainstream. Among them, silica is usually employed because it can very efficiently adsorb proteins and is highly stable even in organic solvents [22]. Notably, gadolinium oxide doped

TABLE 1

SiO <sub>2</sub>	M(NO <sub>3</sub> ) <sub>y</sub> ·zH <sub>2</sub> O (M = Fe, Co, Ni)	Gd(NO <sub>3</sub> ) <sub>3</sub> ·6H <sub>2</sub> O
1.2 g	0.21 g Fe(NO <sub>3</sub> ) <sub>3</sub> ·9H <sub>2</sub> O	0.23 g
1.2 g	0.15 g Co(NO <sub>3</sub> ) <sub>2</sub> ·6H <sub>2</sub> O	0.23 g
1.2 g	0.15 g Ni(NO <sub>3</sub> ) <sub>2</sub> ·6H <sub>2</sub> O	0.23 g

FIGURE 1: Schematic illustration of the preparation of M@Gd<sub>2</sub>O<sub>3</sub> (M = GdNi<sub>2</sub>, Co<sub>5</sub>Gd, Fe<sub>3</sub>O<sub>4</sub>) hollow nanospheres.

with europium ions (Gd<sub>2</sub>O<sub>3</sub> : Eu<sup>3+</sup>) has been proven to be an important red-emitting phosphor [23], which emits light in the near-infrared (NIR) window, between 700 and 900 nm and is of particular interest [24]. Along these lines, luminescent and magnetic nanoparticles may be an appropriate answer to major advances in biological and biomedical imaging.

In this work, we have successfully prepared monodisperse shell/shell nanocomposites comprising magnetic hollow spheres and Gd<sub>2</sub>O<sub>3</sub> shells. The main steps of the preparation involve synthesis of monodisperse SiO<sub>2</sub> templates, installation of inorganic seeds, and growth and formation of inner or outer inorganic shells via a layer-by-layer deposition process [25]. However, the inorganic phase of Gd<sub>2</sub>O<sub>3</sub> was partly soluble in the magnetic shell when the products were reduced in H<sub>2</sub> gas at 450°C. Fortunately, the alloys (GdNi<sub>2</sub> and Co<sub>5</sub>Gd) still possess superparamagnetism. The synthesis strategy is based on a self-assembly diffusion process as illustrated in Figure 1. Our work may open new possibilities to synthesize hollow spheres of other nanocomposites and extend their applications.

## 2. Experimental

**2.1. Materials.** Nickel nitrate hexahydrate, cobalt nitrate hexahydrate, and gadolinium (III) nitrate hexahydrate were from Aladdin Chemistry Co. Ltd. Iron (III) nitrate nonahydrate was from Sinopharm Chemical Reagent Co. Ltd. Other reagents were used without further purification.

**2.2. Preparation of Nickel-Silica Composite Spheres.** The synthesis procedure of silica/Ni<sub>3</sub>Si<sub>2</sub>O<sub>5</sub>(OH)<sub>4</sub> [26] involves (1) preparation of uniform silica balls (500 nm) [27] and (2) preparation of nickel-silica composite spheres via a urea-based homogeneous precipitation approach. The whole synthesis process is illustrated briefly in Figure 1. The synthesis details are as follows: 1.20 g of SiO<sub>2</sub> spheres were separately dispersed in 100 mL of solution containing 0.15 g of Ni(NO<sub>3</sub>)<sub>2</sub>·6H<sub>2</sub>O and 0.30 g of CO(NH<sub>2</sub>)<sub>2</sub>. The mixture (100 mL) was stirred mildly at a constant temperature of 95°C for 4 h for a complete precipitation.

**2.3. Preparation of GdNi<sub>2</sub>@Gd<sub>2</sub>O<sub>3</sub> Hollow Spheres.** The concentrations of gadolinium nitrate, urea, and nickel-silica monodisperse spheres were 0.005 M, 0.05 M, and 12 g/L, respectively, which were prepared by following the same procedure. By immersing the products in 200 mL of 0.5 M NaOH, the silica cores were dissolved by alkaline and the remainder shells were collected by centrifugation. Then, these powders were obtained through heat treatment at 800°C for 2 h in air at a heating rate of 10°C min<sup>-1</sup>. Finally, the particles were reduced in H<sub>2</sub> gas (40 cm<sup>3</sup>/min) at 450°C (at a rate of 10°C/min) for 2 h in the fixed-bed reactor. After the completion of the reduction process, the sample was protected at room temperature in the flowing-inert gas for 12 h. The core-shell structured M@Gd<sub>2</sub>O<sub>3</sub> (M = Fe<sub>3</sub>O<sub>4</sub>, and Co<sub>5</sub>Gd) are prepared by the same method (Table 1).

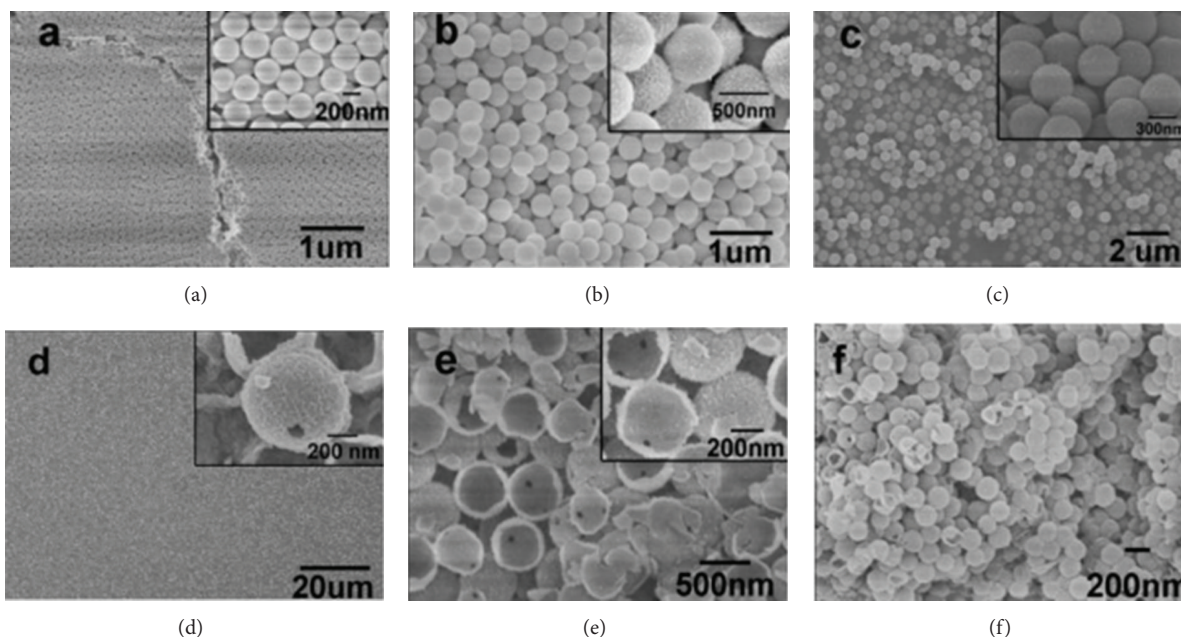


FIGURE 2: SEM images of (a) SiO<sub>2</sub> spheres, ((b) and (d)) silica/Ni<sub>3</sub>Si<sub>2</sub>O<sub>5</sub>(OH)<sub>4</sub> core-shell structures, Ni<sub>3</sub>Si<sub>2</sub>O<sub>5</sub>(OH)<sub>4</sub> hollow spheres with an average size of 580 nm. ((c) and (e)) SiO<sub>2</sub>@Ni<sub>3</sub>Si<sub>2</sub>O<sub>5</sub>(OH)<sub>4</sub>@Gd<sub>2</sub>O<sub>3</sub> core-shell structures, Ni<sub>3</sub>Si<sub>2</sub>O<sub>5</sub>(OH)<sub>4</sub>@Gd<sub>2</sub>O<sub>3</sub> hollow spheres with an average size of 600 nm. (f) Ni<sub>3</sub>Si<sub>2</sub>O<sub>5</sub>(OH)<sub>4</sub>@Gd<sub>2</sub>O<sub>3</sub> hollow spheres (200 nm).

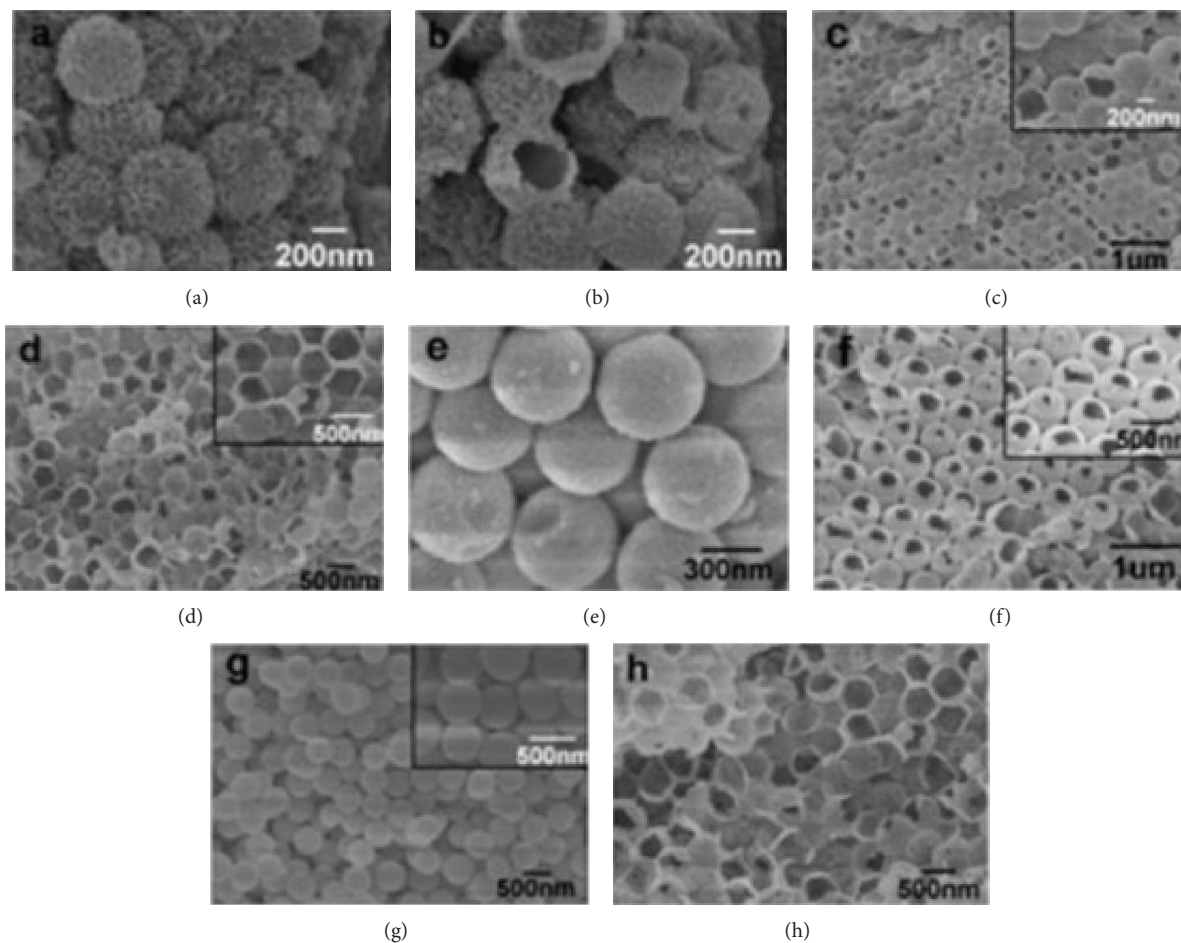


FIGURE 3: SEM image of (a) iron-silica composite nanospheres. (b) Composite hollow spheres (400 ± 5 nm). (c) Iron-gadolinium hollow nanospheres (485 ± 5 nm). (d) After reduction. (e) Cobalt-silica composite nanospheres and (f) removing silica cores (510 ± 5 nm). (g) Precursor nanospheres and (h) removing silica cores after reduction (530 ± 5 nm).

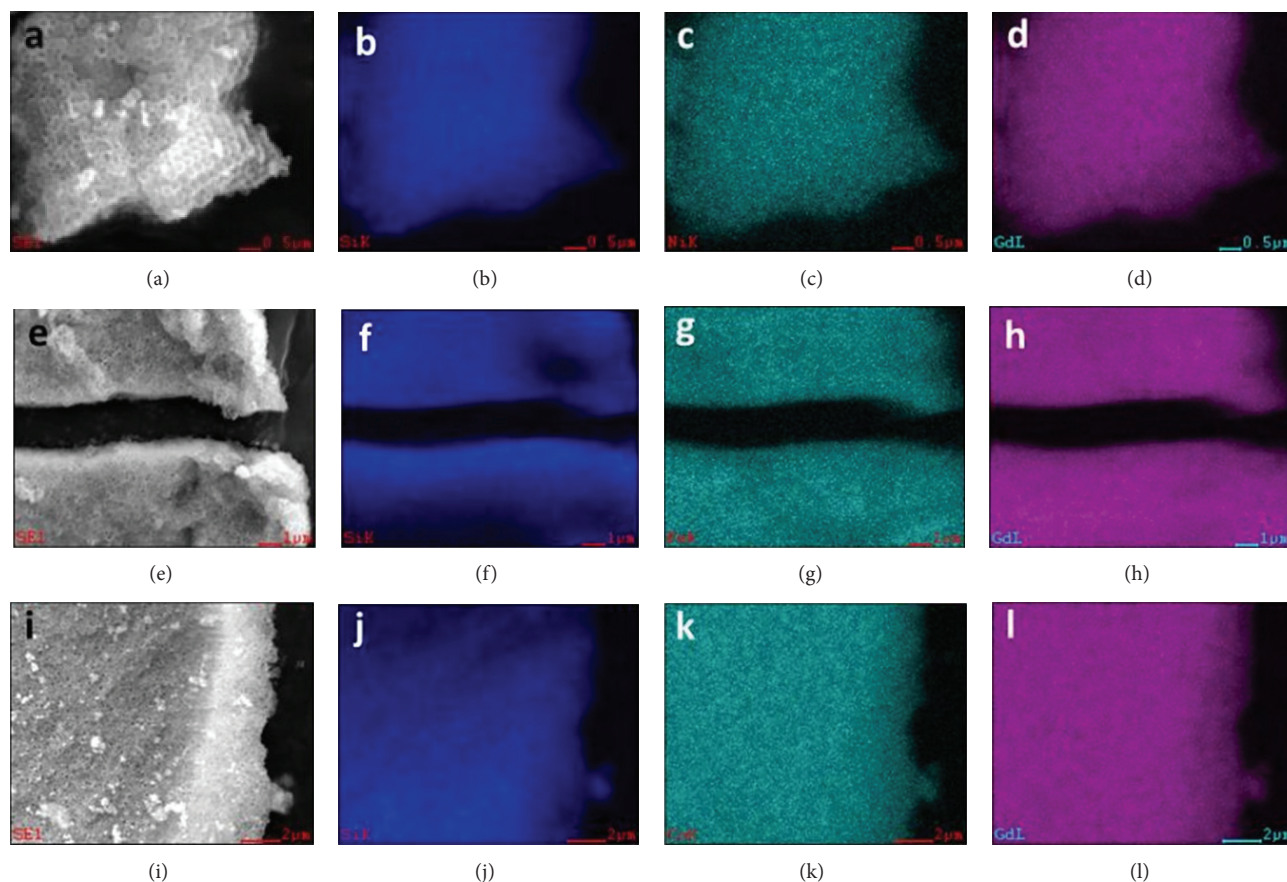


FIGURE 4: EDS surface analysis of nickel-gadolinium, iron-gadolinium, and cobalt-gadolinium composite two-layer hollow spheres: ((a), (e), and (i)) dark field image, ((b), (f), and (j)) silicon map, (c) nickel map, (g) iron map, (k) cobalt map, and ((d), (h), and (l)) gadolinium map.

**2.4. Measurements and Characterization.** The structures of the samples were characterized by X-ray diffractometer (XRD) (Bruker D8 ADVANCE) using Cu-K $\alpha$  radiation (the wave length is 0.15418 nm). The morphology and elements of the sample were measured by scanning electron microscope (FE-SEM SU-70) with energy-dispersive X-ray (EDAX). BET surface area was obtained by analyzing N<sub>2</sub> adsorption/desorption isotherm data and from micromeritics (ASAP 2020M) measurement. The magnetic properties of hollow nanospheres were measured by Quantum Design Vibrating Sample Magnetometer as a function of applied fields ( $-30$  and  $+30$  kOe) at 300 K.

### 3. Results and Discussion

The layer-by-layer (LBL) route was adapted to fabricate the core-shell sphere using SiO<sub>2</sub> as the sacrificed template, followed by deposition of desired coating chemicals or nanoparticles with opposite surface charges [28–30]. The SiO<sub>2</sub> spheres are chosen as the sacrificed template due to their facile removal and their core-shell structure composed of a hydrophobic core and a stabilizing shell that contains vast reactive oxygen functional groups [31]. These SiO<sub>2</sub> spheres were prepared via a hydrolysis method as described above.

The SEM image shows that the SiO<sub>2</sub> spheres have a mean diameter of  $\sim 500$  nm (Figure 2(a)). After being coated with a porous nickel layer, core-shell silica/Ni<sub>3</sub>Si<sub>2</sub>O<sub>5</sub>(OH)<sub>4</sub> composite microspheres with Ni<sub>3</sub>Si<sub>2</sub>O<sub>5</sub>(OH)<sub>4</sub> thin layers of  $\sim 40$  nm were obtained (Figure 2(b)). The subsequent LBL deposition process resulted in a continuous and uniform Gd<sub>2</sub>O<sub>3</sub> coating on the surface of the spheres (Figure 2(c)). Panels (d) and (e) in Figure 2 display typical SEM images of Ni<sub>3</sub>Si<sub>2</sub>O<sub>5</sub>(OH)<sub>4</sub> and Ni<sub>3</sub>Si<sub>2</sub>O<sub>5</sub>(OH)<sub>4</sub>@Gd<sub>2</sub>O<sub>3</sub> hollow microspheres, respectively, illustrating that the particles are well dispersed. From the high-magnification SEM image (inset of Figure 2(e)), one can clearly see the thickness of Ni<sub>3</sub>Si<sub>2</sub>O<sub>5</sub>(OH)<sub>4</sub>@Gd<sub>2</sub>O<sub>3</sub> layer (approximately  $50 \pm 5$  nm). More interestingly, the size of products prepared can be controlled by varying the size of the cores used in the reactions. For example, the resulting Ni<sub>3</sub>Si<sub>2</sub>O<sub>5</sub>(OH)<sub>4</sub>@Gd<sub>2</sub>O<sub>3</sub> hollow microspheres ( $\sim 200$  nm in diameter) are prepared by using SiO<sub>2</sub> (180 nm) as the sacrificed template. Moreover, cobalt-silica and iron-silica hollow spheres were also synthesized via the LBL method by changing the metal precursor (Co, Fe), giving materials a similar spherical morphology and narrow particle size distribution (Co,  $\sim 560$  nm; Fe,  $\sim 580$  nm). Subsequently, depositing Gd<sub>2</sub>O<sub>3</sub> on the surface of the precursors, the sizes of the particles are about 595 nm and 610 nm after reduction. As shown, Fe<sub>3</sub>O<sub>4</sub>@Gd<sub>2</sub>O<sub>3</sub> and Co<sub>5</sub>Gd@Gd<sub>2</sub>O<sub>3</sub> hollow spheres

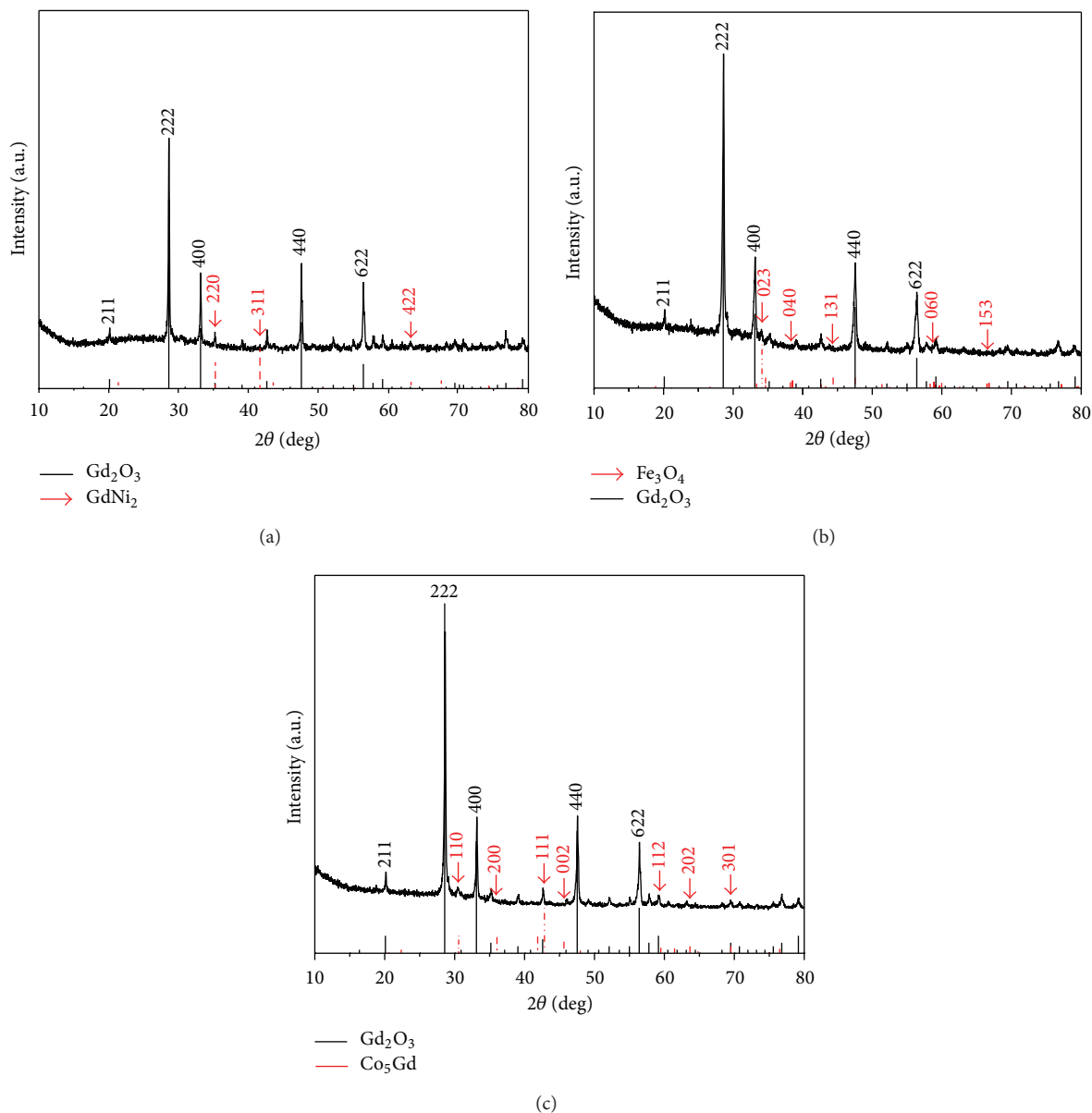


FIGURE 5: The X-ray powder diffraction patterns of  $\text{GdNi}_2@\text{Gd}_2\text{O}_3$ ,  $\text{Fe}_3\text{O}_4@\text{Gd}_2\text{O}_3$ ,  $\text{Co}_5\text{Gd}@\text{Gd}_2\text{O}_3$  hollow spheres after reduction in  $\text{H}_2$  current at  $450^\circ\text{C}$  for 2 h.

have been successfully prepared and the detailed information of sample was displayed in Figure 3.

To confirm the composition of products, EDS mapping was devoted for elaborate analysis of the hollow spheres, as shown in Figure 4. The color intensity serves as a tool to judge the relative amount of element present in this analysis and it allows the visualization of the relative location of the different elements in the sample. The EDS-mapping images ((b), (c), and (d)) labeled Si, Ni, and Gd are those obtained for respective elements in hollow spheres. As we have seen from the maps, elemental Ni, Gd, and Si are distributed throughout the whole hollow microsphere. Meanwhile, elemental Fe, Co, and Gd are homogeneously distributed on the shell-shell structures from the images ((e)–(l)).

These powders were reduced in  $\text{H}_2$  current ( $40\text{ cm}^3/\text{min}$ ) at  $450^\circ\text{C}$  (at a rate of  $10^\circ\text{C}/\text{min}$ ) for 2 h in the fixed-bed reactor. After the completion of the reduction process, the sample was protected at room temperature in the flowing-inert gas for 12 h. These multilayer hollow spheres were also characterized by XRD as shown Figure 5, where the corresponding Bragg peaks are indicated. The diffraction peaks at  $2\theta = 28.6, 33.1, 47.5, \text{ and } 56.4^\circ$  are for (222), (400), (440), and (622) of cubic  $\text{Gd}_2\text{O}_3$  [32], in good accordance with reported data (JCPDS Card number 43-1014). It can also be seen that the diffraction peaks of the  $\text{Gd}_2\text{O}_3$  particles are very strong and sharp, indicating that outer shell layer with high crystallinity can be synthesized by this method. This is important for phosphors because high crystallinity

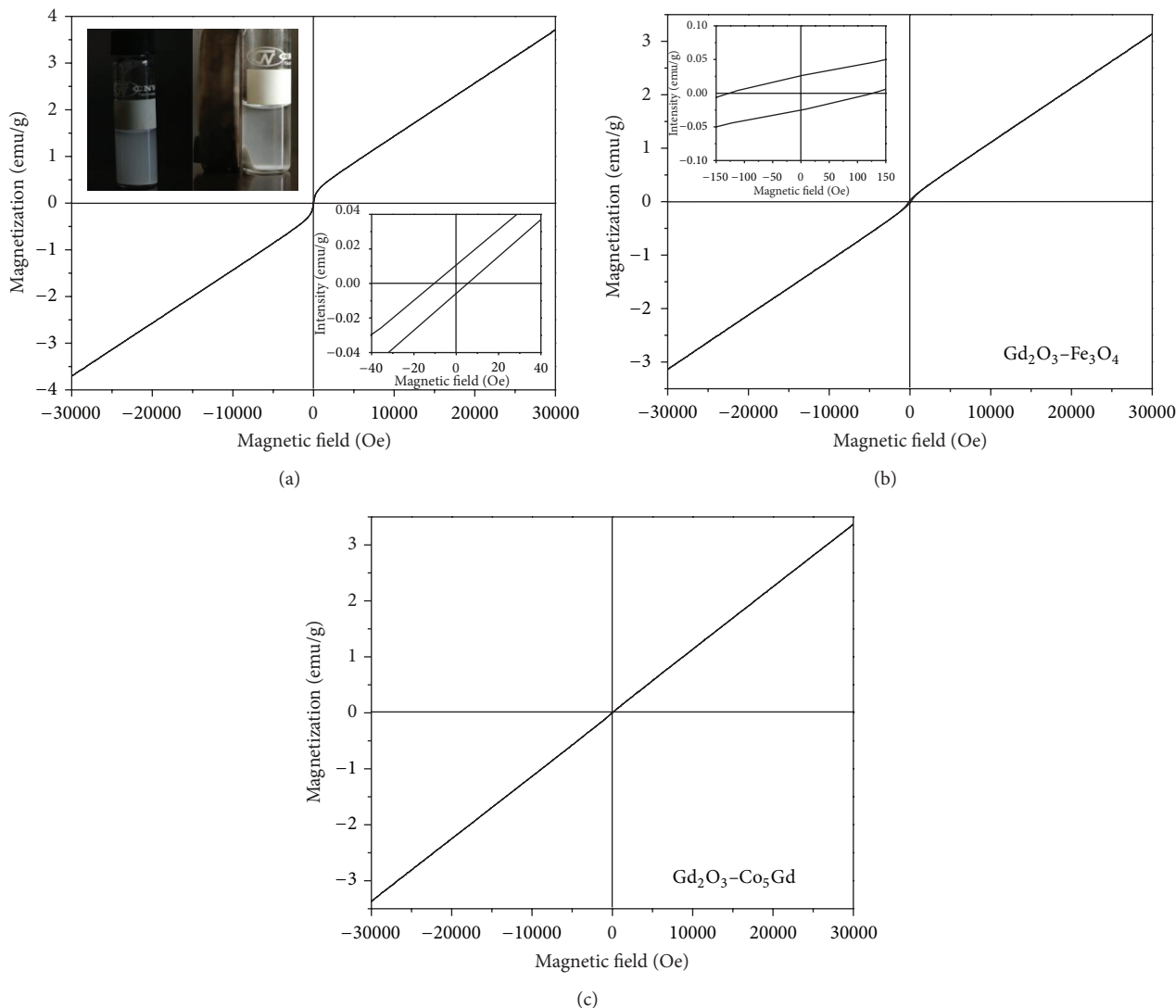


FIGURE 6: Room-temperature (300 K) magnetic hysteresis loops of  $\text{GdNi}_2@Gd_2O_3$ ,  $\text{Fe}_3O_4@Gd_2O_3$ , and  $\text{Co}_5Gd@Gd_2O_3$  hollow spheres, respectively. The upper left inset of (a) shows  $\text{GdNi}_2@Gd_2O_3$  hollow spheres suspended in water and separated from solution under an external magnetic field and the lower right shows close-up of the central region of the magnetization curves. The inset of (b) shows the highlight of low field region.

generally means fewer traps and stronger luminescence [33]. However, a problem has puzzled us that inorganic phase ( $\text{Gd}_2\text{O}_3$ ) is partially soluble in the magnetic shell during the reduction process. Fortunately, the alloy ( $\text{GdNi}_2$ ,  $\text{Co}_5\text{Gd}$ ) has desired magnetic properties. In comparison, a set of very weak diffraction peaks assigned to face-centered cubic  $\text{GdNi}_2$  (JCPDS Card number. 65-9978), hexagonal  $\text{Co}_5\text{Gd}$  (JCPDS Card number 65-9914), and orthorhombic  $\text{Fe}_3\text{O}_4$  (JCPDS Card number 89-6466) was detected at the positions marked by arrows, accompanying the predominant diffraction peaks. No other crystalline impurities were detected by XRD.

The magnetic properties of the heterodimers of  $\text{Gd}_2\text{O}_3$  and  $\text{GdNi}_2$  nanoshells are measured using a vibrating sample magnetometer at room temperature. As shown in Figure 6(a), the sample presented a saturation magnetization ( $M_s$ ) of 3.7 emu/g and a low coercivity of about 10 Oe at room

temperature. The magnified hysteresis loops further confirm the superparamagnetism of these hollow spheres. Compared with the saturation magnetization of the MUC-FNR (1.28 emu/g) [34], it can more easily be directed by an external magnetic field to a specific target. Furthermore, the magnetization values of  $\text{Co}_5\text{Gd}@Gd_2O_3$  and  $\text{Fe}_3O_4@Gd_2O_3$  were 3.38 and 3.15 emu/g (see Figures 6(b) and 6(c)), respectively. For our sample, the main reason may be that the hollow sphere is a compound of  $\text{GdNi}_2@Gd_2O_3$ , not pure nickel. The  $\text{Gd}_2\text{O}_3$  layer also serves as a magnetic layer and exhibits superparamagnetism [35]. Despite this, the powder dried  $\text{Gd}_2\text{O}_3$ -coated  $\text{GdNi}_2$  magnetic shells could be well redispersed in aqueous solutions, and the suspended particles were well collected using a magnet within 0.5 min (Figure 5(a), left inset), which suggests that they can be manipulated by an external small magnetic field. Remarkably,

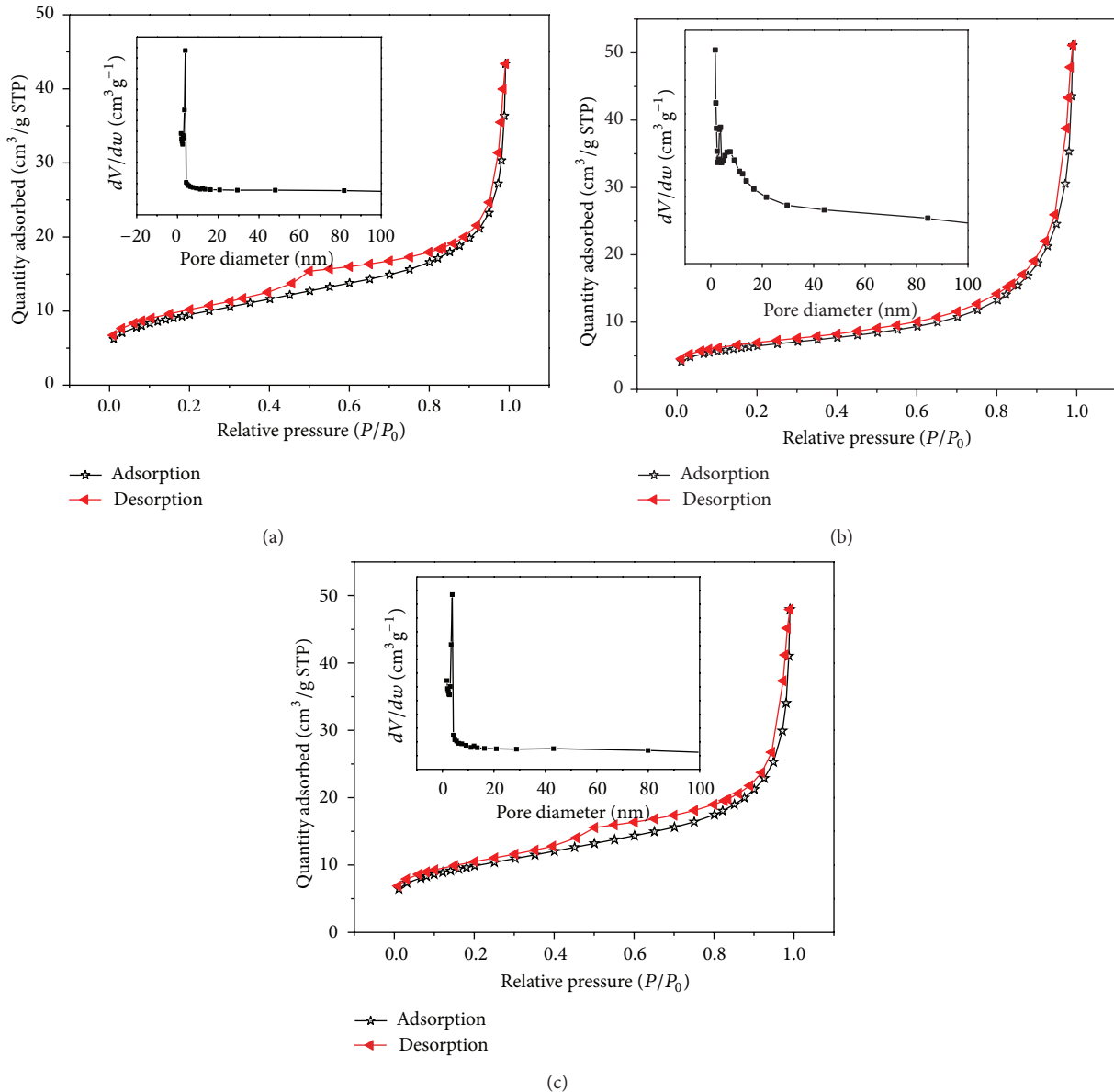


FIGURE 7: The pore diameter distribution and the inset of N<sub>2</sub> adsorption/desorption isotherm of the hollow spheres. (a) GdNi<sub>2</sub>@Gd<sub>2</sub>O<sub>3</sub>; (b) Fe<sub>3</sub>O<sub>4</sub>@Gd<sub>2</sub>O<sub>3</sub>; (c) Co<sub>5</sub>Gd@Gd<sub>2</sub>O<sub>3</sub>.

the separation between the Gd<sup>3+</sup> ions in the matrix is too far to render sufficient overlap of the orbitals associated with the partially filled 4f electrons shells of the Gd<sup>3+</sup> ions, which is necessary for ferromagnetism [36]. And increasing thickness of magnetic nanoshell by the times of coating, the saturation magnetization of products will be much enhanced.

The specific surface area and porosity of the as-prepared M@Gd<sub>2</sub>O<sub>3</sub> (M = GdNi<sub>2</sub>, Co<sub>5</sub>Gd, Fe<sub>3</sub>O<sub>4</sub>) hollow spheres were determined by nitrogen sorption measurements. Figure 7 shows the nitrogen sorption isotherms and the corresponding pore-size distribution of as-prepared GdNi<sub>2</sub>@Gd<sub>2</sub>O<sub>3</sub>, Fe<sub>3</sub>O<sub>4</sub>@Gd<sub>2</sub>O<sub>3</sub>, and Co<sub>5</sub>Gd@Gd<sub>2</sub>O<sub>3</sub> hollow spheres. These samples exhibit a typical IV isotherm with the leap start-points at relative pressures of P/P<sub>0</sub> = 0.2-0.3,

which demonstrates the ordered mesoporous structure. Meanwhile, a large H1-type hysteresis loop appears in its isotherm, which represents narrow pore distributions. The pore size of the product obtained from the analysis of the adsorption branch using the Barrett-Joyner-Halenda (BJH) method was centered at 4.97 nm, as shown in the inset of Figure 7(a). The shell-shell GdNi<sub>2</sub>@Gd<sub>2</sub>O<sub>3</sub> hollow spheres have a specific surface area of 33.84 m<sup>2</sup>·g<sup>-1</sup> and a pore volume of 0.0031 cm<sup>3</sup>·g<sup>-1</sup>, which is close to those of Fe<sub>3</sub>O<sub>4</sub>@Gd<sub>2</sub>O<sub>3</sub> (22.97 m<sup>2</sup>·g<sup>-1</sup>/0.0024 cm<sup>3</sup>·g<sup>-1</sup>), and Co<sub>5</sub>Gd@Gd<sub>2</sub>O<sub>3</sub> (35.00 m<sup>2</sup>·g<sup>-1</sup>/0.0033 cm<sup>3</sup>·g<sup>-1</sup>) (shown in Figures 7(b) and 7(c)). It is clear that the luminescent layer (Gd<sub>2</sub>O<sub>3</sub>) should be responsible for such a low pore volume because the GdNi<sub>2</sub> shell with mesoporous structure

is covered by  $Gd_2O_3$  particles. It is worthwhile to point out that the obtained multifunctional microspheres with mesoporosity still have large BET surface area and small pore volume due to their mesoporous shell-shell structure.

#### 4. Conclusions

In summary, we have demonstrated a feasible route to prepare uniform hollow shell-shell microspheres of composite materials ( $M@Gd_2O_3$ ,  $M = GdNi_2, Co_5Gd, Fe_3O_4$ ) by a template-directed method with silica microspheres as templates. Moreover, the nanoshells thickness can be easily tuned by the times of coating and the diameter of microsphere can also be altered by changing the size of the core. The as-prepared composite materials exhibit excellent adsorption performance for  $N_2$  and superparamagnetism at room temperature and are expected to be useful in water treatment, drug delivery, and many other applications. Thus, the facile synthesis method can readily be extended to the preparation of other magnetic layers  $@RE_2O_3$  functional materials with shell-shell structure.

#### Conflict of Interests

The authors declare that there is no conflict of interests regarding the publication of this paper.

#### Acknowledgments

This work was supported by the National Natural Science Foundation of China (11174165), the Natural Science Foundation of Ningbo (2012A610051), and the K. C. Wong Magna Foundation.

#### References

- [1] Y. F. Zhu, J. L. Shi, W. H. Shen et al., "Stimuli-responsive controlled drug release from a hollow mesoporous silica sphere/polyelectrolyte multilayer core-shell structure," *Angewandte Chemie*, vol. 44, no. 32, pp. 5083–5087, 2005.
- [2] J.-F. Chen, H.-M. Ding, J.-X. Wang, and L. Shao, "Preparation and characterization of porous hollow silica nanoparticles for drug delivery application," *Biomaterials*, vol. 25, no. 4, pp. 723–727, 2004.
- [3] S.-W. Kim, M. Kim, W. Y. Lee, and T. Hyeon, "Fabrication of hollow palladium spheres and their successful application to the recyclable heterogeneous catalyst for suzuki coupling reactions," *Journal of the American Chemical Society*, vol. 124, no. 26, pp. 7642–7643, 2002.
- [4] F. Caruso, "Hollow inorganic capsules via colloid-templated layer-by-layer electrostatic assembly," *Topics in Current Chemistry*, vol. 227, pp. 145–168, 2003.
- [5] Y. N. Xia, B. Gates, Y. D. Yin, and Y. Lu, "Monodispersed colloidal spheres: old materials with new applications," *Advanced Materials*, vol. 12, no. 10, pp. 693–713, 2000.
- [6] X. J. Cheng, M. Chen, L. M. Wu, and G. X. Gu, "Novel and facile method for the preparation of monodispersed titania hollow spheres," *Langmuir*, vol. 22, no. 8, pp. 3858–3863, 2006.
- [7] Z. Liu, D. D. Sun, P. Guo, and J. O. Leckie, "One-step fabrication and high photocatalytic activity of porous  $TiO_2$  hollow aggregates by using a low-temperature hydrothermal method without templates," *Chemistry*, vol. 13, no. 6, pp. 1851–1855, 2007.
- [8] Q. L. Ye, H. Yoshikawa, and K. Awaga, "Magnetic and optical properties of submicron-size hollow spheres," *Materials*, vol. 3, no. 2, pp. 1244–1268, 2010.
- [9] Q.-L. Ye, H. Yoshikawa, S. Bandow, and K. Awaga, "Green magnetite ( $Fe_3O_4$ ): unusual optical Mie scattering and magnetic isotropy of submicron-size hollow spheres," *Applied Physics Letters*, vol. 94, no. 6, Article ID 063114, 2009.
- [10] Q.-L. Ye, Y. Kozuka, H. Yoshikawa, K. Awaga, S. Bandow, and S. Iijima, "Effects of the unique shape of submicron magnetite hollow spheres on magnetic properties and domain states," *Physical Review B*, vol. 75, no. 22, Article ID 224404, 5 pages, 2007.
- [11] M. Yang, J. Ma, C. Zhang, Z. Yang, and Y. Lu, "General synthetic route toward functional hollow spheres with double-shelled structures," *Angewandte Chemie*, vol. 44, no. 41, pp. 6727–6730, 2005.
- [12] H.-R. Kim, K.-I. Choi, K.-M. Kim, I.-D. Kim, G. Cao, and J.-H. Lee, "Ultra-fast responding and recovering  $C_2H_5OH$  sensors using  $SnO_2$  hollow spheres prepared and activated by Ni templates," *Chemical Communications*, vol. 46, no. 28, pp. 5061–5063, 2010.
- [13] H. Xu and W. Wang, "Template synthesis of multishelled  $Cu_2O$  hollow spheres with a single-crystalline shell wall," *Angewandte Chemie*, vol. 46, no. 9, pp. 1489–1492, 2007.
- [14] X.-J. Wu and D. Xu, "Soft template synthesis of yolk/silica shell particles," *Advanced Materials*, vol. 22, no. 13, pp. 1516–1520, 2010.
- [15] Y.-S. Lin, S.-H. Wu, C.-T. Tseng, Y. Hung, C. Chang, and C.-Y. Mou, "Synthesis of hollow silica nanospheres with a microemulsion as the template," *Chemical Communications*, no. 24, pp. 3542–3544, 2009.
- [16] P. Jiang, J. F. Bertone, and V. L. Colvin, "A lost-wax approach to monodisperse colloids and their crystals," *Science*, vol. 291, no. 5503, pp. 453–457, 2001.
- [17] J.-U. Park, H. J. Lee, W. Cho, C. Jo, and M. Oh, "Facile synthetic route for thickness and composition tunable hollow metal oxide spheres from silica-templated coordination polymers," *Advanced Materials*, vol. 23, no. 28, pp. 3161–3164, 2011.
- [18] F. Fujishiro, R. Sekimoto, and T. Hashimoto, "Photoluminescence properties of  $CuLa_{1-x}Ln_xO_2$  ( $Ln$ : lanthanide)—intense and peculiar luminescence from  $Ln^{3+}$  at the site with inversion symmetry," *Journal of Luminescence*, vol. 133, pp. 217–221, 2011.
- [19] W. Li, X. M. Zheng, F. G. Li, and J. Wang, "Facile synthetic route to hollow gadolinium oxide spheres with tunable thickness," *Micro & Nano Letters*, vol. 7, no. 12, pp. 1267–1269, 2012.
- [20] D. Müller-Schulte and H. Brunner, "Novel magnetic microspheres on the basis of poly(vinyl alcohol) as affinity medium for quantitative detection of glycated haemoglobin," *Journal of Chromatography A*, vol. 711, no. 1, pp. 53–60, 1995.
- [21] W. S. Choi, H. Y. Koo, and D.-Y. Kim, "Facile fabrication of core-in-shell particles by the slow removal of the core and its use in the encapsulation of metal nanoparticles," *Langmuir*, vol. 24, no. 9, pp. 4633–4636, 2008.
- [22] Z. F. Wang, H. S. Guo, Y. L. Yu, and N. Y. He, "Synthesis and characterization of a novel magnetic carrier with its composition of  $Fe_3O_4$ /carbon using hydrothermal reaction," *Journal of Magnetism and Magnetic Materials*, vol. 302, no. 2, pp. 397–404, 2006.

- [23] X. L. Kang, Z. Y. Cheng, D. M. Yang et al., "Design and synthesis of multifunctional drug carriers based on luminescent rattle-type mesoporous silica microspheres with a thermosensitive hydrogel as a controlled switch," *Advanced Functional Materials*, vol. 22, no. 7, pp. 1470–1481, 2012.
- [24] W. J. Zhang, G. J. Chen, J. Wang, B. C. Ye, and X. H. Zhong, "Design and synthesis of highly luminescent near-infrared-emitting water-soluble CdTe/CdSe/ZnS Core/Shell/Shell quantum dots," *Inorganic Chemistry*, vol. 48, no. 20, pp. 9723–9731, 2009.
- [25] D. P. Wang and H. C. Zeng, "Multifunctional roles of TiO<sub>2</sub> nanoparticles for architecture of complex core-shells and hollow spheres of SiO<sub>2</sub>-TiO<sub>2</sub>-polyaniline system," *Chemistry of Materials*, vol. 21, no. 20, pp. 4811–4823, 2009.
- [26] P. Jin, Q. W. Chen, L. Q. Hao, R. F. Tian, L. X. Zhang, and L. J. Wang, "Synthesis and catalytic properties of nickel-silica composite hollow nanospheres," *Journal of Physical Chemistry B*, vol. 108, no. 20, pp. 6311–6314, 2004.
- [27] W. Stöber, A. Fink, and E. Bohn, "Controlled growth of monodisperse silica spheres in the micron size range," *Journal of Colloid and Interface Science*, vol. 26, no. 1, pp. 62–69, 1968.
- [28] L. Manna, E. C. Scher, L.-S. Li, and A. P. Alivisatos, "Epitaxial growth and photochemical annealing of graded CdS/ZnS shells on colloidal CdSe nanorods," *Journal of the American Chemical Society*, vol. 124, no. 24, pp. 7136–7145, 2002.
- [29] D. V. Talapin, J. H. Nelson, E. V. Shevchenko, S. Aloni, B. Sadtler, and A. P. Alivisatos, "Seeded growth of highly luminescent CdSe/CdS nanoheterostructures with rod and tetrapod morphologies," *Nano Letters*, vol. 7, no. 10, pp. 2951–2959, 2007.
- [30] J. Schrier, D. O. Demchenko, L.-W. Wang, and A. P. Alivisatos, "Optical properties of ZnO/ZnS and ZnO/ZnTe heterostructures for photovoltaic applications," *Nano Letters*, vol. 7, no. 8, pp. 2377–2382, 2007.
- [31] B. Hu, K. Wang, L. H. Wu, S. H. Yu, M. Antonietti, and M. M. Titirici, "Engineering carbon materials from the hydrothermal carbonization process of biomass," *Advanced Materials*, vol. 22, no. 7, pp. 813–828, 2010.
- [32] J. Choi, T.-K. Tseng, M. Davidson, and P. H. Holloway, "Enhanced photoluminescence from Gd<sub>2</sub>O<sub>3</sub>:Eu<sup>3+</sup> nanocores with a Y<sub>2</sub>O<sub>3</sub> thin shell," *Journal of Materials Chemistry*, vol. 21, no. 9, pp. 3113–3118, 2011.
- [33] G. Jia, H. P. You, K. Liu, Y. H. Zheng, N. Guo, and H. J. Zhang, "Highly uniform Gd<sub>2</sub>O<sub>3</sub> hollow microspheres: template-directed synthesis and luminescence properties," *Langmuir*, vol. 26, no. 7, pp. 5122–5128, 2010.
- [34] F. Zhang, G. B. Braun, A. Pallaoro et al., "Mesoporous multi-functional upconversion luminescent and magnetic "nanorattle" materials for targeted chemotherapy," *Nano Letters*, vol. 12, no. 1, pp. 61–67, 2012.
- [35] C. C. Huang, T. Y. Liu, C. H. Su, Y. W. Lo, J. H. Chen, and C. S. Yeh, "Superparamagnetic hollow and paramagnetic porous Gd<sub>2</sub>O<sub>3</sub> particles," *Chemistry of Materials*, vol. 20, no. 12, pp. 3840–3848, 2008.
- [36] C. F. Xu, M. Ma, L. W. Yang, S. J. Zeng, and Q. B. Yang, "Upconversion luminescence and magnetic properties of ligand-free monodisperse lanthanide doped BaGdF<sub>5</sub> nanocrystals," *Journal of Luminescence*, vol. 131, no. 12, pp. 2544–2549, 2011.

## Research Article

# Indium-Nitrogen Codoped Zinc Oxide Thin Film Deposited by Ultrasonic Spray Pyrolysis on n-(111) Si Substrate: The Effect of Film Thickness

Cheng-Chang Yu,<sup>1</sup> Wen-How Lan,<sup>2</sup> and Kai-Feng Huang<sup>1</sup>

<sup>1</sup> Department of Electrophysics, National Chiao Tung University, Hsinchu 300, Taiwan

<sup>2</sup> Department of Electrical Engineering, National University of Kaohsiung, Kaohsiung 811, Taiwan

Correspondence should be addressed to Wen-How Lan; [wwhlan@gmail.com](mailto:wwhlan@gmail.com)

Received 2 October 2013; Revised 27 November 2013; Accepted 12 December 2013; Published 13 February 2014

Academic Editor: Ajay Soni

Copyright © 2014 Cheng-Chang Yu et al. This is an open access article distributed under the Creative Commons Attribution License, which permits unrestricted use, distribution, and reproduction in any medium, provided the original work is properly cited.

Indium-nitrogen codoped zinc oxide (INZO) thin films were fabricated by spray pyrolysis deposition technique on n-(111) Si substrate with different film thicknesses at 450°C using a precursor containing zinc acetate, ammonium acetate, and indium nitrate with 1 : 3 : 0.05 at.% concentration. The morphology and structure studies were carried out by scanning electron microscopy (SEM) and X-ray diffraction (XRD). The grain size of the films increased when increasing the film thickness. From XRD spectra, polycrystalline ZnO structure can be observed and the preferred orientation behavior varied from (002) to (101) as the film thickness increased. The concentration and mobility were investigated by Hall effect measurement. The p-type films with a hole mobility around  $3 \text{ cm}^2 \text{ V}^{-1} \text{ s}^{-1}$  and hole concentration around  $3 \times 10^{19} \text{ cm}^{-3}$  can be achieved with film thickness less than 385 nm. The n-type conduction with concentration  $1 \times 10^{20} \text{ cm}^{-3}$  is observed for film with thickness 1089 nm. The defect states were characterized by photoluminescence. With temperature-dependent conductivity analysis, acceptor state with activation energy 0.139 eV dominate the p type conduction for thin INZO film. And the Zn-related shallow donors with activation energy 0.029 eV dominate the n-type conduction for the thick INZO film.

## 1. Introduction

In recent years, the zinc oxide (ZnO) based materials have attracted much attention. Lots of devices have been studied in many fields [1–6]. For unintentionally doped ZnO, it is usually an n-type semiconductor with carriers from the donor levels associated with oxygen vacancies and/or interstitial zinc atoms [7, 8]. High quality n-type ZnO with Al, Ga, and In has been reported [9–11]. To achieve p-type ZnO, a popular method is using nitrogen doping as shallow acceptor [12] although the stability of nitrogen in ZnO is a topic [13]. In the meantime, the nitrogen codoping with certain reactive elements such as Al, Ga, and In was proposed to enhance the solubility and stability of nitrogen in ZnO [14–16]. As the nitrogen chemical states varied with the added In element [16], stable and high p-type concentration can be achieved from the In-N codoped ZnO film. Different deposition methods such as sputtering [17, 18], sol-gel spin coating [19], and

ultrasonic spray pyrolysis (USP) [16, 20] were applied. Some studies of the In-N codoped ZnO about the electrical and optical properties [16, 18, 19], different substrate effect [21], and film postannealing effect [17] were performed. In these studies, all the thickness of the In-N co-doped ZnO was less than 0.5  $\mu\text{m}$ , as ZnO film properties show a film thickness-dependent behavior [22–24]. Yet, there is less studies about the thicknesses effects for the In-N codoped ZnO film. In this work, we prepared the In-N codoped ZnO thin films by spray pyrolysis with different film thickness and analyzed their morphology, crystalline, and electrical properties. The photoluminescence and activation energies analysis were applied for understanding the conductivity behaviors.

## 2. Materials and Methods

The indium and nitrogen co-doped ZnO (INZO) thin film was deposited on  $n^+$  (111) Si substrate at 475°C by spray

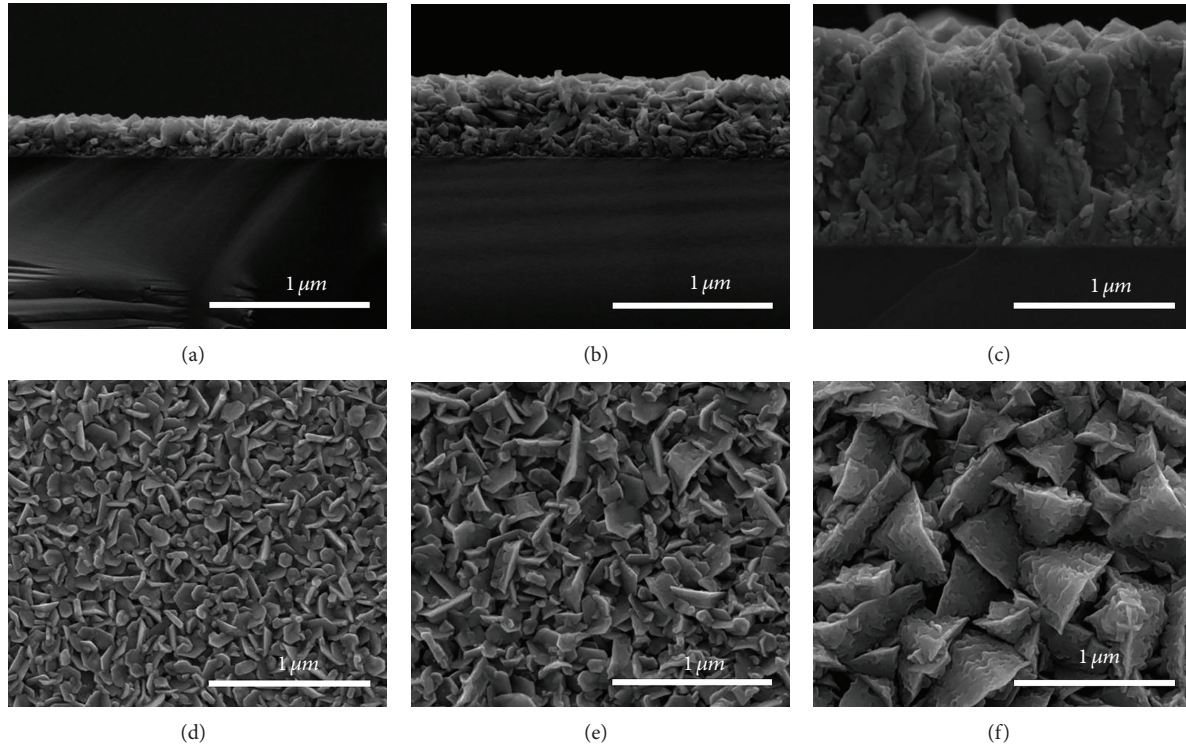


FIGURE 1: SEM view of cross-section for the ZnO films with different deposited thicknesses: (a) 154 nm, S1, (b) 385 nm, S2, and (c) 1089 nm, S3. The corresponding surface morphologies were shown in (d) S1, (e) S2, and (f) S3, respectively.

pyrolysis [8]. Before deposition, the Si substrate was cleaned by standard cleaning process [25] followed by rinse in  $\text{HF}:\text{H}_2\text{O} = 1:20$  for 20 s to remove the oxide layer. The INZO film was formed from the pyrolysis of the precursor of zinc acetate, ammonium acetate, and indium (III) chloride with ratio 1:3:0.05 with different spraying times. The surface morphology and cross-section of the film were studied using scanning electron microscopy (SEM, HITACHI S-4300). The crystalline structure was obtained by X-ray diffraction (XRD, Bruker D8) with Cu K-alpha radiation. The conductivity was obtained by the van der Pauw four-point method (KEITHLEY 2400) and carrier concentration and mobility were obtained by Hall measurement at the magnetic field strength 0.42 T. The temperature-dependent conductivity properties were characterized with a temperature-controlled stage. The photoluminescence (PL) measurement was carried on MiniPL5.0 system (PHOTON SYSTEMS Inc.) with NeCu (248 nm) pulse laser. The depth profile was obtained by secondary ion mass spectrometry (SIMS, Cameca IMS-6f) from MA-tek Inc.

### 3. Results and Discussion

The morphologies of these INZO films were shown in Figure 1. The cross-section was shown in (a) sample S1, (b) sample S2, and (c) sample S3. The film thicknesses measured from the cross-sectional images are 154 nm (S1), 385 nm (S2), and 1089 nm (S3), respectively, as listed in Table 1. The corresponding surface morphologies were shown in (d) S1

(e) S2, and (f) S3, respectively. It is clearly shown that the surface morphologies of the INZO films were considerably affected by film thickness. For thin INZO film as shown in Figure 1(d), the granular structure with some hexagonal plate can be observed. As the film thickness increases by increasing the deposition time, the surface granular structure becomes larger and the cubic-like morphology can be observed in Figure 1(f).

The X-ray diffraction patterns of the INZO films are shown in Figure 2. There are five peaks distinguished in the figure. All these peaks, as labelled in the figure, can be indexed to ZnO structure.

The three obvious ZnO peaks were indexed as (100), (002), and (101) planes. For thin INZO film (S1), a dominant (002) peak can be observed in Figure 2(a). The (002) peak intensity decreased with increasing film thickness. The film with thickness 1089 nm (S3) showed a primary (101) peak. A relative intensity increasing for (110) peak can be observed also as the film thickness increased. The full-width-half-maximum (FWHM) values of (101) peak were evaluated in Figure 3. The FWHM decreasing with film thickness increasing can be observed. Based on Scherrer's formula, the averaged grain size  $D$  for the film can be calculated as [26]

$$D = \frac{0.94\lambda}{\beta \cos \theta}, \quad (1)$$

where  $\theta$  is the Bragg diffraction angle,  $\lambda$  is the wavelength of the incident radiation, and  $\beta$  is FWHM of the diffraction ray. The grain size estimated from the (101) peak in the XRD

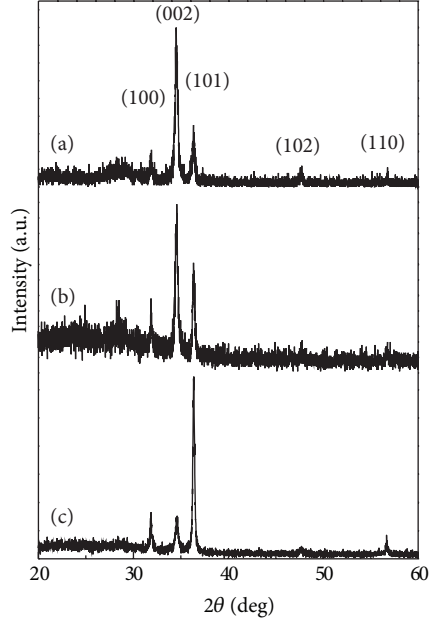


FIGURE 2: XRD spectra for the ZnO films with different deposited thicknesses: (a) S1, (b) S2, and (c) S3.

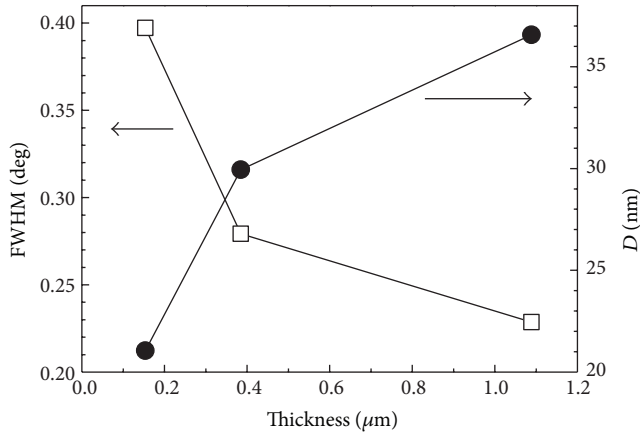


FIGURE 3: The FWHM of the XRD (101) plane and the grain size  $D$ .

pattern was shown in Figure 3 also. The grain size increases as the film thickness increases. For thick sample S3, the calculated grain size 36.6 nm is quite small than the observed cubic size estimated from Figure 1(f). As sectional aligned small grain size formed on the substrate/film interface as shown in Figure 1(c). The calculated grain size shows the average effect on the film.

The texture coefficient  $TC_{(hkl)}$ , which represents the texture of the particular (hkl) plane of a film, was well known as [27]

$$TC_{(hkl)} = \frac{Im_{(hkl)}}{Io_{(hkl)}} \div \frac{1}{N} \sum_1^N \frac{Im_{(hkl)}}{Io_{(hkl)}}, \quad (2)$$

where  $Im_{(hkl)}$  and  $Io_{(hkl)}$  are the measured and referenced peak intensities in JCPDS of the diffraction peak from the

TABLE 1: Texture coefficient  $TC_{(002)}$  and  $TC_{(101)}$  for samples S1 to S3.

Sample	Thickness (nm)	$TC_{(002)}$	$TC_{(101)}$
S1	154	2.44	0.30
S2	385	2.07	0.52
S3	1089	0.66	1.74

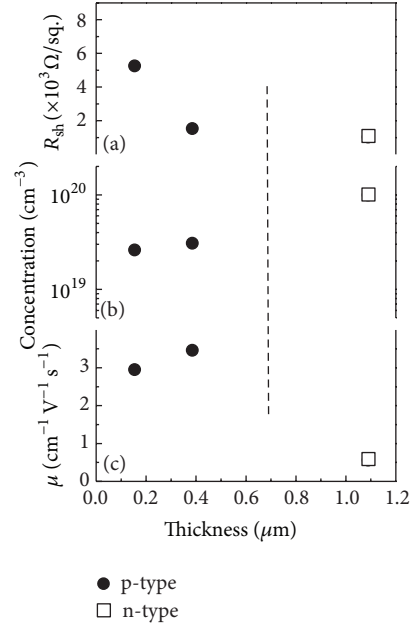


FIGURE 4: The conduction properties of ZnO thin films with different deposited thicknesses: (a) the sheet resistance  $R_{sh}$ , (b) carrier concentration, and (c) Hall mobility  $\mu$ .

(hkl) plane. The number  $N$  is the total number of reflection peaks. The calculated (002) and (101) texture coefficient values  $TC_{(002)}$  and  $TC_{(101)}$  were shown in Table 1. For thin INZO sample S1, the  $TC_{(002)}$  has the highest value. The main structure is (002) plane. The dominant (002) plane phenomenon can be observed in several thin ZnO films [24, 27]. The preferential orientation of c-axis for thin INZO leads to the enhancement of high  $TC_{(002)}$  values. As the film thickness increases, the  $TC_{(002)}$  value decreases and  $TC_{(101)}$  value increases. The preferred texture changed from (002) to (101) with the film thickness increasing. The texture change, which may probably be due to the growth mode variance [24], results in the corresponding surface morphology difference as shown in Figures 1(d)–1(f).

The sheet resistance ( $R_{sh}$ ), concentration, and mobility ( $\mu$ ) for the INZO films with different thickness are shown in Figures 4(a), 4(b), and 4(c), respectively. To verify the stability of the films, these properties were tested again after one month later and the quantity variation less than 12% was observed. The sheet resistance decreases as the film thickness increases. From Hall measurement, p-type conduction was characterized for sample S1 and S2 while the n-type conduction was characterized for sample S3. The p-type concentration around  $2 \times 10^{19} \text{ cm}^{-3}$ , which is near the reported In-N codoped ZnO film values [16, 19, 20], reveals the efficient

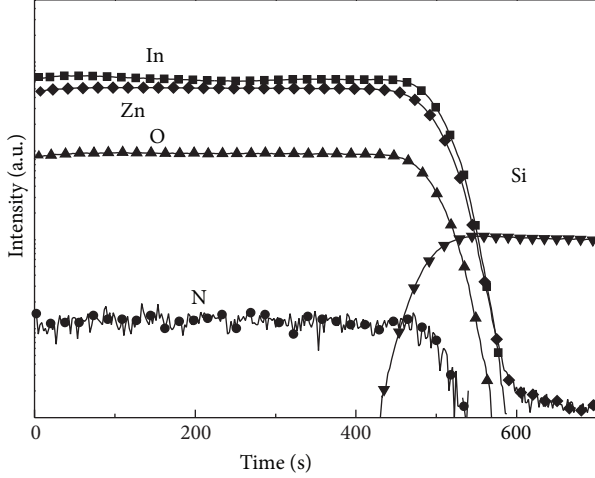


FIGURE 5: SIMS depth profile of sample S3.

nitrogen incorporation in ZnO film [21]. For the thickest sample S3, the n-type conduction around  $1 \times 10^{20} \text{ cm}^{-3}$  can be observed. Compared with sample S2, an enormous change for sample S3 in carrier density from p-type to n-type would require a large carrier compensation mechanism.

In order to clarify the element composition in this INZO film, SIMS depth profile was carried out on sample S3 as shown in Figure 5. The content of In and N as well as Zn and O remains constant throughout the whole film was observed. No obvious In and N composition variation in the film. As the film morphology and preferential orientation change as the film thickness increases, different chemical states may occur with different thickness and dominate the film conduction.

Figure 6 shows the room temperature PL spectra of the three samples. For sample S1, as shown in Figure 6(a), a near band edge emission with peak wavelength 376 nm can be observed [28–30]. This broadened emission may split to two peaks after Gaussian fitting process [29]. Dominant peak with wavelength 376 nm (3.30 eV) is attributed to near band edge emission of bound neutral donors ( $D^{\circ}X$ ). Another emission peak with fitted peak wavelength around 388 nm (3.20 eV) can be observed in the figure. This peak, which is near the reported peak at 384 nm, may be attributed to the complex defects and arises from the energy transition between donor-acceptor pairs (DAP) [29–31]. A small peak around 425 nm (2.92 eV) can be observed in the figure. Lots of emissions originating from interstitial zinc-related defects were found in this range (415–470 nm) in the p-type Al-N codoped ZnO film [22]. The emission at 425 nm may be attributed to the transition related interstitial zinc-related defect ( $Zn_i$ ).

A visible emission with peak wavelength 500 nm (2.48 eV) can be observed. This peak is attributed to the singly ionized oxygen vacancies [ $V_{O}^{+}$ ] [29, 31, 32] or zinc interstitial [33] and can be observed in the p-type N doped ZnO [33].

For sample S2, similar emission peaks can be observed. The increasing of emission intensity ratio of  $D^{\circ}X$ /DAP can be observed. Besides, broadened emission with peak wavelength around 520 nm (2.38 eV) can be observed. The emission with

TABLE 2: The activation energies  $E_A$  for different samples.

Sample	Activation energy $E_A$ (eV)
S1	0.144 ( $T = 300 \text{ K} - 350 \text{ K}$ )
S2	0.139 ( $T = 300 \text{ K} - 390 \text{ K}$ )
S3	0.029 ( $T = 300 \text{ K} - 390 \text{ K}$ )

peak wavelength 498 nm as seen in sample S1 may be included in this broadened emission band. This green emission which can be observed in many ZnO film [28, 29] is attributed to the transition of conduction band to the oxygen antisite state [ $O_{Zn}$ ] [28], radiative optical transition in interstitial oxygen [ $O_i$ ] [29], or the zinc vacancy [ $V_{Zn}$ ]-related defect transition [28, 32].

For sample S3, with film thickness increasing, the emission intensity ratio of  $D^{\circ}X$ /DAP increases more and the fitted bandwidth for DAP decreases. An emission with peak wavelength 415 nm (2.99 eV) can be observed. This emission, which still lies in the spectral range as mentioned (415–470 nm), was attributed to certain  $Zn_i$  defects [22]. Compare with sample S2, the appearance of the peak reveals that some certain  $Zn_i$  defects were enhanced for thick INZO films. As the ionization energy for this n-type defect  $Zn_i$  is only 50 meV [34], high electron concentration may come from such defect state at room temperature.

For further understanding the carrier conduction mechanism, temperature-dependent conductivity measurement was carried out for all samples. For the semiconductor film with grain structure, the film conductivity may be affected by the grain size and electronic mean free path [35, 36]. To estimate the effect of grain boundary scattering, the mean free path  $l$  for carriers in the film can be calculated as [35]

$$l = \left( \frac{h}{2e} \right) \left( \frac{3n}{\pi} \right)^{1/3} \mu, \quad (3)$$

where  $n$  and  $\mu$  are the carrier concentration and mobility, respectively. The calculated values at room temperature are 17 nm (S1), 22 nm (S2), and 5 nm (S3), respectively. These results all are less than the crystalline grain size  $D$ , suggesting that the contribution from the grain boundary scattering mechanism at room temperature can be neglected.

Figure 7 shows the conductivity measured with different temperatures for samples S1 to S3. For semiconductor with electrical conductivity dominated by the activation of doping level, the relationship between electrical conductivity  $\sigma$  and the measurement temperature  $T$  is given by [26]

$$\sigma = \sigma_0 \exp\left(-\frac{E_A}{kT}\right), \quad (4)$$

where  $\sigma_0$  is the preexponential factor,  $k$  is the Boltzmann constant, and  $E_A$  is the activation energy. The calculated  $E_A$  values were listed in Table 2.

For S1, two different regions in different temperature ranges can be observed. This suggests the presence of two different sorts of conduction mechanism in sample S1. Activation energy values for region I (300 K to 350 K) and II (360 to 390 K) were calculate, respectively, from the linear portions.

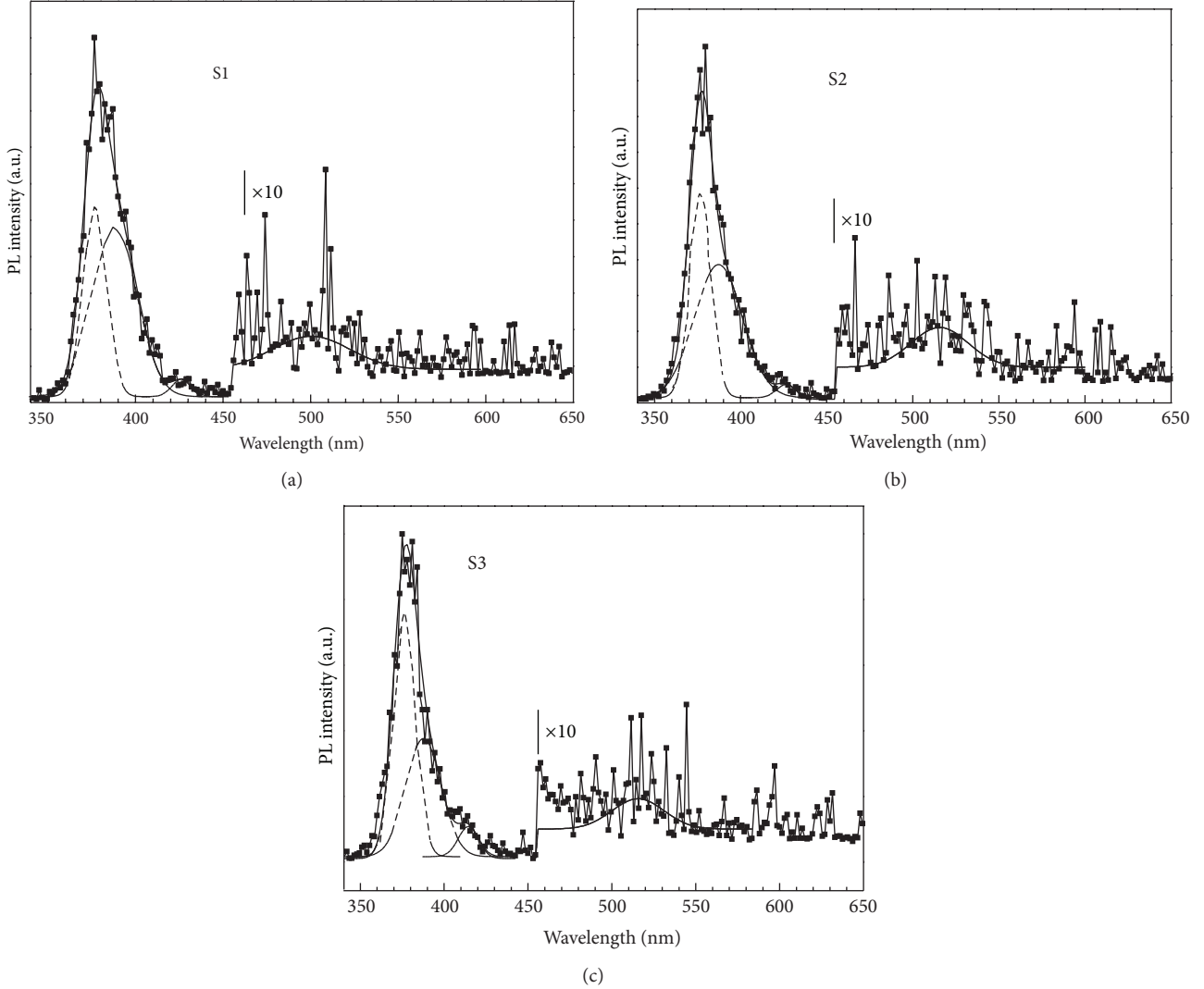


FIGURE 6: Room temperature PL spectra for samples (a) S1, (b) S2, and (c) S3. The Gaussian fitting curves at different spectra ranges were shown.

The obtained  $E_A$  values are 0.144 eV and 0.491 eV, respectively. For region I, this activation energy value is quite near the reported 0.135–0.14 eV for the N-doped ZnO [37, 38] and thus was assigned as the defect complex of O-site N-Zn vacancy ( $N_O-V_{Zn}$ ) [39]. The shallow acceptor coming from this complex takes p-type concentration contribution in region I.

In region II, the obtained active energy value is relatively small compared with the band gap energy of ZnO. Besides, the activation energy calculated from two adjacent points for S1 in region II increases with temperature. This behavior and energy value, which have been observed for other ZnO based films [26], were corresponding to the grain boundary related scattering. With temperature increasing, the conductivity increases as the increasing of carrier concentration. For S1, the conductivity enhancement of 2.4 times can be observed as the temperature increases from room temperature to 87°C ( $1000/T = 2.78 \text{ K}^{-1}$ ). If the concentration increases 2.4 times also with a little mobility drop, the mean free path at 87°C is

then estimated to be 26 nm. In this case, the mean free path of carriers in sample S1 in region II is larger than the grain size  $D$ ; the grain boundary related scattering cannot be neglected. In this case, the conductivity  $\sigma$  controlled by grain boundary can be described as [40, 41]

$$\sigma = \frac{q^2 ND}{\sqrt{2\pi m^* kT}} \exp\left(-\frac{E_B}{kT}\right), \quad (5)$$

where  $N$  is the carrier concentration,  $D$  is the grain size,  $m^*$  is the effective mass, and  $E_B$  is the mean barrier height across the grain boundary. The inset in Figure 7 shows the plot of  $\ln(\sigma T^{1/2})$  versus  $1000/T$  for S1 in region II. The barrier height  $E_B$  of the film was found to be 0.51 eV. The conductivity for S1 in temperature range II (360 K–390 K) is controlled by the grain boundaries. The disordered grain boundaries with trapping state will capture carriers. The conductivity thus is controlled by the transition ability for carriers passing

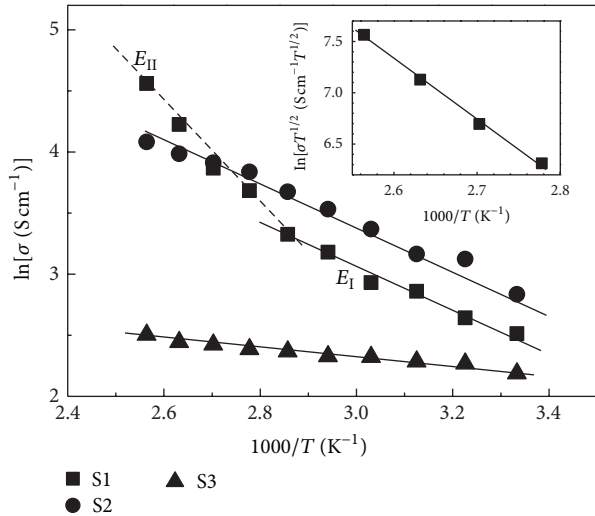


FIGURE 7: Conductivity measured at different temperatures for the ZnO films with different deposited thicknesses.

through the barrier and the conduction mechanism is grain boundary scattering.

For sample S2, a linear relation can be observed in Figure 7. The extracted activation energy by (4) is 0.139 eV. This value, which is near the previous 0.144 eV, reveals the same conduction mechanism for S2 and S1 in region I, which is dominant by the acceptor complex of  $N_O-V_{Zn}$ .

For the thickest sample S3, a linear relation can be observed in Figure 7 also. The extracted activation energy by (3) is 0.029 eV. There is no nitrogen-related state associated with such low activation energy [37–39]. This activation value may correspond to the origin donor level for the indium doped ZnO (0.026 eV) [26] or the interstitial  $Zn_i$ -related complex (0.031 eV) [40]. This shallow donor level, which caused the measured n-type conduction also, dominates the conduction mechanism for the thickest sample S3.

For thick INZO film, the grain size becomes bigger. The effect of hole accumulation in Si substrate interface [42] reduces with the increasing of film thickness. Besides, effect of grain boundary becomes less and the preferential orientation changes also with the increasing of film thickness. The p-type conduction enhanced by grain boundary related states becomes less [42, 43]. Both reduce the acceptor concentration and the shallow donor state corresponding to the interstitial  $Zn_i$ -related complex which has dominant effect on the conduction mechanism for this thick INZO film.

#### 4. Conclusion

In conclusion, INZO thin films were prepared by spray pyrolysis, and the effects of film thickness on structure and surface morphology were studied. The thin INZO films showed preferential orientation along the (002) plane with tiny flake morphology. For INZO film with thickness 1089 nm, the preferential orientation was shifted to (101) plane with cubic-like morphology. The conduction type shows p-type for thin film and changes to n-type for the thick film after

the Hall measurement. From the activation analysis coming from the temperature-dependent conductivity measurement, the nitrogen-related acceptor state and the grain boundary scattering dominate the p-type conduction for thin film. The change from p-type to n-type conduction for thick INZO film was characterized by the photoluminescence and activation energy analysis as the appearance of Zn-related shallow donors.

#### Conflict of Interests

The authors declare that there is no conflict of interests regarding the publication of this paper.

#### References

- [1] J. Hüpkes, B. Rech, O. Kluth et al., "Surface textured MF-sputtered ZnO films for microcrystalline silicon-based thin-film solar cells," *Solar Energy Materials & Solar Cells*, vol. 90, no. 18–19, pp. 3054–3060, 2006.
- [2] W.-C. Shih and R.-C. Huang, "Fabrication of high frequency ZnO thin film SAW devices on silicon substrate with a diamond-like carbon buffer layer using RF magnetron sputtering," *Vacuum*, vol. 83, no. 3, pp. 675–678, 2008.
- [3] S. K. Jha, O. Kutsay, I. Bello, and S. T. Lee, "ZnO nanorod based low turn-on voltage LEDs with wide electroluminescence spectra," *Journal of Luminescence*, vol. 133, pp. 222–225, 2013.
- [4] H. S. Al-Salman and M. J. Abdullah, "Effect of Co-doping on the structure and optical properties of ZnO nanostructure prepared by RF-magnetron sputtering," *Superlattices and Microstructures*, vol. 60, pp. 349–357, 2013.
- [5] L. Luo, L. Gong, Y. F. Liu et al., "Enhanced ultraviolet lasing from europium-doped zinc oxide nanocrystals," *Optical Materials*, vol. 32, no. 9, pp. 1066–1070, 2010.
- [6] G. Z. Xing, D. D. Wang, B. Yao, A. Q. L. F. Nien, and Y. S. Yan, "Structural characteristics, low threshold ultraviolet lasing and ultrafast carrier dynamics in high crystalline ZnO nanowire arrays," *Chemical Physics Letters*, vol. 515, pp. 132–136, 2011.
- [7] J. C. Simpson and J. F. Cordaro, "Characterization of deep levels in zinc oxide," *Journal of Applied Physics*, vol. 63, no. 5, pp. 1781–1783, 1988.
- [8] C. C. Yu, Y. T. Hsu, S. Y. Lee et al., "Effects of doping ratio and thermal annealing on structural and electrical properties of boron-doped ZnO thin films by spray pyrolysis," *Japanese Journal of Applied Physics*, vol. 52, Article ID 065502, 5 pages, 2013.
- [9] P. Nunes, E. Fortunato, P. Tonello, F. Braz Fernandes, P. Vilarinho, and R. Martins, "Effect of different dopant elements on the properties of ZnO thin films," *Vacuum*, vol. 64, no. 3–4, pp. 281–285, 2002.
- [10] Y. Morinaga, K. Sakuragi, N. Fujimura, and T. Ito, "Effect of Ce doping on the growth of ZnO thin films," *Journal of Crystal Growth*, vol. 174, no. 1–4, pp. 691–695, 1997.
- [11] A. Tiburcio-Silver, J. C. Joubert, and M. Labeau, "Études sur la croissance, la structure et la composition de couches minces de ZnO et ZnO dopé à l'indium, obtenues par procédé pyrosol," *Thin Solid Films*, vol. 197, no. 1–2, pp. 195–214, 1991.
- [12] A. Kobayashi, O. G. Sankey, and J. D. Dow, "Deep energy levels of defects in the wurtzite semiconductors AlN, CdS, CdSe, ZnS, and ZnO," *Physical Review B*, vol. 28, pp. 946–951, 1983.

- [13] X. Chen, Z. Zhang, B. Yao et al., "Effect of compressive stress on stability of N-doped p-type ZnO," *Applied Physics Letters*, vol. 99, no. 9, Article ID 091908, 3 pages, 2011.
- [14] T. Yamamoto and H. Katayama-Yoshida, "Physics and control of valence states in ZnO by codoping method," *Physica B*, vol. 302-303, pp. 155-162, 2001.
- [15] M. Joseph, H. Tabata, H. Saeki, K. Ueda, and T. Kawai, "Fabrication of the low-resistive p-type ZnO by codoping method," *Physica B*, vol. 302-303, pp. 140-148, 2001.
- [16] J. M. Bian, X. M. Li, X. D. Gao, W. D. Yu, and L. D. Chen, "Deposition and electrical properties of N-In codoped p-type ZnO films by ultrasonic spray pyrolysis," *Applied Physics Letters*, vol. 84, no. 4, pp. 541-543, 2004.
- [17] N. Yuan, L. Fan, J. Li, and X. Wang, "Post-annealing influence on properties of N-In codoped ZnO thin films prepared by ion beam enhanced deposition method," *Applied Surface Science*, vol. 253, no. 11, pp. 4990-4993, 2007.
- [18] N. Yuan, J. Li, L. Fan, X. Wang, and Y. Zhou, "Structure, electrical and optical properties of N-In codoped ZnO thin films prepared by ion-beam enhanced deposition method," *Journal of Crystal Growth*, vol. 290, no. 1, pp. 156-160, 2006.
- [19] Y. Cao, L. Miao, S. Tanemura, M. Tanemura, Y. Kuno, and Y. Hayashi, "Low resistivity p-ZnO films fabricated by sol-gel spin coating," *Applied Physics Letters*, vol. 88, no. 25, Article ID 251116, 3 pages, 2006.
- [20] J. Bian, X. Li, L. Chen, and Q. Yao, "Properties of undoped n-type ZnO film and N-In codoped p-type ZnO film deposited by ultrasonic spray pyrolysis," *Chemical Physics Letters*, vol. 393, no. 1-3, pp. 256-259, 2004.
- [21] L. L. Chen, J. G. Lu, Z. Z. Ye et al., "p-type behavior in In-N codoped ZnO thin films," *Applied Physics Letters*, vol. 87, Article ID 252106, 3 pages, 2005.
- [22] A. Zhong, J. Tana, H. Huanga, S. Chena, M. Wanga, and S. Xua, "Thickness effect on the evolution of morphology and optical properties of ZnO films," *Applied Surface Science*, vol. 257, no. 9, pp. 4051-4055, 2011.
- [23] Y. H. Kang, J.-H. Choi, T. I. Lee, W. Lee, and J.-M. Myoung, "Thickness dependence of the resistive switching behavior of nonvolatile memory device structures based on undoped ZnO films," *Solid State Communications*, vol. 151, no. 23, pp. 1739-1742, 2011.
- [24] L. Xu, X. Li, Y. Chen, and F. Xu, "Structural and optical properties of ZnO thin films prepared by sol-gel method with different thickness," *Applied Surface Science*, vol. 257, no. 9, pp. 4031-4037, 2011.
- [25] W. Kern, "The evolution of silicon wafer cleaning technology," *Journal of the Electrochemical Society*, vol. 137, no. 6, pp. 1887-1892, 1990.
- [26] M. Benhaliliba, C. E. Benouis, M. S. Aida, F. Yakuphanoglu, and A. Sanchez Juarez, "Indium and aluminium-doped ZnO thin films deposited onto FTO substrates: nanostructure, optical, photoluminescence and electrical properties," *Journal of Sol-Gel Science and Technology*, vol. 55, no. 3, pp. 335-342, 2010.
- [27] S. Ilican, Y. Caglar, M. Caglar, and F. Yakuphanoglu, "Electrical conductivity, optical and structural properties of indium-doped ZnO nanofiber thin film deposited by spray pyrolysis method," *Physica E*, vol. 35, no. 1, pp. 131-138, 2006.
- [28] A. S. Gadallah and M. M. E. Nahass, "Structural, optical constants and photoluminescence of ZnO thin films grown by Sol-Gel spin coating," *Advances in Condensed Matter Physics*, vol. 2013, Article ID 234546, 11 pages, 2013.
- [29] A. C. Rastogi, S. B. Desu, P. Bhattacharya, and R. S. Katiyar, "Effect of strain gradation on luminescence and electronic properties of pulsed laser deposited zinc oxide thin films," *Journal of Electroceramics*, vol. 13, no. 1-3, pp. 345-352, 2004.
- [30] C. V. Manzano, D. Alegre, O. C. Calero, B. Alen, and M. S. M. Gonzalez, "Synthesis and luminescence properties of electrodeposited ZnO films," *Journal of Applied Physics*, vol. 110, Article ID 043538, 3 pages, 2011.
- [31] J. C. Fan, K. M. Sreekanth, Z. Xie, S. L. Chang, and K. V. Rao, "p-type ZnO materials: theory, growth, properties and devices," *Progress in Materials Science*, vol. 58, no. 6, pp. 847-985, 2013.
- [32] S. Golshahi, S. M. Rozati, R. Martins, and E. Fortunato, "p-type ZnO thin film deposited by spray pyrolysis technique: the effect of solution concentration," *Thin Solid Films*, vol. 518, no. 4, pp. 1149-1152, 2009.
- [33] J. C. Sun, H. W. Liang, J. Z. Zhao et al., "Ultraviolet electroluminescence from n-ZnO:Ga/p-ZnO:N homojunction device on sapphire substrate with p-type ZnO:N layer formed by annealing in N<sub>2</sub>O plasma ambient," *Chemical Physics Letters*, vol. 460, no. 4-6, pp. 548-551, 2008.
- [34] L. Schmidt-Mende and J. L. MacManus-Driscoll, "ZnO—nanostructures, defects, and devices," *Materials Today*, vol. 10, no. 5, pp. 40-48, 2007.
- [35] M. Chen, Z. L. Pei, X. Wang et al., "Intrinsic limit of electrical properties of transparent conductive oxide films," *Journal of Physics D*, vol. 33, no. 20, pp. 2538-2541, 2000.
- [36] L. L. Chen, Z. Z. Ye, J. G. Lu et al., "Co-doping effects and electrical transport in In-N doped zinc oxide," *Chemical Physics Letters*, vol. 432, no. 1-3, pp. 352-355, 2006.
- [37] D. C. Look, "Electrical and optical properties of p-type ZnO," *Semiconductor Science and Technology*, vol. 20, no. 4, pp. 55-61, 2005.
- [38] H. B. Ye, J. F. Kong, W. Z. Shen, J. L. Zhao, and X. M. Li, "Temperature-dependent photoluminescence of undoped, N-doped and N-In codoped ZnO thin films," *Journal of Physics D*, vol. 40, no. 18, pp. 5588-5591, 2007.
- [39] L. Liu, J. Xu, D. Wang et al., "p-type conductivity in N-doped ZnO: the role of the N<sub>Zn</sub>-V<sub>O</sub> complex," *Physical Review Letters*, vol. 108, no. 21, Article ID 215501, 5 pages, 2012.
- [40] Ü. Özgür, Y. I. Alivov, C. Liu et al., "A comprehensive review of ZnO materials and devices," *Journal of Applied Physics*, vol. 98, Article ID 041301, 4 pages, 2005.
- [41] N. C. C. Lu, L. Gerzberg, C. Y. Lu, and J. D. Meindl, "Modeling and optimization of monolithic polycrystalline silicon resistors," *IEEE Transactions on Electron Devices*, vol. 28, no. 7, pp. 818-830, 1981.
- [42] J. L. Zhao, X. M. Li, A. Krtshil et al., "Ultraviolet and visible electroluminescence from n-ZnO/SiO<sub>x</sub>/(n,p)-Si heterostructured light-emitting diodes," *Applied Physics Letters*, vol. 90, Article ID 062118, 3 pages, 2007.
- [43] B. Wang, J. Min, Y. Zhao, W. Sang, and C. W. Gao, "The grain boundary related p-type conductivity in ZnO films prepared by ultrasonic spray pyrolysis," *Applied Physics Letters*, vol. 94, Article ID 192101, 3 pages, 2009.

## Research Article

# Synthesis of Vertically Aligned Carbon Nanotubes on Silicalite-1 Monolayer-Supported Substrate

Wei Zhao,<sup>1</sup> Bijay Basnet,<sup>2</sup> Sukeyoung Kim,<sup>1</sup> and Ik Jin Kim<sup>2</sup>

<sup>1</sup> School of Materials Science & Engineering, Yeungnam University, Gyeongsan City, Gyeongbuk 712-749, Republic of Korea

<sup>2</sup> Department of Materials Science and Engineering, Institute of Processing and Application of Inorganic Materials, Hanseo University, Seosan City, Chungnam 356-706, Republic of Korea

Correspondence should be addressed to Sukeyoung Kim; [sykim@yu.ac.kr](mailto:sykim@yu.ac.kr) and Ik Jin Kim; [ijkim@hanseo.ac.kr](mailto:ijkim@hanseo.ac.kr)

Received 19 October 2013; Accepted 23 December 2013; Published 10 February 2014

Academic Editor: Alireza Talebitaher

Copyright © 2014 Wei Zhao et al. This is an open access article distributed under the Creative Commons Attribution License, which permits unrestricted use, distribution, and reproduction in any medium, provided the original work is properly cited.

Monodisperse magnetic Fe<sub>3</sub>O<sub>4</sub> nanoparticles (NPs) with the size of ca. 3.5 nm were prepared and used as the catalysts for the synthesis of vertically aligned carbon nanotube (VACNT) arrays. A silicalite-1 microcrystal monolayer was used as the support layer between catalyst NPs and the silicon substrate. Compared to our previous report which used radio-frequency- (rf-) sputtered Fe<sub>2</sub>O<sub>3</sub> film as the catalyst, Fe<sub>3</sub>O<sub>4</sub> NPs that were synthesized by wet chemical method showed an improved catalytic ability with less agglomeration. The silicalite-1 crystal monolayer acted as an effective “buffer” layer to prevent the catalyst NPs from agglomerating during the reaction process. It is believed that this is the first report that realizes the vertical alignment of CNTs over the zeolite monolayer, namely, silicalite-1 microcrystal monolayer, instead of using the intermediate anodic aluminum oxide (AAO) scaffold to regulate the growth direction of CNT products.

## 1. Introduction

Carbon nanotubes (CNTs) have become the target of intense study owing to their unique nanostructure-dependent physical and chemical properties [1]. These distinctive characteristics arise from their different atomic structures and sizes. For example, CNTs can be either metallic or semiconducting according to their helicity and diameter [2]. The latter can also influence their mechanical properties, which can have a significant impact on their promising applications in many potential fields, such as nanoelectronic devices [3], composite materials [4], hydrogen storage media [5], and field emission devices [6].

Although not all the reported applications will require large scale CNT use, there are still some where the mass production of CNTs is strongly in demand. As a result, there is a need for facile and inexpensive approaches for the large scale production of CNTs. For some applications, such as scanning probes [7] and sensors [8] and field emitters in nanoelectronics [9], vertically aligned CNT (VACNT) arrays are particularly required through control and optimization of the diameter, wall structure, and areal density of CNTs.

A range of techniques have been developed for VACNT synthesis, such as HiPco [10], fluidized bed [11], and chemical vapor deposition (CVD) [12], and CVD has proven to be the most effective one. Although the growth of VACNT reduces or eliminates the necessity of postprocessing the as-produced CNTs, it is still dependent on the use of expensive substrate materials and deposition equipment, such as electron beam evaporation, which reduces the potential for scaling-up CNT production.

An important issue impeding such growth is the limited thermal stability of nanoparticles (NPs), because they tend to agglomerate into larger ones at elevated temperatures through atomic interdiffusion, also known as “Ostwald ripening” [13]. This will result in catalyst clusters without monodisperse diameters and quantifiable areal densities so that it is hardly to achieve self-oriented CNTs perpendicular to the substrate. Therefore, an efficient substrate that can stabilize catalyst NPs at high temperatures is necessary. Many templates, such as porous anodic aluminum oxide (AAO) [14] and block copolymer micelles [15], have been used.

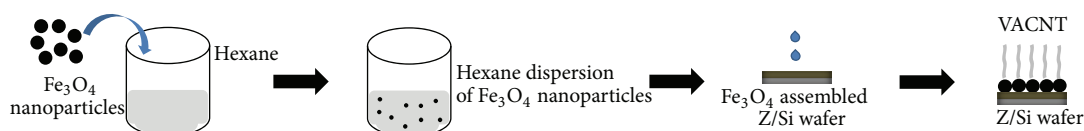


FIGURE 1: Synthesis of VACNT arrays on a silicalite-1 monolayer-assembled Si wafer using the synthesized  $\text{Fe}_3\text{O}_4$  NPs as the catalysts.

In this study, we reported a simple approach that used pre-made monodisperse  $\text{Fe}_3\text{O}_4$  nanoparticles (NPs),  $\sim 3.5$  nm in size, as the catalysts and self-assembled silicalite-1 monolayer as the support layer to synthesize VACNT arrays by catalytic CVD (CCVD). The difference of this study from others is that the silicalite-1 microcrystals were self-assembled on the silicon (Si) wafers in the form of a monolayer to be used as a “buffer” layer, instead of AAO scaffold [16] or  $\text{Al}_2\text{O}_3$  layer [17], to support  $\text{Fe}_3\text{O}_4$  catalyst NPs. As far as we know, this is the first report on the synthesis of VACNTs using well-oriented zeolite monolayer to replace other commonly-used templates mentioned above as the support layer.

## 2. Experimental

**2.1. Preparation of  $\text{Fe}_3\text{O}_4$  NPs.** Monodisperse  $\text{Fe}_3\text{O}_4$  NPs were prepared using the method reported elsewhere [18]. Briefly, 1 mmol  $\text{Fe}(\text{acac})_3$ , 5 mmol 1,2-hexadecanediol (HDD), 4.5 mmol oleic acid (OA), 3 mmol oleylamine (OAm), and 10 mL phenyl ether (PE) were mixed and heated under reflux for 30 min with vigorous stirring under a mild nitrogen ( $\text{N}_2$ ) flow. Subsequently, the black mixture was cooled to room temperature by removing the heat source. The product was then precipitated with ethanol, centrifuged, and redispersed several times in hexane, resulting in a fine hexane dispersion of  $\text{Fe}_3\text{O}_4$  NPs.

**2.2. Self-Assembly of Silicalite-1 Monolayer onto the Si Wafer.** A silicalite-1 microcrystal monolayer was simply assembled using a previously reported procedure [19]. Briefly, Si wafers ( $1\text{ cm} \times 1\text{ cm}$ ) were cleaned thoroughly, and immersed in a diluted hydrofluoric acid solution to eliminate the oxidized surface. They were then rinsed with distilled (DI) water and dried in a high-purity  $\text{N}_2$  steam. To self-assemble the silicalite-1 microcrystals on the Si wafer, an ethanol solution of poly(ethylenimine) (PEI) was first spin-coated on the substrate. Approximately 5 mg of silicalite-1 microcrystals was gently rubbed on the wafer by a finger for 30 s to form a monolayer. Mild sonication of the coated wafer for several seconds in DI water is essential for removing the crystals physically-adsorbed on the monolayer. Subsequently, the silicalite-1-assembled Si wafers were dried by  $\text{N}_2$ , and they are signified as Z/Si.

**2.3. Synthesis of VACNT Arrays by CCVD.** To prepare the catalyst-supported substrate, one drop of a hexane dispersion of  $\text{Fe}_3\text{O}_4$  NPs was dropped onto Z/Si. The substrate is designated  $\text{Fe}_3\text{O}_4/\text{Z/Si}$ . After being dried in air for a short time, the substrate was inserted into a horizontal electric tubular furnace. Under an  $\text{Ar}/\text{H}_2$  atmosphere, the substrates were

heated from room temperature to 973 K. After pretreatment for 10 min,  $\text{C}_2\text{H}_2$  (10 sccm) was fed into the furnace with an  $\text{Ar}/\text{H}_2$  (200 sccm) flow at this temperature for CNT synthesis and growth.  $\text{C}_2\text{H}_2$  was then cut off and the reactor was cooled to room temperature under an  $\text{Ar}/\text{H}_2$  flow. Figure 1 shows the process for synthesizing the VACNT arrays.

## 3. Characterization

Powder X-ray diffraction (XRD, Rigaku D/max 2500 VL/PC) was performed using a  $\text{Cu K}\alpha$  radiation (40 kV, 40 mA,  $k = 1.5418 \text{ \AA}$ ). The patterns were recorded from  $10$  to  $80^\circ 2\theta$  in  $0.04^\circ$  steps with a counting time of 2 s per step. Field emission scanning electron microscopy (FESEM) images were collected on a SEM LEO 1530 VP microscope. High resolution transmission electron microscopy (HRTEM, JEOL JEM-3011) was carried out at an accelerating voltage of 200 kV. The samples were prepared by evaporating drops of a sonicated ethanol suspension onto a carbon-coated lacy film supported on a 3 mm diameter, 300-mesh copper grid.

## 4. Results and Discussion

The synthesized  $\text{Fe}_3\text{O}_4$  NPs were characterized by TEM, as shown in Figure 2. Figures 2(a) and 2(c) showed low and high magnification HRTEM images of the as-produced  $\text{Fe}_3\text{O}_4$  NPs without further size-sorting, respectively. Clear lattice fringes were observed (Figure 2(c)), indicating a single crystalline structure [20]. The distance between the two adjacent planes was  $\sim 2.52 \text{ \AA}$ , which corresponds to the (311) plane of the FCC structured  $\text{Fe}_3\text{O}_4$ .

The selected area electron diffraction (SAED) patterns revealed six distinct rings, and the calculated d-spacings matched well with the interplanar distances of face-centered cubic (FCC)  $\text{Fe}_3\text{O}_4$ , as shown in Figure 2(b).

More than 100 NPs were measured to obtain the size distribution, which is shown in Figure 3. The particles were monodisperse with a size of approximately 3.5 nm, which is also in accordance with the TEM results shown above.

According to a previous report [19], the silicalite-1 crystals with a mean size of  $1.5 \times 1.1 \times 0.6 \mu\text{m}^3$  were assembled onto a Si wafer in the form of a monolayer by finger rubbing, as shown in Figures 4(a) and 4(b). Compared to the random orientation of pristine silicalite-1 crystals shown in the inset of Figure 4(a), Figures 4(a) and 4(b) show crystals all with b-axes perpendicular to the Si wafer surface, which was confirmed by the cross-sectional view, as shown in Figure 4(c). In addition, almost the entire Si surface was covered with the crystals. The same results were verified by

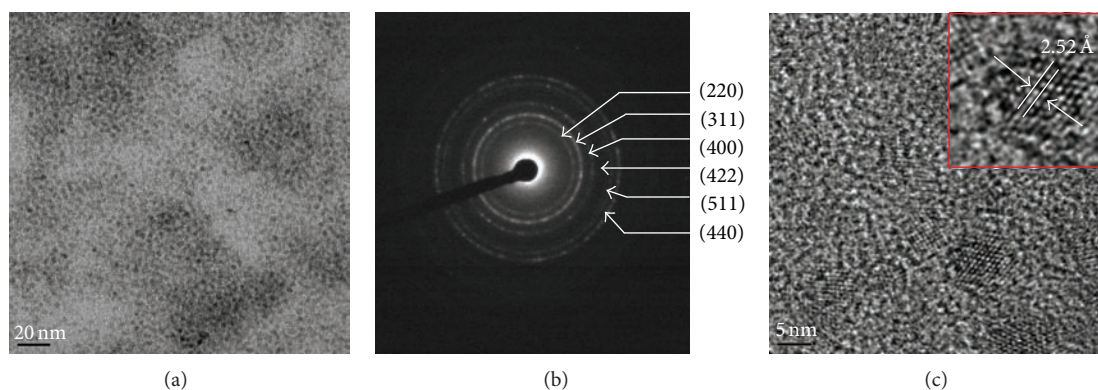


FIGURE 2: (a) Low magnification TEM image, (b) selected area electron diffraction pattern, and (c) high magnification TEM image of synthesized  $\text{Fe}_3\text{O}_4$  NPs (inset: a single  $\text{Fe}_3\text{O}_4$  NP).

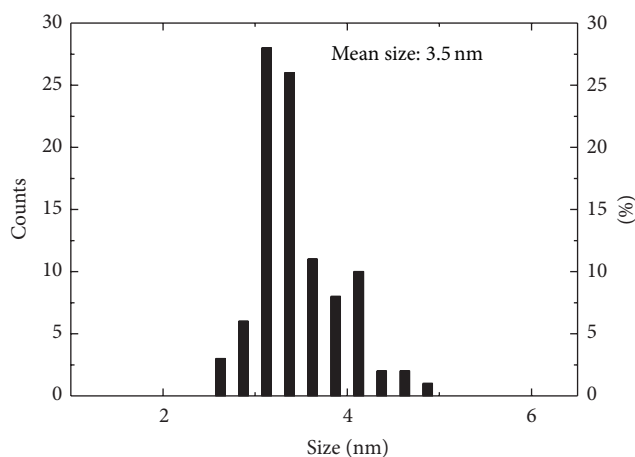


FIGURE 3: Size distribution of the synthesized  $\text{Fe}_3\text{O}_4$  NPs.

XRD patterns of monolayer-assembled and pristine silicalite-1 crystals, as shown in Figure 4(d) and its inset, respectively. A comparison between the two patterns revealed that only five ( $0\ k\ 0$ ) reflection planes ( $k = 2, 4, 6, 8,$  and  $10$ ) at  $8.9, 17.8, 26.8, 36.0,$  and  $45.5^\circ\ 2\theta$  were shown after the assembling of the silicalite-1 crystal monolayer, as shown in Figure 4(d), indicating the uniform orientation of the microcrystals on the Si wafer. This is obviously different from that of the pristine random crystals, shown by the XRD pattern in the inset of Figure 4(d).

VACNT arrays on the Z/Si were synthesized according to the experimental procedures described above. Figure 5 shows representative FESEM images of the samples. As shown in Figure 5(a), a CNT “carpet” formed on top of the Z/Si. From the view of the locally enlarged area, as presented in Figure 5(b), the CNTs exhibited a vertical orientation to a large extent. In addition, the CNTs synthesized were typically multiwalled CNTs, and their mean inner and outer diameters were estimated to be 7.5 and 17.5 nm, respectively, as shown in the inset of Figure 5(b). Compared with our previous study [19] that used radio-frequency- (rf-) sputtered  $\text{Fe}_2\text{O}_3$  film as the catalysts, the CNTs synthesized

in this study showed a great improvement. As shown in Figure S1(a) in the Supplementary Material available online at <http://dx.doi.org/10.1155/2014/327398>, CNTs synthesized from rf-sputtered  $\text{Fe}_2\text{O}_3$  film showed random growth directions and distinct diameter distribution. Quite a number of CNTs grew directly on the Si wafer surface between silicalite-1 crystals, and even those grown on the silicalite-1 crystals could hardly keep vertical-alignment tendency, as shown in Figure S1(b). Moreover, some fiber-like thick products were observed, as shown in Figure S1(a), indicating the formation of more defects and broad diameter distribution. One explanation for this phenomenon is the serious agglomeration of catalyst NPs [19], which could be observed from Figure S2. In Figure S2(a), the continuous  $\text{Fe}_2\text{O}_3$  film showed domains of  $\text{Fe}_2\text{O}_3$ , with the size being approximately 15~18 nm, which seemed enough for CNT synthesis. However, in Figure S2(b), the  $\text{Fe}_2\text{O}_3$  particles showed a strong agglomeration, leading to even large clusters. As a result, it not only led to a lower catalytic ability for CNT formation but also shrank areal density of catalyst NPs, which could compromise their initial crowding and continuous growing upward [21]. In addition, when the catalyst clusters were too large, the role of silicalite-1 crystal layer became insignificant because the pore size of the silicalite-1 crystals is just a few Angstroms. In contrast, in this study, monodisperse  $\text{Fe}_3\text{O}_4$  NPs with the 3.5 nm size were used, aiming at increasing the areal density [22] of the catalyst NPs on the substrate. Moreover,  $\text{H}_2$  used in this study reduced  $\text{Fe}_3\text{O}_4$  NPs to discrete Fe NPs, preventing them from agglomeration [23] and also reduced the rate of carbon production by dehydrogenation [24] so that the more ordered and thermodynamically stable CNTs can be produced rather than the less ordered and unstable soot and carbon fibers obtained in our previous study. As shown in Figure 5, it is confirmed that main products were MWCNTs without thicker carbon fibers, and synthesized CNTs showed a uniform vertical-alignment tendency, indicating the advantage of using smaller monodisperse catalyst NPs over rf-sputtered ones and that of adding  $\text{H}_2$ .

The mean diameter of the synthesized CNTs was several times larger than the original NP size, which can be explained by unavoidable coalescence during the heat-treatment.

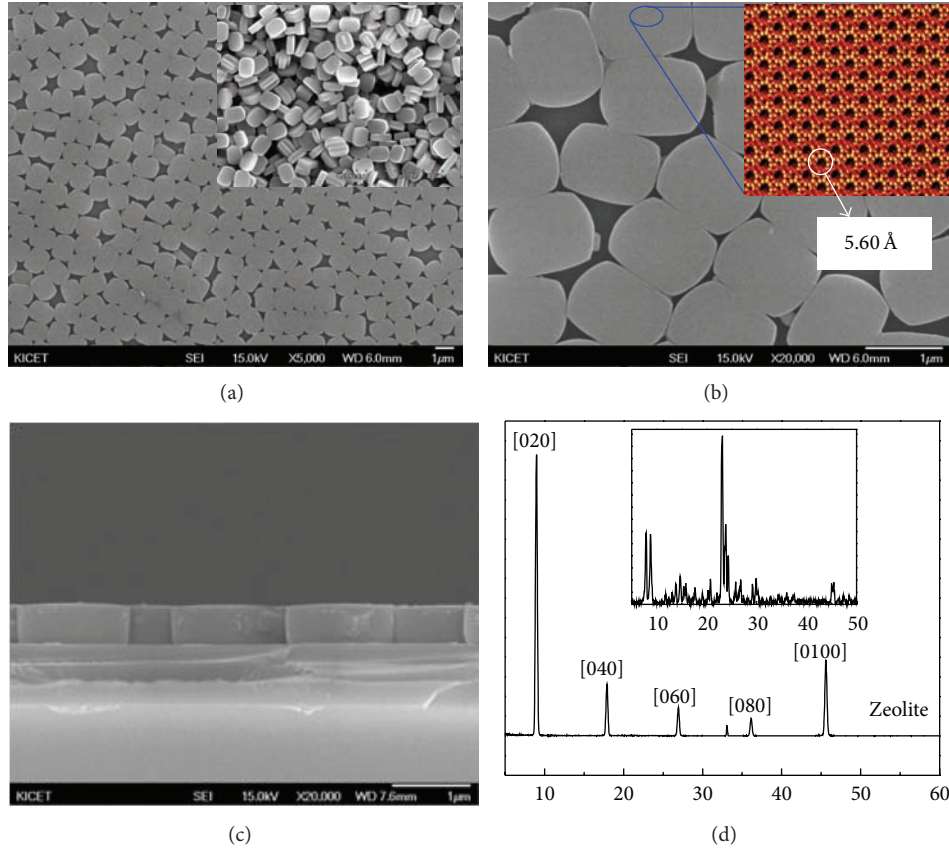


FIGURE 4: (a) Low magnification SEM image of the Z/Si substrate (vertical view) and as-synthesized silicalite-1 crystals (inset), (b) high magnification SEM image of uniformly oriented Z/Si substrate (vertical view) and the pore structure on the (100) sheet (inset), (c) SEM image of uniformly-oriented Z/Si substrate (sectional view), and (d) XRD pattern of uniformly-oriented silicalite-1 monolayer-assembled Si wafer and as-synthesized silicalite-1 crystals (inset).

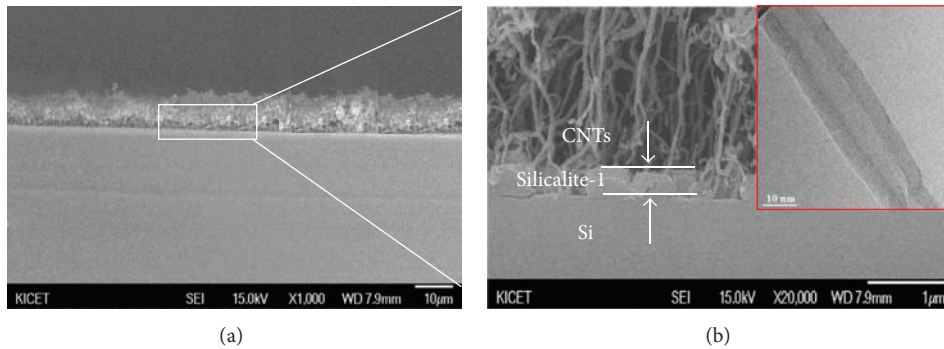


FIGURE 5: Cross-sectional SEM images of vertically aligned carbon nanotube arrays synthesized from  $\text{Fe}_3\text{O}_4/\text{Z}/\text{Si}$ . (a) Macroscale view and (b) enlarged view of the selected area (inset: synthesized MWCNT along with the mean diameter).

Despite this, the relatively thinner diameters compared to the previous results suggest that silicalite-1 crystals played a significant role in stabilizing and isolating the catalyst NPs to prevent them from coalescing under elevated temperatures. Therefore, the high density of NPs on the substrate could be retained to guarantee the synthesis of VACNT arrays with thinner diameters.

## 5. Conclusions

In this study, we reported the synthesis of vertically-aligned carbon nanotube (VACNT) arrays by using monodisperse magnetic  $\text{Fe}_3\text{O}_4$  NPs with the size of ca. 3.5 nm as the catalysts and a silicalite-1 microcrystal monolayer as the “buffer” layer between catalyst NPs and the silicon substrate.

As far as we know, this is the first report succeeding in VACNT synthesis using the assembled silicalite-1 monolayer as the support layer rather than intermediate AAO scaffold and others. Fe<sub>3</sub>O<sub>4</sub> NPs of 3.5 nm size that were synthesized by wet chemical method showed an improved catalytic ability and provided a large catalyst surface density. And the silicalite-1 crystal monolayer acted as an effective “buffer” layer to stabilize the catalyst NPs from agglomerating during the reaction process. An ensemble of VACNT arrays was obtained despite some disturbance of a small number of random CNTs catalyzed from the NPs deposited directly on the Si wafer between the gaps of the silicalite-1 crystals.

## Conflict of Interests

The authors declare that there is no conflict of interests regarding the publication of this paper.

## Acknowledgments

This study was supported by a grant from the 2012 Fundamental R&D Program of Hanseo University, Korea, and by the National Research Foundation of Korea (NRF) grant funded by the Korean government (MEST).

## References

- [1] C. H. Yu, L. Shi, Z. Yao, D. Li, and A. Majumdar, “Thermal conductance and thermopower of an individual single-wall carbon nanotube,” *Nano Letters*, vol. 5, no. 9, pp. 1842–1846, 2005.
- [2] T. W. Odom, J.-L. Huang, P. Kim, and C. M. Lieber, “Structure and electronic properties of carbon nanotubes,” *Journal of Physical Chemistry B*, vol. 104, no. 13, pp. 2794–2809, 2000.
- [3] A. Bachtold, P. Hadley, T. Nakanishi, and C. Dekker, “Logic circuits with carbon nanotube transistors,” *Science*, vol. 294, no. 5545, pp. 1317–1320, 2001.
- [4] P. Calvert, “Nanotube composites: a recipe for strength,” *Nature*, vol. 399, no. 6733, pp. 210–211, 1999.
- [5] A. C. Dillon, K. M. Jones, T. A. Bekkedahl, C. H. Kiang, D. S. Bethune, and M. J. Heben, “Storage of hydrogen in single-walled carbon nanotubes,” *Nature*, vol. 386, no. 6623, pp. 377–379, 1997.
- [6] W. I. Milne, K. B. K. Teo, G. A. J. Amaratunga et al., “Carbon nanotubes as field emission sources,” *Journal of Materials Chemistry*, vol. 14, no. 6, pp. 933–943, 2004.
- [7] T. W. Odom, J. H. Hafner, and C. M. Lieber, “Scanning probe microscopy studies of carbon nanotubes,” in *Carbon Nanotubes*, vol. 80 of *Topics in Applied Physics*, pp. 173–211, Springer, Berlin, Germany, 2001.
- [8] G. Chen, T. M. Paronyan, E. M. Pigos, and A. R. Harutyunyan, “Enhanced gas sensing in pristine carbon nanotubes under continuous ultraviolet light illumination,” *Scientific Reports*, vol. 2, article 343, pp. 1–7, 2012.
- [9] A. D. H. Walt, A. Châtelain, and D. Ugarte, “A carbon nanotube field-emission electron source,” *Science*, vol. 270, no. 5239, pp. 1179–1180, 1995.
- [10] P. Nikolaev, M. J. Bronikowski, R. K. Bradley et al., “Gas-phase catalytic growth of single-walled carbon nanotubes from carbon monoxide,” *Chemical Physics Letters*, vol. 313, no. 1-2, pp. 91–97, 1999.
- [11] Q. Zhang, M.-Q. Zhao, J.-Q. Huang et al., “Vertically aligned carbon nanotube arrays grown on a lamellar catalyst by fluidized bed catalytic chemical vapor deposition,” *Carbon*, vol. 47, no. 11, pp. 2600–2610, 2009.
- [12] R. Xiang, G. Luo, Z. Yang, Q. Zhang, W. Qian, and F. Wei, “Large area growth of aligned CNT arrays on spheres: cost performance and product control,” *Materials Letters*, vol. 63, no. 1, pp. 84–87, 2009.
- [13] X. Wang, P. J. Krommenhoek, P. D. Bradford et al., “Coating alumina on catalytic iron oxide nanoparticles for synthesizing vertically aligned carbon nanotube arrays,” *ACS Applied Materials & Interfaces*, vol. 3, no. 11, pp. 4180–4184, 2011.
- [14] E. J. Bae, W. B. Choi, K. S. Jeong et al., “Selective growth of carbon nanotubes on pre-patterned porous anodic aluminum oxide,” *Advanced Materials*, vol. 14, no. 4, pp. 277–279, 2002.
- [15] R. D. Bennett, G. Y. Xiong, Z. F. Ren, and R. E. Cohen, “Using block copolymer micellar thin films as templates for the production of catalysts for carbon nanotube growth,” *Chemistry of Materials*, vol. 16, no. 26, pp. 5589–5595, 2004.
- [16] P. Hou, C. Liu, C. Shi, and H. Cheng, “Carbon nanotubes prepared by anodic aluminum oxide template method,” *Chinese Science Bulletin*, vol. 57, no. 2-3, pp. 187–204, 2012.
- [17] K. Hata, D. N. Futaba, K. Mizuno, T. Namai, M. Yumura, and S. Iijima, “Water-assisted highly efficient synthesis of impurity-free single-walled carbon nanotubes,” *Science*, vol. 306, no. 5700, pp. 1362–1364, 2004.
- [18] S. Sun, H. Zeng, D. B. Robinson et al., “Monodisperse MFe<sub>2</sub>O<sub>4</sub> (M = Fe, Co, Mn) Nanoparticles,” *Journal of the American Chemical Society*, vol. 126, no. 1, pp. 273–279, 2004.
- [19] W. Zhao, H. S. Kim, D. N. Seo, A. Pokhrel, H. T. Kim, and I. J. Kim, “Assembled monolayer of silicalite-1-supported iron oxide nanoparticles for carbon nanotube growth by catalytic chemical vapour deposition,” *Asian Journal of Chemistry*, vol. 24, no. 11, pp. 5249–5252, 2012.
- [20] X. Li, H. Si, J. Z. Niu et al., “Size-controlled syntheses and hydrophilic surface modification of Fe<sub>3</sub>O<sub>4</sub>, Ag, and Fe<sub>3</sub>O<sub>4</sub>/Ag heterodimer nanocrystals,” *Dalton Transactions*, vol. 39, no. 45, pp. 10984–10989, 2010.
- [21] R. D. Bennett, A. J. Hart, and R. E. Cohen, “Controlling the morphology of carbon nanotube films by varying the areal density of catalyst nanoclusters using block-copolymer micellar thin films,” *Advanced Materials*, vol. 18, no. 17, pp. 2274–2279, 2006.
- [22] Y. M. Li, W. Kim, Y. G. Zhang, M. Rolandi, D. W. Wang, and H. J. Dai, “Growth of single-walled carbon nanotubes from discrete catalytic nanoparticles of various sizes,” *Journal of Physical Chemistry B*, vol. 105, no. 46, pp. 11424–11431, 2001.
- [23] H. Kim, J. Kang, Y. Kim, B. H. Hong, J. Choi, and S. Iijima, “Synthesis of ultra-long super-aligned double-walled carbon nanotube forests,” *Journal of Nanoscience and Nanotechnology*, vol. 11, no. 1, pp. 470–473, 2011.
- [24] W. Wasel, K. Kuwana, P. T. A. Reilly, and K. Saito, “Experimental characterization of the role of hydrogen in CVD synthesis of MWCNTs,” *Carbon*, vol. 45, no. 4, pp. 833–838, 2007.